



University
of Glasgow

Watts, Christopher Mark (2009) *A comparison study of biologically inspired propulsion systems for an autonomous underwater vehicle*. PhD thesis.

<http://theses.gla.ac.uk/1672/>

Copyright and moral rights for this thesis are retained by the author

A copy can be downloaded for personal non-commercial research or study, without prior permission or charge

This thesis cannot be reproduced or quoted extensively from without first obtaining permission in writing from the Author

The content must not be changed in any way or sold commercially in any format or medium without the formal permission of the Author

When referring to this work, full bibliographic details including the author, title, awarding institution and date of the thesis must be given.

*A Comparison Study of Biologically Inspired
Propulsion Systems for an Autonomous
Underwater Vehicle.*

A Thesis submitted in partial fulfilment
for the Degree of Doctor of Philosophy
to the Faculty of Engineering
at the University of Glasgow

By

Christopher Mark Watts

September 2009

Abstract

The field of Autonomous Underwater Vehicles (AUVs) has increased dramatically in size and scope over the past two decades. Application areas for AUVs are numerous and varied; from deep sea exploration, to pipeline surveillance to mine clearing. However, one limiting factor with the current technology is the duration of missions that can be undertaken and one contributing factor to this is the efficiency of the propulsion system, which is usually based on marine propellers.

As fish are highly efficient swimmers greater propulsive efficiency may be possible by mimicking their fish tail propulsion system. The main concept behind this work was therefore to investigate whether a biomimetic fish-like propulsion system is a viable propulsion system for an underwater vehicle and to determine experimentally the efficiency benefits of using such a system. There have been numerous studies into biomimetic fish like propulsion systems and robotic fish in the past with many claims being made as to the benefits of a fish like propulsion system over conventional marine propulsion systems. These claims include increased efficiency and greater manoeuvrability. However, there is little published experimental data to characterise the propulsive efficiency of a fish like propulsive system. Also, very few direct experimental comparisons have been made between biomimetic and conventional propulsion systems. This work attempts to address these issues by directly comparing experimentally a biomimetic underwater propulsion system to a conventional propulsion system to allow for a better understanding of the potential benefits of the biomimetic system.

This work is split into three parts. Firstly, the design and development of a novel prototype vehicle called the *RoboSalmon* is covered. This vehicle has a biomimetic tendon drive propulsion system which utilizes one servo motor for actuation and has a suite of onboard sensors and a data logger. The second part of this work focuses on the development of a mathematical model of the *RoboSalmon* vehicle to allow for a better understanding of the dynamics of the system. Simulation results from this model are compared to the experimental results and show good correlation.

The final part of the work presents the experimental results obtained comparing the *RoboSalmon* prototype with the biomimetic tail system to the propeller and rudder system. These experiments include a study into the straight swimming performance, recoil motion, start up transients and power consumption. For forward swimming the maximum surge velocity of the *RoboSalmon* was 0.18ms^{-1} and at this velocity the biomimetic system was found to be more efficient than the propeller system. When manoeuvring the biomimetic system was found to have a significantly reduced turning radius.

The thesis concludes with a discussion of the main findings from each aspect of the work, covering the benefits obtained from using the tendon drive system in terms of efficiencies and manoeuvring performance. The limitations of the system are also discussed and suggestions for further work are included.

Acknowledgements

My appreciation and thanks go to Dr Euan McGookin for his supervision and guidance over the past four years.

I would also like to thank Dr Martin Macauley for his guidance, support and advice throughout my time at the University of Glasgow.

This work would not have been possible without the funding provided by the EPSRC so I would like to thank them for the opportunity to conduct this research. Also, without the support of the Department of Electronics & Electrical Engineering and the Department of Aerospace Engineering at the University of Glasgow this research would not have been possible.

I would like to thank the following two organisations:

The IEEE Oceanic Engineering Society, especially Col. Norman Miller, for the Travel Grant to attend the MTS/IEEE Oceans Vancouver 2007 Student Poster Program and subsequent prize awarded by them to myself

DSTL for the organising and running of the 2006 SAUC-E Challenge and for the prize awarded to the University of Glasgow Team.

Throughout the course of this project a numerous people have provided guidance, assistance and advice so I would also like to offer thanks to the following people:

Dr David Muir, Dr Kevin Worrall, Dr Dave Anderson, Jon Trinder, Stuart Mclean, Lynsey Stewart, Neil Owen, Tony Smedley, Ian Brown, Brian McNally, Scott Devine, Stephen Glancy, David Watson, Stephen Watson, Colin Souza, Alan Birkbeck, Dr Colin Adams, Guillaume Dauphin, Nicola Bissett, Shona Ballantyne, Stuart Fairbairn, and Peter McKenna,

I would like to thank my family for all their patience and support throughout the course of this project especially my Gran, Uncle Gary, Auntie Mary and Cousin Amy.

A special thank you must go to my girlfriend Patricia Doyle for all her support, encouragement and assistance throughout this project.

Most of all I must say a huge thank you to my sister Laura, my Mum, Jean Watts and my Dad, Dr Mark Watts for the vast amounts of support and encouragement they provided. Without their input this thesis would not have been possible.

Contents

Abstract	i
Acknowledgments	ii
Table of Contents	iii
Table of Figures.....	vii
Table of Tables	xiv
1. Introduction	
1.1. Preface	1
1.2. Biomimetics	2
1.3. Why a Salmon?	3
1.4. Biomimetic Propulsion Research	4
1.5. Objectives	4
1.6. Contribution to the field.....	5
1.7. Thesis Structure	6
2. Background & Literature Review	
2.1. Introduction	8
2.2. Submarines, Submersibles & Unmanned Underwater Vehicles.....	8
2.2.1. Remotely Operated Vehicles (ROVs)	9
2.2.2. Autonomous Underwater Vehicles	10
2.2.3. Undersea Gliders.....	12
2.3. Biomimetics	13
2.3.1. Biomimetic Robots	14
2.3.2. Fish- Like Biomimetic Underwater Propulsion	15
2.4. Robotic Fish Projects.....	16
2.4.1. Mitsubishi Heavy Industries	16
2.4.2. MIT: <i>RoboPike</i> , <i>RoboTuna</i> & <i>The VCUUV</i>	17
2.4.3. University of Essex Robotic Fish.....	20
2.4.4. University of Washington	21
2.4.5. PoTuna	21
2.4.6. Chinese Academy of Science & Peking University.....	21
2.5. Student Autonomous Underwater Challenge – Europe (SAUC-E)	22
2.6. Summary	23
3. The <i>RoboSalmon</i>	
3.1. Introduction	24
3.2. Basic Biology of Fish	25
3.2.1. Fish Morphology.....	25
3.2.2. Fish Fins	26
3.2.3. Buoyancy.....	27
3.2.4. Stability	28
3.2.5. Propulsion Techniques & Classifications	28
3.3. <i>RoboSalmon</i> Hardware	30
3.3.1. <i>RoboSalmon</i> V1.0 Prototype.....	31
3.3.2. <i>RoboSalmon</i> V2.0.....	31

3.3.3.	Tail Propulsion Systems	33
3.3.3.1.	<i>Tendon Drive System</i>	34
3.3.3.2.	<i>Caudal Fin</i>	35
3.3.3.3.	<i>Propeller and Rudder System</i>	36
3.3.4.	Body Section	38
3.3.4.1.	<i>Central PIC</i>	40
3.3.4.2.	<i>Data Logger</i>	40
3.3.4.3.	<i>Inertial Measurement Unit</i>	42
3.3.4.4.	<i>CAN Communications</i>	43
3.3.4.5.	<i>Remote Control</i>	44
3.3.4.6.	<i>Umbilical Connection</i>	46
3.3.4.7.	<i>Pectoral Fins</i>	46
3.3.4.8.	<i>Actuated Head</i>	48
3.3.4.9.	<i>Power System</i>	48
3.4.	Summary	50
4.	Mathematical Model of the <i>RoboSalmon</i>	
4.1.	Introduction	52
4.2.	State Space Modelling	53
4.3.	Model Variables and Reference Frames	54
4.4.	Vehicle Kinematics	56
4.5.	Vehicle Dynamics	57
4.5.1.	Rigid Body Dynamics	57
4.5.2.	Inertia Matrix	58
4.5.3.	Coriolis & Centripetal Terms	59
4.5.4.	Hydrodynamic Added Mass Terms	60
4.5.5.	Restoring Forces and Moments	61
4.5.6.	Hydrodynamic Damping Terms	63
4.6.	Propulsion System Modelling	64
4.6.1.	Tendon Drive System	64
4.6.1.1.	<i>Servo Motor Model</i>	65
4.6.1.2.	<i>Tendon Displacements</i>	66
4.6.1.3.	<i>Tendon Tail Kinematics</i>	68
4.6.1.4.	<i>Tendon Tail Thrust Estimate</i>	70
4.6.1.5.	<i>Tendon Tail Manoeuvring</i>	72
4.6.1.6.	<i>Recoil Motion</i>	73
4.6.1.7.	<i>Tendon Drive System: Input Forces & Moments</i>	75
4.6.2.	Propeller and Rudder System	75
4.7.	<i>RoboSalmon</i> State Space Equations	78
4.8.	Model Validation & Data Collection	79
4.8.1.	Model Validation	79
4.8.1.1.	<i>Analogue Matching</i>	79
4.8.1.2.	<i>Integral Least Squares</i>	80
4.8.2.	Data Collection	81
4.8.2.1.	<i>Laboratory Equipment</i>	81
4.8.2.2.	<i>Camera System</i>	82
4.8.2.3.	<i>Image Processing</i>	78
4.8.2.4.	<i>Sensor Data Post Processing</i>	84
4.9.	Summary	86
5.	Experimental Results: <i>Forward Motion</i>	
5.1.	Introduction	87
5.2.	Experimental Procedure	87
5.2.1.	Experimental Programmes	89

5.3. Tail Beat Frequency & Amplitude	92
5.3.1. Comparison to real Salmon Performance	95
5.3.2. Tendon Drive Start Up Characteristics	97
5.3.3. Strouhal Number	99
5.3.4. Power	100
5.3.4.1. Real Salmon Power Output	103
5.4. Recoil Motion	105
5.4.1. Phase of Recoil.....	110
5.4.2. Power Expended due to recoil.....	110
5.5. Actuated Head.....	112
5.6. Mechanical Tail Vs. Propeller System.....	116
5.6.1. Speed Comparisons.....	118
5.6.2. Start up transients.....	119
5.6.3. Power Comparisons	122
5.7. Summary	124
6. Results: <i>Manoeuvring</i>	
6.1. Introduction	126
6.2. Experimental Approach.....	126
6.2.1 Standard Turns	126
6.2.2 Turning Circle.....	127
6.2.3 Zig-Zag.....	127
6.2.4 Pull Out manoeuvre	128
6.2.5 Stopping Test.....	128
6.2.7 Spiral Manoeuvre.....	128
6.3. Standard Turning	128
6.3.1. Turning from Stationary	129
6.3.2. Turning at Speed.....	134
6.3.3. Coasted Turns	137
6.4. Actuated Head.....	139
6.4.1. Actuated Head Only Turning	139
6.4.2. Actuated Head and Tail.....	142
6.4.2.1. Turning from Stationary.....	142
6.4.2.2. Turning at Speed.....	144
6.5. Turning Circle.....	147
6.6. Pull Out Manoeuvre	148
6.7. Power Consumption	151
6.8. Propeller & Rudder Based System	152
6.8.1. Turning from Stationary	152
6.8.2. Turning at Speed.....	154
6.9. Comparison of Tendon drive and Propeller/Rudder Systems	155
6.10 Summary	157
7. Results: <i>Simulation</i>	
7.1. Introduction	159
7.2. Tendon Drive Simulation.....	159
7.2.1. Swimming with High Tail Beat Frequencies	159
7.2.2. Turning Circle.....	163
7.2.3. Burst-Coast Swimming.....	164
7.2.4. Zig-Zag Manoeuvre	165
7.3. Individually Actuated System Simulation.....	167
7.3.1. Modelling	167
7.3.1.1. Kinematic Curve Fitting.....	167
7.3.2. Servo Motors	169

7.3.3. Recoil Motion	169
7.3.4. Individually Actuated System: Overall Input Forces & Moments.....	170
7.3.5. Individually Actuated System: Surge Simulations	171
7.3.6. Individually Actuated System : <i>Manoeuvring</i> Simulations	172
7.4 Summary	173
8. Conclusions and Further Work	
8.1. Conclusions.....	175
8.2. Further Work.....	178
8.3. Modelling and Simulation.....	178
8.4. Further Experimentation with RoboSalmon	179
8.5. Improvements to <i>RoboSalmon</i> Platform and System.....	179
9. References	181
Appendix A.1 <i>RoboSalmon</i> Circuit Schematics	193
Appendix A.2 Propeller System Bollard Pull Test Results	200
Appendix A.3 <i>RoboSalmon</i> Vehicle Specifications	202
Appendix B <i>RoboSalmon</i> Model Equations.....	204
Appendix C <i>RoboSalmon</i> Model Validation Results	206

Table of Figures

Chapter 2

Figure 2.1: Miniature ROV from RovTech Systems Limited.....	9
Figure 2.2: REMUS 100 System.....	11
Figure 2.3: Glider Illustration.....	13
Figure 2.4: Second <i>RoboTuna</i> prototype.....	19
Figure 2.5: University of Glasgow Entry to 2006 SAUC-E competition, the SHARC vehicle.....	23

Chapter 3

Figure 3.1: Features of fish.....	25
Figure 3.2: Pectoral fin arrangements in rainbow trout.....	26
Figure 3.3: Example of Fish Pectoral Fin.....	27
Figure 3.4: BCF Swimming Modes.....	29
Figure 3.5: RoboSalmon V1.0 initial prototype vehicle.....	31
Figure 3.6: <i>RoboSalmon</i> V2.0 vehicle with Tendon drive tail attached.....	32
Figure 3.7: Photograph of body section of RoboSalmon V2.0.....	33
Figure 3.8: Tendon drive tail assembly.....	34
Figure 3.9: Caudal Fin from <i>RoboSalmon</i> & Caudal fin from real Atlantic Salmon...36	
Figure 3.10: Propeller and Rudder Tail Actuation System.....	37
Figure 3.11: Propellers evaluated for prop tail system	37
Figure 3.12: Photograph of completed propeller and rudder tail assembly.....	38
Figure 3.13: <i>RoboSalmon</i> V2.0 Sub-System Interconnection.....	39
Figure 3.14: RF Remote Control Handset.....	44
Figure 3.15: MATLAB GUI for control of <i>RoboSalmon</i> over RF Remote Control.....	45
Figure 3.16: Diagram of NACA 0012 section.....	47
Figure 3.17: Plan view of pectoral fin dive planes.....	47
Figure 3.18: Diagram of actuated head.....	48

Figure 3.19: Simplified current sense circuit.....50

Chapter 4

Figure 4.1: Flowchart of state space modelling technique.....53

Figure 4.2: Illustration of Body-Fixed and Earth-Fixed reference Frames.....54

Figure 4.3: Prolate Ellipsoid with semi-axes a, b and c.....60

Figure 4.4: Restoring forces for roll on x-z plane.....62

Figure 4.5: Flowchart of Tendon Drive Propulsion System Model.....65

Figure 4.6: Simulated servo model response to step changes of ± 30 degrees.....66

Figure 4.7: Individual revolute joint assembly showing tendons and rib sections.....67

Figure 4.8: Joint and link representation of *RoboSalmon* tail assembly.....68

Figure 4.9: Comparison of Ideal and Obtained Tail Kinematics.....70

Figure 4.10: Plots of surge thrust X_t (top) and drag force X_{dn} (bottom)72

Figure 4.11: Diagram of tail sweep and thrust force.....72

Figure 4.12: Representation of recoil motion in roll.....73

Figure 4.13: Representation of recoil motion in yaw.....74

Figure 4.14: Thrust/Rotational speed relationship of 3 blade 50mm brass propeller...76

Figure 4.15: Diagram of forces and moments produced by rudder.....77

Figure 4.16: Analogue Matching Validation for Program 5.....80

Figure 4.17: Set up of laboratory experimental equipment.....82

Figure 4.18: Steps used in image processing.....83

Figure 4.19: Selection of logged onboard sensor readings.....85

Figure 4.20: Raw position data from image processing of video footage.....	85
----------------------------------------------------------------------------	----

Chapter 5

Figure 5.1: Flowchart of experimental procedure for 5 experimental runs.....	88
Figure 5.2: Data gathered from image processing.....	91
Figure 5.3: Sensor data logged onboard the tendon drive vehicle for Program 5.....	91
Figure 5.4: Plots of surge velocity versus tail beat frequency.....	93
Figure 5.5: 3D plot of all useable forward motion results.....	94
Figure 5.6: Illustration of caudal fin bending during one complete tail cycle.....	95
Figure 5.7: Comparison of estimated speed of real Atlantic Salmon to <i>RoboSalmon</i> ...	96
Figure 5.8: Start up characteristics in surge, u , & sway, v , for Program 18.....	97
Figure 5.9: Start up transients for 3 different programs	98
Figure 5.10: Trajectories of 5 runs of various programs indicating the x-y position data	99
Figure 5.11: Typical plots of <i>RoboSalmon</i> tail current, etc.....	101
Figure 5.12: Electrical power input to the tendon drive system.....	101
Figure 5.13: Plots of tail servo motor position.....	102
Figure 5.14: Surge Swimming Power calculated.....	103
Figure 5.15: Estimates of Salmon swimming power vs swimming speed.....	104
Figure 5.16: Typical yaw rate r (deg/s) experimental data.....	106
Figure 5.17: Typical Roll rate p (deg/s) experimental data from runs of all 9 experimental programs.....	107
Figure 5.18: Pitch rate q (deg/s) experimental data 15 runs experimental programs...	108
Figure 5.19: Quantitative comparison of magnitudes of recoil effects in roll, pitch and yaw angular velocities for straight swimming.....	108

Figure 5.20: Quantitative comparison of magnitudes of recoil oscillation effects in roll (phi), pitch (theta) and yaw (psi) angular displacements for straight swimming.....	109
Figure 5.21: Comparison of phase between tail motion; lateral velocity, yaw angular velocity and roll angular velocity.....	110
Figure 5.22: Average power expended for recoil motion in Roll and Yaw.....	112
Figure 5.23: <i>RoboSalmon</i> vehicle using actuated head whilst swimming.....	113
Figure 5.24: X-Y positional data for the <i>RoboSalmon</i> using Program 5.....	113
Figure 5.25: Roll rate for Program 5.....	114
Figure 5.26: Yaw rate for Program 5.....	115
Figure 5.27: Propeller current consumption and propeller rotational speed for typical run of Propeller Program 5.....	117
Figure 5.28: Surge velocity versus propeller speed for the Propeller based system for forward motion.....	118
Figure 5.29: Start up transients using Program 2, 3, 4 & 5 for propeller based system	119
Figure 5.30: Roll rate start up transients for propeller system.....	120
Figure 5.31: Pitch rate start up transients for propeller system.....	120
Figure 5.32: Yaw rate start up transients for propeller system.....	121
Figure 5.33: Power consumption vs surge velocity for propeller based system.....	122
Figure 5.34: Comparison of power consumption of tendon drive & propeller.....	123
Figure 5.35: Comparison of propulsive efficiencies for the tendon drive system and propeller system for surge motion.....	124

Chapter 6

Figure 6.1: Illustration of parameters calculated during <i>Turning Circle</i> manoeuvre ..	127
----------------------------------------------------------------------------------------------------	------------

Figure 6.2: x-y positional data for typical runs with beat amplitude 0.105m and beat frequency of 0.61Hz.....	129
Figure 6.3: Yaw rate data for typical runs with beat amplitude 0.105m and beat frequency of 0.61Hz	130
Figure 6.4: Yaw angle data for typical runs with beat amplitude 0.105m and beat frequency of 0.61Hz.....	130
Figure 6.5: Roll rate data for typical runs with beat amplitude 0.105m and beat frequency of 0.61Hz.....	131
Figure 6.6: Roll angle data for typical runs with beat amplitude 0.105m and beat frequency of 0.61Hz.....	132
Figure 6.7: Relationship between yaw rates and tail beat frequency and amplitude...134	
Figure 6.8: X-Y trajectory turning at speed manoeuvre for tail beat amplitude of 0.15m.....	135
Figure 6.9: Turning at speed manoeuvre yaw rates for tail beat amplitude of 0.15m..135	
Figure 6.10: Yaw angle for Turning at speed manoeuvre.....	136
Figure 6.11: X-Y positional data for coasted turns with three offsets with initial tail beat frequency.....	137
Figure 6.12: Yaw rate data for coasted turns for three tail offsets.....	138
Figure 6.13: Current consumption for coasted turn and turning at speed manoeuvre.139	
Figure 6.14: X-Y positional data for (a) Turning with head angled at 13.5°	140
Figure 6.15: Yaw rate data for Turning with head angled at 13.5°.....	141
Figure 6.16: X-Y positional data for turning from stationary manoeuvre.....	142
Figure 6.17: Yaw rate data for turning from stationary manoeuvre with actuated head	143
Figure 6.18: Roll rate data for turning from stationary manoeuvre with actuated head	143

Figure 6.19: Yaw angles for turning with actuated head and tail.....	144
Figure 6.20: X-Y positional data for powered turns with head offsets and head centred for comparison.....	145
Figure 6.21: Yaw rate data for powered turn with tail beat frequency of 0.48Hz.....	146
Figure 6.22: Roll rate data for powered turn with tail beat frequency of 0.48Hz.....	147
Figure 6.23: Turning circle parameters for RoboSalmon tendon drive system.....	148
Figure 6.24: X-Y positional data for Pull Out manoeuvre.....	149
Figure 6.25: Yaw rate and roll rate data for Pull Out manoeuvre.....	150
Figure 6.26: Current consumption for straight swimming and turning.....	151
Figure 6.27: X-Y trajectory of propeller and rudder system for rudder angles.....	153
Figure 6.28: Yaw rates obtainable for different propeller speeds for the propeller and rudder based system.....	153
Figure 6.29: X-Y trajectory for turning at speed manoeuvre for the propeller and rudder based system.....	155
Figure 6.30: Comparison of power consumptions for turning from stationary manoeuvre for tendon drive system and propeller system.....	156

Chapter 7

Figure 7.1: Simulated surge velocities at high tail beat frequencies with beat amplitude of 0.085m	160
Figure 7.2: Simulated surge velocities obtained for three tail beat frequencies.....	161
Figure 7.3: Comparison of estimated surge velocities with real Salmon.....	163
Figure 7.4: Simulated recoil motion in yaw & roll angles for high tail beat frequencies	163

Figure 7.5: Turning circle for tendon drive system with tail beat frequency of 1Hz and beat amplitude of 0.15m.....	164
Figure 7.6: Simulated Burst-Coast swimming for RoboSalmon.....	165
Figure 7.7: Simulated 20-20 Zig-Zag manoeuvre with tail beat frequency of 1Hz.....	166
Figure 7.8: Angular displacements of each individually actuated tail segment.....	168
Figure 7.9: Kinematics of <i>RoboSalmon</i> tail actuation systems.....	168
Figure 7.10: Illustration of tail mass distribution.....	170
Figure 7.11: Simulated surge velocities for the individually actuated tail system.....	171
Figure 7.12: Peak yaw angle and roll angle recoil for individually actuated system... 	172
Figure 7.13: Turning circle for individually actuated system with tail offset of 20° ...	173

Table of Tables

Chapter 3

Table 3.1: BCF Swimming Sub-Categories.....	30
Table 3.2: Data Logger sensor parameters.....	41

Chapter 4

Table 4.1: SNAME notation for marine vessels.....	55
Table 4.2: D-H Parameter Table Representation of Tendon Drive Tail.....	69

Chapter 5

Table 5.1: Tendon drive tail parameters altered for forward motion experiments.....	90
Table 5.2: Calculation of Strouhal Number of forward swimming.....	100
Table 5.3: Comparison of estimate of output swimming powers.....	105
Table 5.4: Surge velocities obtained when using Actuated Head.....	116
Table 5.5: Forward Motion Programs for Propeller System.....	117

Chapter 6

Table 6.1: Yaw and roll rates for turning from stationary manoeuvre.....	133
Table 6.2: Tail Parameters and Yaw rates for Turning at speed manoeuvre.....	136
Table 6.3: Average Yaw rates from Head Only Turning.....	140
Table 6.4: Tail Parameters and Yaw rates for Turning at speed manoeuvre.....	146
Table 6.5: Power consumption for turning with tendon drive system.....	152

Chapter 1 - Introduction

1.1 Preface

The interesting and diverse field of underwater robotics has increased extensively over the last two decades with numerous application areas driving the technological advancement [Wernli, 2002; Bingham, Drake, Hill & Lott, 2002]. One particular area that has developed rapidly is the multi-disciplinary field of unmanned underwater vehicles (UUVs) [Roberts & Sutton, 2006]. These are mobile underwater robots that are able to perform tasks in areas of underwater operation that may be restrictive or hazardous for human divers. The initial activity in this field involved maintenance and monitoring activities for the oil industry. This has developed into other application areas with more complex operational demands e.g. oceanographic surveys, pipeline surveillance [Norcross & Mueter, 1999], mine detection [Purcell, 2000] and deep sea exploration [Wernli, 2002]. These types of vehicles have proved to be extremely versatile and useful tools for assisting with the human exploration and utilisation of underwater natural resources.

UUVs fall into one of two main categories: remotely operated vehicles (ROVs) and Autonomous Underwater Vehicles (AUVs) [Roberts & Sutton, 2006]. ROVs, as the name suggests, are UUVs that receive operator commands and power via a tethered umbilical [Wernli, 2002]. This umbilical connects the ROV to a surface ship or platform where a human operator guides the vehicle remotely. The main advantage of this type of vehicle is that it does not need to carry its power supply onboard (i.e. no onboard batteries) and is supplied externally from an independent source [Blidberg, 2001]. This independence allows the vehicle to operate for a longer period of time as the power source is provided by a surface source. However, the umbilical physically restricts the operation range of the vehicle and its dexterity. This severely limits the utilisation capability of the ROV.

In contrast, AUVs are UUVs that operate without commands from a human operator and therefore do not require a physical umbilical connection [Wernli, 2002]. Although this provides manoeuvring freedom and a larger operational range than ROVs, as it does not have the restriction imposed by the umbilical, it does have to carry its own power supply and navigation systems. Both add to the payload of the vehicle and the capacity of the onboard power supply limits the range of the vehicle. Naturally extending the operational lifespan of the vehicle through improvements in power consumption is very desirable. Nevertheless, the main advantage of the AUV is the flexibility that the autonomy provides.

The onboard power source for most AUVs is usually electrical batteries [Wernli, 2002]. These batteries have to power all the onboard systems, including the propulsion system, which for most AUVs is based on marine propellers and control surfaces. This reliance on batteries limits the range and operational time available for the AUV to carry out its mission, which is usually in the region of

around 20 hours for mid-size AUVs [Purcell, *et al*, 2000]. There are also a number of mission types that require an AUV to maintain a low speed such as for inspection or intervention work [Bingham, *et al*, 2002]. AUVs are usually designed for high speed and are usually flight vehicles i.e. they rely on control surfaces and the lift they provide to manoeuvre. Using this type of design can lead to the performance of the AUV at low speed to be inefficient, which is a waste of valuable battery life and can therefore further reduce the mission duration.

Another issue with some conventional AUVs is their manoeuvrability at low speeds, which in some cases can limit the performance and operational capability of the vehicle [Anderson & Chhabra, 2002; Saunders & Nahon, 2002]. This manoeuvrability issue arises from the use of control surfaces on the flight vehicle type of AUVs. For these to provide control forces (i.e. a lift force similar to an aircraft wing) the vehicle has to be in motion and generate sufficient flow over the control surface. Some AUV designs utilise multiple propeller based thrusters positioned at each vehicle axis to increase the manoeuvrability. However this has the disadvantage of adding significantly to the power consumption requirements thus draining the battery more quickly.

Naturally, a more efficient and manoeuvrable means of propulsion would lead to an increase in the mission duration as well as the general performance of the vehicle. To find an alternative underwater propulsion technique to a propeller based system one does not have to look any further than nature. Fish have been propelling themselves in the aquatic environment for millions of years using only their tail and fins [Videler, 1993]. In addition certain species of fish show propulsion and manoeuvring characteristics that are far in advance of that capable of current AUV technology [Wolfgang, *et al*, 1999]. Such characteristics include accelerations of greater than 25g for short periods found in observations of pike [Videler, 1993], turning in under a body length in a fraction of a second for a numerous species including the angelfish [Videler, 1993] and a very high propulsive efficiency in a tuna [Triantafyllou & Triantafyllou, 1995]. The propulsion technique used by fish has been optimised by millions of years of biological evolution and could therefore be considered an optimal solution for underwater propulsion. By mimicking the method a fish uses to propel itself through the water (i.e. a fish tail) an underwater vehicle could obtain some of the beneficial swimming characteristics of fish.

This idea of mimicking concepts and solutions found in nature is not new, it has been around for centuries but only fairly recently has it been given the name *biomimetics* [Bar-Cohen, 2006]. The concept of *biomimetics* and its application to propulsion systems for underwater vehicles is the underlying theme of this work.

1.2 Biomimetics

The area of biomimetics involves the study of natural processes and using them to solve engineering problems [Bar-Cohen, 2005]. There are a number of benefits of looking to nature for the solutions to engineering problems as the solutions found there have been optimised by millions of years of evolution [Bar-Cohen, 2006].

Interest in this field is increasing rapidly due to many factors such as the potential benefits from biomimetic concepts and current technology reaching a level which allows these concepts and related designs to be realised. Several famous examples of biomimetics already exist and are in everyday use such as ‘Velcro’ [Vincent, 2003].

One particular area of biomimetics that is gaining popularity is in the field of biomimetic robotics. This is where robots are developed that mimic living creatures, perhaps the most famous one to date is ‘Azimo’ the humanoid robot who walks on two legs just like a human [Honda Motor Co., 2007]. The potential advantages that biomimetic robots and systems have to offer are numerous. One example of this is using legs for propulsion instead of wheels for land based mobile robots. The use of wheels restricts the terrain that the robot can traverse to reasonably flat environments. However, with the use of legs the robot could travel over rougher terrain inaccessible to wheeled vehicles such as dense woodland. One example of a robot that could handle terrain that a wheeled vehicle would find difficult is ‘Big Dog’ which is a four legged robot that resembles a mule that can travel over ice, rubble and uneven ground [Raibert, *et al*, 2008].

A biomimetic approach is central to this investigation, and as with the land based robots, benefits may be obtained from utilizing a biomimetic system for underwater propulsion. The majority of the work presented here focuses on a vehicle called the *RoboSalmon*. This vehicle utilizes a biomimetic fish-tail for its main propulsion system and as the name implies is based on the size and swimming style of an atlantic salmon.

1.3 Why a Salmon?

When designing the *RoboSalmon* vehicle the aim has been to imitate the appearance and approximate the swimming motion of an atlantic salmon [Young, 1962]. This particular species has been selected due to a number of factors including the importance of this species to the national economy and the requirement to better understand the current decline in the stocks of this fish [SPICE Research Paper 00-17, 2000]. Work carried out on the design of fish passes for dams has also been a factor because of the need to understand the swimming motions and behaviour of salmon. This crucial understanding of the biological behaviour of Salmon has allowed optimum, environmentally friendly fish passes to be developed [Guiny, *et al*, 2003]. Also, in terms of swimming performance a salmon has a good balance between speed and manoeuvrability, as is demonstrated in their interesting life cycle which requires them to swim in fast flowing rivers and in the ocean [Young, 1962]. Lastly, from a technical perspective the size of adult atlantic salmon should allow the prototype to have sufficient internal volume for location of all the required electrical and mechanical systems. The manageable size of the atlantic salmon is also beneficial as it enables a relatively smaller water tank to be used in the testing process, which is in stark contrast with some larger underwater vehicles that require specialist testing facilities and a team of operators.

The aim of developing the biomimetic *RoboSalmon* vehicle is to allow for experimental trials to be conducted. These trials are intended to investigate the dynamics of the vehicle and determine the benefits of utilizing a biomimetic propulsion system for an underwater vehicle.

1.4 Biomimetic Propulsion Research

There are numerous other research projects investigating biomimetic propulsion and robotic fish that have been conducted over the past two decades [Yamamoto, *et al*, 1995; Anderson & Chhabra, 2002; Morgansen, *et al*, 2007]. These other research projects have various objectives such as to investigate the performance of a fish like robot with a biomimetic fish tail propulsion system [Yu, *et al*, 2004; Liu & Hu, 2005a] or to develop appropriate control algorithms for a robot fish [Listak, *et al*, 2005; Terada & Yamamoto, 2006; Morgansen, *et al*, 2001]. Several of the more well known projects are covered in more detail in Chapter 2.

In the majority of the published papers found on this topic, claims are made that imply robotic fish should be more efficient than conventional propulsion techniques because real fish are efficient swimmers [Yu, *et al*, 2005; Liu, *et al*, 2005a]. Another common claim made is that robotic fish should be more manoeuvrable than marine vehicles with conventional propulsion systems [Liu & Hu, 2005b; Yu, *et al*, 2005]. However, little work appears to have been published directly analysing the efficiency of a free swimming fish like robot experimentally. Also, with the literature surveyed very few direct experimental comparisons are made between a biomimetic system and a conventional marine propulsion system. This is also the case for the manoeuvring of robotic fish. Many of the papers state that robotic fish should be more manoeuvrable. However, they tend to focus their analysis on the turning performance of their robot and do not draw comparisons with the manoeuvring performance using a conventional marine propulsion system [Liu & Hu, 2005b].

The work carried out as part of this thesis therefore attempts to provide a detailed investigation into the experimentally determined efficiency of a vehicle with a biomimetic fish tail and how this efficiency compares to a vehicle of similar size but with a conventional propulsion system. Similarly, as well as determining experimentally the manoeuvring performance of the vehicle a comparison is made between this manoeuvring performance of the biomimetic system and the performance of a vehicle with a conventional propulsion system. This will allow for the claims of increased efficiency and manoeuvrability to be better understood.

1.5 Objectives

The main objectives of this work can be summarised as follows:

- To analyse the swimming performance of a vehicle with a biomimetic propulsion system and characterise its performance through physical trials.
- Improve the understanding of the potential efficiencies and benefits that may come from utilising a biomimetic propulsion system for AUV design

- To develop a mathematical model to assist with the understanding of the dynamics of the system and to estimate the performance of the prototype hardware.
- To compare experimentally the performance of the biomimetic system to a conventional underwater propulsion system utilizing a propeller and rudder.

1.6 Contribution to the field

The work undertaken in this project is aimed at contributing to the field of underwater biomimetic propulsion systems and biomimetic robotics by investigating the potential benefits of utilising a biomimetic propulsion system for underwater vehicles.

The contributions of this work can be summarized as follows:

- The design, development and construction of a simple, low-cost, underwater vehicle that utilises a biomimetic propulsion system and whose performance could be evaluated experimentally.
- The development of a mathematical model of the vehicle with a biomimetic propulsion system which draws on methods used for modelling conventional marine craft.
- A detailed study into the recoil motion caused by the biomimetic propulsion system whilst swimming.
- The implementation of an actuated head on the vehicle and experimental determination of its effects on forward swimming performance and manoeuvring.
- Experimental determination of the power consumption of the biomimetic propulsion system.
- To complete a detailed experimental comparison between a biomimetic propulsion system and a conventional propulsion system to address the lack of readily available data on this aspect in the current literature.

The publications resulting from this work to date are listed below –

Watts, C.M., McGookin, E & Macauley, M., “Modelling and Control of a Biomimetic Underwater Vehicle with a Tendon Drive Propulsion System”, IEEE/OES Oceans 2007, Aberdeen, 18th-21st June, 2007.

Watts, C.M., McGookin, E & Macauley, M., “Biomimetic Propulsions Systems for Mini-Autonomous Underwater Vehicles”, Student Paper/Poster MTS/IEEE Oceans 2007, Vancouver, Canada, 29th Sept – 4th Oct, 2007.

Watts, C.M. & McGookin, E, “Modelling and Simulation of a Biomimetic Underwater Vehicle”, Grand Challenges in Modelling and Simulation, SummerSim’08, Edinburgh, 16th - 19th June, 2008.

Work is currently underway on a number of additional publications involving the experimental aspects of this project.

1.7 Thesis Structure

The focus of this project is an investigation into the use of a fish-like biomimetic propulsion system for underwater vehicles to ascertain performance and determine any potential benefits obtained from using such a system. To accomplish this, a test vehicle, called the *RoboSalmon*, has been designed and constructed to measure the dynamic performance of the biomimetic propulsion system experimentally. In parallel with the vehicle hardware development a mathematical model of the *RoboSalmon* has been developed to determine the full performance range of the vehicle through simulation studies.

This thesis outlines the study and analysis of this vehicle's performance and its comparison against a propeller based benchmark. It achieves this through the following chapters that are organised in the manner outlined below:

Chapter 2 contains a review of the current state of the art and supporting literature relevant to technology discussed in this investigation. Due to the wide ranging, multi-disciplinary nature of this project Chapter 2 covers aspects of fields such as; a summary of current ROV and AUV technology, an overview of the developing field of biomimetics, a review of other projects investigating biomimetic propulsion and robotic fish.

The experimental *RoboSalmon* hardware is discussed in detail in Chapter 3. However, before discussing the hardware in detail a number of relevant aspects relating to fish biology and fish swimming are discussed to provide background for the design of the hardware. Both the mechanical and the electronic systems implemented within the *RoboSalmon* are described together with a discussion of the rationale behind a number of the biologically inspired design decisions. The design of the tendon drive tail system is introduced and discussed along with its limitations.

The development of the mathematical model based on the dynamics of the *RoboSalmon* is described and discussed in Chapter 4. This model describes the dynamic motion of the *RoboSalmon* and covers details of the modelling of the propulsion system. This chapter also includes details of the experimental laboratory apparatus used for the trials of the *RoboSalmon* vehicle and the validation process for the mathematical model.

Chapter 5 presents the experimental results from the trials of the *RoboSalmon* vehicle for forward motion. The first results present the effects on forward motion of varying the tail beat frequency followed by the results for varying the tail beat amplitude. Results are then presented which characterise the recoil motion and relate it to the varying parameters of the biomimetic propulsion system. The experimental effects of the use of the actuated head during forward motion are then presented and discussed. Finally, the chapter concludes with an experimental comparison of the

performance of the biomimetic tendon drive system with a conventional propeller based system on a similar vehicle. The comparison is based on propulsion efficiency and power consumption.

The results for the manoeuvring performance of the *RoboSalmon* vehicle are presented in Chapter 6. Results are presented and discussed which illustrate the manoeuvring capability of the *RoboSalmon*. In addition, these results demonstrate the relationship between the offset of the tail centreline and the maximum turning rate. The manoeuvring performance is also evaluated using two of the standard manoeuvres used for the evaluation of conventional marine craft; the *turning circle* and a *pull-out manoeuvre*. Also shown in this chapter are results that demonstrate the effect the actuated head has on the manoeuvring performance. Finally, the manoeuvrability of the tendon drive tail is compared to the manoeuvring performance of a conventional propeller and rudder based system. Again the analysis of the manoeuvring capability and power consumption form the basis of the comparison.

Chapter 7 presents simulation results obtained from the use of the mathematical model developed in Chapter 4. A number of trials that have not been conducted using the hardware are carried out in simulation. This includes swimming at high tail beat frequencies, burst-coast swimming and a simulated 20-20 zig-zag manoeuvre. The next aspect covered in this chapter is the simulation study of the estimated propulsion performance of a tail actuation which uses five individually actuated segments. Firstly, the modelling of this system is discussed followed by simulations of the system carrying out forward motion trials which are compared with the results obtained from the tendon drive system. Manoeuvring trials including turning circles and a zig-zag manoeuvre are then simulated and again compared with the performance obtained from the tendon drive system.

Finally, Chapter 8 presents the conclusions that have been drawn from this work along with a brief overview of how the results compare with the main aims and objectives set out at the start of this thesis. A section on suggestions for further work is also provided which details improvements that could be made to the *RoboSalmon* hardware and software, along with areas that could be investigated further.

Chapter 2: Background & Literature Review

2.1 Introduction

The field of *biomimetic* robotics is multi-disciplinary in nature and involves the fusion of numerous different subject areas. This chapter gives a general review of the relevant topics related to the development of the *RoboSalmon* vehicle and accompanying simulation model. Firstly, a brief overview of current underwater vehicle technology including remotely operated vehicles (ROVs) and autonomous underwater vehicles (AUVs) is presented. This is followed by a review of the field of *biomimetics* including some background and a number of examples from across the field. The field of biomimetics and how it can be applied to underwater vehicle technology is discussed along with the benefits of using a biomimetic propulsion system. There then follows a review section discussing other significant biomimetic robotic fish projects from around the world. The chapter then concludes with a brief discussion about student AUV competitions and the University of Glasgow entry to the 2006 Student Autonomous Underwater Challenge – Europe.

2.2 Submarines, Submersibles & Unmanned Underwater Vehicles

The idea of developing vehicles to travel underwater is not a new idea. One of the first underwater vehicle concepts was developed as far back as the seventeenth century and was intended to be used to explore the underwater environment [Burcher & Rydill, 1994]. As with many technologies, when the military benefits of underwater vehicles became apparent much more emphasis was put on their development. The first military submarine, called the *Turtle*, was developed by American David Bushnell during the American War of Independence and was used unsuccessfully against the British Warship HMS *Eagle* at the blockade of New London Harbour in 1776 [Blidberg, 2001; Roberts & Sutton, 2006].

Within the field of underwater vehicle technology there are a number of different types of vehicle, which can broadly be categorised into two classes; manned and unmanned vehicles [Blidberg, 2001]. Manned systems are perhaps the most well known of the underwater vehicle technologies, with systems ranging from the military submarines used by navies around the world to small submersibles used for observations of marine life made famous by Jacques-Yves Cousteau [Cousteau Society, 2009].

Unmanned underwater vehicles can be further subdivided into three rough sub classes; towed vehicles, ROVs and AUVs [Blidberg, 2001]. Towed vehicles are quite simply platforms that are towed behind a ship which usually carry a number of sensors, such as sonar, and can be used for applications such as surveying the ocean floor [Blidberg, 2001; Ballard, *et al*, 1991].

As this project deals with investigation into a novel propulsion system for underwater vehicles the following sections give a more detailed, but still brief, introduction and overview of current ROV and AUV technology.

2.2.1 Remotely Operated Vehicles (ROVs)

The field of ROVs is now a multi-million dollar industry with the majority of application areas within the oil industry but with other application areas in the military, environmental and biological fields [Whitcomb, 2000; Norcross & Mueter, 1999; Yuh, 1995]. Specific applications of ROV are for example water pipe inspection [Rives & Borrelly, 1997], harbour inspection [Martins, *et al*, 1999] and underwater survey [Jalving, 1999].

A ROV is a vehicle which operates in the underwater environment and is usually connected to a control station or ship located on the water surface by means of a tether [Roberts & Sutton, 2006]. This tether allows a human pilot to send control commands to the vehicle and for data, such as a camera feed or sensor readings, to be retrieved from the vehicle in real time [Blidberg, 2001]. ROVs vary in size from small portable vehicles like the Seabotix LBV300 [Seabotix, 2009] to vehicles weighing several tonnes used for deep submergence operations such as the SMD Hydrovision QUANTUM [SMD Hydrovision, 2009]. An example of a portable ROV by Rovtech Systems Limited [ROVTECH Systems, 2009] is shown in Figure 2.1.

Figure image has been removed due to Copyright restrictions

Figure 2.1: Miniature ROV from RovTech Systems Limited [ROVTECH Systems, 2009]

Although the majority of ROV applications are within the oil and gas industry ROVs have successfully been used in the environmental and biological fields. For example, in the biological field ROVs have been used as a lower cost alternative to using manned submersibles to study marine life [Norcross & Mueter, 1999].

Perhaps the most famous of ROV operations to date has been the use of the technology to explore the wreck of the RMS *Titanic* in 1986 [Ballard, *et al*, 1991; Michel & Ballard, 1994]. The ROV *Jason Jr* developed by the Wood Hole Oceanographic Institute was used to obtain spectacular close up images and video footage of the wreck located at a depth of just under 4000 ft. *Jason Jr* was controlled via a

300 ft fibre optic cable to a larger manned deep submergence vehicle, the DSV *Alvin*, which is now operated by WHOI [WHOI Website, 2009].

2.2.2 Autonomous Underwater Vehicles (AUVs)

An AUV is a vehicle capable of operating in the underwater environment, similar to a ROV, but usually without a tether and with some degree of autonomous operation and an onboard power supply [Wernli, 2002; Blidberg, 2001]. One of the earliest examples of a system that could be classed as an AUV is a torpedo [Blidberg, 2001]. AUVs have a number of benefits over ROVs such as not requiring a tether and so can potentially have longer range. Also, there are certain logistical benefits to the vehicle being fully autonomous in that it may not require a dedicated support vessel for its entire mission duration thus allowing the support vessel to carry out other tasks. This could potentially lead to large savings as the cost for a support vessel can be in the region of several thousand dollars per hour [Podder, *et al*, 2004].

However, currently one of the main disadvantages of AUV technology is that if there is a malfunction on board or the vehicle or it is damaged it makes recovery of the vehicle a difficult and potentially costly [Podder, *et al*, 2004; Wernli, 2002]. As AUVs are usually very costly to develop loss of the vehicle is an unacceptable risk, but as this technology matures and the costs are reduced, AUVs could potentially replace ROVs in a number of applications [Bingham, *et al*, 2002]. Also of interest for the reduction of risk within AUVs is the use of re-configurable control systems [Yuh, 2000]. These are control systems such that, when a fault occurs, they alter their control algorithms to maximise the performance from the system [Bakeric, *et al*, 2003]. This would allow the vehicle to continue with its mission in the presence of tolerable faults or to change the control strategy to allow the vehicle to surface and be recovered [Yuh, 2000; Bakeric, *et al*, 2003].

Many AUV systems have been developed over the past two decades. A large number of these AUVs have been developed by academic institutions for research and development purposes. One such AUV is the *Dorado* class AUV developed by the Monterey Bay Aquarium Research Institute (MBARI) [MBARI, 2007]. This AUV is based on a modular architecture which allows different modules/payloads to be incorporated into the vehicle as required by the mission [Sibenac, *et al*, 2002]. By doing this the flexibility of the vehicle is greatly increased and therefore appeals to a wide variety of users. Due to this flexibility the 21” diameter torpedo shaped *Dorado* vehicle can vary in length between 8 feet to 21 feet depending on the configuration [MBARI, 2007].

Another interesting AUV is the AutoSub AUV developed by National Oceanographic Centre at Southampton [Griffiths, *et al*, 1999]. The rationale behind the development of the AutoSub AUV was to produce a demonstrator vehicle to show that routine ocean scientific data relevant to climate change, which was usually collected by ships, could be collected at a lower cost by an AUV [Collar & McPhail, 1995]. To date the Autosub project has produced two vehicles which have been used extensively for ocean science missions over the past decade at a lower cost than some large pieces of

towed equipment. One of the achievements of the AutoSub-2 is that it has been used under ice sheets to gather biological data in place of a ship. This has shown reduced disturbance caused by the AUV compared to a ship [Brierley, *et al*, 2003]. Due to the success of the Autosub project, sub-sea engineering and construction firm Subsea 7 entered into a licensing partnership with the National Oceanographic Centre and has used the Autosub vehicle as a basis to develop their own AUV for commercial purposes called the GeoSub [Underwater.com, 2004].

Currently there are a number of specific applications for AUV technology and due to the nature of the autonomy of the vehicle a large number of these applications are military [Wernli, 2002]. Perhaps the prime military application is that of mine detection and clearing [Wernli, 2002]. This is most likely due to the potential to detect and clear mines without any risk to human operators or personnel [Corfield & Hillenbrand, 2003]. One AUV which has been used successfully for this task is the Remote Environmental Measuring Units (*REMUS*) vehicle [Purcell, 2000]. *REMUS* was used successfully in the opening stages in Operation Iraqi Freedom in 2003 to assist the US Navy search for and clear mines in the waters near the Port of Umm Qasr [Intl. Oceans Systems, 2003; Underwater Magazine, 2003]. The *REMUS* 100 system, shown in Figure 2.2 is a 4 foot long torpedo shaped vehicle capable of operating at depths up to 100 meters. For mine hunting operations the *REMUS* vehicle is programmed to follow a pre-determined search path which can be up to 60 miles in length and is equipped with sidescan sonar and mine detection software which detects mine like objects from the sonar images [Vonalt, 2003; Underwater Magazine, 2003].

Figure image has been removed due to Copyright restrictions

Figure 2.2: *REMUS* 100 System [Vonalt, 2003]

At present AUV operations are by no means common place but there are currently a growing number of AUVs in operation around the world in a variety of different operational applications. The past decade has also seen the emergence of a number of commercially available AUVs indicating that the technology has reached a milestone. One such commercially available AUV is the *REMUS* vehicle mentioned earlier. Although developed by the WHOI, the vehicle has been commercialised by Hydroid Inc and is available in a number of different configurations depending on the end application [Vonalt, 2003]. Other commercially available AUVs are the SeaOtter vehicles developed by Atlas

Maridan and the HUGIN series of AUVs developed by Kongsberg Maritime and a number of partner companies which are perhaps currently the most successful commercial AUVs to date [Vestgard, 2003; Marthinussen, *et al*, 2004].

Although it could be argued that that HUGIN AUVs are not truly autonomous due to their acoustic tether they have been used extensively for deepwater surveys for the oil and gas industry. The *HUGIN 3000*, which has operated at depths of almost 3000 metres in the Gulf of Mexico [Wernli, 2002] has shown that a cost saving of around one third to one half can be achieved compared to traditional systems for offshore surveying missions [Marthinussen, *et al*, 2004].

2.2.3 Undersea Gliders

Recent years have seen a growing interest in the field of undersea glider technology. An undersea glider is special type of AUV that uses a change in buoyancy in conjunction with wings to produce forward propulsion [Griffiths, *et al*, 2007]. This propulsion technique has the advantage of allowing the vehicles to undertake missions with required durations far exceeding that of conventional AUVs [Rudnick, *et al*, 2004] due the small power consumption required by the buoyancy change propulsion system. Due to the long mission durations possible with gliders, which can be many months compared to the tens of hours obtainable from propeller driven craft [Eriksen, *et al*, 2001], they are ideally suited to oceanographic sensing missions [Graver, 2003] and military patrol and reconnaissance operations [Griffiths, *et al*, 2007]. For ocean sensing and survey missions the gliders could be equipped to carry a number of sensors to collect useful data about the ocean such as conductivity, temperature and depth (CTD) sensor packages [Griffiths 2007].

The principal of operation of an undersea glider is that at deployment it is negatively buoyant and therefore tends to dive, during which the wings develop a component of the downward motion in the horizontal plane thus producing a forward force. Once a predetermined depth is reached the vehicle changes its buoyancy to become positively buoyant. This is could be done by pumping oil from an internal bladder to a bladder external to the vehicle, thus increasing the vehicle volume but keeping the mass constant [Griffiths, *et al*, 2007]. This process of altering the buoyancy then continually cycles to allow very large distances to be covered using very little onboard power. The only disadvantage of this propulsion technique is that the saw tooth depth profile created by the vehicle as it moves which may limit the vehicles use in certain applications. An illustration of a glider is shown in Figure 2.3.

Figure image has been removed due to Copyright restrictions

Figure 2.3: Glider Illustration [IEEE Spectrum, 2008]

Manoeuvring of the vehicle is usually achieved by moving mass within the vehicle to control roll and pitch, thus simplifying the design of the vehicle as no external actuators or control surfaces are required [Eriksen, *et al*, 2001].

From the available literature surveyed there appears to be three makes of underwater glider currently in operation around the world; *Seaglider* from the University of Washington [Eriksen, *et al*, 2001], *Spray* from the Scripps Institute of Oceanography [Sherman, *et al*, 2001] and the *Slocum* from the Webb Research Corporation which uses energy harvested from its environment [Webb, *et al*, 2001]. There are also numerous institutes developing laboratory-scale underwater gliders for research purposes such as Leonard & Graver, [2001] and Wood, *et al*, [2007].

One goal for underwater glider technology is for fleets of gliders to operate together to survey continuously an area of ocean returning to the surface occasionally to transmit their sensor data and to receive new commands [Sherman, *et al*, 2001].

A recent major boost for underwater glider technology is that the US Navy has recognized the potential of this technology and is soon going to announce the winner of a large contract to produce 154 such gliders as part of its *Littoral Battlespace Sensing, Fusion and Integration* program [IEEE Spectrum, 2008].

2.3 Biomimetics

The area of *biomimetics* involves the study of systems, processes and methods found in nature and using them as the basis for solving engineering problems [Bar-Cohen, 2005]. The term '*biomimetics*' comes from the ancient Greek words *bios*, meaning life, and *memisis*, meaning to copy [Bar-Cohen, 2006].

Interest in this field is increasing rapidly due to many factors such as the potential benefits obtainable from biomimetic concepts and current technology reaching a level which allows certain biomimetic concepts and designs to be implemented and explored [Triantafyllou & Triantafyllou, 1995], [Sfakiotakis, *et al*, 1999] and [Liu, *et al*, 2005]. The field of *biomimetics* is wide ranging and can be

said to include any technological system or process which was inspired by nature or is indeed a copy or adaptation of a natural system or process [Bar-Cohen, 2006].

There are a number of famous examples of biomimetics that are common in everyday use such as 'Velcro'. After walking his dog, George de Mestral the inventor of Velcro was inspired by the hook system that burdock seeds used to attach themselves to his dog's fur [Vincent, 2003]. Biomimetics not only covers imitating a particular physical function such as walking or flying but also to imitating the underlying concepts or principals found in nature. Genetic Algorithms (GAs) used for optimisation problems are an example that draws inspiration from the Darwinian theory of natural selection [Bar-Cohen, 2006].

Biomimetic systems can have a number of advantages over conventional systems for certain applications. As any biological system has evolved to its current state over several millions of years of evolution, nature has in effect optimised the system for its environment and the tasks it has to accomplish [Bar-Cohen, 2003]. For a number of engineering applications nature's solution to the problem is superior to the conventional engineering solutions and methods. However, in many such circumstances the development of a direct copy of the natural system is limited by current technology. Indeed the concept of biomimetics is not new; Leonardo DaVinci's design for a flying, machine modelled on a bird, is an early example [Dickinson, 1999] but the technology was not sufficiently developed to allow the design to be implemented.

There are examples where technology has been inspired by nature, only for humans to further develop it to make it superior to the natural design. One example of this is supersonic aircraft [Bar-Cohen, 2006]. The development of aircraft was inspired originally by bird flight [Anderson, 1978], then over decades of development aircraft technology was developed to a level where it was possible to fly faster than the speed of sound [Bar-Cohen, 2006].

Biomimetic concepts have also entered the field of control theory where control algorithms have been developed that are inspired by the biological neural networks found in living brains [Betchtel & Abrahamsen, 1991]. These artificial neural networks have been used successfully in a number of applications such as industrial process control [Stich, *et al*, 2000] and control of a robot manipulator [Lewis, *et al*, 1999]. There are several benefits of using artificial neural networks for control systems including the ability to learn the system characteristics and interactions for complex systems purely from the input/output behaviour of the system [Chung & Jeon, 1993].

2.3.1 Biomimetic Robotics

The area of robotics and autonomous systems has potentially much to gain from the field of biomimetics. Robotic applications have used certain biomimetic concepts of varying complexity for some time now. One example of this is the whiskers used on some mobile land based robots for collision avoidance which are similar in concept to the whiskers on rodents [Gravagne, *et al*, 2001].

Another area of biomimetic robotics is legged robots. The idea behind using multiple legs on a robot is that it should be able to traverse terrain that wheeled robots would find difficult. Currently the two best examples of legged robots are Asimo [Honda, 2009] and Big Dog [Boston Dynamics, 2008]. Asimo is a two legged humanoid robot developed by Honda that is able to walk unaided on two legs [Honda Motor Co, 2007]. It is also capable of climbing stairs, a feat that most wheeled robots would find near impossible.

Big Dog is a four legged robot 1m tall weight 109kg and is powered by an internal combustion engine [Raibert, *et al*, 2008]. The robot is capable of walking in various gaits, including crawl, trot and running, and can walk over uneven ground, ice, rubble and snow – terrain that a wheeled vehicle would find troublesome [Raibert, *et al*, 2008].

Using legs to move a robot is not the only form of biomimetic propulsion that roboticists have investigated. There have been a number of snake like robots developed that undulate like a snake for propulsion on land [Yamakita, *et al*, 2003; Paap, *et al*, 2000]. One of the applications of snake like land based propulsion is for survivor location operations after a disaster such as an earthquake [Shan & Koren, 1993]. A subset of these snake-like robots are also capable of swimming in water in a similar undulatory fashion to an eel [Crespi, *et al*, 2005]. Eels and fish are not the only type of underwater creatures to be imitated in robotics, there have been numerous studies into robotic turtles [Kemp, *et al*, 2005; Wolf, *et al*, 2006; Daou, *et al*, 2008]. These robotic turtles use a number of flapping-flipper like fins to produce the propulsion force [Kemp, *et al*, 2005]. However, the focus of this project is on a robot that utilises a fish tail for propulsion.

2.3.2 Fish-like Biomimetic Underwater Propulsion

In the aquatic environment fish are exceptionally versatile swimmers. In some cases they can be extremely fast, reaching accelerations in excess of 25g for very short periods [Videler, 1993]. Also, they can be highly manoeuvrable with some fish being able to change course by 180 degrees, within less than a body length, in under several tens of milliseconds [Wolfgang, *et al*, 1999].

In comparison, current underwater vehicle technology can appear slower and cumbersome compared to the characteristics of some fish. The past decade or so has seen the development of many robotic fish-like vehicles with biomimetic propulsion systems and these have generated significant interest in the field of AUVs [Barrett, *et al*, 1996], [McIssac & Ostrowski, 2003], [Liu, *et al*, 2005]. This interest is due to the potential benefits of biomimetic propulsion techniques over conventional methods. The benefits may include improved propulsion system efficiency [Triantafyllou & Triantafyllou, 1995], increased manoeuvrability [Wolfgang, *et al*, 1999] and less disturbance of the surrounding water [Sfakiotakis, *et al*, 1999].

From the literature available and from the work completed as part of this thesis, a number of specific potential applications of biomimetic underwater propulsion systems have become apparent. As well as being able to perform tasks that conventional underwater vehicles can undertake such as underwater

observation, there are a number of additional tasks for which a biomimetic propulsion system would be ideally suited due to the potential benefits described previously [Sfakiotakis, *et al*, 1999; Barrett, *et al* 1996; Yu, *et al*, 2004;]

- *Biological research:* The efficiency and low noise nature would allow for longer and more detailed studies of aquatic species to be conducted while minimising disturbance to their natural environment.
- *Environmental Monitoring:* Increased manoeuvrability in confined spaces and efficiency of biomimetic vehicles should allow for increased mission duration and the ability to visit locations currently unsuitable for conventional vehicles. When the vehicle is equipped with a compliment of sensors such as to detect oxygen and pollutants the vehicle would be ideal for environmental monitoring.
- *Military:* The potential ability to cause less disturbance than a conventional vehicle coupled with a fish like appearance and higher efficiency could give the vehicle an element of stealth which would be well suited to surveillance and reconnaissance tasks.

2.4 Robotic Fish Projects

Over the past few decades there have been numerous projects and investigations that have been carried out in the field of biomimetic propulsion and robotic fish by industry and other academic institutions for research and commercial purposes. These projects range from conceptual studies to development of oscillating foil propulsion systems to full autonomous robotic fish. The University of Glasgow carried out a preliminary investigation into oscillating foil propulsion in the late 1980s [Lai, 1990]. The projects on this subject have a diverse range of aims and objectives, such as imitating fish closely to understand how they swim and investigating the use of flapping hydrodynamic foils for propulsion of surface vehicles. However, as noted in Chapter 1 from the literature surveyed there does not appear to be much published data on the experimental analysis of the propulsive efficiency of robotic fish and how it compares to conventional marine propulsion systems. Also, in terms of manoeuvring the focus of the robotic fish projects tend to be on the turning performance of their vehicles and little work appears to have been done onto how the manoeuvring performance compares to that of a conventional marine propulsion system

It is impossible to cover all the previous projects and investigations in this area so several of the well known and more advanced robotic fish projects are discussed in the following section.

2.4.1 Mitsubishi Heavy Industries

Perhaps the first investigation to produce a fish like underwater robot was the investigation by Mitsubishi Heavy Industries in the early 1990's. The aim of this work was to investigate the feasibility of using an oscillating fin for a vehicle actuator [Yamamoto, *et al*, 1995]. This work started with cruising tank investigations using a fin configuration that was capable of movement in the sway and

yaw directions. The fin elasticity and shape was also investigated which indicated that increasing fin elasticity can increase the thrust generated and efficiency over a totally rigid fin. Their results also indicate that a fish shaped flexible fin generated more thrust and greater efficiency than all of the other combinations of fin shape and elasticity investigated [Yamamoto, *et al*, 1995].

This work on oscillating fin propulsion lead on to the development of several animatronic robotic fish systems including a robotic *sea-bream* and a replica of a prehistoric *coelacanth* [Yamamoto & Terada, 2003]. The work also produced a surface vehicle which used two oscillating fins for propulsion [Terada & Yamamoto, 2006]. The conclusions of the work state that the oscillating fin propulsion device is an effective propulsor and is particularly effective in a number of circumstances such as in operation in muddy water, an area where a quiet propulsor is required and hovering is required [Terada & Yamamoto, 2006]. Other physical benefits of implementing the system are that the system is potentially safer than a propeller system because of the high speed of the blades and the inherent rolling motion generated [Yamamoto & Terada, 2003]. The work also indicates that a potentially more compact actuation system could be developed because utilizing one mechanism the thrust and its direction can be controlled at the same time unlike other systems which require both a propeller and a rudder for this task [Yamamoto & Terada, 2003].

2.4.2 MIT: *RoboPike, RoboTuna & The VCUUV*

Perhaps the most well know work on fish-like propulsion has been carried out at the Department of Oceanic Engineering at the Massachusetts Institute of Technology (MIT) in the USA by Triantafyllou and his research group in the 1990's. The thrust of their work appears to be aimed at obtaining a better understanding of the hydrodynamic aspects of fish like propulsion and the use of flapping foils as a propulsion system for underwater vehicles. They have also attempted to describe the interaction of their vehicles with the surrounding water and to model the hydrodynamics using various techniques including computational fluid dynamics (CFD) [Triantafyllou, *et al* 2000].

Due to the difficulties in obtaining experimental data from live fish relating to their hydrodynamic performance, they reasoned that by developing a controllable platform that imitated a fish that a better understanding of fish propulsion could be achieved [Triantafyllou, *et al*, 2000].

One significant contribution that MIT have made to the area of fish propulsion is the discovery that for efficient swimming that the Strouhal (St) number should be in the range 0.25 to 0.35 [Triantafyllou & Triantafyllou, 1995]. This was proved by experimental work from their prototype mechanical fish; the *RoboTuna*. The Strouhal number is a non-dimensional parameter which was originally specified to characterize the wake produced by objects, however it can also be used to describe the jets produced by the Reverse Karman Vortex Street [Triantafyllou, M.S., Triantafyllou, G.S., 1995]. Within this range the vortices produced by the undulation of the fin and tail are arranged in such a pattern to produce a jet of water which causes a thrust force. This range of optimum St numbers applies to many

species of fish suggesting it is a major contributing factor to fish propulsion techniques [Triantafyllou, G.S., et al, 1993]. The equation for calculation of the Strouhal number is shown in Equation (2.1)

$$St = \frac{fA}{U} \quad (2.1)$$

where U is the swimming velocity (ms^{-1}), f is the frequency of oscillation of the fin (Hz) and A is the width of the wake (assumed to be same as the peak to peak deflection of the tail) (m). The Strouhal number indicates how often vortices are generated in the wake of the fish and how far apart they are [Triantafyllou, M.S., Triantafyllou, G.S., 1995]. Increasing Strouhal numbers indicate that the vortices are spaced further apart and lower values indicate that the vortices are spaced closer together.

The original *RoboTuna* was 1.25 metres in length and was designed as a test bed to investigate fish like swimming [Barrett, et al, 1999]. It has an external power supply and utilizes cable pulleys and tendon wires driven by motors to drive the tail section [Techet, et al, 2003]. Both power and the tendon wires are fed through a tether to a movable carriage above the water. The tail assembly is flooded and is made up of eight movable links surrounded by a Lyrca and foam skin and all fins on both versions of the *RoboTuna* are rigid.

The argument put forward for imitating a tuna related to its high cruising speed, good efficiency and that it would fit in the MIT testing tanks [Triantafyllou & Triantafyllou, 1995].

Although the main thrust of the work at MIT appears to be aimed more at the hydrodynamic analysis of fish like propulsion they have also carried out some interesting work on control systems for their biomimetic vehicle. The *RoboTuna's* control system was developed from knowledge of oscillating foils, fish motion and an understanding of the kinematics of the tail section [Barrett, et al, 1999]. A GA was also used in the control system to search for the optimum swimming motion.

The second *RoboTuna* is described as an improved version of the “Charlie” *RoboTuna*. A photograph of the complete second *RoboTuna* is shown in Figure 2.4.

Another vehicle developed at MIT, the *RoboPike*, was designed after the development of the first *RoboTuna* and is 32 inches in length. A pike was chosen to imitate due to its good manoeuvrability and high acceleration [Triantafyllou, et al, 2000]. Just like its *RoboTuna* relatives it uses a flooded hull tail section however, it only has three segments in its tail. The number of tail

Figure image has been removed due to Copyright restrictions

Figure 2.4: Second *RoboTuna* prototype [MIT RoboTuna II Webpage, 2008]

segments was limited to three to allow the overall size of the vehicle to be kept to a minimum. Unlike the *RoboTuna* the *RoboPike* is untethered and not mounted to a carriage allowing it to swim freely.

One offshoot of the work on the *RoboTuna* was the vorticity controlled unmanned underwater vehicle (VCUUV) [Anderson & Chhabra, 2002]. The VCUUV was developed by the Draper laboratories on a continuation of the *RoboTuna* vehicle developed at MIT [Anderson & Kerrebrock, 1999]. The VCUUV uses an experimentally optimized version of the *RoboTuna* and was designed to be autonomous and have an on-board power supply. It was designed to be large enough to be fitted with sensors and equipment to allow it to accomplish tasks and missions such as underwater surveillance. The 2.4m VCUUV has a maximum speed of 1.25ms^{-1} and has a turning rate of up to 75 degrees per second. A 4 segment flooded tail is used for the design with each segment actuated hydraulically [Anderson & Chhabra, 2002]. However, papers on the VCUUV indicate that there are a number of issues that have to be worked on before a fully operational vehicle can be produced, such as significant oscillation in pitch under certain conditions [Anderson & Chhabra, 2002]. Also, the vehicle does not appear to be fully autonomous and only open loop testing has been accomplished so far.

Over the past few years there has been a resurgence in the biomimetic work carried out at MIT, this time by the Mechatronics Research Laboratory within the Department of Mechanical Engineering. This work investigates using a body made from a compliant material instead of using a segmented or jointed tail with one servomotor for actuation [Alvarado & Yousef-Toumi, 2006]. They indicate that this approach is simpler and more robust than the usual methods for mechanical realization of a fish tail. Their results indicate that although the tail system cannot accurately represent the kinematics of a real fish the performance obtained was around one third that of a real fish for forward propulsion [Alvarado & Yousef-Toumi, 2006]. The experimentation for forward propulsion was carried out using prototypes 0.3m in length mounted on a carriage that measured thrust, velocity and the tail kinematics [Alvarado & Yousef-Toumi, 2006]. Manoeuvrability of the prototype was also investigated using a tethered free swimming version of the prototype which found it to have increased manoeuvrability over a conventional underwater vehicle but was found to be not as manoeuvrable as the VCUUV [Mazumdar, *et al*, 2008].

Another very recent offshoot of the *RoboTuna* work at MIT is the news that a former member of the team that worked on the *RoboTuna* now working for Boston Engineering is to develop a working untethered prototype that proves the advantages of the biomimetic concept for naval applications [US Navy SBIR Website, 2009], [Piotrowski, 2008; US Navy SBIR Website, 2009; Boston Engineering Corporate Website, 2009]. News of this is perhaps the strongest indication that biomimetic propulsion for underwater vehicles is starting to be considered a serious possibility for future underwater applications.

2.4.3 University of Essex Robotic Fish

The Human Centred Robotics Research Group from the Department of Computing Science at the University of Essex has been working on the development of robotic fish for many years now. Whereas MIT focused on understanding the hydrodynamic effects of fish like swimming, the University of Essex aim to develop a life like robotic fish capable of autonomous navigation [Liu & Hu, 2005a]. The research is funded by the London Aquarium and in late 2005 the robotic fish prototypes were displayed to the public at the aquarium.

The researchers at the University of Essex have developed a 3D Simulator to assist with predicting and optimizing the performance of their robotic fish [Liu, *et al*, 2004b]. The model and simulator describes the kinematics of their fish in detail however it does not give much information about the kinematics related to the hydrodynamic aspects.

From their kinematic model they have developed a control system that allows the fish to accomplish a series of manoeuvres similar to that of a real fish [Liu & Hu, 2004a]. Their experimentation indicates that the performance achievable by the robot is similar to that obtainable by a real fish [Liu, *et al*, 2005a].

This work has led the development of many prototype robot fish which are split into several series, including the G series and the MT series [Liu, *et al*, 2005a]. Neither of these series appear to be based on a specific species of fish; however they do resemble tropical fish.

The G series uses a “multi-motor-multi-joint” tail structure, with the latest version having four joints driven by four servo motors [Liu, *et al*, 2005a]. There appear to have been a number of problems with this family, which mainly seem to stem from the use of a flexible waterproof tail skin which deformed under pressure at a certain water depth. With the deformation under pressure the volume of the robot was altered and this lead to buoyancy issues.

To combat some of the difficulties in their G series the Essex researchers moved to a different mechanical construction using one motor to drive several tail links [Liu, *et al*, 2005a]. This allowed the motor and control electronics to be placed in a waterproof hull and connected to the tail via a waterproof housing with the tail itself open to the water. Through work on the MT series the Essex researchers have experimented with different materials for the fins and the results of their

experimentation indicates the use of a flexible fin is preferable to a rigid fin. This is due to the deformation of the flexible fin during the fin-water interaction which produces a motion more closely matched to a real fish [Liu, *et al*, 2005a].

2.4.4 University of Washington

At the University of Washington, a number of fin actuated underwater vehicles have been developed. The aim of this study is to investigate analytical geometric methods for motion planning and control of shape actuated mechanical systems operating in a fluid environment [Morgansen, *et al*, 2007].

A number of hardware prototypes have been developed for this project, with the most recent being made of two sealed compartments which house the electronics, control and fin actuation servo motors. The tail is made of two links, actuated by two separate servo motors, with a rigid hydrofoil attached to the tail links to represent the caudal fin [Morgansen, *et al*, 2007].

The latest research to come out of this investigation is coordinated swimming of three such fin actuated vehicles [University of Washington, 2008].

2.4.5 PoTuna

The Pohang University of Science and Technology in South Korea has developed a robotic fish based on a tuna [Kim & Youm, 2004]. The biomimetic fish uses one motor to drive a two link tail and the overall vehicle is 1m in length and weighs 25kg [Kim & Youm, 2004]. The information available on this vehicle indicates that progress has been made in developing a model for the system by modelling the robot as a rigid body with an external propulsion force using the standard equations of motion for marine vehicles [Kim & Youm, 2004]. The investigation appears to be more simulation based with no experimental results shown.

They have also carried out a simulation study to investigate the effects of different types of fish swimming using the body and caudal fin (BCF) technique [Kim & Youm 2005]. This particular type of swimming is described in Chapter 2. Their simulation results indicate that the angulliform mode is more suited to quick turning motions and that the thunniform mode is more suitable for sustained propulsion.

2.4.6 Chinese Academy of Science & Peking University

The Institute of Automation at the Chinese Academy of Science have developed a 4-link radio controlled biomimetic robot fish with the aim of developing preliminary motion control strategies that utilize an external visual feedback for path planning [Yu, *et al*, 2003]. The robot developed has a four link tail actuated by four DC servomotors which are programmed to oscillate in a similar fashion to the undulatory motion of a fish. The speed of the vehicle is altered by adjusting the tail oscillation frequency and the direction is altered by adjusting the joint deflections. Through experimentation with their prototype they found a steady speed at which the rolling and yawing motion (i.e. recoil motion) is minimized [Yu, *et al*, 2003]. A Proportional – Integral control algorithm is implemented to control the

speed of the vehicle and a fuzzy logic controller for orientation control [Yu, *et al*, 2003]. In order to position accurately the vehicle at desired positions for the point to point control strategy they developed a speed profile with four phases acceleration, constant, deceleration and drift [Yu, *et al*, 2003]. By implementing this they take into account the optimum speed for minimizing recoil and also account for the drift due to the momentum of the vehicle in the fluid environment, thus allowing them to position the robot at the desired position.

Experimentation was also carried out to investigate different propulsive wave amplitude coefficients c_1 and c_2 [Yu & Wang, 2005] (see Chapter 4 for more detail). The work also investigates the optimization of the link lengths and provides a method for determining the optimum link length based on the propulsive body wave and the number of links. As expected the results indicate that the greater the number of links the better the representation of a real fish [Yu & Wang, 2005]. This work also involved developing a simplified propulsive model to estimate the performance of carangiform propulsion [Yu, *et al*, 2004].

2.5 Student Autonomous Underwater Challenge - Europe (SAUC-E)

The continued research and development activities within the field of AUVs has lead to the organization of competitions aimed at students and academic institutions with the aim of designing and developing AUVs to perform a specific mission. One of the aims of these competitions is to increase interest in AUVs amongst students and to promote research within the field. AUV competitions organized by the Association for Unmanned Vehicle Systems International (AUVSI) and the US Navy Office of Naval Research (ONR) have been running in the US for over a decade. The first European AUV competition, called the Student Autonomous Underwater Challenge – Europe, was held in 2006 and was organized by DSTL [DSTL, 2009].

Objectives of the 2006 SAUC-E competition were to develop an autonomous underwater vehicle that could complete an underwater obstacle course in a set time. Extra credit was given to the teams who used readily available materials in an innovative fashion.

A small multi-disciplinary team of undergraduate and postgraduate students from the University of Glasgow developed an entry for the 2006 SAUC-E competition based on a biomimetic approach. This involved designing and constructing a vehicle based on the dimensions of a shark with a fish-tail like biomimetic propulsion system. The vehicle named the submersible hybrid autonomous rover craft (SHARC) was approximately 1.5m in length and used a five segment tail, with each segment being actuated by a geared DC motor [Watts, *et al*, 2006].

A picture of the SHARC vehicle is shown in Figure 2.5. At the 2006 competition the University of Glasgow team had some success with an overall position of 5th and an award for having ‘The Most Challenging Design’ which came with a prize of £500.



Figure 2.5: University of Glasgow Entry to 2006 SAUC-E competition, the SHARC vehicle

2.6 Summary

This chapter has reviewed a number of topics relevant to this investigation from underwater technology currently in use such as ROVs and AUVs to the relatively recent development of underwater glider technology. The field of biomimetics is described briefly with a number of examples presented from across the field. The discussion then focuses on biomimetic underwater propulsion and the potential benefits and applications thereof.

A description of several other projects involving studies into fish propulsion using mechanical or robotic fish are discussed including the development of the *RoboTuna* by MIT and the early studies by Mitsubishi Heavy Industries. The description of these projects includes details of the hardware developed and information on any modeling and simulation if available along with the important research findings of these projects.

Finally there is a short discussion of the Student Underwater Challenge – Europe (SAUC-E) which was a competition for students to design and build an AUV to undertake a specific mission. An overview of the 2006 entry by the University of Glasgow team is described briefly.

The material discussed in this Chapter, particularly the sections on AUVs and other robotic fish projects, were crucial to this project as they gave ideas, examples and inspiration to the development of the *RoboSalmon* prototype vehicle.

Chapter 3 – The *RoboSalmon*

3.1 Introduction

The aim of this work was to investigate the propulsion characteristics of an underwater vehicle with a biomimetic propulsion system. Material covered in the previous chapter on AUVs provides an insight into the current uses of AUVs and shows how the application of biomimetics may provide certain benefits to underwater propulsion, in particular the propulsion efficiencies. This chapter covers the design and development of the prototype *RoboSalmon* hardware, covering the initial prototype and the *RoboSalmon* V2.0 that has been used to obtain the experimental data. One of the aims of developing the *RoboSalmon* vehicle is to investigate the propulsion efficiencies experimentally whereas the development of the mathematical model of the vehicle, presented in the next chapter, is to better understand the dynamics of the system.

However, before the hardware is discussed a number of relevant aspects relating to fish biology and propulsion are presented to give a general background to some of the concepts used in the design of the *RoboSalmon* hardware. These include the some basic biology of fish covering a number of the terms used when describing the anatomy of fish and a description of the swimming modes used by different species of fish.

The *RoboSalmon* vehicle, as the name implies, is modelled on the dimensions and morphology of an adult atlantic salmon. A general overview of the *RoboSalmon* hardware is given starting with the initial prototype with a discussion of the qualitative data and observations obtained from the experimentation with this prototype. The *RoboSalmon* V2.0 is then discussed starting with an overview of the vehicle. One of the design methodologies used is to make the hardware modular to allow for two tail systems, the tendon drive system and the propeller and rudder system, to be investigated using a common body section. This common body section contains the sensors, control and data logging systems that both systems require for experimentation.

The tail actuation systems are covered first starting with the tendon drive system. This biomimetic system consists of a tail made from ten revolute joint and uses one DC servo motor connected to two tendon wires for actuation. Using the reciprocal motion of the servo motor the tail can be made to flap from side to side in a similar manner to a real fish. The propeller and rudder system is based on conventional technology and was designed to allow for a comparison to be made between the biomimetic system and conventional system on a vehicle of similar size. A description of the hardware used in the propeller and rudder system along with the method used for determining the appropriate propeller to use within the experiment is also given.

There then follows a detailed description of the design and function of each system, both electrical and mechanical, used in the body section of the vehicle. This section covers systems such as the control microcontrollers, remote control, data logger and the controller area network (CAN) communications used.

3.2 Basic Biology of Fish

Throughout this thesis reference is made to many of the biological and morphological features of fish as well as various swimming modes used by different species. The following sections aim to give an introduction to fish biology and provide brief descriptions of the biological terms used in relation to real fish. As this thesis is about mimicking fish swimming, the descriptions are limited to the biological terms related to swimming as trying to give an overview of the entire field of fish biology is impossible in the space available.

A fish is a cold blooded, aquatic vertebra [Young, 1962; Bone & Moore, 2008] and the field relating to the study of fish is termed *Ichthyology* [Moyle & Cech, 2004]. There are currently over 28000 known species of fish identified to this day [Lauder & Madden, 2006], all of which have been categorized by biologists in the standard way using biological classification [Moyle & Cech, 2004]. The class of fish central to this investigation is *Actinopterygii*, or the ray finned fishes [Young, 1962]. The ray finned fish class is subdivided further into three infraclasses and the one most relevant to this investigation is the *Teleostei* as this group contains roughly 96% of all living fish species [Bone & Moore, 2008], including *Salmo Salar*; the atlantic salmon.

3.2.1 Fish Morphology

In order to understand how fish propel themselves through the water it is necessary to have an understanding of the morphological features common to most fish species. The diagram in Figure 3.1 shows the various fish features of interest for this project.

Figure image has been removed due to Copyright restrictions

Figure 3.1: Features of fish [Sfakiotakis, Lane & Davies, 1999]

From the diagram in Figure 3.1 it can be seen that fish have a number of different fins which can be used for propulsion and manoeuvring. In many fish species it is the caudal fin which produces the

main forward thrust, with the pectoral fins being used for low speed propulsion, manoeuvres and diving [Lauder & Drucker, 2002].

3.2.2 Fish Fins

As shown in Figure 3.1 there are various types of fin that appear on fish, all of which usually fall into two classes; fins which are along the body centreline called median fins and paired fins [Hoar & Randall, 1978]. Fins play a very important part in fish swimming as they allow for forward propulsion, manoeuvring, hovering and braking [Videler, 1993]. One important feature of fish fins is that they are not rigid control surfaces like aircraft wings or submarine dive planes, but are flexible structures that can stiffen, bend and flex [Lauder & Drucker, 2004]. This flexibility allows for thrust production and vectoring. This is one of the reasons for the great manoeuvrability exhibited by fish while swimming [Lauder & Drucker, 2006].

In active swimming it is thought that each type of fin has a different use. This use also depends on the swimming mode, or gait, at that time. For example, during steady swimming a rainbow trout uses the caudal fin for main forward propulsion and the pectoral fins are held swept back against the body. But during manoeuvring the pectoral fins take on differing configurations. Figure 3.2 indicates some of the pectoral fin configurations for a rainbow trout under three types of swimming behaviours [Lauder & Drucker, 2004]. Other fins such as the dorsal and anal fins are thought to provide stability while swimming and the pelvic fins are used to assist with braking and some manoeuvres [Moyle & Cech, 2004].

Figure image has been removed due to Copyright restrictions

Figure 3.2: Pectoral fin arrangements in rainbow trout. The grey colour shows the dorsal surface of the fin. The asterisk indicates the location of the front fin base shown by the dotted line [Lauder & Drucker, 2004].

Fish fins are complicated structures made up of skeletal elements wrapped in folds of skin [Videler, 1993] providing great flexibility. These skeletal elements are called *fin rays* which can be seen as thin

grey lines in Figure 3.3 Fin rays are attached to bony elements shown in dark grey. The fins can be classified as either *short based* or *long based* depending on the ratio of fin length to body length. Fin dimensions parallel to the water flow is called the *chord* and dimensions perpendicular to the flow is called *span*. The fin base is the part where the fin is attached to the body [Videler, 1993].

Figure image has been removed due to Copyright restrictions

Figure 3.3: Example of Fish Pectoral Fin [Lauder & Drucker. 2002]

One interesting aspect of the caudal fins of some fish is that, as well as not being rigid, they can also vary their shape slightly over a tail beat cycle [Hoar & Randall, 1978]. This enables the fin to vary the surface area exposed to the water flow and thus manipulate the associated thrust produced during the cycle.

3.2.3 Buoyancy

In the water environment fish not only control their movements in the horizontal plane but also control the depth at which they swim. Therefore, their bodies have to counteract the buoyancy force generated by the displacement of their bodies in order to maintain depth. One way to accomplish this is to become *neutrally buoyant*, this means their body weight is exactly the same as the buoyancy force acting on them. However, in practice this is difficult to achieve due to changing water conditions. Statically most fish species are slightly negatively buoyant [Lauder & Madden, 2006] so fish have developed a number of strategies for depth control [Moyle & Cech, 2004].

One such strategy is the use of a *swim bladder* [Moyle & Cech, 2004]. A swim bladder is an organ which can be used to store a certain volume of gas, thus allowing accurate control of the buoyancy by effectively altering the density of the fish. Another strategy for depth control is to angle the pectoral fins to produce a lift force when the fish is in motion [Videler, 1993]. This is similar to the way older submarines use their control surfaces to produce a force to facilitate depth control [Burcher & Rydill, 1994]. An example of this is the heterocercal tails of sharks which produce such a downward force when in motion [Chopra, 1974]. One other way fish, such as trout, counteract this is to swim in a tilted fashion at low speeds [Videler, 1993]. For example at low speeds when the lift force produced by the

pectoral fins is small, the body is tilted so there is a component of force generated by the tail which acts in the vertical direction to compensate for the unequal gravitational and buoyancy forces [Videler, 1993]. In addition to dynamic depth control, fish have evolved static anatomical features such as the reduction of bone mass and the incorporation of low density compounds within the body to reduce improve their weight/buoyancy ratio. [Moyle & Cech, 2004].

3.2.4 Stability

One other important aspect of any body in the underwater environment is the body's stability [Colgate & Lynch, 2004]. For example if the body is neutrally buoyant but it is not statically stable then when the body is at rest it might tilt to one side rather than stay horizontal.

The stability of a body underwater is determined by the relative positions where the gravitational and buoyancy force vectors act. These positions are termed the centre of gravity (COG) and centre of buoyancy (COB) [Tupper, 2004]. For the body to remain at a constant depth the magnitudes of the gravitational and buoyancy forces acting through the COG and COB respectively must be equal. However, for the vehicle to be statically stable the COG and the COB must coincide so there is not rotational force moment produced. Ships and other man-made objects sometimes use the properties of the COG and COB to provide a degree of roll stability of self righting [Fossen, 1995]. They accomplish this by placing the COG below the COB on the body's z-axis whilst leaving the COG and COB to coincide on the x and y axes. This causes a rotational rolling moment which restores the body back to its horizontal position after any external forces have been removed.

Fish are however unusual in this respect as they are statically unstable, their COG is above their COB. The literature on the subject indicates that most fish when anaesthetized turn upside down due to the relative locations of their COB and COG [Lauder & Madden, 2006; Sfakiotakis, Lane & Davies, 1999]. Therefore, when swimming fish must have some means of counteracting this instability in order to propel themselves in the manner that they do [Videler, 1993; Colgate & Lynch, 2004].

3.2.5 Propulsion Techniques & Classifications

Like many other animals fish move in a variety of different ways depending on the situation [Alexander, 2002; Hoar & Randall, 1978]. In order to catch prey or avoid being prey fish can make sharp turning manoeuvres or produce sudden bursts of acceleration. These movements are called '*unsteady movements*' and often only last for milliseconds [Triantafyllou, Triantafyllou & Yue, 2000]. They can also swim at a steady speed in a straight line to traverse large distances, referred to as '*steady swimming movements*' [Sfakiotakis, Lane & Davies, 1999]. Both types of movement, steady and unsteady are important, however, this thesis focuses mainly on steady manoeuvres.

Within the area of fish propulsion there are several different methods used by various aquatic species to propel and manoeuvre themselves. For the types of fish related to this project the propulsion techniques can be grouped into two broad categories - *body and caudal fin* (BCF propulsion) and

median and paired fins (MPF propulsion) [Colgate & Lynch, 2004]. See Figure 3.1 for a diagram of location and names of fish fins. The majority of fish species use BCF propulsion and it is this swimming method that is investigated in this thesis. The BCF swimming technique for forward propulsion comprises passing a propulsive wave along a length of their body. The propulsive wave starts from the anterior of the body and travels towards the caudal fin. It is this *undulatory* motion that produces a net forward thrust [Videler, 1993].

Depending on where in the body the propulsive wave starts to appear (i.e. how much of the propulsive wave is visible), BCF fish species can be further sub-divided [Moyle & Cech, 2004] into *anguilliform*, *sub-carrangiform*, *carrangiform*, *thunniform* and *ostriform*. Figure 3.4 shows the various swimming modes and Table 3.1 shows the characteristics of each type of BCF swimmer and gives some examples of each mode.

Figure image has been removed due to Copyright restrictions

Figure 3.4: BCF Swimming Modes [Modified from Hoar & Randall, 1978]

Table 3.1: BCF Swimming Sub-Categories [Moyle & Cech, 2004]

Swimming Mode	Wavelength Visible in body/tail (λ)	Example Species	Characteristics
<i>Angulliform</i>	>1	Eel	Highly manoeuvrable, slow, can swim backwards
<i>Sub-Carrangiform</i>	0.5 - 1	Salmon, Trout	Versatile swimmers
<i>Carrangiform</i>	<0.5	Jacks	Fast, less manoeuvrable
<i>Thunniform</i>	Caudal peduncle and caudal fin Only	Tuna	Fastest, <i>fusiform</i> body, lunate tail
<i>Ostriform</i>	Oscillating Caudal Fin Only	Boxfish	Slow

The arrows in Figure 3.4 indicate the relative characteristics of each swimming mode; *Augulliform* is the most manoeuvrable and the manoeuvrability of the other swimming modes decreases towards the right. *Thunniform* is the fastest swimming mode and the speed of the other modes decreases towards the left. This indicates a naturally evolved trade-off between speed and manoeuvrability.

Thunniform and *ostraciform* swimmers are slightly different from the other swimming modes. *Thunniform* fish are the fastest swimmers and have well streamlined, low drag bodies (referred to as *fusiform* in shape) [Moyle & Cech, 2004]. They swim by undulating their narrow caudal peduncle and possess a large *lunate* caudal fin. Not shown in Figure 3.4, but included in Table 3.1 are *Ostraciform* swimmers, they only oscillate their caudal fin to produce forward motion [Sfakiotakis, Lane, & Davies, 1999]. With all the swimming modes, except for *ostraciform* swimming, the amplitude of the propulsive wave usually increases toward the posterior of the fish [Videler, 1993].

For this project, the swimming type selected to investigate are sub-carrangiform. The reasons for this are that this mode falls within the middle of the swimming characteristics illustrated in Figure 3.4 i.e. this mode is manoeuvrable and reasonably fast. Sub-carrangiform form is also the swimming type used by Atlantic Salmon [Hoar & Randall, 1978].

3.3 RoboSalmon Hardware

The following sections present the work on the development of the *RoboSalmon* prototype hardware starting with the initial prototype, called *RoboSalmon* V1.0, then moving onto *RoboSalmon* V2.0 which was the vehicle used to obtain the experimental results presented in Chapters 5 and 6.

3.3.1 RoboSalmon V1.0 Prototype

The first vehicle to be constructed for this project used a legacy ten segment tail from a previous project attached to a newly developed body section and new control electronics. As this was the first attempt to design and build a custom biomimetic fish-like vehicle for this project the prototype had

many limitations and reliability issues which prevented the gathering of any meaningful quantitative experimental data. A photograph of this prototype is shown in Figure 3.5.



Figure 3.5: *RoboSalmon V1.0* initial prototype vehicle

However, experimental trials did show that the tendon drive system did provide a forward surge force and offsetting the tail did allow the vehicle to carry out slow speed manoeuvring. It also highlighted a number of aspects of this propulsion technique which were unexpected such as the amount of recoil motion present in yaw and roll. It was decided that this warranted more detailed investigation with the next prototype. A number of practical and design issues were noted during experimentation with this prototype. The three main issues were the water tightness of the flexible tail system, the ease of dismantling and the feedback from the vehicle. The method used to seal the flexible tail led to significant leaks during operation which limited the time the vehicle could be in the water. Due to the water ingress the vehicle had to be dismantled after every run to dry it out, however due to the design this was a difficult and time consuming task. Finally, there was no feedback from the vehicle to indicate whether or not a command had been received and processed so it was difficult to determine quickly the source of errors when the vehicle did not function as expected.

Therefore, the time spent developing this prototype has been useful as many valuable lessons about the design and construction of biomimetic vehicles have been learned which were then incorporated in the design of the next generation vehicle.

3.3.2 *RoboSalmon V2.0*

The main aim with the design of the *RoboSalmon V2.0* has been to develop a low cost, reliable and easy to use vehicle which would be a platform to allow various experiments to be carried out to determine the effectiveness of biomimetic propulsion systems. To this end, using the experience of building the first *RoboSalmon* and the requirements of the project, the *RoboSalmon V2.0* has been designed and constructed. A photograph of the *RoboSalmon V2.0* is shown in Figure 3.6.

As the aim of the project is to investigate different tail actuation schemes for biomimetic propulsion the experimental *RoboSalmon* hardware has been designed to be modular so as to allow multiple tail systems to be attached to a common body. Adopting this approach has reduced costs and construction time as only one body section would be needed for the project and different tail sections could be attached as and when completed. It also allows for easy expansion for future investigations out with the scope of this project.

The *RoboSalmon* V2.0 vehicle is 0.85m in length, weighs 4.88kg and is modelled on the relative dimensions of an adult atlantic salmon. The vehicle is split into two sections; *the body* which contains the sensors, batteries and various other systems and *the tail* which is used for propulsion.



Figure 3.6: *RoboSalmon* V2.0 vehicle with Tendon drive tail attached

The body section is constructed using a rigid aluminium frame onto which the housings for the electronics are fixed. Three waterproof enclosures are available for the electronics within the body, two on the main body and one small enclosure located in the head. This arrangement is illustrated in the photograph shown in Figure 3.7. The body section is designed to be flooded so as to make ballasting the vehicle for correct trim as simple as possible. Thin shaped sections, constructed from fibreglass, are secured around the body section to give the vehicle the shape and appearance of a fish. Shaped styrofoam was attached around the head section to give the appearance of a fish head instead of fibreglass due to buoyancy requirements and to reduce the load on the head servo.

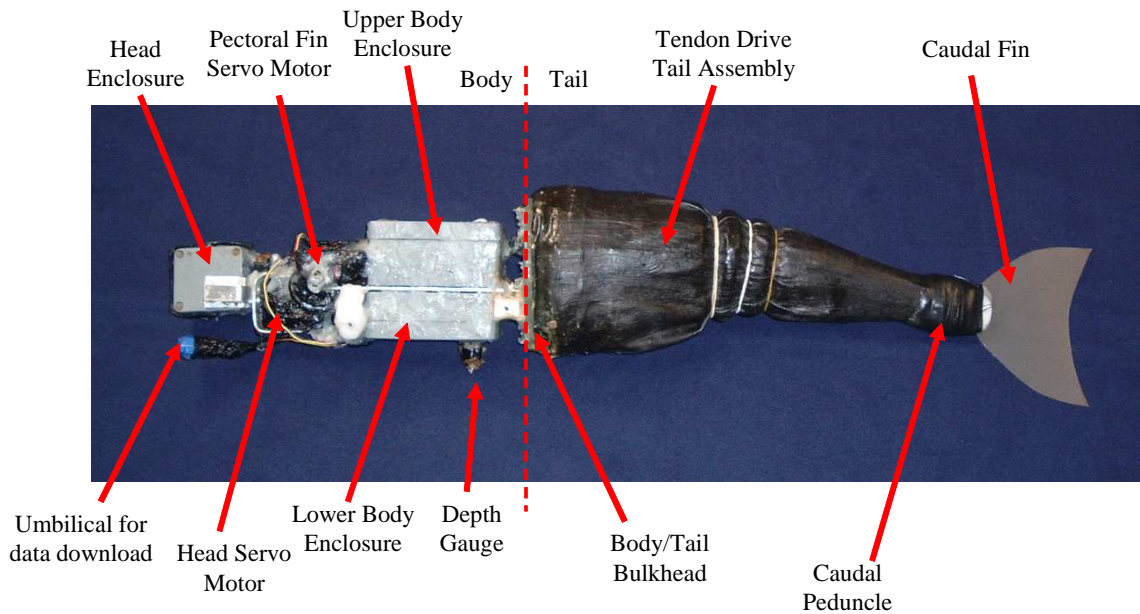


Figure 3.7: Photograph of body section of *RoboSalmon* V2.0 with shaped fibreglass body sections removed.

In addition the body section also houses two systems to assist with the investigation into the swimming characteristics of the vehicle; two servos which operate together and have rigid fins connected which are intended to act as dive planes to allow the vehicle to alter its depth, and one servo which actuates the head of the vehicle allowing it to turn from side to side with respect to the body.

The main cause of the reliability issues with the initial *RoboSalmon* prototype has been with respect to the methods used to waterproof the vehicle. From the experience of working with the initial prototype water leaking into sensitive areas of the *RoboSalmon* causing a number of problems, not just electrical short circuits. As soon as significant amounts of water leak into the hull the buoyancy and trim of the vehicle is altered, this is usually fairly easy to notice and is one way to determine if there is a leak. One other problem is that any metal within the hull corrodes if it is not designed for use underwater. This includes some machine screws and bolts as well as electronic components and printed circuit boards.

To provide another layer of protection for the printed circuit boards and electric components they were given a coating of special waterproof lacquer. Also, the PCBs are, where possible, mounted towards the top of the hull boxes so that if a leak does occur then it would be some time before water comes into contact with the circuit board.

3.3.3 Tail Propulsion Systems

This project involved developing two tail propulsion systems, the first was the biomimetic tendon drive system. The second system was a propulsion system based on a conventional propeller and rudder system. Experimentation with both systems would allow for a comparison to be made between

a biomimetic propulsion system and a more conventional system. The design, mechanics and control electronics of each actuation system is discussed in the following sections.

3.3.3.1 Tendon Drive System

The first tail actuation system to be developed for the *RoboSalmon V2.0* was the tendon drive system. This system has utilised some components from the tendon drive tail from the initial prototype but is a significant improvement over the initial design. The basis for this design is a similar concept to the spine found on living fish i.e. many joints actuated by the contraction and expansion of the muscles on either side of the spine [Young, 1962].

This tail section is made up of a central spine comprising ten plastic joints. Oval shaped rib sections made of thin PVC sheet are attached to the spine to provide the required external shape of the tail. Two tendon wires, which are attached to the front end of the caudal fin, run along each side of the spine and are connected to the arms of a DC servo-motor. It is the reciprocal motion of the arms of servo motor that pulls the tendon wires causing the tail to move. This pulling motion is designed to emulate the muscle contraction in a real salmon tail. In total the tail system occupies just under half of the overall length of the vehicle; therefore it can be thought to approximate the *sub-carangiform* swimming mode.

This design of tail has been adopted because it provides a simple and cost effective method of realising fish like propulsion. By using a single motor and tendons the complexity of the control and electronic systems is reduced. Figure 3.8 shows a photograph of the bare tendon drive system.

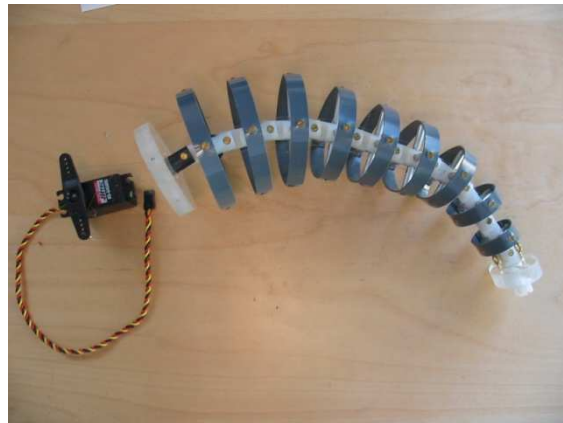


Figure 3.8: Tendon drive tail assembly

The tendon drive tail is actuated using a Hitec HS-5645 Digital Servo [Hitec RCD, 2007]. The tail control system consists of a PIC 18F2480 8-bit microcontroller [Microchip, 2008] programmed in the C language and a Pololu Micro Servo Control Board [Pololu, 2005]. A single turn rotary potentiometer is attached to the output shaft of the servo to give the servo shaft positional information. This information is useful as it can be used to determine the actual rotational position of the servo

motor output shaft as the servo itself provides no feedback on whether it has reached the desired commanded position. The information can also be differentiated numerically to obtain an estimate of the rotational speed of the output shaft. When this rotational velocity is scaled up by the gear ratio used in the servo an estimate of the actual DC motor speed can be also obtained.

The tail control system receives tail commands over the CAN bus. These commands consist of the desired tail beat frequency, tail amplitude and tail offset for manoeuvring. The microcontroller in the tail system translates these commands to the required servo position using a look-up table and outputs serial commands to the servo control board which directly controls the servo. The look-up table contains 20 values corresponding to a sinusoidal function. In order to alter the amplitude of the tail the numerical sine values stored in the look-up table are scaled up or down accordingly and to alter the beat frequency the rate at which the positional commands are sent to the servo controller is increased or decreased. To offset the tail for turning, a constant value is either added or subtracted to the values in the look-up table. This addition and subtraction effectively makes the tail flap more to one side than the other which facilitates turning measurements from the potentiometer are taken using the 10-bit analog-to-digital converter on the microcontroller and sent out onto the CAN bus.

To waterproof the tendon tail assembly a bespoke tail skin has been manufactured from liquid latex coated onto a thin nylon base material. This skin is flexible enough not to restrict the motion of the tail too severely whilst maintaining a waterproof barrier. The elastic nature of the skin also assists with the tail motion by providing a degree of restoring force during motion. The tail skin is sealed to the body by means of a compression fit between two plastic plates.

A moulded plastic caudal peduncle assembly is attached over the tail skin at the rear of the tail. An illustration of this can be seen in Figure 3.9. To this assembly numerous caudal fins of differing sizes and materials can be attached to allow for future experimentation.

3.3.3.2 Caudal Fin

For the biomimetic tail actuation system a caudal fin attached to the posterior of the tail is required in order to closely mimic a Salmon. Three main factors have to be considered when selecting a fin; shape, size and material.

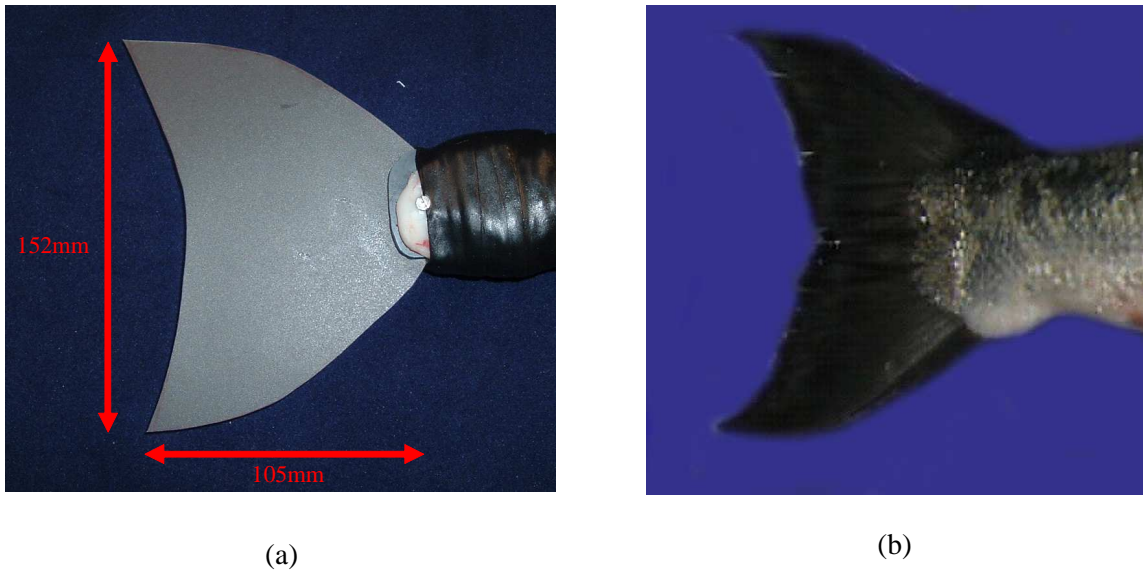


Figure 3.9: (a) Caudal Fin used on tendon drive tail propulsion system (b) Caudal fin from real atlantic salmon for comparison [Photo provided by G. Dauphin]

A number of previous studies on the shape of fins for underwater propulsion applications have indicated that a shape close to that of real fish is optimal for developing maximum thrust [Yamamoto, *et al*, 1995]. Therefore, the shape of the fin has been designed to be as close to the caudal fin shape of a real salmon as possible. The size of the caudal fin is then scaled from the measurements obtained from a real salmon to the dimensions of the *RoboSalmon* vehicle.

The last parameter required is the material from which to make the caudal fin. The first material that has been investigated is 1mm thick rigid PVC sheet; however, initial water tests with this caudal fin produced a load in the tendon drive system which caused the steel tendon wires to break. This is then replaced with a flexible fin of identical dimensions made from flexible plastic. During initial testing this fin has been found to provide a surge force without creating an excessive load for the servo motor in the tendon drive system. This decision is supported by the literature available on fish fins [Videler, 1994; Lauder, & Madden, 2006] which indicate that fish fins are flexible and that a flexible fin produces more thrust than a rigid fin [Yamamoto, *et al*, 1995].

3.3.3.3 Propeller and Rudder System

Development of a tail with a propeller for propulsion and a rudder for manoeuvring allows a comparison to be made between conventional underwater propulsion systems and biomimetic fish-tail systems.



Figure 3.10: Propeller and rudder tail actuation system

The propeller and rudder tail system has been designed to be as similar as possible to the shape of the tendon drive tail and match the existing hull structure. The motor used to drive the propeller is a MFA Comodrills RE540/1 DC motor with a MFA 919D 10:1 reduction gear box attached [MFA ComoDrills, 2008]. The speed of the output shaft of the gear box is measured and the values transmitted on the CAN bus for logging. This speed measurement is achieved by means of an infrared sensor and a small segmented black and white disc attached to the output shaft of the gearbox.

The task of selecting an optimum propeller for the system is complex as indicated by the literature available on the subject [Burcher & Rydill, 1994; Tupper, 2004]. Even if an optimum propeller could be designed, manufacturing such a propeller would be impossible with the resources available for this project. The decision has been made to select a number of commercially available *off the shelf* propellers designed for marine modelling applications and to evaluate the performance of each one in this system. Four propellers have been considered for investigation; a 3 blade 35mm diameter brass prop, a 6 blade 35mm diameter brass prop, a 3 blade 50mm brass prop, a 4 blade 50mm brass prop and a 6 blade high speed 70mm prop. These propellers are shown in Figure 3.11.

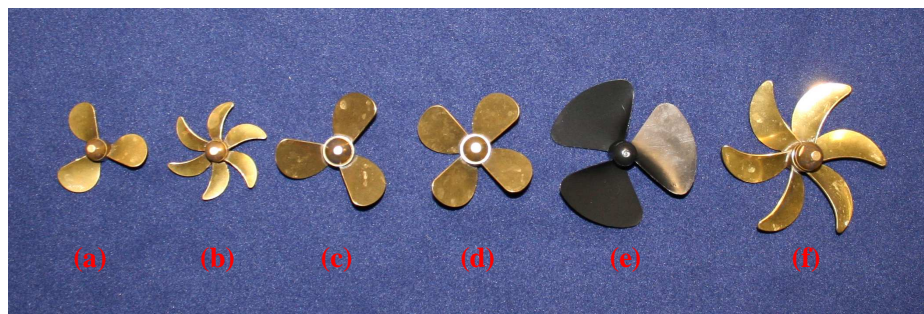


Figure 3.11: Propellers evaluated for prop tail system. (a) 35mm 3 blade brass (b) 35mm 6 blade brass (c) 50mm 3 blade brass (d) 50mm 4 blade brass (e) 3 blade 60mm plastic (f) 6 blade 70mm brass

Each propeller shown in Figure 3.11 has been evaluated in a bollard pull test to determine how each propeller compared in terms of thrust, rotational velocity and current draw. Results for the bollard pull experiments are presented in Appendix A.2. The propeller selected for the experimental trails was the

3 blade 50mm brass propeller. This was due to the thrust produced which was similar in magnitude to the theoretical thrust produced by the tendon drive system. Using this propeller would allow a comparison to be made between the two propulsion systems over a similar range of velocities.

The rotational velocity of the propeller is measured during operation using a photodiode and black and white segmented disc attached to the output motor shaft which drives the propeller directly. As the shaft rotates with the segmented disc attached the photodiode outputs a logic one or zero depending on the particular colour of the segment currently presented to the photodiode. This produces a train of pulses whose period is proportional to the rotational speed of the output shaft and propeller. The microcontroller in the tail performs this calculation and outputs this value onto the CAN bus.

The rudder has dimensions 70mm in height by 35mm in length and is a standard plastic rudder with a tiller arm which has been designed for use in model ships. The tiller arm end points are attached to the arms of a Hitec HS-311 servo motor [Hitec RCD, 2007] which is connected to a Pololu Serial Controller [Pololu, 2005]. A photograph of the completed propeller and rudder assembly is shown in Figure 3.12.



Figure 3.12: Photograph of completed propeller and rudder tail assembly

3.3.4 Body Section

The common body section, onto which each tail assembly attaches, is comprised of three housings for the electronic systems. For the purposes of discussion these boxes have been termed the upper body enclosure, lower body enclosure and the head enclosure. The enclosures used are plastic ABS boxes with a rating of IP65 [Rapid Electronics, 2008]. These enclosures are not ideal as a rating of IP68 would have been more suitable to underwater use [BSI, 1992]. However the expense and size of the available IP68 enclosures prohibited their use within this project. A number of additional sealing measures were taken to modify the IP65 boxes for underwater use which included replacing the gasket seals with o-rings and coating the joins of the enclosure in vaseline to prevent water ingress.

A complete systems diagram, which includes all the system interconnects and system locations, for the *RoboSalmon* is shown in Figure 3.13 and a photograph of the body section of the *RoboSalmon* with the shaped fibreglass body covers removed is shown in Figure 3.7.

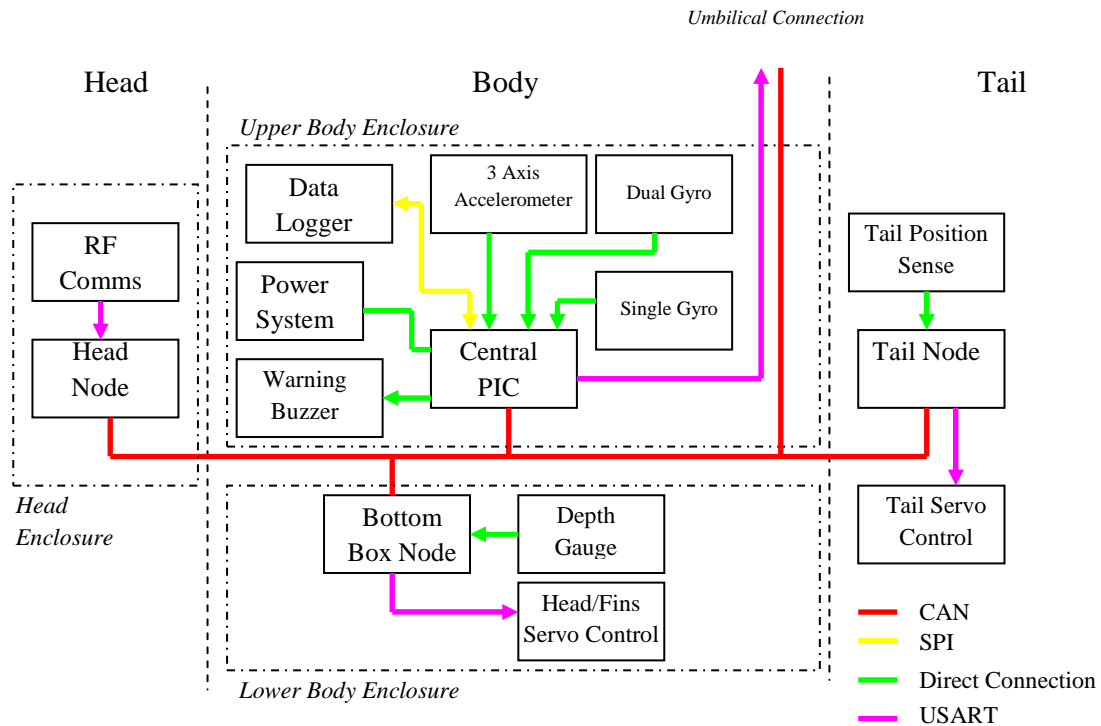


Figure 3.13: *RoboSalmon* V2.0 Sub-System Interconnection, shown with tendon drive tail attached

The systems diagram shown in Figure 3.13 highlights the distributed nature of the systems within the *RoboSalmon* and shows physically where each system is located. A brief overview of the systems located within each enclosure is included next. Full circuit schematics and Printed Circuit Board (PCB) layouts for each system are shown in Appendix A.1.

Head Enclosure

Within the head enclosure is located the head node and radio frequency communications. This comprises a PIC18F2480 microcontroller [Microchip, 2007] to act as a CAN node (i.e. deal with all CAN communications) and to receive commands from the RF data link which is made up of a RF600 Encryption IC [RF Solutions Ltd, 2004] and a 433MHz RF receiver.

Upper Body Enclosure

The central PIC located within the upper body enclosure performs a number of vital tasks – firstly it collects the data from the MEMs IMU components (the accelerometer and the rate gyros), processes it and then sends it to the data logger for storage. This PIC is also connected to the CAN bus so that it can receive messages from the distributed sensors, such as the depth gauge and the tail position sensor and pass this to the data logger. Also located within the upper body enclosure are the warning buzzer and the power system that consists of a custom battery pack and a current sense circuit.

Lower Body Enclosure

Within the lower body enclosure there is another PIC18F2480 acting as a CAN node which receives commands via the CAN bus for the fin and head positions and outputs serial commands to the servo

controller. This PIC also takes readings from the depth gauge and transmits them on the CAN bus at regular intervals.

Tail

Located within the tail is the actuation system for the tendon drive tail system or the propeller and rudder based system. Both of these systems were discussed in the previous sections.

3.3.4.1 Central PIC

The central PIC microcontroller, located in the Upper Body Enclosure, has a number crucial of functions it has to perform. Firstly, it has to use its analogue to digital converter to sample all of the analogue outputs of the Inertial Measurement Unit and power system. It then communicates these to the FLASH Memory of the data logger via a Serial Peripheral Interface bus.

Another function this processor performs is to control a 5V buzzer located in the upper body box. The buzzer is used as a means to alert the vehicle operator that certain events have occurred. For example when the *RoboSalmon* is powered up the buzzer produces three short ‘buzzes’ in quick succession to indicate a successful power up sequence. The need for such a means of indication became apparent during the experimentation using the initial prototype as it is difficult to determine which tail command had been selected.

The PIC microcontroller selected for this role is a dsPIC30F4013 and features a 16-bit core, 13 channel, 12-bit analogue to digital converter and its inbuilt CAN and SPI modules. This particular PIC microcontroller was selected for this task was because its processing power and peripheral features are ideally suited for the central control tasks. For the experimental trials conducted this processor had to carry out the functions described above. However, it was not fully utilized by these tasks and could therefore be used to implement other control algorithms or functions required in future experimental trials.

3.3.4.2 Data Logger

For sensor data from the *Robosalmon* vehicle systems to be of any use it has to be stored in order to be analysed post experiment. The initial idea to recover the sensor readings has been to have a telemetry link with the vehicle transmitting the data back to a computer. However, there are difficulties using radio frequency transmissions underwater as certain commonly used frequencies severely are attenuated making them unusable [Vasilescu, *et al*, 2005]. Therefore, it has been decided that all sensor readings should be logged onboard the vehicle during experimental runs and then be able to be downloaded once the *Robosalmon* vehicle has been recovered. A total of 16 onboard sensor readings/parameters are logged. These parameters are outlined in Table 3.2 along with the relevant details of each sensor reading such as the device used for the measurement, range of the sensor and the source of the sensor reading. The source of the sensor indicates whether the sensor is connected

directly to the analogue to digital converters of the data logger or if the data is received via the CAN bus.

Table 3.2: Data Logger sensor parameters

<i>Parameter</i>	<i>Device</i>	<i>Supply Voltage (V)</i>	<i>Range</i>	<i>Accuracy (% FS)</i>	<i>Source</i>
<i>X Acceleration</i>	MMA7260QT	3.3V	±1.5g	±1.0%	ADC
<i>Y Acceleration</i>	MMA7260QT	3.3V	±1.5g	±1.0%	ADC
<i>Z Acceleration</i>	MMA7260QT	3.3V	±1.5g	±1.0%	ADC
<i>Roll Angular Velocity</i>	IDG-300	3.3V	±500°/s	±<1.0%	ADC
<i>Pitch angular velocity</i>	IDG-300	3.3V	±500°/s	±<1.0%	ADC
<i>Yaw angular velocity</i>	ADXRS300	5V	±300°/s	±0.1%	ADC
<i>Single Gyro Temperature</i>	ADXRS300	5V	-40° to +85°	-	ADC
<i>Single Gyro Reference Voltage</i>	ADXRS300	5V	2.5V	-	ADC
<i>Dual Gyro Reference Voltage</i>	IDG-300	3.3V	1.23V	-	ADC
<i>Pressure sensor reading</i>	MPX4250A	-	20kPa to 250kPa	±1.5%	CAN
<i>Tail Potentiometer reading (tendon drive system) / Motor shaft RPM (prop/rudder system)</i>	Potentiometer /optical encoder	-	±180°/	±5.0%	CAN
<i>Battery Voltage</i>	Potential Divider	5V	0-18V	±1.0%	ADC
<i>Propulsion System current</i>	Current sense resistor	5V	0-6A	±1.0%	ADC
<i>Body System current</i>	Current Sense Resistor	5V	0-6A	±1.0%	ADC
<i>Head Position</i>	-	-	±22.5°	-	CAN
<i>Fins Position</i>	-	-	±45°	-	CAN

An investigation has been conducted to ascertain whether there are any commercially available data loggers that were within budget, fitted within the space available and could log data at the rates required. Unfortunately, none could be found so a custom data logger has been developed using a Spansion S25FL128A 128Mbit serial FLASH memory IC [Spansion, 2008] connected via the serial peripheral interface (SPI) to the dsPIC20F4013 [Microchip, 2008]. This device provides storage for 16 Mbytes of data, and for this application; logging 16 parameter values, two bytes in length at 10ms intervals, provides logging for just over 87 minutes worth of run time. The serial FLASH IC is controlled by firmware on the central dsPIC. This processor controls all read/write commands to the device and implements all the relevant timings.

The rate at which the data is sampled and stored is 100Hz, i.e. all 16 parameters logged every 10ms. This sampling rate will be sufficient to capture the required signals without aliasing as the dynamics of the vehicle will not change faster than a few Hertz. Due to the Nyquist-Shannon sampling theorem if

the signals are sampled at 100Hz, frequencies of up to 50 Hz can be adequately represented [Stremmer, 1992]. The maximum speed at which data can be written to the Serial FLASH as quoted in the device data sheet is 50 MHz but in practice the maximum speed that could be used to ensure reliable transmission is 78 kHz. This is due to the noisy environment, lack of shielding and the layout of the printed circuit board. At this speed the transmission of data to the memory takes around 3.3 ms and the maximum time taken for the device to write to its memory is 3 ms. Adding to this the 3.45ms taken by the processor to complete the operation, the maximum time required to sample and store all 16 sensor readings/parameters is 9.75 ms. This maximum time has been rounded up to 10ms to give some extra time in case of a delay such as an interrupt occurring. Unfortunately, this sample rate is slower than desired as it was hoped to reduce the sampling interval to around 1ms which would be a similar time step to that used by the MATLAB simulation of the *RoboSalmon* vehicle.

The data logger system can be controlled via the CAN bus using three simple commands; one for *erase memory*, one to *start logging* and one to *start a download of the flash memory contents*. When the download command is received the dsPIC reads the memory contents in 256 byte pages, it then converts each 2 byte integer parameter value to an ASCII value and transmits it via the USART. By converting the raw binary values into ASCII the data can be read in through a standard computer RS232 serial port, using a level shifter to convert the 5V USART signals to the RS232 standard. This ASCII data can then be stored as a text file in imported into Microsoft excel or MATLAB for post processing and analysis.

3.3.4.3 Inertial Measurement Unit

In order to evaluate the performance of the *RoboSalmon* vehicle a method of measuring its motion in the six degrees of freedom is required. The apparatus used for this in commercial and military applications is an inertial measurement unit (IMU). This device measures the body-fixed accelerations and rotations of a vehicle onto which they are mounted and by using a combination of these measurements is able to determine the position of that vehicle [Titterton, & Weston, 1997].

Off the shelf IMUs are commercially available but are far out with the budget of this project. Therefore, a cheaper solution has been developed using MEMs accelerometers and gyroscopes. MEMs, or micro-electro-mechanical structures, technology has been a rapidly growing area since the 1980s and deals with making small electromechanical devices on a similar scale and using a similar manufacturing process to conventional integrated circuits [Sze, 2002].

The accelerometer selected for use in the *RoboSalmon* is the Freescale MMA7260QT [Freescale Semiconductor, 2008] mounted on an evaluation board provided by Sparkfun Electronics [Sparkfun Electronics, 2008]. The advantages of using this accelerometer are that it is a single chip solution that measures accelerations in the x, y and z axes and has four sensitivity selections between 1.5g – 6g. For use in the *RoboSalmon* the sensitivity has been fixed at $\pm 1.5g$ as it is unlikely that the vehicle would experience accelerations greater than this and this setting would also produce the maximum resolution.

Initially it was hoped that the acceleration readings from the accelerometer could be integrated twice to give the displacements but after some experimentation it was found that the accumulated error was too great due to the drift of the sensors. Even after a few seconds the error was in the order of meters. Therefore, equipment external to the vehicle would be used to measure the linear velocities and displacements. However, when stationary the 3 axis accelerometer can be used as an inclinometer to measure the static roll and pitch angles [Tuck, 2007]. This initial value for roll and pitch can be used as the initial set point for roll and pitch which will be updated by the integrating the rate gyro readings. Details on the IMU sensor data and associated camera data fusion is presented in Chapter 4.

The rate gyros selected for the *RoboSalmon* vehicle is an InvenSense IDG-300 a dual axis gyro [InvenSense, 2008] mounted on a evaluation board provided by Sparkfun Electronics and an Analog Devices ADXRS300 single axis MEMS gyro evaluation board [Analog Devices, 2004]. The combination of these gyros has been selected due to the space restrictions within the vehicle, ideally three of the same gyros or a triple axis gyro could be used. The dual axis gyro is positioned to measure the roll and pitch angular velocities and the single axis gyro is used to measure the yaw angular velocity.

3.3.4.4 CAN Communications

One of the vital aspects of the vehicle which greatly simplifies the implementation of the distributed systems and modular concept of the vehicle is the use of the Controller Area Network (CAN) for robust and reliable intersystem communication. The CAN protocol, developed by Bosch in the 1980s, was originally designed for automotive applications as a robust and reliable communications protocol for the harsh environments found in cars [Pazul, 1999]. However, over the past decade CAN has been implemented in many other areas such as industrial automation and medical equipment [Ibrahim, 2008]. It is also recommended by organisations that develop AUVs, one such organisation is MBARI, who advocate that CAN is an ideal protocol for maintaining timing synchronisation between various onboard systems [Kirkwood, 2007].

CAN is a message based protocol rather than an address based protocol, this means that every node connected to the bus receives every message and it is up to the individual nodes to decide whether to accept the message or not [Pazul, 1999].

Some of the robustness of the CAN protocol is due to the physical layer implementation which utilizes two wires to transmit a differential voltage signal to represent the message [Richards, 2002]. By doing this any electrical radiated noise from nearby noise sources, such as DC motors, appears simultaneously on both wires and is effectively cancelled out.

The implementation of a CAN bus around the *RoboSalmon* has proven to be invaluable for the simple interconnection of all the distributed systems around the vehicle. Implementation has also minimized the amount of wiring required and also allows significant scope for modifications and upgrades. The CAN hardware is implemented using the CAN module on PIC18F2480 in conjunction with a

MCP2551 physical layer transceiver to connect to the bus. The CAN bus within the *RoboSalmon* operates at a speed of 125kbits/sec and uses the standard message identifiers for communications.

3.3.4.5 Remote Control

One of the main improvements of the final vehicle over the initial prototype is the implementation of a Radio Frequency (RF) remote control. The remote control has a number of functions; to control various parameters of the vehicle using the controls located on the top of the enclosure, to transmit serial commands received from the PC running the corresponding custom MATLAB graphical user interface (GUI), and finally to directly connect to the *RoboSalmon* vehicle through the umbilical connection to allow for retrieval of the logged sensor data and access to the CAN bus for troubleshooting.

Radio Frequency

The RF modules used for transmission and reception are RF Solutions 434MHz T5 and R5 respectively. From experimentation it was found that these modules could penetrate to a depth of a few cm in water which was all that was required. Ideally a module that used a lower frequency for transmission and reception would have been used but as these modules are difficult to source the more readily available modules have been used. As well as for experimental runs, the remote control proved to be invaluable during bench development and testing. A photograph of the remote control is shown in Figure 3.14.



Figure 3.14: RF Remote Control Handset

As can be seen from the photograph of the remote control in Figure 3.14 there are a number of control knobs and switches located on the top of the remote control box. At the top left is the on/off toggle switch which disconnects the remote control electronics from the 9V battery within the enclosure. The toggle switch next to the power switch allows the remote control to switch between commands sent from the MATLAB GUI (discussed in the following section) or the hardwired controls mounted on the box. The control knobs below the toggle switches allow the head and fin positions to be varied when

the remote control is set to 'RC'. To the right of the knobs are four red push buttons which allow for commands to be sent to the *RoboSalmon* to produce forward motion (FW), faster forward motion (FW FAST), to turn to the left (LEFT) and to turn right (RIGHT). Again, these push buttons are only active when the toggle switch is set to 'RC'.

MATLAB Graphical User Interface

The remote control hardware shown in Figure 3.15 can be connected to a PC via a standard RS232 serial port. A custom GUI developed in MATLAB is used to send commands via the computers serial port to the remote control handset. The GUI, shown in Figure 3.15, contains a number of buttons and slider bars that mirror the commands that can be sent using the hardwired buttons. This allows the *RoboSalmon* vehicle to carry out basic movements such as flapping the tail at two different beat frequencies for forward motion, two tail offsets for turning to the left and right. The GUI also allows for control of individual position for each fin and the head using the slider bars shown.

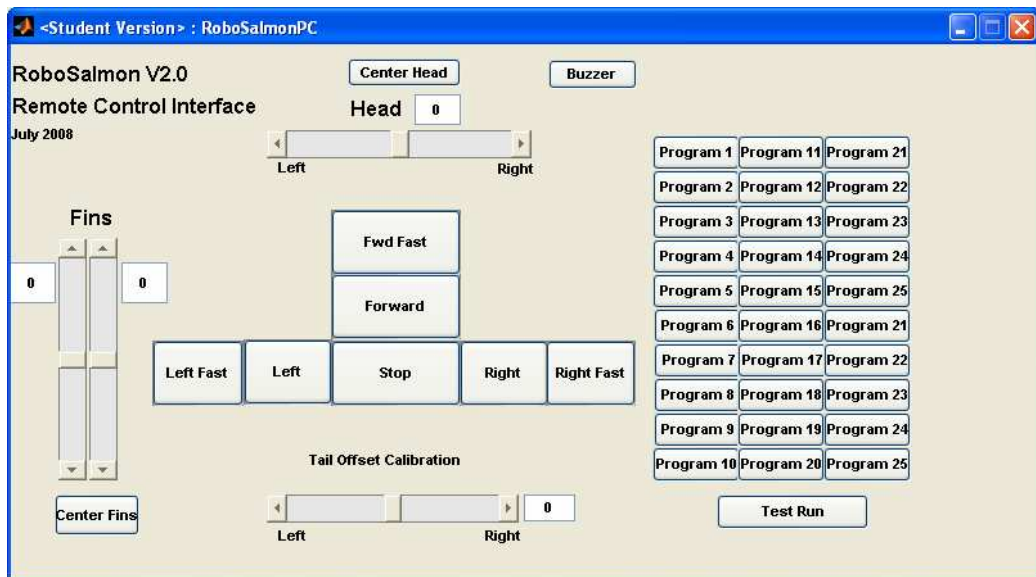


Figure 3.15: MATLAB GUI for control of *RoboSalmon* over RF remote control

A button is present that controls of the buzzer located within the vehicle. This is particularly useful for initial testing of the operation of the remote control and RF link after power on.

One other useful function of the GUI and remote control is that it enables the tail centre position to be adjusted in order to calibrate the tail before each set of experimental trails if necessary. This is useful as there could be variations in the tail centre position over the course of the experimental trails. The variation was due to several factors such as different tensions in the tendon wires and slight differences in the positioning of the flexible tail skin. Variations in the tendon wires were caused by factors such as tendon wear and tail maintenance when the tendon wires were removed. Tail skin variations were caused because at the end of each day of experimentation the tail skin was removed to check for water leakage and when the skin was replaced there would be slight differences in its positioning.

As well as the commands for basic movements the remote control handset is the main method of sending the program commands to the *RoboSalmon* vehicle using a number of buttons on the right hand side of the GUI, shown as buttons labelled *Program 1* to *Program 25*. These program commands are combinations of preset commands. For example program 1 is forward for 25 seconds at a tail beat frequency of 0.61Hz and beat amplitude of 0.105m. Once a program button is pushed the corresponding series of commands is sent to the *RoboSalmon*. When the command is received the vehicle will buzz a number of times corresponding to the number of the program selected e.g. for program 5 there will be five buzzes to indicate that the command had been received correctly.

3.3.4.6 Umbilical Connection

In order to retrieve the logged data from the *RoboSalmon* the remote control handset is fitted with a short umbilical cable. This cable utilises a Bulgin IP68 inline connector [Bulgin, 2007] which connects to the vehicle once it is out of the water to allow for retrieval of the logged sensor data stored in the data logger. The cable has four wires; two for the CAN bus, one for USART Transmit and battery ground. The commands to read the data stored in the data logger are sent via CAN and the data is sent to the PC via the remote control handset where the USART signal is level shifted to RS-232 voltage levels to be compatible with the serial port on the PC.

3.3.4.7 Pectoral Fins

In order for the vehicle to move in a 3D environment a means of altering the depth of the vehicle is required. To this end a simple system that utilises fin structures as hydroplanes or dive planes is used [Burcher, & Rydill, 1994].

This system operates on a similar principle to that of aircraft wings; as the vehicle moves forward, water flows above and below the angled fins at different velocities. This creates a lift force which acts at the centre of the fins and can be used to make the vehicle to dive [Burcher, & Rydill, 1994]. This force is dependent on the angle of the fins with respect to the water flow, the shape of the fins themselves and the speed of the oncoming water flow [Perez, 2005].

The fin dive planes are positioned at a similar position to where the pectoral fins would be located on a real atlantic salmon. In order to be able to estimate the forces produced by the fins they have been designed to be as close as possible to a NACA 0012 section [Goett & Bullivant, 1939]. A diagram of this section is shown in Figure 3.16.

Figure image has been removed due to Copyright restrictions

Figure 3.16: Diagram of NACA 0012 section [Goett & Bullivant, 1939]

This type of section has been selected as a number of other robotic fish and underwater vehicles have used this section for dive planes [Morgansen, *et al*, 2007] and data about the lift and drag coefficients are readily available.

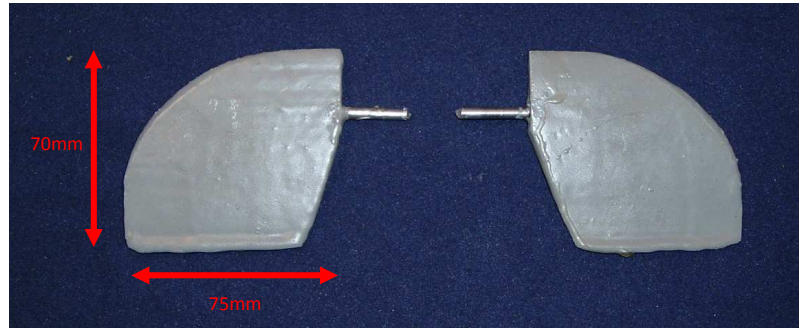


Figure 3.17: Plan view of pectoral fin dive planes

The fins have been constructed from styrofoam shaped to the NACA 0012 section coated in four thin layers of epoxy resin. A steel shaft has been inserted into the fin to allow for connection to a Hitec HS-311 servo [Hitec RCD, 2007] motor mounted onto the body section at a 30° angle to the horizontal. A photograph of the completed pectoral fins is shown in Figure 3.17. Due to the space restrictions within the body section the servos to actuate the fins are mounted at an angle of around 40 degrees to more closely represent the pectoral fins on a real atlantic salmon. The disadvantage of mounting the fins at an angle like this is that not all the force generated act in the vertical plane, there is a component in horizontal direction. Only around 86% of the force generated acts in the vertical direction and would be useful for diving.

Both servos are connected to a Pololu micro servo control board [Pololu, 2005] which receives serial commands from the PIC 18F2480 in the lower body box. This allows both fins to be controlled individually and each has a movable range of $\pm 45^\circ$ from the centre position. Positional commands for each fin are received via the CAN bus from either the RF control or the central PIC controller.

3.3.4.8 Actuated Head

RoboSalmon has a unique feature that very few other biomimetic vehicles possess in that it has an actuated head. This controlled actuation allows the head to move from side with a range of movement of approximately $\pm 27^\circ$. The head is actuated by a Hitec HS-311 servo motor [Hitec RCD, 2007] fixed to the body section. This servo motor is connected to the same Pololu MicroServo motor controller as the fin actuation servos and like the fin servos the head servo is controlled by commands received via the CAN bus. An illustration of the actuated head system is shown in Figure 3.18.

The head contains a small enclosure which contains the RF communications modules which allows commands to be received from the remote control handset. A styrofoam mould coated in liquid latex is used to cover the head enclosure and give the appearance of a fish head.

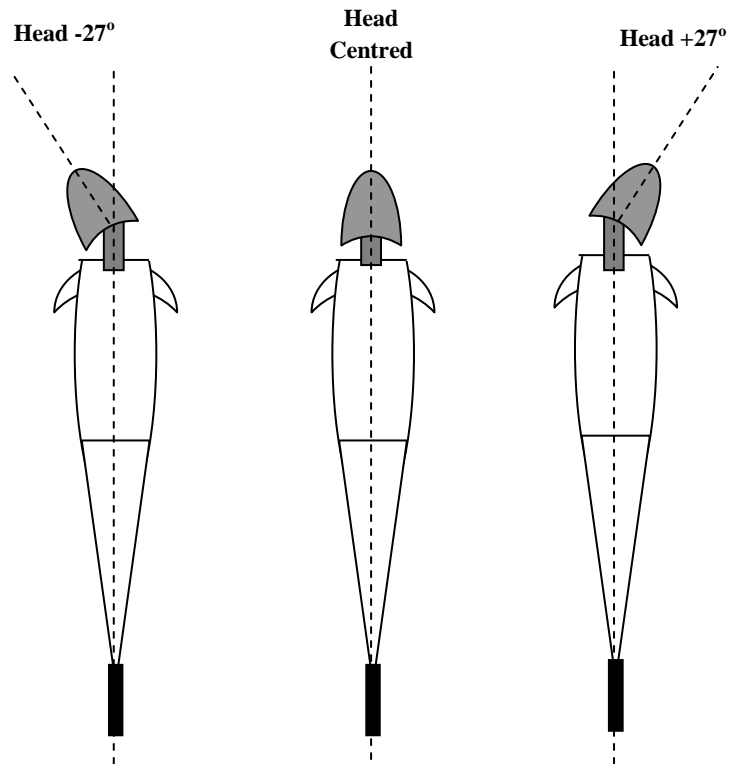


Figure 3.18: Diagram of actuated head (a) head to left at -27° (b) head centred 0° and (c) head to right at $+27^\circ$

The reason for implementing a method for actuating the head is to determine experimentally whether using an actuated head can improve manoeuvring performance and assist with the reduction of recoil motion in steady swimming.

3.3.4.9 Power System

Due to the differing nature of each tail actuation system investigated a slightly different power supply system is required for each. The main difference in the power systems is the types and voltages of the batteries used. Initial research into the optimum batteries to use for underwater vehicle applications indicated a number of competing technologies. One such technology that appears to be very well suited to underwater applications is lithium polymer [Bradley, *et al*, 2001; Griffiths, 2003]. Lithium polymer, or LiPo, batteries have very high charge density to weight and volume ratios. This means that for a similar volume LiPo batteries have higher capacities than conventional Lead Acid or NiMH cells making them ideal for applications where space is severely limited such as underwater vehicles [Griffiths, 2003]. They also have very high discharge capacities making them ideal for driving motors such as those used for AUV thrusters. However, the technology has a number of problems associated with it such as the charging of the cells which is a more complicated process than conventional NiMH

cells. Also, due to the presence of Lithium within the battery there are potential hazards if the battery is exposed to water. Both of these problems can be overcome using an advanced battery management system/charging unit [Reap Systems, 2009] and a properly rated enclosure. However, due to the increased cost and complexity of implementing the additional hardware for Lithium Polymer and the packaging of the available LiPo batteries they have not been used.

Therefore, conventional NiMH batteries were selected for use in the power systems for each tail actuation system after careful investigation into the capacities, maximum discharge currents and costs. Custom battery packs have been made for each actuation system from standard 1.2V AA size NiMH 2800mAh cells with solder tags.

Each actuation system requires a different voltage to power the actuation system. For the tendon drive system where one 5V servo is used to actuate the tail a pack consisting of six AA cells connected in series was used giving a supply voltage of around 7.2V. For the propeller/rudder and the individually actuated system a battery pack consisting of ten AA cells connected in series is used giving a supply voltage of around 12V.

Current and Voltage Sensing

As already mentioned one of the aims of this project is to determine the efficiency of the biomimetic propulsion systems investigated. Efficiency is the ratio of output power to input power therefore a means of calculating both these values is required to obtain the efficiency. The output power can be determined from the motion of the vehicle. The input power comes from the energy stored in the battery and can be calculated using the equation for electrical power i.e.

$$P_{IN} = I_T V_B \quad (3.1)$$

Here P_{IN} is the input power in *Watts*, I_T is the current to the tail actuation system in *Amps* and V_B is the battery voltage in *Volts*.

In order to log the current values they needed to be represented by a voltage signal to be compatible with the analogue to digital converter (ADC) onboard the central PIC microcontroller. The simplified circuit in Figure 3.19 was used to achieve this.

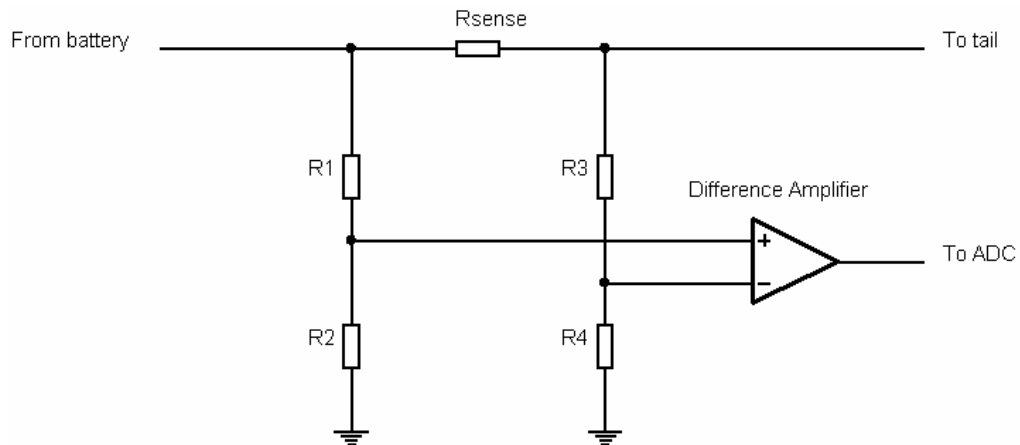


Figure 3.19: Simplified current sense circuit

As the tail actuation system draws current from the battery a voltage is developed across R_{sense} . According to Ohm's law this voltage is proportion to the current flowing through the resistor. The value of R_{sense} used for the circuit is 0.1 Ohm with a 1% tolerance and a power rating of 30 Watts. The voltage at each side of R_{sense} potentially divided using R1, R2, R3 and R4 to a voltage within the 0-5V input range of the difference amplifier. The differential voltage is then amplified and passed to an input channel central PIC for analog to digital conversion.

Two current sense circuits are present within the *RoboSalmon*; one as described above to measure the tail current and another identical circuit to measure all the current taken by the systems within the body.

Measurement of the battery voltage is obtained using a simple potential divider to reduce the voltage to a level within the input range of the microcontroller ADC. All components within the current and voltage sense circuits have been selected to allow for operation with the different battery voltages present in each system.

3.4 Summary

This chapter covers the development of the *RoboSalmon* hardware. Firstly some initial background material on basic fish biology is presented which includes a definition of some of the fish terminology used throughout this work. A number of relevant topics on fish are also discussed including fish fins and the swimming modes used by certain fish.

The next section covers in detail all of the experimental hardware designed and implemented for this project. It starts with a brief description of the initial *RoboSalmon* Prototype developed. Although this prototype has not provided any quantitative data it has shown that the tendon drive tail system is able to provide a surge force and it indicated a number of areas where the design could be improved. It also highlighted some additional aspects of the propulsion system for further investigation.

The next version of the *RoboSalmon*, called the *RoboSalmon V2.0*, is then discussed in detail, firstly covering the modular methodology used which allowed two propulsion systems to be attached to a common body section. Each of the two propulsion systems used are then discussed starting with the tendon drive propulsion system. This is followed by the development of the propeller and rudder system which was implemented to allow for a comparison between a biomimetic system and a conventional system. The common body section onto which each tail propulsion system attaches is then discussed. This includes an overview of all the onboard systems followed by a detailed description of each system in turn starting with the central processor. The other systems covered are the custom inertial measurement unit that uses MEMs components, the data logger designed specifically for the *RoboSalmon*, the remote control system and corresponding MATLAB GUI, the actuation systems for the fins and the head and finally the power system that includes the current sense circuitry.

Chapter 4 – Mathematical Model of the *RoboSalmon*

4.1 Introduction

The development and use of simulation models is becoming an ever more important process in industry and academia for problem solving and to aid in decision making [Sargent, 2005]. In many circumstances the development of prototype hardware is an expensive and time consuming task so it is increasingly common place to develop simulation models to predict how a system will perform in software before it is physically constructed [Murray-Smith, 1995]. Mathematical models and simulations also allow the development of control algorithms and theories and provide a means for these to be tested before implementation on hardware [Dutton *et al*, 1998; Murray-Smith, 1995].

One of the objectives of this work is to develop and validate a simple mathematical model of the biomimetic *RoboSalmon* vehicle which can then be used to estimate the performance of the system and allow for the future investigation of control systems for such a vehicle. The development of the model draws on methods used for modelling conventional marine vessels and techniques used for modelling robot manipulators. Aspects of the hydrodynamics, biology and morphology of fish are also factored into the model. The conventional marine modelling techniques have been modified with additional or replacement terms to represent the biomimetic nature of the prototype vehicle such as the thrust and drag equations for fish propulsion. Another modification is that the shape of the modelled vehicle hull is selected to approximate that of a fish body.

The mathematical model consists of three main parts – the modelling of the *tail propulsion system*, the *vehicle dynamics* and the *vehicle kinematics*. The modelling of the tail propulsion system describes how the actuation system used within the tail generates a motion of the caudal fin. The dynamics section allows for the calculation of how the forces and moments generated by the mechanical tail cause the vehicle to move with reference to the body-fixed frame. The vehicle kinematics section describes how the body-fixed vehicle velocities generated by the dynamics section translate to an inertial fixed reference frame. Once the model differential equations have been developed they are put into state space form and a multi-rate simulation is constructed using the *MATLAB* environment.

This Chapter is organized as follows; firstly a brief overview of the state space modelling technique is given followed by a description of the reference frames and model variables used within this Chapter. Each section of the model is then presented in turn starting with the vehicle dynamics, followed by the modelling of the propulsion system section which discusses the different tail actuation schemes investigated and finally the vehicle kinematics are discussed.

4.2 State Space Modelling

In order to analyse the mathematical model of the *RoboSalmon* vehicle to estimate vehicle performance a means of simulating the model is required. One common technique used for simulation of mathematical models, which is particularly suited to execution on a standard desktop computer using mathematical software such as *MATLAB*, is the state space technique [Schwarzenbach, & Gill, 1992; Dutton *et al*, 1998].

The state space technique allows for the simulation of time invariant, multi-input, multi-output systems and is used extensively in marine vessel modelling [McGookin, 1997; Perez, 2005] and robotics applications [Worrall & McGookin, 2006]. In order to use state space techniques the system, which is described by first order differential equations, model has to be represented as state equations [Vaccaro, 1995]. State space simulation techniques are used as they are especially suited to the programming techniques used in modern computer systems [Murray-Smith, 1995]. The value for each state is updated at each discrete simulation time step.

The general format of a state space model of a system is shown in Equation 4.1 [Schwarzenbach & Gill,1992].

$$\dot{\mathbf{x}} = \mathbf{Ax} + \mathbf{Bu} \quad (4.1)$$

Where \mathbf{x} is the state vector, $\dot{\mathbf{x}}$ is the state derivative vector, \mathbf{u} is the input vector, \mathbf{A} is the process matrix and \mathbf{B} is the input matrix. To simulate the *RoboSalmon* model the various input and control parameters are used to calculate the *state derivative* terms. Numerical techniques are then used to integrate the derivative of the state vector to give the state vector [Murray-Smith, 1995]. The flowchart in Figure 4.1 gives an overview of the state space model simulation

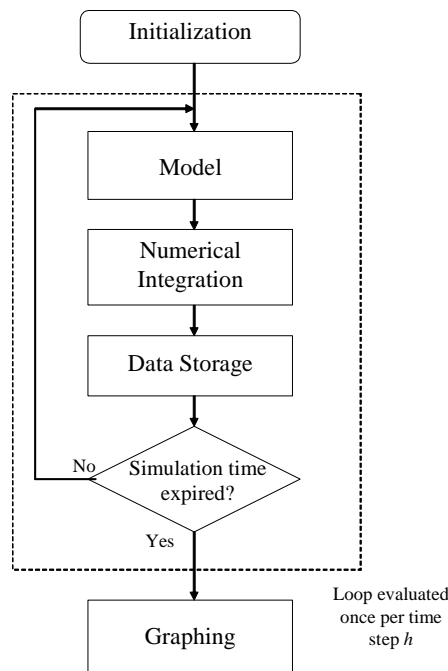


Figure 4.1: Flowchart of state space modelling technique

Firstly, the model is initialized by clearing all variables and the simulation time set to zero. The state space model is then executed and the state derivatives are calculated. Numerical integration is then used to integrate the state derivatives to give the states. All of the current variables including the state vector, state derivatives and control terms are stored. The simulation time is then incremented by the time step and the process continues until the simulation end time has been reached. The flowchart above could also include a control block which would allow control parameters to be varied to obtain desired outputs.

The model described in this Chapter also uses a multi-rate simulation approach with the vehicle dynamics running at five times the step size of the motor dynamics. This was implemented in order to decrease the time to complete simulations and is possible as the motor dynamics will respond faster than the vehicle dynamics.

4.3 Model Variables and Reference Frames

When working with any vehicular system such as marine vessels, aircraft, spacecraft or automobiles it is convenient to define a number of standard variables for describing velocity, displacement, etc and also to define reference frames or coordinate systems [Fossen, 1994]. For this model two reference frames are used, the body-fixed frame and an inertial Earth-fixed frame [Fossen, 1994]. The body-fixed frame is attached to the vehicle and moves with the vehicle as it moves. For simplicity the body-fixed frame usually has its origin located at the vehicles centre of gravity [Fossen, 1994]. The Earth-fixed frame is assumed to be an inertial frame, i.e. it is fixed and does not move [Fossen, 2002]. Figure 4.2 shows a diagram with the notation used for the body-fixed and Earth-fixed reference frames.

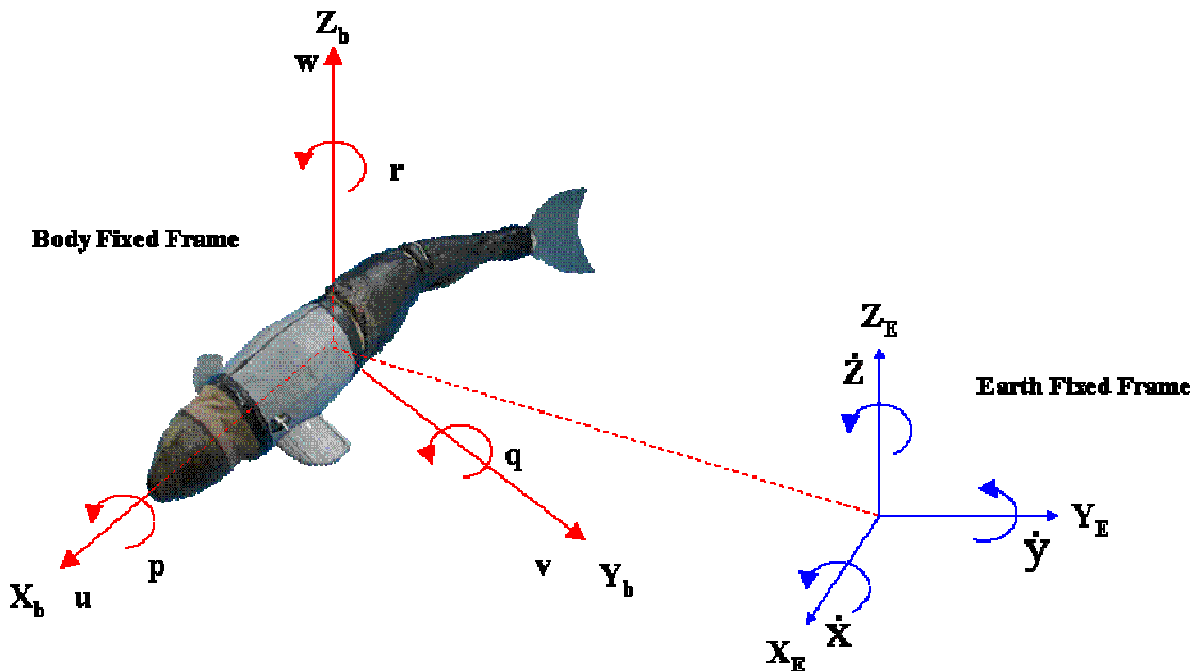


Figure 4.2: Illustration of Body-Fixed and Earth-Fixed reference Frames

The velocities and accelerations generated by the dynamics section of the model are calculated with respect to the body-fixed reference frame. In most cases it is useful, particularly for navigation purposes, to know how the vehicle is moving in the Earth fixed reference frame. It is therefore usually necessary to translate the forces and velocities generated in the moving body fixed frame to forces and velocities in the Earth-fixed frame which is stationary relative to the body-fixed frame. This translation process is described in the vehicle kinematics section which follows after this section.

As well as defining reference frames for the model it is convenient to define a number of variables which describe the motion of the vehicle within each of these reference frames. A standard notation has been developed for use with marine vessels by the Society of Naval Architects and Marine Engineers (SNAME) for describing the various forces and moments [Fossen, 2002] in each of the six degrees of freedom (DOF). This notation is shown in Table 4.1.

Table 4.1: SNAME notation for marine vessels (given in [Fossen, 1994])

Degrees of Freedom	Motion Description	Name	Forces & Moments	Linear and Angular Velocities	Positions and Euler Angles
1	Motions in the x-direction	Surge	X (N)	u (ms^{-1})	x (m)
2	Motions in the y-direction (sway)	Sway	Y (N)	v (ms^{-1})	y (m)
3	Motions in the z-direction (heave)	Heave	Z (N)	w (ms^{-1})	z (m)
4	Rotation about the x-axis (roll)	Roll	K (Nm)	p (rads^{-1})	ϕ (rad)
5	Rotation about the y-axis (pitch)	Pitch	M (Nm)	q (rads^{-1})	θ (rad)
6	Rotation about the z-axis (yaw)	Yaw	N (Nm)	r (rads^{-1})	ψ (rad)

For the purposes of developing mathematical models these variables are usually presented in vector form as shown in Equations (4.2), (4.3) and (4.4) [Fossen, 2001].

$$\eta = [\eta_1 \quad \eta_2]^T, \text{ where } \eta_1 = [x \quad y \quad z]^T \text{ and } \eta_2 = [\phi \quad \theta \quad \psi]^T \quad (4.2)$$

$$\nu = [\nu_1 \quad \nu_2]^T, \text{ where } \nu_1 = [u \quad v \quad w]^T \text{ and } \nu_2 = [p \quad q \quad r]^T \quad (4.3)$$

$$\tau = [\tau_1 \quad \tau_2]^T, \text{ where } \tau_1 = [X \quad Y \quad Z]^T \text{ and } \tau_2 = [K \quad M \quad N]^T \quad (4.4)$$

Where η is the vector of linear and angular positions within the Earth-fixed reference frame, \mathbf{v} is the vector of linear and angular velocities within the body-fixed frame and $\boldsymbol{\tau}$ is the vector of forces and moments in the body-fixed frame. This notation shall be used throughout the remainder of this thesis.

4.4 Vehicle Kinematics

To translate the body-fixed velocities generated by the dynamics section of the model to velocities in the inertially fixed Earth frame a transformation is required. The transformation is made up of a series of rotations carried out in a specific order as outlined by *Euler's Theorem on Rotation* [Fossen, 1994].

In order to carry out this transformation the linear and angular velocities are dealt with separately, therefore the velocity vector \mathbf{v} is split into two separate vectors \mathbf{v}_1 and \mathbf{v}_2 which are the linear and angular velocities in the body-fixed frame as shown previously in Equation (4.3). The corresponding vectors of linear and angular positions in the Earth-Fixed reference frame are given the notation $\boldsymbol{\eta}_1$ and $\boldsymbol{\eta}_2$ respectively also shown previously in Equation (4.2).

The standard notation for this transformation is shown in Equation (4.5) for the linear velocities and in Equation (4.6) for the angular velocities.

$$\dot{\boldsymbol{\eta}}_1 = \mathbf{J}_1(\boldsymbol{\eta}_2)\mathbf{v}_1 \quad (4.5)$$

$$\dot{\boldsymbol{\eta}}_2 = \mathbf{J}_2(\boldsymbol{\eta}_2)\mathbf{v}_2 \quad (4.6)$$

Where $\dot{\boldsymbol{\eta}}_1$ and $\dot{\boldsymbol{\eta}}_2$ are the linear and angular velocities in the Earth-fixed frame respectively and \mathbf{J}_1 and \mathbf{J}_2 are the transformation matrices used; \mathbf{J}_1 for the linear velocities shown in Equation (4.7) [Fossen, 1994] and \mathbf{J}_2 for the angular velocities shown in Equation (4.8) [Fossen, 2002].

$$\mathbf{J}_1(\boldsymbol{\eta}_2) = \begin{bmatrix} c\psi c\theta & -s\psi c\phi + c\psi s\theta s\phi & s\psi s\phi + c\psi c\phi s\theta \\ s\psi c\theta & c\psi c\phi + s\phi s\theta s\psi & -c\psi s\phi + s\theta s\psi c\phi \\ -s\theta & c\theta s\phi & c\theta c\phi \end{bmatrix} \quad (4.7)$$

$$\mathbf{J}_2(\boldsymbol{\eta}_2) = \begin{bmatrix} 1 & s\phi t\theta & c\phi t\theta \\ 0 & c\phi & -s\phi \\ 0 & \frac{s\phi}{c\theta} & \frac{c\phi}{c\theta} \end{bmatrix} \quad (4.8)$$

Here for compactness c represents the cosine function, s represents the sine function and t represents tan.

Therefore, the complete kinematic equation for translating from velocities in the body fixed frame to velocities in the Earth frame is given in Equation (4.9) [Fossen, 1994].

$$\dot{\boldsymbol{\eta}} = \mathbf{J}(\boldsymbol{\eta}_2) \cdot \mathbf{v} \Leftrightarrow \begin{bmatrix} \dot{\boldsymbol{\eta}}_1 \\ \dot{\boldsymbol{\eta}}_2 \end{bmatrix} = \begin{bmatrix} \mathbf{J}_1(\boldsymbol{\eta}_2) & \mathbf{0}_{3 \times 3} \\ \mathbf{0}_{3 \times 3} & \mathbf{J}_2(\boldsymbol{\eta}_2) \end{bmatrix} \begin{bmatrix} \mathbf{v}_1 \\ \mathbf{v}_2 \end{bmatrix} \quad (4.9)$$

4.5 Vehicle Dynamics

The dynamic model of the biomimetic *RoboSalmon* vehicle draws on techniques used to model conventional marine vessels such as AUVs and ROVs [Nahon, 1996; Fossen, 1994]. These techniques are modified with addition or replacement of terms to represent the biomimetic nature of the prototype such as the thrust and drag equations for fish propulsion and the shape of the vehicle altered to resemble a fish.

Any model developed will have to take into account the dynamics and kinematics of the vehicle. Therefore, the standard vehicular model for a 6 DOF system is used for modelling this system and is shown in Equation (4.10) [Fossen, 1994]. This equation has the origin of the body fixed frame located at the centre of gravity of the vehicle.

$$\mathbf{M} \dot{\mathbf{v}} + \mathbf{C}(\mathbf{v})\mathbf{v} + \mathbf{D}(\mathbf{v})\mathbf{v} + \mathbf{g}(\boldsymbol{\eta}) = \boldsymbol{\tau} \quad (4.10)$$

where \mathbf{M} is the inertia matrix (including added mass), $\mathbf{C}(\mathbf{v})$ is the matrix of Coriolis and centripetal terms (including added mass), $\mathbf{D}(\mathbf{v})$ is the damping matrix, $\mathbf{g}(\boldsymbol{\eta})$ is the vector of gravitational forces and moments, $\boldsymbol{\tau}$ is the vector of control inputs and \mathbf{v} is the linear and angular velocity vector. How each of these terms is dealt with in relation to the modelling of the *RoboSalmon* vehicle is covered within the following sections.

4.5.1 Rigid Body Dynamics

For the purposes of modelling the dynamics of the system, the *RoboSalmon* vehicle is assumed to be a rigid body. This assumption implies that the vehicle mass does not alter with time and that the shape remains constant [Humphrey & Topping, 1961]. The first assumption is reasonable as no fuel is consumed during the running of the vehicle as it is battery powered; the second assumption is not so easy to justify as the propulsion system is made up of a moving tail. However, due to the fact that most of the mass is concentrated within the body of the vehicle, assuming that the vehicle is a rigid body is considered to be a reasonable approximation.

The development of the rigid body equations of motion is based on the Newton-Euler Formulation which is based on Newton's Second Law [Fossen, 1994] which relates the acceleration and mass of an object to the force acting on it [Young & Freedman, 2000; Benson, 1996]. Mathematically, this is represented as [Young, Freedman, 2000]:

$$\Sigma \vec{\mathbf{F}} = m\vec{\mathbf{a}} \quad (4.11)$$

Where m is the mass of the object in kg, $\vec{\mathbf{a}}$ is the acceleration of the object in ms^{-2} and $\Sigma \vec{\mathbf{F}}$ is the summation of all the forces acting on the body in Newtons.

To develop the rigid body equations of motion Euler's first and second axioms are used [Fossen, 1994]. These axioms express Newton's Second Law in terms of both linear momentum \mathbf{p}_C and angular momentum \mathbf{h}_C shown in Equations (4.12) and (4.13) [Fossen, 1994].

$$\text{Euler's 1}^{st} \text{ Axiom} \quad \dot{\mathbf{p}} = \mathbf{f}_C \quad \mathbf{p}_C = m\mathbf{v}_C \quad (4.12)$$

$$\text{Euler's 2}^{nd} \text{ Axiom} \quad \dot{\mathbf{h}}_C = \mathbf{m}_C \quad \mathbf{h}_C = \mathbf{I}_C\boldsymbol{\omega} \quad (4.13)$$

Here \mathbf{f}_C and \mathbf{m}_C are forces and moments referred to the body's centre of gravity, $\boldsymbol{\omega}$ is the angular velocity vector, m is the mass of the body and \mathbf{I}_C is the Inertia about the body's centre of gravity [Fossen, 2002].

The derivation of rigid body equations of motion from Newton's Second Law and Euler's first and second Axioms can be found in [Fossen, 1994] and [Fossen, 2002]. The rigid body equations of motion for each of the 6 degrees of freedom for the *RoboSalmon* vehicle can be stated as shown in Equations (4.14) to (4.19) [Fossen, 1994].

$$\text{Surge} \quad X = m[\dot{u} - vr + wq] \quad (4.14)$$

$$\text{Sway} \quad Y = m[\dot{v} - wp + ur] \quad (4.15)$$

$$\text{Heave} \quad W = m[\dot{w} - uq + vp] \quad (4.16)$$

$$\text{Roll} \quad K = I_x\dot{p} + (I_z - I_y)qr \quad (4.17)$$

$$\text{Pitch} \quad M = I_y\dot{q} + (I_x - I_z)rp \quad (4.18)$$

$$\text{Yaw} \quad N = I_z\dot{r} + (I_y - I_x)pq \quad (4.19)$$

Here I_x , I_y and I_z are the moments of inertia of the vehicle about the X_B , Y_B and Z_B axes respectively.

4.5.2 Inertia Matrix

The inertia matrix \mathbf{M} is composed of two components as shown in Equation (4.20), the rigid body inertia matrix and the added inertia matrix to take effects due to the added mass forces and inertia into account [Fossen, 1994]:

$$\mathbf{M} = \mathbf{M}_{RB} + \mathbf{M}_A \quad (4.20)$$

To simplify the matrices it is assumed that the centre of gravity is located at the same position as the origin of the body-fixed frame. To give the vehicle a degree of metastability the centre of buoyancy is set to coincide with the centre of gravity in the X_B and Y_B axes but is set slightly above the centre of buoyancy. This means that:

$$r_G = \begin{bmatrix} x_G \\ y_G \\ z_G \end{bmatrix} = \begin{bmatrix} 0 \\ 0 \\ 0 \end{bmatrix} \quad (4.21)$$

$$r_B = \begin{bmatrix} x_B \\ y_B \\ z_B \end{bmatrix} = \begin{bmatrix} 0 \\ 0 \\ 0.02 \end{bmatrix} \quad (4.22)$$

A large number of marine vessel models assume that the vehicle to be modelled is neutrally buoyant; the weight (i.e. downward force due to gravity) is equal to the buoyancy force (i.e. upward force due to the water). In reality achieving neutral buoyancy is a near impossible task without a dynamic ballast system [Burcher & Rydill, 1994]. The *RoboSalmon* vehicle has been designed to be slightly positively buoyant so if any malfunctions occur it rises to the surface.

Therefore, the rigid body inertia matrix for the *RoboSalmon* simplifies to:

$$M_{RB} = \begin{bmatrix} m & 0 & 0 & 0 & 0 & 0 \\ 0 & m & 0 & 0 & 0 & 0 \\ 0 & 0 & m & 0 & 0 & 0 \\ 0 & 0 & 0 & I_x & 0 & 0 \\ 0 & 0 & 0 & 0 & I_y & 0 \\ 0 & 0 & 0 & 0 & 0 & I_z \end{bmatrix} \quad (4.23)$$

The moments of inertia for the vehicle are calculated using the standard equation for the moment of inertia of a cylinder [Humphrey & Topping, 1961].

4.5.3 Coriolis & Centripetal Terms

For modelling purposes the effect of the Coriolis and centripetal forces acting on the vehicle, the two forces are dealt with together within one matrix $C(\mathbf{v})$. The centripetal force is caused when the motion of the vehicle follows a curved path [Benson, 1996]. The Coriolis effect is due to motion of the vehicle within a rotating reference frame e.g. moving over the surface of the Earth [Benson, 1996; Fossen, 2002]. The $C(\mathbf{v})$ matrix provides the correction required to model these additional movements within the model.

Like the inertia matrix, the Coriolis and centripetal matrix is made up of two components; the Coriolis and centripetal terms due to the rigid body, $C_{RB}(\mathbf{v})$, and the terms relating to the added mass effect, $C_A(\mathbf{v})$.

$$C(\mathbf{v}) = C_{RB}(\mathbf{v}) + C_A(\mathbf{v}) \quad (4.24)$$

Here $C_{RB}(\mathbf{v})$ can be represented as shown in Equation (4.24), assuming that the origin of the body-fixed reference frame coincides with the centre of gravity [Fossen, 1994].

$$C_{RB}(v) = \begin{bmatrix} 0 & 0 & 0 & 0 & mw & -mv \\ 0 & 0 & 0 & -mw & 0 & mu \\ 0 & 0 & 0 & mv & -mu & 0 \\ 0 & mw & -mv & 0 & I_z r & -I_y q \\ -mw & 0 & mu & -I_z r & 0 & I_x p \\ mv & -mu & 0 & I_y q & -I_x p & 0 \end{bmatrix} \quad (4.25)$$

The actual effects of the added mass terms shown previously in Equation (4.25) and (4.20) and the calculation of the appropriate terms are covered in the next section.

4.5.4 Hydrodynamic Added Mass Terms

The added mass is a representation of the pressure induced forces and moments due to a forced harmonic motion of the body that are proportional to the acceleration of the body [Fossen, 2001]. This phenomenon manifests itself mathematically within the mass and Coriolis matrices.

The standard added inertia matrix M_A containing the added mass derivatives is shown as:

$$M_A = \begin{bmatrix} X_{\ddot{u}} & X_{\ddot{v}} & X_{\ddot{w}} & X_{\ddot{p}} & X_{\ddot{q}} & X_{\ddot{r}} \\ Y_{\ddot{u}} & Y_{\ddot{v}} & Y_{\ddot{w}} & Y_{\ddot{p}} & Y_{\ddot{q}} & Y_{\ddot{r}} \\ Z_{\ddot{u}} & Z_{\ddot{v}} & Z_{\ddot{w}} & Z_{\ddot{p}} & Z_{\ddot{q}} & Z_{\ddot{r}} \\ K_{\ddot{u}} & K_{\ddot{v}} & K_{\ddot{w}} & K_{\ddot{p}} & K_{\ddot{q}} & K_{\ddot{r}} \\ M_{\ddot{u}} & M_{\ddot{v}} & M_{\ddot{w}} & M_{\ddot{p}} & M_{\ddot{q}} & M_{\ddot{r}} \\ N_{\ddot{u}} & N_{\ddot{v}} & N_{\ddot{w}} & N_{\ddot{p}} & N_{\ddot{q}} & N_{\ddot{r}} \end{bmatrix} \quad (4.26)$$

In order to simplify the model, assumptions can be made that simplify the matrix shown in Equation (4.26). The two assumptions made are that firstly the motion of an underwater vehicle is usually low speed, non-linear and coupled and secondly that there are certain symmetries within the hull form [Fossen, 1994]. The hull of the *RoboSalmon* vehicle is also assumed to be prolate ellipsoid in shape, shown in Figure 4.3, and due to both these assumptions the added mass matrix can be simplified to only the diagonal elements as shown in Equation (4.27) [Fossen, 2001; Imlay, 1961].

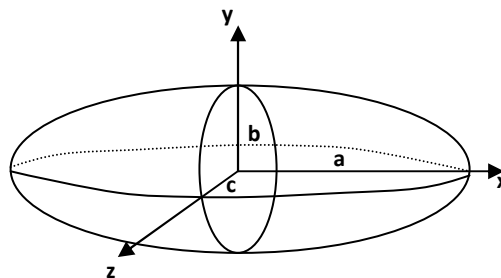


Figure 4.3 – Prolate Ellipsoid with semi-axes a,b and c [Fossen, 2001]

$$M_A = \begin{bmatrix} X_{\dot{u}} & 0 & 0 & 0 & 0 & 0 \\ 0 & Y_{\dot{v}} & 0 & 0 & 0 & 0 \\ 0 & 0 & Z_{\dot{w}} & 0 & 0 & 0 \\ 0 & 0 & 0 & K_{\dot{p}} & 0 & 0 \\ 0 & 0 & 0 & 0 & M_{\dot{q}} & 0 \\ 0 & 0 & 0 & 0 & 0 & N_{\dot{r}} \end{bmatrix} \quad (4.27)$$

These assumptions also lead to the added mass terms for the Coriolis and centripetal terms being simplified as shown in Equation (4.28) [Fossen, 1994]

$$C_A(v) = \begin{bmatrix} 0 & 0 & 0 & 0 & -Z_{\dot{w}}w & Y_{\dot{v}}v \\ 0 & 0 & 0 & Z_{\dot{w}}w & 0 & -X_{\dot{u}}u \\ 0 & 0 & 0 & -Y_{\dot{v}}v & X_{\dot{u}}u & 0 \\ 0 & -Z_{\dot{w}}w & Y_{\dot{v}}v & 0 & -N_{\dot{r}}r & M_{\dot{q}}q \\ Z_{\dot{w}}w & 0 & -X_{\dot{u}}u & N_{\dot{r}}r & 0 & -K_{\dot{p}}p \\ -Y_{\dot{v}}v & X_{\dot{u}}u & 0 & -M_{\dot{q}}q & K_{\dot{p}}p & 0 \end{bmatrix} \quad (4.28)$$

Using a prolate ellipsoid as the shape for the hull the model only has to consider six added mass derivative terms which can be calculated as shown in Equations (4.29) to (4.33) [Fossen, 2001; Imlay, 1961].

$$e = 1 - \left(\frac{b}{a}\right)^2 \quad (4.29)$$

$$X_{\dot{u}} = -\frac{\alpha_0}{2 - \alpha_0} m \quad (4.30)$$

$$Y_{\dot{v}} = Z_{\dot{w}} = -\frac{\beta_0}{2 - \beta_0} m \quad (4.31)$$

$$K_{\dot{p}} = 0 \quad (4.32)$$

$$N_{\dot{r}} = M_{\dot{q}} = -\frac{1}{5} \frac{(b^2 - a^2)^2 (\alpha_0 - \beta_0)}{2(b^2 - a^2) + (b^2 + a^2)(\beta_0 - \alpha_0)} \quad (4.33)$$

Here e is the eccentricity and α_0 and β_0 are constants [Fossen, 1994].

4.5.5 Restoring Forces and Moments

The restoring forces and moments are the terms which take into account the gravitational and buoyancy forces [Fossen, 2001]. Two important parameters in calculating these forces and moments for underwater vehicles are the distance between the origin of the body-fixed reference frame, the centre of gravity (COG) and the centre of buoyancy (COB) of the vehicle.

In many underwater vehicle models for simplicity the vehicle is assumed to be neutrally buoyant [Pettersen & Egeland, 1996; Cavallo *et al*, 2003]. As previously mentioned obtaining neutral buoyancy is a near impossible task within the hardware but making this assumption simplifies a number of terms within the model. The complete vector of restoring forces and moments due to gravitational and buoyancy terms are shown in Equation (4.34).

$$g(\eta) = \begin{bmatrix} (W - B) \sin \theta \\ -(W - B) \cos \theta \sin \phi \\ -(W - B) \cos \theta \cos \phi \\ -(y_G W - y_B B) \cos \theta \cos \phi + (z_G W - z_B B) \cos \theta \sin \phi \\ (z_G W - z_B B) \sin \theta + (x_G W - x_B B) \cos \theta \cos \phi \\ -(x_G W - x_B B) \cos \theta \sin \phi - (y_G W - y_B B) \sin \theta \end{bmatrix} \quad (4.34)$$

One important aspect to consider in all marine vehicle design is the stability in roll. It is possible with correct positioning of the COG and COB to create a roll restoring moment which acts when the vehicle is subject an angular roll displacement taking it away from its upright position. For underwater vehicles this is usually achieved when the COB is positioned above the COG on the z-axis.

For the *RoboSalmon* it is assumed that the COB is higher than the COG on the z-axis, but has equal x and y-axis terms. This produces moments which act to bring the vessel back to its equilibrium after the removal of any external forces as illustrated in Figure 4.4.

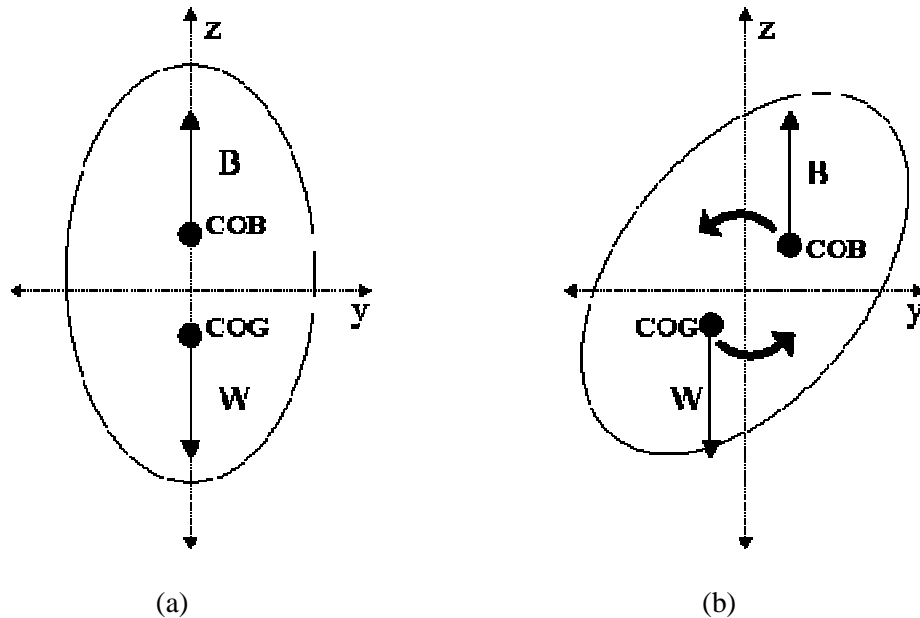


Figure 4.4: Restoring forces for roll on x-z plane (a) when upright i.e. no roll angular displacement and (b) with angular roll displacement, with COB and COG differ on z-axis.

Many conventional underwater vehicles utilize this approach for passive roll control as no actuators are required [Von Alt, *et al*, 1994]. Therefore, as well as being slightly positively buoyant the COB of

the *RoboSalmon* vehicle is located above the COG and much effort has been expended to make the COG and COB as close as possible on the x and y axes.

However, as briefly mentioned in Chapter 2, real fish are usually statically unstable as they have their COB below their COG [Lauder & Madden, 2006]. Although the aim of this project is to mimic a fish as accurately as possible, making the vehicle statically unstable would create a number of difficult problems with the design and control of the vehicle. Therefore, it has been decided to opt for simplicity and make the COG below the COB.

The gravitational and buoyancy vector used for the simulation of the *RoboSalmon* vehicle is given in Equation (4.35).

$$g(\eta) = \begin{bmatrix} 0 \\ 0 \\ 0 \\ (z_G W - z_B B) \cos \theta \sin \phi \\ (z_G W - z_B B) \sin \theta \\ 0 \end{bmatrix} \quad (4.35)$$

4.5.6 Hydrodynamic Damping Terms

One force that acts on any vehicle operating in the underwater environment is *hydrodynamic damping* or *drag* [Fossen, 1994]. This force is one of the forces that contribute to the dynamics of the vehicle and as such a term is required in the forces and moments section of the model to represent the drag force. The notation used for the drag forces in this investigation is X_{dn} for the drag force in surge, Y_{dn} for the drag force in sway, etc.

The various types of drag acting on a body submerged in water are covered in more detail in Chapter 2. Damping is approximated using the standard equation for drag shown in Equation (4.36) [Hoerner, 1965; Fossen, 1994].

$$f(U) = -\frac{1}{2} \rho C_D A |U| U \quad (4.36)$$

where ρ is the density of fluid (kgm^{-3}), C_D is the drag coefficient, A is the cross-sectional area (m^2) and U is the velocity of the vehicle (ms^{-1}). This equation is used to calculate the drag force acting in surge, sway and heave and also used to estimate the rotational drag terms in roll, pitch and yaw.

The equation for drag requires the drag coefficient C_D to be known in each degree of freedom. As the body of the *RoboSalmon* is not just a prolate ellipsoid but an ellipsoid with fins, the drag due to these fins has to be taken into account when calculating the overall drag coefficient in each DOF.

Firstly, for the main body in surge, sway and yaw directions the drag force can be estimated using the equation for the drag coefficient for simple streamlined ellipsoidal bodies at sub-critical Reynolds Numbers [Hoerner, 1965],

$$C_D = 0.44\left(\frac{b}{a}\right) + 0.016\left(\frac{a}{b}\right) + 0.016\sqrt{\left(\frac{a}{b}\right)} \quad (4.37)$$

where a is radius of ellipsoid along x-axis and b is the radius of ellipsoid along y-z plane.

The drag force produced by the fins located on the body is estimated using the standard drag equation and knowledge of the shape of the fins, which have been designed to be as close to NACA 0012 sections as possible [Goett & Bullivant, 1938]. Knowing the NACA section of these fins and the angle these fins make to the oncoming flow of fluid allows calculation of the drag force in surge produced from data tables of angle of attack versus drag coefficient [Kermode, 1987]. The drag force in heave is calculated simply from the planform area of the fins and the drag coefficient of a flat plate [Hoerner, 1965]. Combining the methods described above an approximation for the rigid body drag can be deduced in the 6 DOF.

However, as indicated in Chapter 2 the drag on a swimming fish is not as straight forward as using the rigid body drag due the complex interactions between the undulating fish body and the water [Videler, 1993; Triantafyllou & Triantafyllou, 1995]. An attempt has been made to model the drag produced by the moving tail by assuming the caudal fin is a wedge that has a surface area which is dependant on the angle the fin make with the oncoming water flow. The drag coefficient used for this wedge that represents the caudal fin is 0.5 [Hoerner, 1965]. If the fin is at its maximum amplitude then its surface area is maximum and therefore increasing the drag force. However, if it is in line with the body then the drag is reduced. By making this assumption the drag force produced by the caudal fin varies over one tail beat cycle and when viewed over several tail beat cycles the drag appears to oscillate about a steady value.

4.6 Propulsion System Modelling

The aim of modelling the propulsion system is to allow for estimates of the control forces and moments (i.e. thrust and manoeuvring forces) to be made using the input commands to the system. These approximations of thrust are then feed into the dynamic section of the model. The control forces and moments for the *RoboSalmon* vehicle are dependant on which tail actuation system is being used at the time. As such the calculation of the control forces and moments for each tail actuation system are dealt with separately.

4.6.1 Tendon Drive System

The aim of modelling the propulsion system is to allow for estimates of the thrust and manoeuvring forces to be made using the input commands to the system. For the model the system has been subdivided into four sections as shown in Figure 4.5.

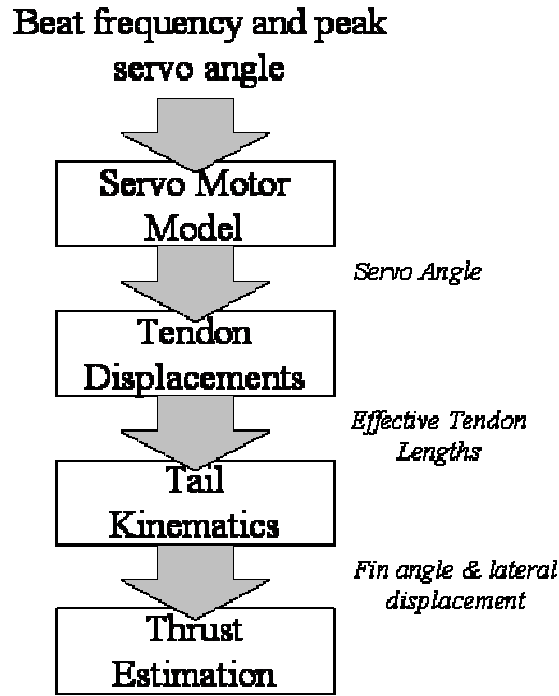


Figure 4.5: Flowchart of Tendon Drive Propulsion System Model

This flowchart shows the main components of the model. The input to the model is the desired tail beat frequency and amplitude which is passed to the servo motor model. This then causes the servo to move in the reciprocal manner to the servo motor parameters that will correspond to the desired tail commands. The output of the servo motor model are the displacements of the servo motor arms, these values are then used to calculate the changes in the tendons. These tendon displacements are fed into the tail kinematics which relates the tendon lengths to the angular positions of each revolute joint in the tail. Knowing the angular position of each of the ten revolute joints allows the caudal fin tip displacement to be calculated along with the angle the caudal fin makes with the tail centre line. With these caudal fin parameters known over time it is possible to estimate the thrust produced.

4.6.1.1 Servo Motor Model

For actuation of the tendon drive system a Hitec HS-5645 Digital Servo [Hitec RCD, 2007] motor is used. This servo operates by moving the output servo arm to an angular position which corresponds to the pulse width of the input *pulse width modulated* (PWM) signal.

This servo motor system is modelled as a DC motor with a reduction gearbox attached. The standard electrical and mechanical equations for a DC motor [Franklin, *et al*, 1991], which are shown in Equations (4.38) and (4.39), are used to describe the motor.

$$L \frac{di}{dt} + Ri = V - K_e \dot{\theta}_{MOTOR} \quad (4.38)$$

$$J \ddot{\theta}_{MOTOR} + b \dot{\theta}_{MOTOR} = K_t i - T_l \quad (4.39)$$

Here L is the inductance of the motor (H), I is the motor current (A), R is the motor resistance (Ω), V is the applied voltage (V), K_e is the motor emf constant ($V\text{rad}^{-1}\text{s}^{-1}$), θ is the motor angular displacement (radians), J is the inertia of the motor shaft and load (kgm^2), b is the viscous friction coefficient, K_t is the motor torque constant (NmA^{-1}) and T_l is the load torque (Nm).

It is assumed that a proportional-integral-derivative (PID) controller is used within the servo for positional control of the servo arm [Behnke & Schreiber, 2006].

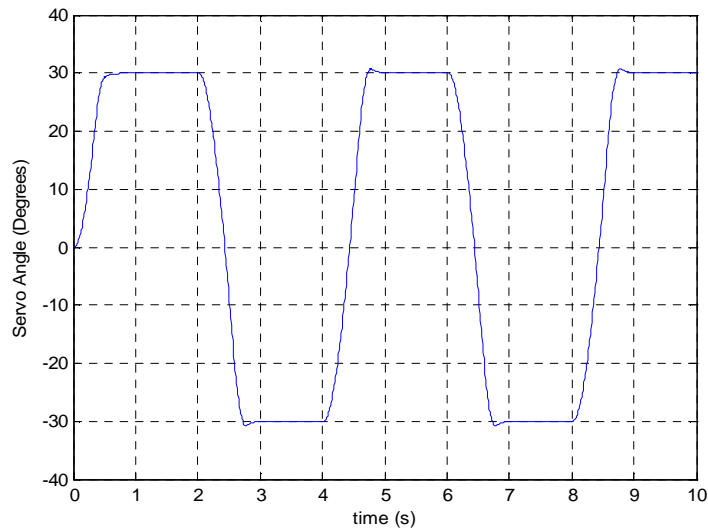


Figure 4.6: Simulated servo model response to step changes of ± 30 degrees

The simulated servo response to step changes of commands of $\pm 30^\circ$ is shown in Figure 4.6. This shows that the PID controller is effective in allowing the servo to reach its commanded position with only slight overshoot.

Commands are sent to this servo which generates a reciprocal rotational motion of between ± 45 degrees. The maximum frequency of this motion is limited to approximately 1Hz due to the mechanical limitations of the whole tendon drive system.

4.6.1.2 Tendon Displacements

In order to determine the revolute joint variables for a particular servo-motor angle the relationship between the servo-motor arm, tendons and joint assemblies has to be known. Firstly, the servo motor receives an input PWM signal that contains a duty cycle corresponding to the desired output angle of the servo-motor arms. This movement of the servo arms pulls on one of the tendons. This pulled tendon is referred to as the active tendon as it is this tendon which causes the deflection in the tail. The tendon that is not being pulled is assumed not to contribute to the motion at this instant. As the servo-motor is mounted in the body section the length of tendon wire within the tail assembly is reduced, this is referred to as effective shortening of the tendon.

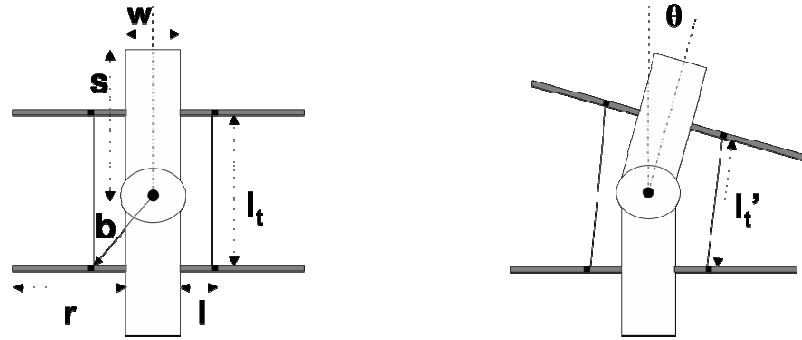
The relationship between the servo-motor angle and the effective shortening is calculated using the geometry of the internal mechanics of the tail/servo assembly. Equations (4.40) and (4.41) represent the relationship between the servo angle (β) and the change in tendon lengths (x_L and x_R) [Watts, McGookin & Macauley, 2008a].

$$x_L = \sqrt{(l_{arm} \cos(\phi_{SERVO}) - z)^2 + (l_{servo} - l_{arm} \sin(\beta))^2} - xc \quad (4.40)$$

$$x_R = \sqrt{(l_{arm} \cos(\phi_{SERVO}) - z)^2 + (l_{servo} + l_{arm} \sin(\beta))^2} - xc \quad (4.41)$$

The other parameters l_{arm} , l_{servo} and z represent the length of the servo arm, distance from the motor shaft to the start of the tail assembly and the distance between the tendons at the start of the tail respectively. The servo-motor angle is ϕ_{SERVO} and the final parameter xc , is the length of the tendons when the tail is at its centre position.

This overall change in tendon length is distributed among the ten revolute joints. From experimentation with the prototype it has been apparent that this distribution is not equal. This is because the joint angles towards the fin end of the tail are greater than those towards the body due to the mechanics of the tail. For this reason a linearly increasing distribution of the change in tendon length is assumed over the ten revolute joints. A diagram of the plan view of one revolute joint from the tail assembly is shown in Figure. 4.7.



(a) Tendon lengths equal.

(b) Right tendon shortened

Figure 4.7.: Individual revolute joint assembly showing tendons and rib sections.

The joint angle of a revolute joint can be calculated from the corresponding change in length of the active tendon for that joint assembly using trigonometry. This is shown in Equation (4.42).

$$\theta_x = - \left(180 - 2 \sin^{-1} \left(\frac{l + \frac{w}{2}}{b} \right) - 2 \sin^{-1} \left(\frac{l_t'}{2b} \right) \right) \quad (4.42)$$

Here θ_x is the angle for joint x , l is the distance of the tendon from the segment at the shortest point (m), w is the width of the segment (m), l_i and l_i' represent the lengths of the tendon at its centre position and when shortened respectively.

4.6.1.3 Tendon Tail Kinematics

Due to the design of the tail it can be thought of as a robot manipulator with ten revolute joints. As such the kinematic equations used to describe robot manipulators can be applied to describe the tendon drive tail.

The standard method used to model the forward kinematics of robot manipulators is the Denavit-Hartenberg (D-H) representation [Niku 2001]. This method involves assigning each joint and link a reference frame according to a set procedure. The joint-link representation for the 10 segment tendon drive *RoboSalmon* tail is shown in Figure 4.8.

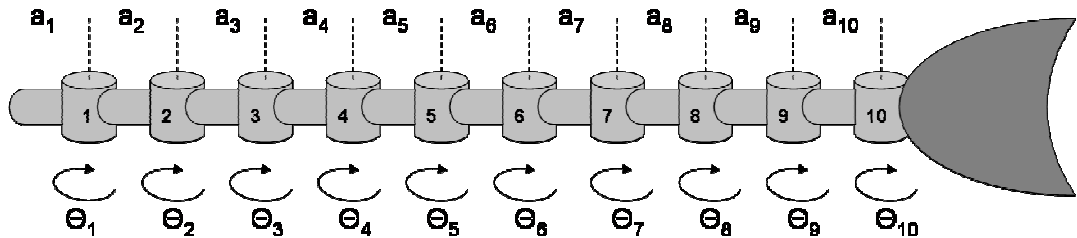


Figure 4.8: Joint and link representation of *RoboSalmon* tail assembly

The parameters for all the joints are then assembled into a table referred to as a D-H parameter table. By creating a table of parameters like this, it allows easy calculation of the 'A' matrix for each joint. The 'A' matrix is a combination of all four movements (rotation about the x,y and z axes and a translation). Using the A matrix for each joint allows for transformation between the successive joint frames of reference.

The parameters included in the D-H parameter table are Joint number #, Rotation about the z-axis of revolute joint Θ (rad), distance between two common normals (joint offset) d (m), Link length a (m) and the angle between two successive z-axes α (rad). The D-H parameter table for the tendon drive tail assembly is shown in Table 4.2.

Table 4.2: D-H Parameter Table Representation of Tendon Drive Tail

#	θ	d	a	α
1	θ_1	0	0.03	0
2	θ_2	0	0.03	0
3	θ_3	0	0.03	0
4	θ_4	0	0.03	0
5	θ_5	0	0.03	0
6	θ_6	0	0.03	0
7	θ_7	0	0.03	0
8	θ_8	0	0.03	0
9	θ_9	0	0.03	0
10	θ_{10}	0	0.03	0
11	0	0	0.105	0

By using the A matrices derived from the D-H parameter table transformation between the first segment frame (the one connected to the body) and the last joint (joint representing the caudal peduncle) is possible. By doing this it allows the position of each joint to be determined in the caudal peduncle reference frame.

This process of transformation between the body and caudal peduncle is carried out as follows in Equation (4.43).

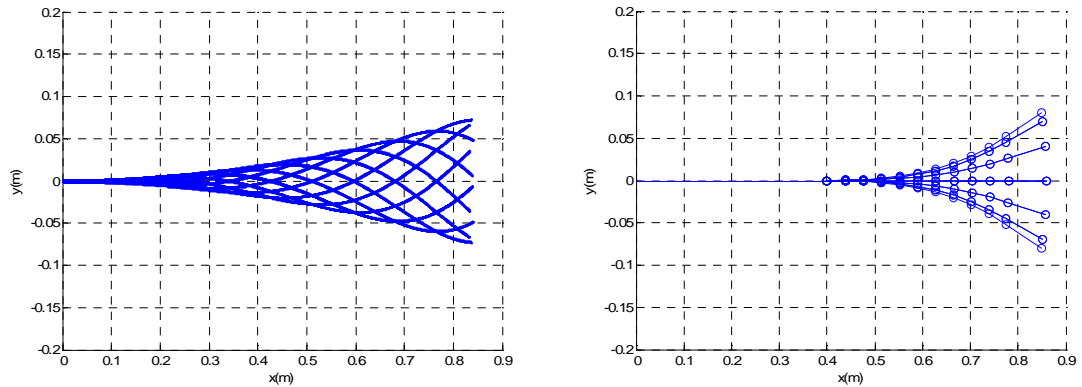
$$T=^{0(Body)}T_1^1T_2^2T_3^3T_4^4T_5^5T_6^6T_7^7T_8^8T_9^9T_{10(CaudalPeduncle)}^{10} = A_1A_2A_3A_4A_5A_6A_7A_8A_9A_{10} \quad (4.43)$$

In order to know the position of each joint in the tail, the transformation matrices the frame for each joint is transformed into the body frame as shown below in Equations 4.44 :-

$$\begin{aligned}
 \text{frame1 to body: } T &=^{0(Body)}T_1^1 = A_1 \\
 \text{frame2 to body: } T &=^{0(Body)}T_1^1T_2^2 = A_1A_2 \\
 \text{frame3 to body: } T &=^{0(Body)}T_1^1T_2^2T_3^3 = A_1A_2A_3 \\
 \text{frame4 to body: } T &=^{0(Body)}T_1^1T_2^2T_3^3T_4^4 = A_1A_2A_3A_4 \\
 \text{frame5 to body: } T &=^{0(Body)}T_1^1T_2^2T_3^3T_4^4T_5^5 = A_1A_2A_3A_4A_5 \\
 \text{frame6 to body: } T &=^{0(Body)}T_1^1T_2^2T_3^3T_4^4T_5^5T_6^6 = A_1A_2A_3A_4A_5A_6 \\
 \text{frame7 to body: } T &=^{0(Body)}T_1^1T_2^2T_3^3T_4^4T_5^5T_6^6T_7^7 = A_1A_2A_3A_4A_5A_6A_7 \\
 \text{frame8 to body: } T &=^{0(Body)}T_1^1T_2^2T_3^3T_4^4T_5^5T_6^6T_7^7T_8^8 = A_1A_2A_3A_4A_5A_6A_7A_8 \\
 \text{frame9 to body: } T &=^{0(Body)}T_1^1T_2^2T_3^3T_4^4T_5^5T_6^6T_7^7T_8^8T_9^9 = A_1A_2A_3A_4A_5A_6A_7A_8A_9 \\
 \text{peduncle to body: } T &=^{0(Body)}T_1^1T_2^2T_3^3T_4^4T_5^5T_6^6T_7^7T_8^8T_9^9T_{10(CaudalPeduncle)}^{10} = A_1A_2A_3A_4A_5A_6A_7A_8A_9A_{10}
 \end{aligned} \quad (4.44)$$

Using the above transformation matrices the location of the origin of each joint frame in the body reference frame can be plotted in two dimensions from the x and y translational coordinates in each of the matrices. This method also allows the lateral displacement of the caudal fin from the tail centre line to be calculated.

From the above discussion of the various aspects of the tail system, the overall kinematics of the tail can be computed knowing the input angle from the servo motor. A plot of the *RoboSalmon* tendon tail assembly kinematics and ideal fish kinematics is shown for one instant during a tail beat cycle in Figure 4.9.



(a) Ideal fish kinematics

(b) kinematics from *RoboSalmon* Tail assembly

Figure 4.9: Comparison of Ideal and Obtained Tail Kinematics (Solid line shows ideal kinematics and circled line shows *RoboSalmon* tail)

From this comparison the limitations of the *RoboSalmon* Tail assembly is apparent. Although, the position of the tail tip of *RoboSalmon* is fairly close to the tail tip position in the ideal kinematics, the shape of the *RoboSalmon* tail differs from the ideal situation. Also, the tail tip amplitude and the angle of the tail fin are in phase whereas from observations of real fish they appear to be 90° out of phase. These differences are unavoidable due to the mechanical design and actuation method of the tail assembly. However, the simplicity and low cost nature of this approach should compensate for the difference in the kinematics and any adverse effect this may have on the performance of the vehicle.

4.6.1.4 Tendon Tail Thrust Estimate

For this model a method of estimating the thrust produced by the tail motion was required. From surveys of the available literature on fish propulsion there does not appear to be an exact and definitive, theoretical method for easily calculating the thrust produced by the undulating tail and fin movements of fish swimming. Some sources suggest that solving the Navier-Stokes equation gives an accurate prediction of the thrust, however, this method requires the use of computational fluid dynamics and would take a substantial amount of time to solve due to its complexity [Colgate & Lynch, 2004].

From the literature surveyed there appears to be two main methods for estimating this thrust force: vortex theory [Streitlein & Triantafyllou, 1998] and elongated body theory and its derivatives [Lighthill, 1971]. Both methods have their advantages and disadvantages.

The vortex method estimates the thrust produced by analysing the vortices left in the wake as the fish swims. This method uses parameters of the vortex wake such as circulation, size, positioning and number of vortices in the wake [Streitlein & Triantafyllou, 1998].

However, this method is of limited use for the modelling and simulation of the propulsion system. At present there does not appear to be a simple method of predicting the formation of the vortices and vortex parameters from the movements of the fish without the use of complex computational fluid dynamics methods, or direct observation and measurement of the vortices produced while swimming [Videler, 1993]. Using this method in runtime while the vehicle is in operation would be difficult due to the speed at which the vortex information could be obtained and processed.

The other method that can be used to estimate the thrust produced by fish like propulsion is Lighthill's *Large Amplitude Elongated Body Theory* [Lighthill, 1971]. The idea behind this theory is the transfer of momentum between fish and water and assumes that the majority of this transfer happens at the caudal fin [Videler, 1993]. Therefore, only the heave and pitch motion of the caudal fin is used in the calculation. In the context of this theory heave motion is the side to side displacement of the caudal fin and pitch is the angle of the caudal fin to the centreline of the fish [Triantafyllou, Triantafyllou & Yue, 2000]. These two parameters are different from the standard heave and pitch used to describe marine vessels. This is due to the initial investigations into propulsion using a species that had a horizontal caudal fin and so heave and pitch were used to describe the motion. However, the same theory applies to both horizontal and vertical fin orientation [Lighthill, 1970].

Both heave and pitch are assumed to be sinusoidal functions [Triantafyllou, Techtet, & Hover, 2004] and from observations of real fish and simulations the heave and pitch are approximately 90° out of phase from one another. The equation used for the thrust estimate is given in Equation (4.45).

$$F_{Thrust} = m_v w W - \frac{1}{2} w^2 m_v \quad (4.45)$$

Where F_{Thrust} is the surge thrust force (N), m_v is the virtual mass per unit length (kg), w is the perpendicular velocity of tail (ms^{-1}) and W is the lateral velocity of the tail tip (ms^{-1}). Figure 4.10 shows plots of the thrust and drag force in surge for a tail beat frequency of 1Hz starting initially from rest.

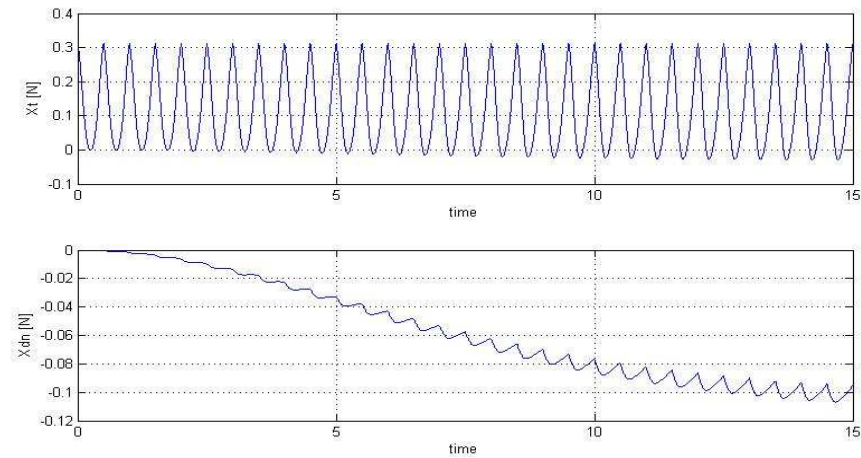
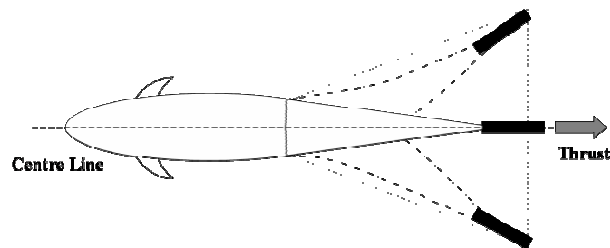


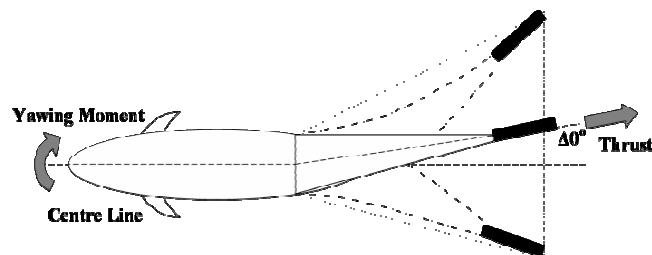
Figure 4.10 Plots of surge thrust X_t (top) and drag force X_{dn} (bottom) for a tail beat frequency of 1Hz
 Although the thrust force varies dramatically over one tail beat cycle when the instantaneous force is averaged for steady swimming it coincides with the drag force produced.

4.6.1.5 Tendon Tail Manoeuvring

In order for the vehicle to manoeuvre the centreline of the tail oscillation can be altered. For forward propulsion the tail centreline is in line with the body. When the position of the undulation centreline is altered (by angle $\Delta\theta$) then it is assumed that a component of the thrust force acts in sway and thus yaw. This is illustrated in Figure 4.11.



(a) Thrust force when tail beat centred (Forward Motion)



(b) Thrust force when tail beat offset (Turning Motion)

Figure 4.11: Diagram of tail sweep and thrust force

With the tail oscillating with the centreline offset the force components in surge, sway and yaw are calculated using trigonometric relationships. This allows for the model to represent the manoeuvring forces generated by the tail.

4.6.1.6 Recoil Motion

From experimentation with the initial tendon drive *RoboSalmon* prototype one aspect of the swimming that has become apparent is the level of recoil motion generated by the tail. This recoil motion occurs when the tail moves one way and the rest of the body recoils in reaction. This causes the vehicle to exhibit unwanted roll, pitch and yaw motions. Real fish experience recoil motion [Fish, 2002] but it is not as severe as the recoil present in certain biomimetic vehicles like the *RoboSalmon*. This is because real fish have a number of methods of dealing with recoil motions such as having a flat body profile which increases lateral drag [Webb, 1977]. Another way they deal with recoil is in the undulatory motion of the body/tail during swimming which, at any one instant, there are parts of the body/tail at both sides of the fishes centreline and as the undulatory motion is cyclical the lateral forces causing the recoil are thought to cancel out [Lighthill, 1971].

From testing of the initial prototype it has become apparent that the recoil motion is most evident in yaw and roll. Therefore, the model has to take this recoil motion into account in its representation of these particular degrees of freedom. Firstly, in roll the recoil is assumed to be caused by a combination of two factors. One is the moment created by the mass of the tail as it moves a certain distance away from a pivot point the centre line of the vehicle as indicated by Figure 4.12.

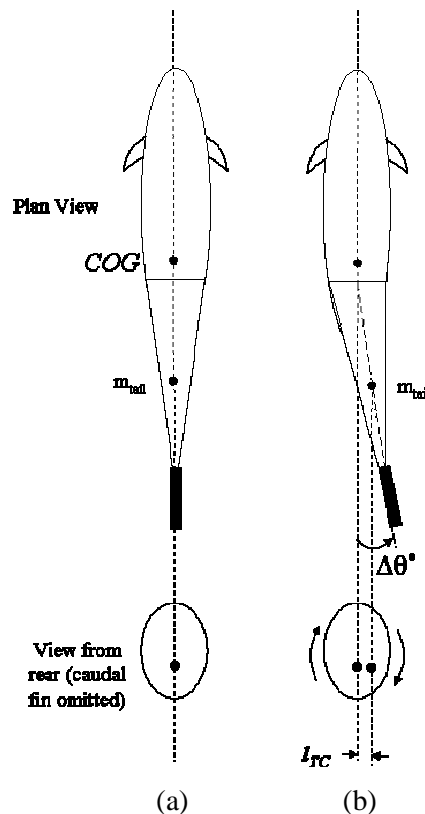


Figure 4.12: Representation of recoil motion in roll. (a) tendon tail in centre position (b) tendon tail offset (c) moment diagram representation of roll recoil

In Figure 4.12 m_{tail} is in kg and the position of it indicates the approximate centre of mass of the tail and l_{TC} is the distance between the centreline of the *RoboSalmon* vehicle and the centre of mass of the

tail in meters. As the centre of mass of the tail moves from the centreline it generates a moment about the x-axis, with magnitude of the weight of the tail multiplied by the l_{TC} . The second factor contributing to the roll recoil is the moment caused by the drag force acting on the caudal fin as it moves through the water. As the caudal fin is mounted above the centreline of the vehicle by a distance, l_{cf} , the drag force acting on the fin will create a moment in the roll axis.

The recoil motion in yaw is slightly more difficult to represent within the mathematical model. From observations of the *RoboSalmon* vehicle swimming in a straight line the recoil in yaw presents itself as a rotational motion of the body as the tendon drive tail moves away from its centreline. The rotational motion of the body is in the opposite direction to the motion of the tail if the COG is taken as the pivot point i.e. as the tail moves clockwise the body recoils anti-clockwise.

This effect is represented within the model in terms of the moment produced by the lateral drag force of the caudal fin as it moves in the tendon tail actuation system. If the tendon drive *RoboSalmon* is actuated out of the water on a bench say, no recoil is observed as the drag force on the fin due to the air resistance is significantly less than in water and also the friction between the vehicle and the bench prevents the body from moving in reaction to the tail moving. However, when the system is actuated in the water environment the hydrodynamic drag due to the movements of caudal fin is significantly greater and so will produce a moment about the COG of the vehicle acting in the yaw axis.

Within the model this is represented by using the drag force produced by the caudal fin to create a recoil torque, τ_{RECOIL} , as it moves to create a moment about the vehicle COG which is assumed to be located half a body length in front of the caudal fin. An illustration of this is shown in Figure 4.13.

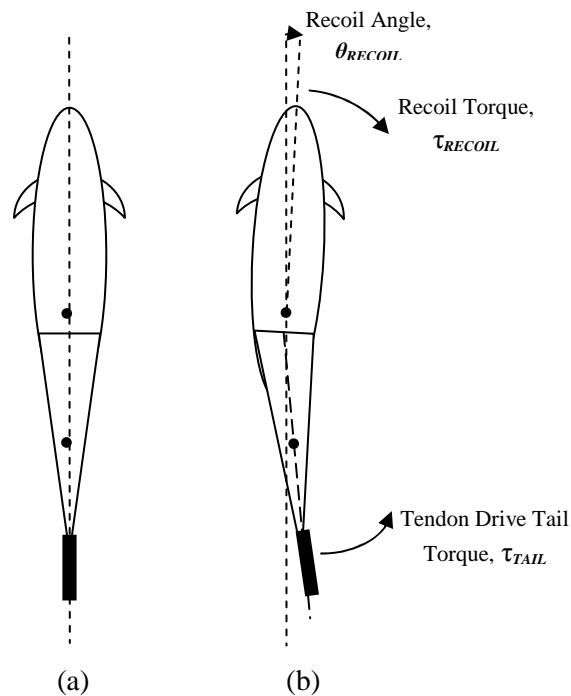


Figure 4.13: Representation of recoil motion in yaw. (a) tendon tail in centre position (b) tail offset with recoil motion present in yaw

4.6.1.7 Tendon Drive System: Input Forces & Moments

The overall control forces and moments due to the tendon drive tail are shown in Equation (4.46).

$$\begin{aligned}
 X_T &= F_{Thrust} \cdot \cos(\theta_{center}) \\
 Y_T &= F_{Thrust} \cdot \sin(\theta_{center}) \\
 K_T &= 0.5 \cdot m_{tail} \cdot g \cdot l_{TC} - l_{cf} \cdot D_{FIN} \\
 N_T &= Y_T \cdot \frac{l}{2} + \tau_{RECOIL}
 \end{aligned} \tag{4.46}$$

The surge force X_T is calculated from the estimate of the thrust produced by the tail motion F_{Thrust} multiplied by the cosine of the tail centreline to take into account the reduction in thrust when manoeuvring. The sway force Y_T is represented in a similar way to the surge force except it is multiplied by a sine of the tail centreline to produce a manoeuvring force with the tail is offset. The roll term is produced by the recoil motion as shown in Figure 4.12. Finally, the yaw term consists of a turning component produced by the moment arm produced by the sway term multiplied by half the body length and an additional term to represent the recoil as discussed in 4.6.1.6.

4.6.2 Propeller and Rudder System

There are many different types of propeller used in marine applications from the large propellers used on ocean liners to small propellers used in thrusters for ROVs and AUVs [Kim *et al*, 2004]. The main purpose of the propeller is to develop a direct thrust force to overcome the vehicles resistance to motion [Burcher & Rydill, 1994].

As discussed briefly in Chapter 3, selection of an optimum propeller is a complex task. Optimum propeller selection should investigate all the relevant parameters of the vehicle onto which it has to be fitted such as the required thrust to weight ratio and desired speeds. A suitable propeller is then either designed or selected using the characteristics for a propeller such as diameter, blade pitch, number of blades, etc [Tupper, 2004].

The standard equation for the thrust produced by a propeller is shown in Equation (4.47) [Fossen, 1994].

$$T = \rho D^4 K_T (J_0) |n| n \tag{4.47}$$

In this equation T is the propeller thrust (N), ρ is the water density in kgm^3 , K_T is the thrust coefficient, J_0 is the advance number and n is the rotational speed of the propeller in rads^{-1} .

The propellers selected for this study are commercially available propellers that have been designed for model boat/submarines. A bollard-pull [Greer, 2001] test was carried out to obtain the relationship between the thrust produced, shaft rotation speed and the current drawn. The results for the bollard-pull test for the propellers investigated are shown in Appendix A.2. From the bollard pull tests the thrusts produced by each propeller were estimated. The propeller that was selected for use on the

RoboSalmon was the 3 blade 50mm brass propeller as it would allow for a range similar speeds to the speeds obtainable from the tendon drive system.

The thrust/speed characteristic measured during the bollard pull test for this propeller is shown in Figure 4.14 and is measured when the vehicle is stationary.

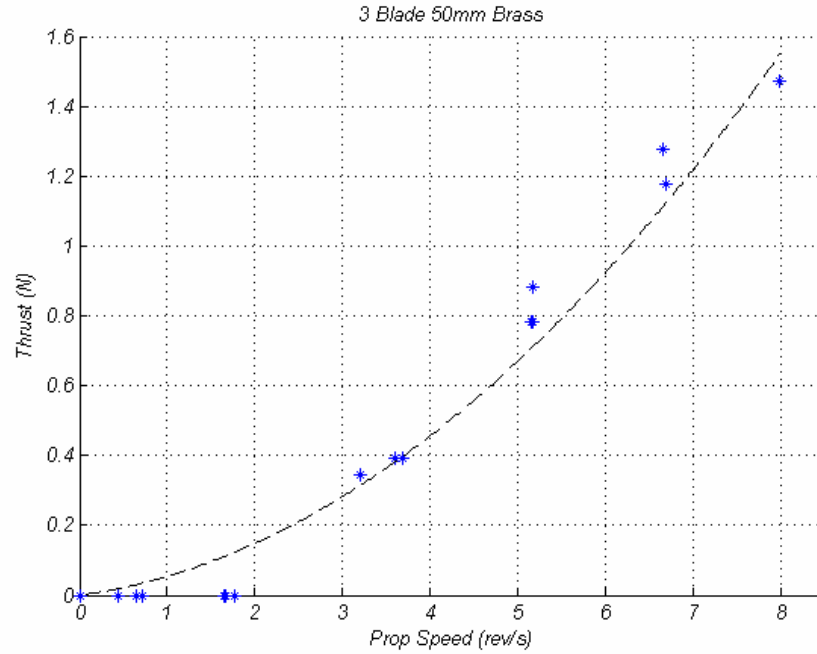


Figure 4.14: Thrust/Rotational speed relationship of 3 blade 50mm brass propeller

However, during normal operation of a propeller the vehicle will be moving and so the water incident on the propeller will have a velocity associated with it. This velocity is called the ambient water velocity and is represented by u_a and can be calculated using Equation (4.48) [Fossen, 2002].

$$u_a = (1 - w)u \quad (4.48)$$

Where w is the wake fraction number and is typically between 0.1 and 0.4[Fossen 1995] and u is the surge velocity of the vehicle. The model used to estimate the thrust produced by the propeller during operation is the quasi-steady thrust [Fossen, 2002]. This method uses thrust coefficients to represent the lift and drag produced by the propeller surfaces. Details of this method can be found in [Fossen, 2002]. The equation used for thrust generation using this model is shown in Equation (4.49) [Fossen, 2002].

$$T = T_{|n|} |n| - T_{|n|u_a} |n| u_a \quad (4.49)$$

Where n is the propeller rotational speed (rev/s), $T_{|n|}$ and $T_{|n|u_a}$ are propeller coefficients that can be calculated using the results of the bollard pull test, data obtained from [Fossen, 2002] and from the propeller characteristics.

Using the above method the final equation, with the coefficients calculated, used to estimate the thrust for the model is shown in Equation (4.50)

$$T_{PROP} = 0.03295n^2 - 0.04875nu_a \quad (4.50)$$

This method of modelling the propeller system was used in conjunction with the equations for modelling a DC motor, given earlier in Equations (4.36) and (4.37). By doing this it allows the whole propeller drive system to be represented, from the input voltages to the DC motor to the output thrust generated by the propeller.

In order for this system to achieve manoeuvres the rudder is used in conjunction with the force produced by the propeller. The rudder operates in a similar fashion to a wing on an aircraft, i.e. as the angle of the rudder is changed relative to an oncoming fluid flow, resulting lift and drag forces are produced [Perez, 2006]. Therefore, the rudder is modelled as a foil with a variable angle of attack which allows the lift and drag to be calculated using the lift and drag coefficients for the particular shape of rudder. The rudder is assumed to resemble a NACA 0012 aerofoil and so the lift and drag coefficients, C_L and C_D respectively, can be calculated from available data [Goett & Bullivant, 1939]. With the coefficients known for a particular angle of attack, the speed of water across the rudder (assumed to be equal to the surge velocity) and the area of the rudder A , the lift and drag forces can be calculated using Equations (4.51) and (4.52) [Perez, 2006].

$$L_{Rudder} = \frac{1}{2} \rho A u_a^2 C_L \quad (4.51)$$

$$D_{Rudder} = \frac{1}{2} \rho A u_a^2 C_D \quad (4.52)$$

The diagram in Figure 4.15 shows the location of the rudder as it is commonly found on ships and indicates the forces and moments caused by the rudder.

Figure image has been removed due to Copyright restrictions

Figure 4.15: Diagram of forces and moments produced by rudder [Perez, 2006]

Here L is the lift force generated by the rudder, α is the angle of attack of the rudder, CG is the vehicles centre of gravity, LCG is the distance between the COG and the pivot point of the rudder and r_r is the rudder roll arm [Perez, 2006].

Mathematically these forces and moments produced by the rudder can be represented in 4 DOF by the terms shown in Equation (4.53) [Perez, 2006].

$$\begin{aligned}\tau_{1rudder} &= -D_{Rudder} \\ \tau_{2rudder} &= L_{Rudder} \\ \tau_{4rudder} &= -r_r L_{Rudder} \\ \tau_{6rudder} &= -LCGL_{Rudder}\end{aligned}\tag{4.53}$$

Here L_{Rudder} and D_{Rudder} are the lift and drag forces produced by the rudder respectively in Newtons and r_r and LCG are the dimensions illustrated in Figure 4.15.

As with the propeller system, the model for the rudder system also contains the equations for a DC motor with additional positional control so as to represent the analog servo motor used within the hardware. The drag forces are represented in the same way as in the representation for rigid body drag within the model for the tendon drive system.

The overall control forces and moments due to the propeller and rudder system are shown in Equation (4.54).

$$\begin{aligned}X_T &= T_{Prop} - D_{Rudder} \\ Y_T &= L_{Rudder} \\ K_T &= -r_r L_{Rudder} \\ N_T &= -LCGL_{Rudder}\end{aligned}\tag{4.54}$$

The surge thrust X_T is formed from the thrust from the propeller T_{Prop} and the drag force produced by the rudder, D_{Rudder} . The sway force due to the rudder, L_{Rudder} , is calculated using the lift force generated by the rudder as described earlier in this section. This lift force also produces a roll moment, K_T , which is calculated using the lift force multiplied the distance, r_r , which is the distance between the COG and the effective centre of the rudder. Finally, the yaw moment N_T is calculated by moment produced by the lift force of the rudder multiplied by the distance, LCG , which is the distance between the rudder centre and the vehicle COG as shown in Figure 4.15.

4.7 RoboSalmon State Space Equations

The standard equation of motion for modelling the dynamics of the *RoboSalmon* vehicle, shown previously in Equation (4.10) can be rearranged into state space form as shown in Equation (4.55):

$$\dot{\mathbf{v}} = \mathbf{M}^{-1}(\boldsymbol{\tau} - \mathbf{C}(\mathbf{v})\mathbf{v} + \mathbf{D}(\mathbf{v})\mathbf{v} + \mathbf{g}(\boldsymbol{\eta}))\tag{4.55}$$

The complete set of *state space* equations for each degree of freedom and all associated constants for the *RoboSalmon* vehicle model are given in Appendix B.

4.8 Model Validation & Data Collection

Any mathematical model requires that it be compared to the physical system it is describing in order to determine if the model provides a suitable representation of that physical system, this is called model validation [Murray-Smith, 1995]. In order to carry out model validation experimental data has to be collected which relates to the performance of the physical system to which the model output can be compared. If the model output differs significantly from the experimental data then certain model parameters are tuned to bring the model output in line with the gathered data. For the *RoboSalmon* model the parameters that were used to tune the model were the horizontal and lateral drag coefficients for the vehicle and the a, b and c dimensions of the prolate ellipsoid, shown in Figure 4.3, which represents the vehicle body. This section covers the process used to validate the mathematical model of the *RoboSalmon* vehicle and the method used for the collection of the performance data of the system.

4.8.1 Model Validation

The model validation process comprises of a number of different validation techniques with the aim of providing a measure of how accurately the model represents the real system or process [Sargent, 2005]. This section describes the validation procedure used for the *RoboSalmon* model. In order to validate the model experimental data relating to the performance of the *RoboSalmon* had to be obtained. This section starts with description of the model validation techniques used and then a discussion of the laboratory equipment and systems used to obtain the experimental data.

Within this investigation two techniques are used for model validation; the first is analogue matching and the second is the integral least squares method. Both these validation techniques have been used in practice for validation of mathematical models [Gray, 1992; Worrall, 2008]. The following sections provide details of each validation method.

4.8.1.1 Analogue Matching

One of the simplest techniques available for model validation which provides a qualitative measure of the models accuracy is analogue matching or visual inspection [Gray, 1992]. This technique involves plotting the time response of the simulation and overlaying experimental response data from the actual system on the same plot [Gray, *et al*, 1998]. With the responses overlaid this technique then relies on human observation rather than a mathematical qualification to determine the accuracy of the model. One of the benefits of this technique is that it gives a visual representation of the accuracy of the model. Using this technique of overlaying simulated and experimental responses allows for parameters of the simulation to be altered to determine the best visual fit of the experimental data and therefore facilitate validation of the model.

An example of the analogue matching technique is shown in Figure 4.16 for an experimental program conducting straight swimming with a nominal tail beat frequency of 0.38Hz and a nominal beat amplitude of 0.105m.

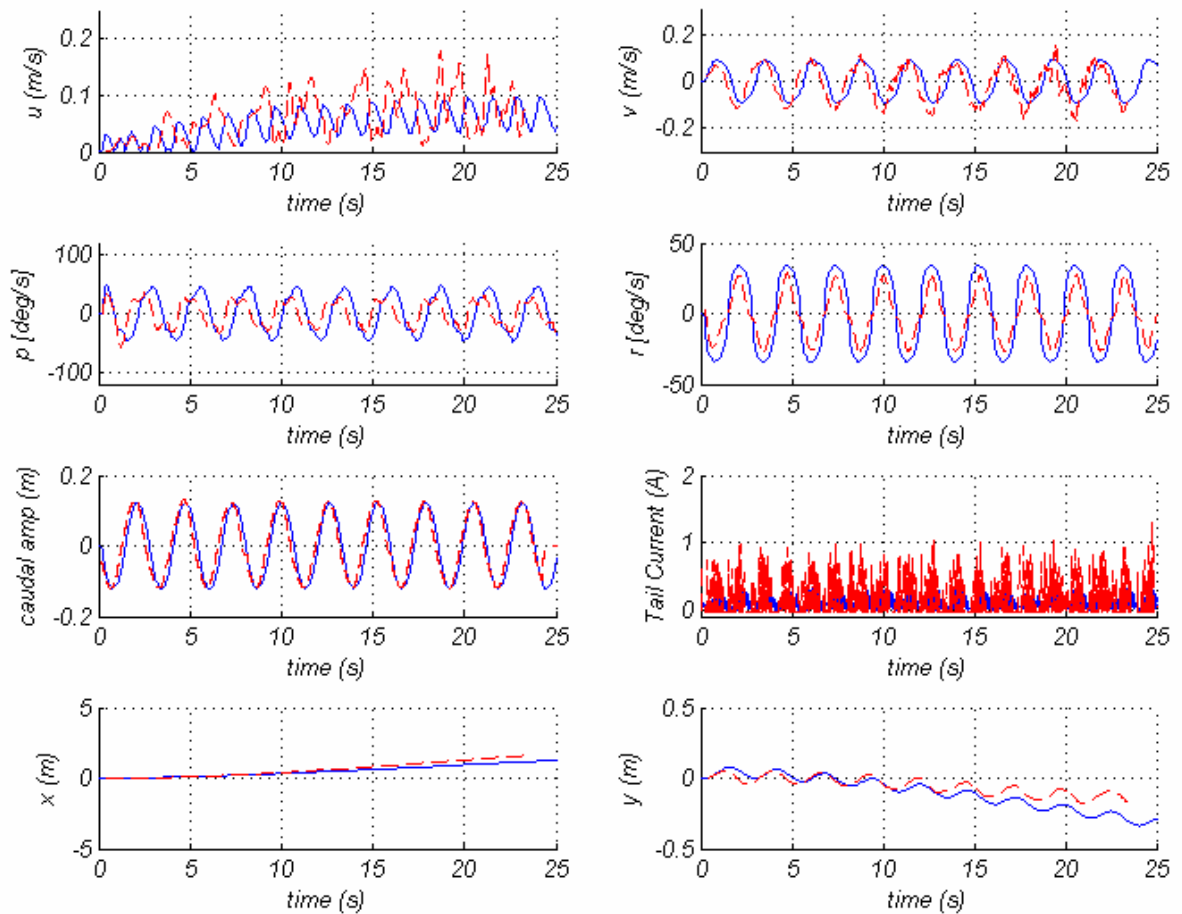


Figure 4.16: Analogue Matching Validation for Program 5 (Forward Motion), red trace experimental data, blue trace simulation

From Figure 4.16 it can be seen that the model results appears to correlate reasonably well with the experimental data. The only parameter which is not a close fit is the surge velocity. This is due to the noise found on the experimental surge signal, if the time averaged values are compared then a reasonable match is achieved.

The validation results from the analogue matching technique used are shown for a selection of experimental trials in Appendix C for the *RoboSalmon* tendon drive model.

4.8.1.2 Integral Least Squares

The other method to be used within this investigation for model validation is the integral least squares (ILS) method [Murray-Smith, 1995]. The benefit of this method is that it provides a quantitative measure of the accuracy of the model. In practice this validation technique is implemented by taking the summation of the square of the error at each available data point across the simulation run time,

shown in Equation (4.56). The error is the difference at one instance between the simulated response and the experimental response.

$$Q_m = \sum (error^2) \quad (4.56)$$

As is implied from the equation; the smaller the value of Q_m the higher the accuracy of the simulation. The validation results from the ILS technique are shown along with the analogue matching results in Appendix C for the *RoboSalmon* Tendon drive

4.8.2 Data Collection

To facilitate the model validation process described in section 4.8.1 experimental data relating to the performance of the *RoboSalmon* was gathered. Two sources were used to gather all the required data from the vehicle; the first is the onboard IMU described in detail in Chapter 3. The IMU allows the roll, pitch and yaw rates to be measured and logged onboard the *RoboSalmon* as it swims. This data allows the angular rates and angular displacements within the model to be validated. The second source of data is the video camera mounted on a rig above the test pool. This camera points directly downwards at the pool surface and captures video footage of the *RoboSalmon* as it swims across the pool. Post processing of the video footage allows the positions and velocities of the vehicle to be obtained in the Earth-fixed reference frame [Fossen, 2002]. This data in conjunction with the body-fixed angular velocities allows for validation of the surge and sway velocities. The following sections give more detail on the equipment used within this data gathering process and the post-processing used on the data gathered from each source.

4.8.2.1 Laboratory Equipment

As well as the *RoboSalmon* vehicle itself, all of its onboard sensors and a PC to download the sensor data, a number of other items of equipment have been required to complete the experimental trials. This other equipment includes:

- A pool of water of sufficient size to allow the vehicle to obtain a steady state speed and complete manoeuvres.
- A camera system to allow overhead video footage of the vehicle in motion in surge and sway to be obtained and analysed.

A pool of dimensions 4.14m x 216m x 0.79m was obtained for experimentation along with a number of white ceramic tiles of dimension 33cm x 25cm to cover the floor of the pool and provide a background grid for the camera. A frame constructed from wood and 40mm PVC tubing was constructed to mount the camera over the pool. A picture of the experimental set up is shown in Figure 4.17 below. The depth of water used in the pool was chosen to 0.48m due to reasons relating to the weight of the water within the laboratory. This depth was thought to be sufficient as calculation of the Froude depth number was less than 0.12 for the range of speeds obtainable for the *RoboSalmon*

[Carlton, 2007; Hydrocomp, 2003]. A Froude depth number of 0.7 or greater would indicate the water depth may begin to cause a surge velocity reduction during the trials [Carlton, 2007].



Figure 4.17: Set up of laboratory experimental equipment

4.8.2.2 Camera System

The camera system has been used to obtain motion data relating the vehicles movements in the Earth-fixed x - y plane. This information, coupled with the onboard sensor data retrieved from the vehicle after each run, allows the performance of the vehicle to be measured in 6 degrees of freedom with reference to the body-fixed frame attached to the COG of the *RoboSalmon*.

The camera used for the video capture is a Sony DCR19E MiniDV Camcorder [Sony, 2005]. This camera is mounted on a custom built frame and points downwards to capture the motion of the vehicle from above as it moves.

4.8.2.3 Image Processing

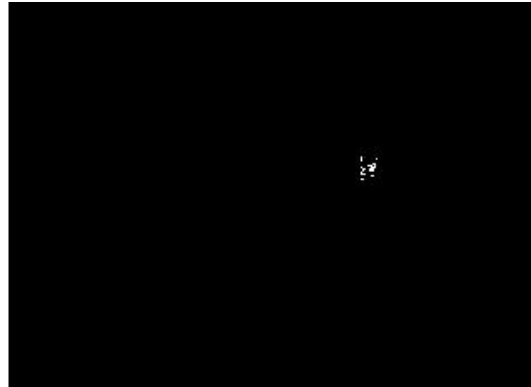
In order to obtain usable estimates of x and y position from the camera information, the video footage had to be processed in such a way that the coordinates of the COG of the *RoboSalmon* vehicle could be identified within each frame of the video. To make this task possible a red circle has been attached to the top surface of the *RoboSalmon* vehicle above its centre of gravity, this can be seen in Figure 4.18(a).

Once the video footage has been captured using the camcorder mounted above the pool the first stage in the image processing is to decompose the AVI video file into individual image frames of resolution 240x320 pixels in bitmap format. By doing this it allowed each frame of the image to be analysed individually to determine the position of the red circle on the *RoboSalmon* within that frame. As successive frames have been analysed it built up the positional data of the vehicle as time progresses.

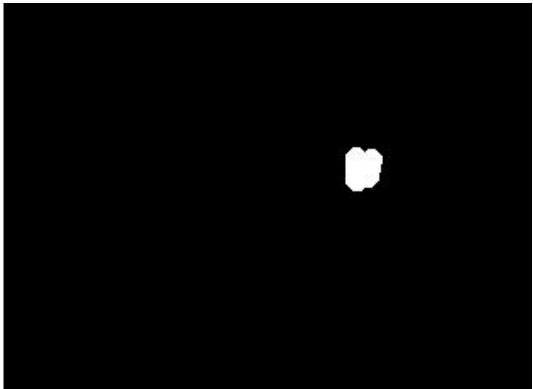
The camera recorded with a frame rate of 25 frames per second, therefore 25 image frames are analysed for each second of video with 25 corresponding x-y coordinate pairs per second.



(a) – Original image frame decomposed from AVI video captured from camcorder



(b)– Image with pixels within range of accepted RGB values made white, all others black



(c) – Morphological opening operation



(d) – Original image frame with overlaid blue circle indicating centre of red circle

Figure 4.18: Steps used in image processing

To determine the location of the red circle within each frame, a range of red, green and blue (RGB) values for corresponding to the red pixels within the red circle was determined manually by averaging the RGB values from several pixels within three images. MATLAB code has been written which scans through each pixel within the image to determine whether it was in the range of expected RGB values for the red circle. If the pixel value is not within the range it is set to black and if it is within the range of the expected values then it is set to white. This produces a binary image frame which can be used with the inbuilt functions from the MATLAB Image Processing Toolbox [MathWorks, 2007].

From experimentation it has been found that usually only a small number of pixels are detected using the expected range of RGB values as shown in Figure 4.18(b). If the range is increased too much then numerous erroneous points start to be detected across the frame. At this stage a morphological operation called *opening* is used which has the effect of smoothing object contours [Gonzalez, 2004]. The result of this opening operation is shown in Figure 4.18(c).

Finally, in order to determine the centre of the white blob the MATLAB command *bwlabel* [MathWorks, 2007] is used to determine whether there are any objects within the image frame and if so how many. Ideally there should either be one object detected, corresponding to the red circle being in the frame, or zero objects, red circle out with the frame. If an object is detected then the *bwlabel* function returns a matrix containing a label matrix of the objects and the number of labelled objects detected. Figure 4.18(d) shows the calculated position of the centre of the red circle plotted as a blue circle overlaid on the original unprocessed image. This indicates that the process described above gives a usable method for determining the position of the red circle on the vehicle. All that has to be done then is to scale the calculated position to metres using the grid produced by the tiles on the floor of the pool.

Once the image frame has been analysed, the centre of the red circle on the *RoboSalmon* determined and the resulting coordinates scaled accordingly, the process is repeated for all the available image frames decomposed from the AVI file and an ASCII text file is produced which contains all the x and y coordinate pairs for that particular AVI video.

4.8.2.4. Sensor Data Post Processing

The raw sensor data retrieved from the vehicle after each set of 5 runs is downloaded and stored as an ASCII text file which contains the 3200 12-bit unsigned integer data points for each of the 16 logged variables per run. The first stage in post processing the data is to import the data into MATLAB and scale each variable appropriately to transform the raw unsigned integer value read from the ADC into the correct units such as Volts, Amps, rads^{-1} , etc. The data from the onboard sensors are then filtered using an averaging function to eliminate any high frequency noise present. A complete data set collected from a sample run of the *RoboSalmon* vehicle is shown in Figure 4.19 and Figure 4.20. Figure 4.19 contains the logged onboard sensor readings and Figure 4.20 contains the positional data from the raw image processed video footage.

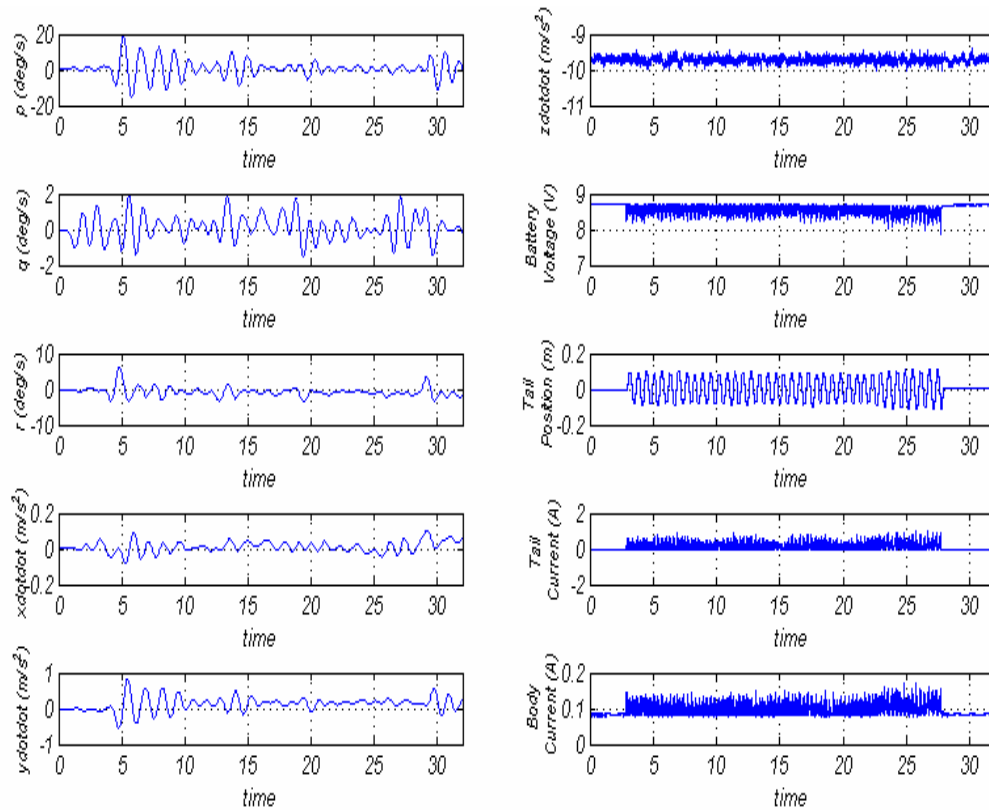


Figure 4.19: Selection of logged onboard sensor readings for sample run of *RoboSalmon* vehicle

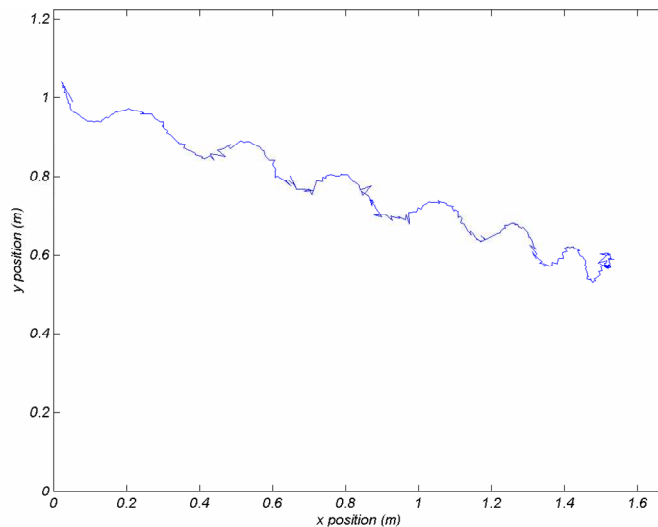


Figure 4.20: Raw position data from image processing of video footage

In order to simplify the process of comparing the data collected from numerous runs, all the measurement values should be given with respect to the body fixed frame. This task is simple for the onboard sensors as they produce measurements in the body fixed frame. However, as previously mentioned the x-y information obtained from the camera is in the Earth fixed frame therefore a translation is required to give the x-y positional information with respect to the body fixed frame.

The standard transformation matrix to convert body fixed velocities to Earth fixed velocities, shown in Equation (4.55) [Fossen, 1994] can be used by taking its inverse as shown in Equation (4.56). This

then allows the calculation of the body-fixed velocities from velocity data obtained in the Earth-fixed frame.

$$\dot{\eta}_1 = J_1(\eta_2)v_1 \quad (4.57)$$

$$v_1 = J_1(\eta_2)^{-1}\dot{\eta}_1 \quad (4.58)$$

From experimentation, the body-fixed angular velocities (v_2) and the Earth-fixed positions (η_1) are known. The Earth-fixed velocities can easily be determined by numerical differentiation so $\dot{\eta}_1$ is also known. From Equation (4.58) it can be seen that the transformation matrix J_1 requires the angular position data in the Earth-fixed frame. This information can be determined using a Predictor-Corrector method [Matko, Karba & Zupancic, 1992] which utilises initial conditions for the angular positions in the Earth-fixed frame and the angular velocities from the sensors measure in the body-fixed frame. These are used to predict the velocities in the Earth-fixed frame.

Once this has been carried out all the measured parameters are given with respect to the body-fixed frame and this allowed the data to be analysed and compared in more detail. This analysis and comparison along with a selection of the results is presented and discussed in Chapter 5 and Chapter 6.

4.9 Summary

This Chapter has described the development of the mathematical model for the dynamics of the *RoboSalmon* vehicle which includes modelling the individual propulsion systems investigated. Firstly, the state space modelling technique used for the model simulation is discussed including a flowchart of the simulation together with the two relevant reference frames and the various variables used within the model have been defined. The rigid body dynamics of the vehicle are then described starting with a definition of the equations of motion in six degrees of freedom followed by a discussion of the terms used for representing the hydrodynamic added mass, gravitational and buoyancy forces, and the hydrodynamic damping or drag force.

The modelling of each propulsion system investigated is then discussed starting with the tendon drive system, followed by the propeller and rudder system. Within the discussion of each propulsion system the characteristics and properties of each system are highlighted and explained such as the estimate of the thrust produced and for the biomimetic tail a discussion of how the recoil motion is modelled is included.

The model representation of the actuated head is then discussed followed by the overall state space equations for the models. The vehicle kinematics are covered which shows how the velocities calculated within the body fixed frame are translated to the Earth-fixed reference frame.

Finally, the techniques used for validating the model against the experimental results are described along with the experimental set-up and sensor post processing used to obtain the data. These validation techniques give both a qualitative and quantitative method for comparing the simulation of the mathematical model with the experimental results obtained from the real system.

Chapter 5 – Experimental Results: Forward Motion

5.1 Introduction

One of the aims of this project is to investigate the benefits of underwater propulsion systems which mimic the propulsion technique utilised by most fish. To this end a prototype vehicle has been developed as described in Chapter 3. In order to characterize the performance of this vehicle, the *RoboSalmon*, has been put through an extensive set of experimental trials. These trials have allowed the performance and characteristics of the vehicle to be determined for forward motion.

This Chapter presents and discusses the results for the *RoboSalmon* vehicle for forward or surge motion using its biomimetic tendon drive propulsion system. The two main variables that can alter the performance of the tendon drive propulsion system in forward motion are the tail beat frequency and the tail beat amplitude. The effect of varying these two parameters is investigated and the corresponding results are presented. These are used to analyse the effect each has on the forward motion of the vehicle. In addition, a comparison of the swimming performance obtained from *RoboSalmon* and real atlantic salmon is presented in terms of speed and power output.

As discussed earlier one of the unexpected characteristics of the vehicle is the amount of recoil motion present when the *RoboSalmon* is swimming. Results are presented which indicate the extent of this recoil motion along with a discussion of the relationships between this recoil and the other parameters of the tail propulsion system. An attempt has been made to compensate for this recoil motion in yaw and roll using *RoboSalmon's* actuated head. The results of using the actuated head whilst undertaking forward swimming are presented and discussed.

Finally, the performance of the biomimetic *RoboSalmon* vehicle is compared with the performance of a system of similar dimensions but using a propeller for forward motion. For this comparison the speed and efficiency of each system is evaluated.

5.2 Experimental Procedure

The experimental apparatus used for the trials of the *RoboSalmon* vehicle is described earlier in Chapter 3. Each experiment was repeated five times and average values calculated. This would allow for an indication of the errors expected in the results using the standard deviation and standard error and was the maximum number of runs that could be completed in the available time frame. Using this analysis indicated that the maximum expected error in the measured velocities was $\pm 0.01\text{ms}^{-1}$.

A detailed discussion of the experimental set up used was covered in Chapter 4 and a flowchart of the experimental procedure for carrying out five runs is shown in Figure 5.1 below.

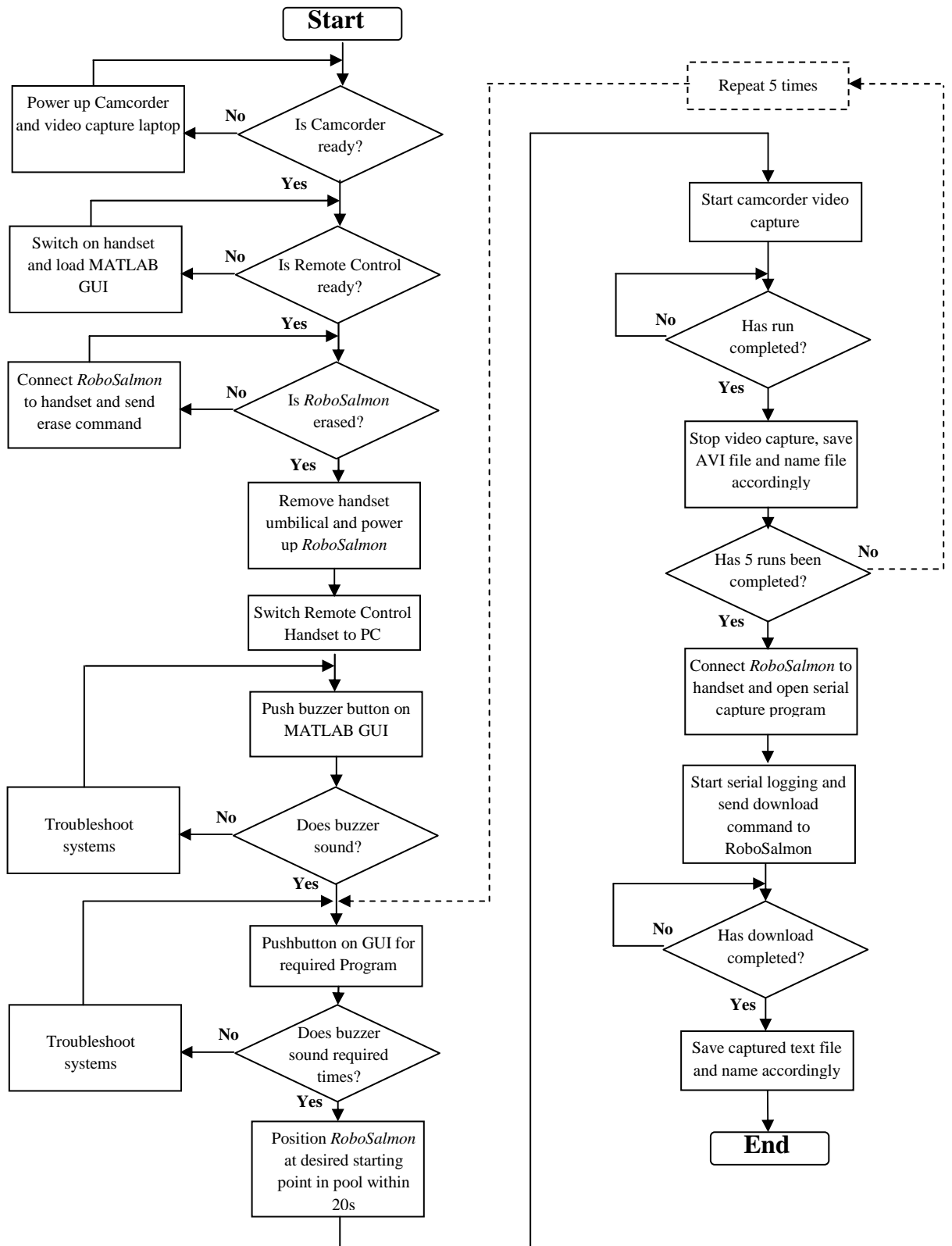


Figure 5.1: Flowchart of experimental procedure for 5 experimental runs

The experimental procedure, illustrated visually in the flowchart of Figure 5.1 has been used to obtain all the results from the *RoboSalmon* vehicle. The first two stages deal with setting up the laboratory equipment, namely the camcorder system and the computer running the MATLAB GUI. The next

stage is to determine if the *RoboSalmon*'s onboard data logger is blank; if not then an erase operation was carried out by connecting the handset umbilical to the vehicle and sending the erase command via the CAN bus.

At this point the *RoboSalmon* is powered up by connecting the on/off plug and the toggle switch on the handset is set to 'PC'. The next stage is to test the data link between the MATLAB GUI and the *RoboSalmon*. This is achieved by pressing the buzzer button on the GUI and waiting for the buzzer to sound on the vehicle.

After successful testing of the data link by means of the buzzer, the required program can be selected on the MATLAB GUI. The vehicle will then buzz a number of times equal to the program selected. There is then a delay of 20 seconds to allow the *RoboSalmon* to be positioned at the correct position within the pool. The correct positioning depends on the program being selected, but for the majority of the forward motion experiments the initial position is the position where the red circle on the top of *RoboSalmon* is just visible in the frame of the camcorder video stream. At this point the video capture should be started. Each program for the forward motion experiments last 32 seconds. This comprises 3.5 seconds of stationary motion at the start, 25 seconds of swimming and 3.5 seconds at the end with the tail in its centre position. The start of the 32 second run is indicated by one buzz from the *RoboSalmon* with the end being indicated by a double buzz. After this double buzz to indicate the end of the program the video capture should be stopped and the AVI file stored and named so it can be matched up with the onboard logged sensor data later. This process can then be repeated up to five times to log the data from up to five programs. Once the required number of programs has been completed the *RoboSalmon* is then removed from the test pool, placed on the bench and connected to the handset via the umbilical. With the serial capture program running on the PC connected to the handset the download command is sent to the vehicle via CAN which will initiate the process of transmitting the contents of the data logger via the serial port to the PC for storage. Once the download has been completed the text file containing the logged sensor readings is saved and named so it can be matched with the corresponding AVI video files of the runs.

5.2.1 Experimental Programs

In order to evaluate the forward motion characteristics a set of twenty different parameter sets were tested experimentally. For the purposes of this discussion each parameter set is referred to as a *program*. Table 5.1 indicates the parameters used in each of the twenty programs used. The parameters outlined in this table are the desired values of these parameters which are sent to the tail propulsion system.

Table 5.1: Tendon drive tail parameters altered for forward motion experiments

Program	Desired Amplitude (m)	Desired Frequency (Hz)
1	0.105	1.56
2	0.105	0.88
3	0.105	0.61
4	0.105	0.47
5	0.105	0.38
6	0.077	1.56
7	0.077	0.88
8	0.077	0.61
9	0.077	0.47
10	0.077	0.38
11	0.034	1.56
12	0.034	0.88
13	0.034	0.61
14	0.034	0.47
15	0.034	0.38
16	0.150	1.56
17	0.150	0.88
18	0.150	0.61
19	0.150	0.47
20	0.150	0.38

These particular nominal tail beat amplitudes were selected for two reasons. Firstly, because 0.077m and 0.105m are in the approximate range of beat amplitudes used by real fish i.e. around 10% of the body length of the fish. Secondly, these values related to the servo command signals of 25, 50, 75 and 100 used sent to the servo control board and simplified the control firmware used.

When a number of these programs were tested the desired responses cannot be achieved due to limitations of the actuator in the tendon drive tail, namely the servo motor. This only occurred in some of the programs with the higher frequencies and is characterized by the desired amplitude not being reached during each tail beat cycle. However, even under the conditions of actuator saturation the results from these programs can still be partially utilized for characterization of the vehicle performance.

Each program is executed a minimum of five times to allow average performance for each program to be determined. A complete set of data obtained for a typical run of Program 5 is shown in Figures 5.2 and 5.3 below to illustrate the extent of the data gathered in a single experimental run. During this particular experiment the *RoboSalmon* is instructed to swim in a straight line starting from a stationary position.

The data obtained from the image processing of the camera data is shown in Figure 5.2, which shows the x-y positional data of the path followed by the vehicle during the experiment and the corresponding surge and sway velocities derived from numerical differentiation of the low pass filtered positional data. Figure 5.3 shows the sensor data with individual values for each parameter,

including the linear accelerations, angular rates, tail position, current and voltages sensed during the experiment.

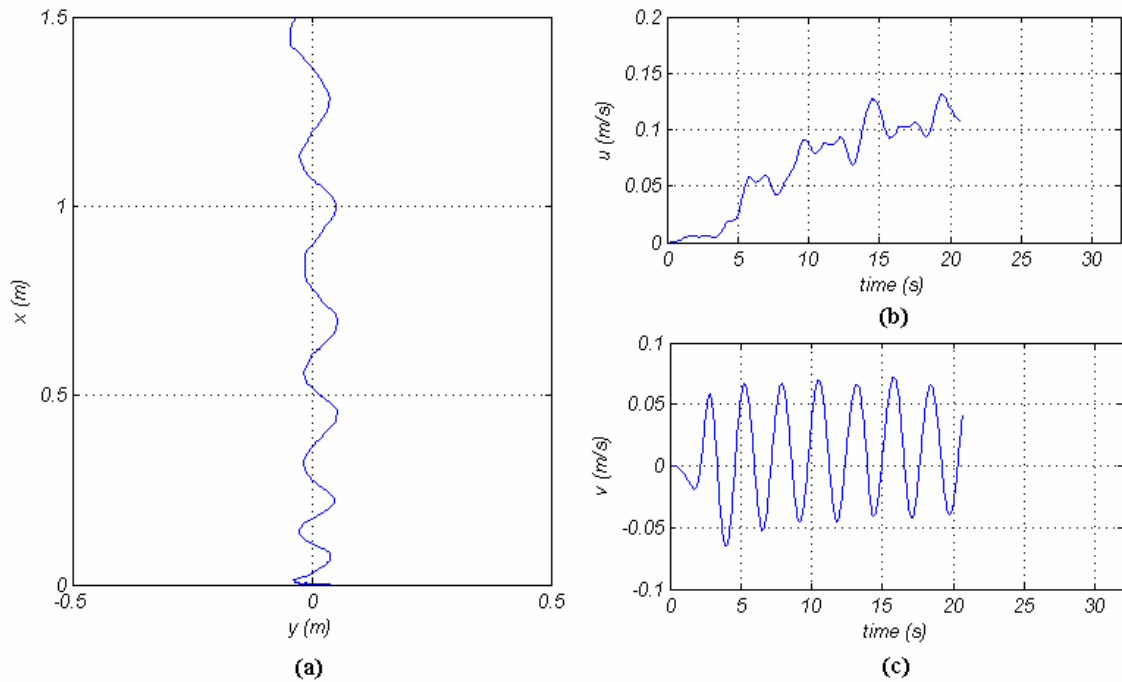


Figure 5.2: Data gathered from image processing of captured video footage of the tendon drive vehicle for program 5 showing (a) x-y positional data, (b) surge velocity u and (c) sway velocity v

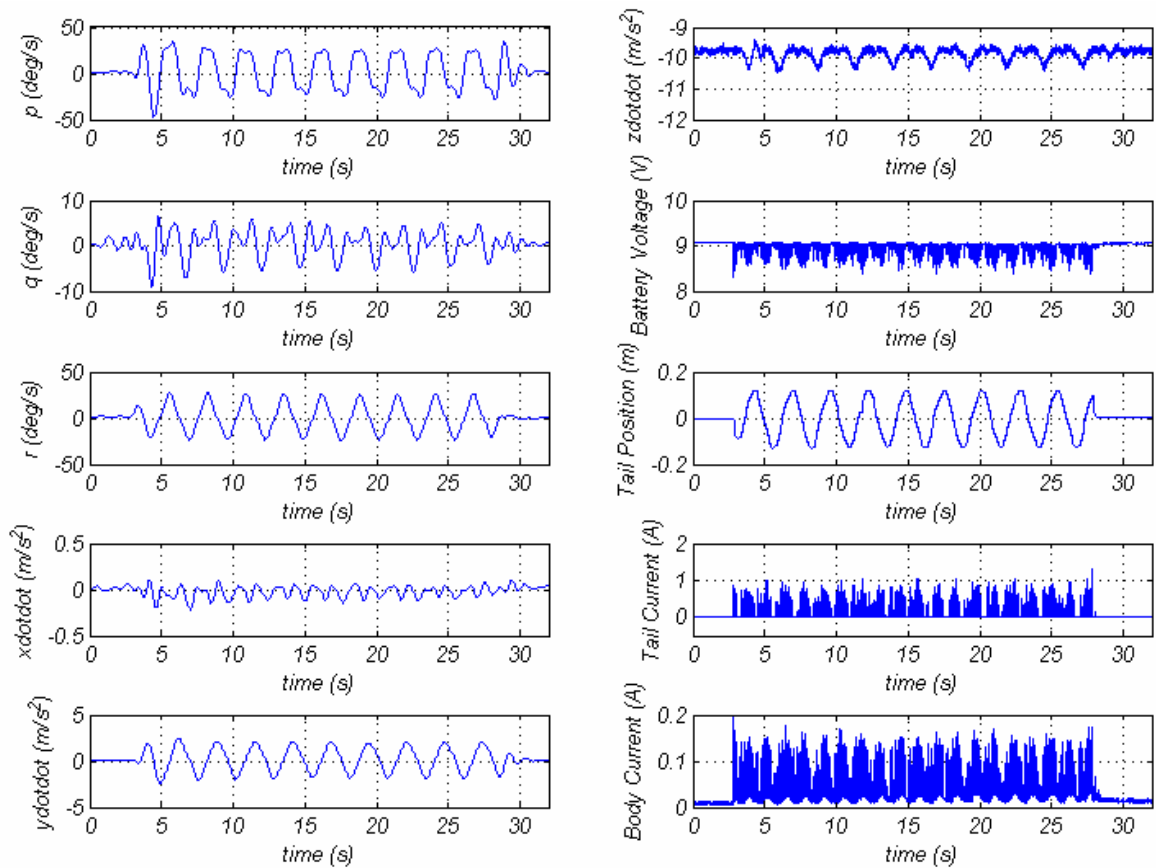


Figure 5.3: Sensor data logged onboard the tendon drive vehicle for Program 5.

The data shown in these figures illustrate the difference in the data length obtained from the camera system and the onboard sensors (21 seconds of data for the image processing and 32 seconds for the onboard sensors). As discussed previously this is due to the limited field of view of the camera which is only able to view an area of the pool approximately 1.68m by 1.22m whereas the onboard sensor system was capable of logging the full 32 seconds of each experimental run. This means that the length of data obtained from the camera is dependent on the speed of the vehicle i.e. at higher speeds the vehicle swims out of the field of view quicker. Due to this limited field of view of the video camera used for the video acquisition the *RoboSalmon* is started out of the field of view to allow a greater distance for the steady state speed to be achieved. In order to allow for the start up transients to be analysed at least one of the runs in each program was started in the camera field of view.

5.3 Tail Beat Frequency & Amplitude

Much of the literature on fish swimming indicates that the swimming speed relies on several variables relating to the movement of the fish tail [Videler, 1993; Hoar & Randall, 1978]. For the tendon drive system the two variables that can be altered for straight swimming are the tail beat amplitude and frequency. One of the aims of these forward motion experiments was to determine the relationship between tail beat frequency, tail beat amplitude and average forward swimming velocity.

A subset of the twenty experimental programs, shown in Table 5.1 was used to investigate this relationship. These twenty programs include four different tail beat amplitudes, each being evaluated at five different frequencies.

However, at the higher frequencies it has been found that actuator limitations became apparent and the desired tail beat amplitudes were not reached within the tail beat cycle. The programs where this occurs are excluded for this comparison as are the programs using the smallest amplitude where the movement of the vehicle using these programs is negligibly small. The average forward motion for the remaining nine programs is shown graphically in Figure 5.4 with the error bars indicating the range of results obtained for the five runs of each experimental program.

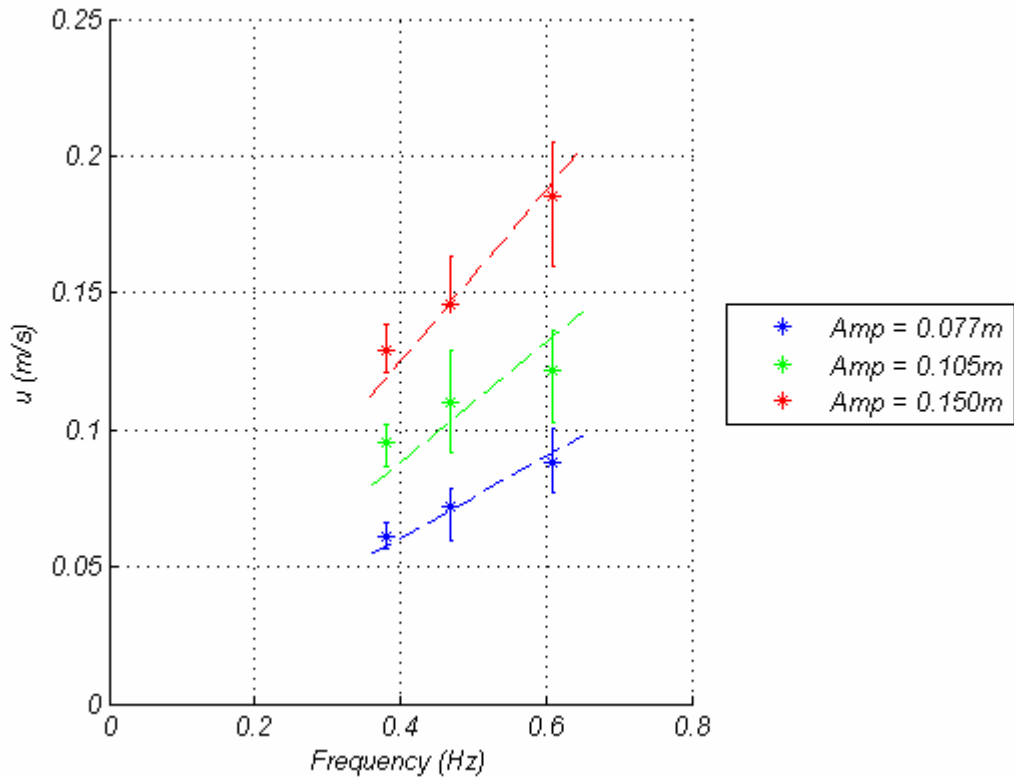


Figure 5.4: Plots of surge velocity versus tail beat frequency for three different tail beat amplitudes with no actuator saturation

From the graph in Figure 5.4 two important trends for the tendon drive system can be observed. Firstly, for a constant tail beat amplitude it can be seen that as the frequency increases the average forward velocity increases. Secondly, with constant tail beat frequency it can be seen that increasing the tail beat amplitude also increases the surge velocity.

In order to be able to use the experiments in which actuator saturation occurred the data must be displayed on a 3D plot as shown in Figure 5.5 to allow for the differing tail beat amplitudes obtained. Figure 5.5 gives a visual indication of the tail beat parameters that caused actuator saturation.

With no actuator saturation the slope of the 3D plot is reasonably constant. However as the frequency increases above 0.88Hz the gradient of the slope reduces for the lower beat amplitudes ($<0.12\text{m}$) and peaks for the higher beat amplitudes.

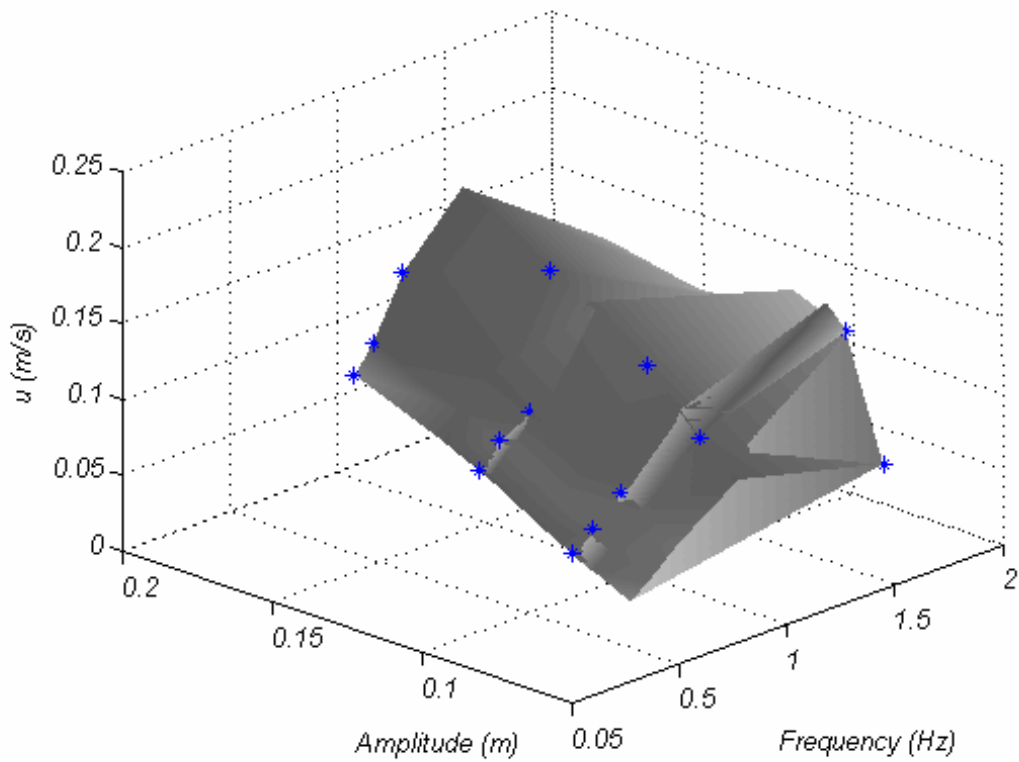
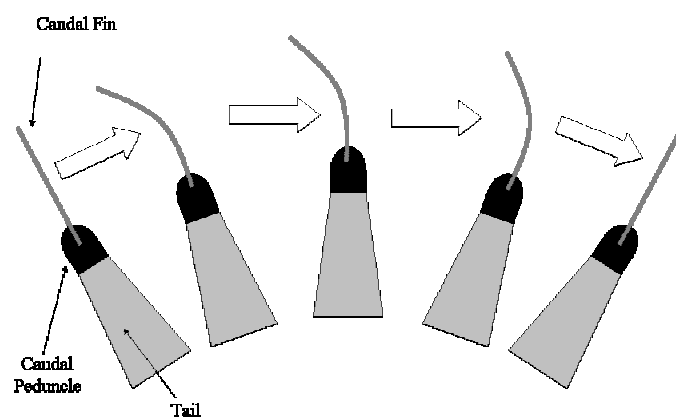
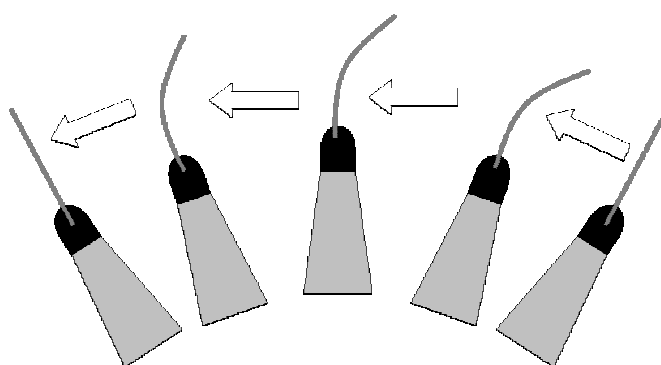


Figure 5.5: 3D plot of all useable forward motion results including those with actuator limitation present

During these experiments one interesting aspect of the motion of the caudal fin motion was observed. Due to the flexibility of the caudal fin as the tendon tail moved from side to side the caudal fin bent in the opposite direction. This was due to the drag force produced by the surface area of the fin as the tail moves it through the water. An illustration of this bending is shown in Figure 5.6. When viewed from above this bending of the caudal fin and associated tail motion produced an approximate undulatory motion.



(a) tail moving from left to right



(b) tail moving from right to left

Figure 5.6: Illustration of caudal fin bending during one complete tail cycle

5.3.1 Comparison to Real Salmon Performance

One of the aims of this research was to determine the benefits of using a biologically inspired propulsion system over conventional underwater propulsion systems. However, it is also important to determine how the performance of the system compares to the biological system being imitated.

From the data available it is apparent that the top speed achievable by the tendon drive system is substantially lower than the 2 body lengths per second quoted as the maximum sustained swimming speeds for atlantic salmon [Tang & Wardle, 1992]. This is due to the limitations of the servo motor actuator used within the tendon drive system which limits the tail beat frequency of operation to less than 2Hz which is a fraction of the beat frequencies that real salmon are able to achieve.

Therefore, a better comparison is between the performance of the tendon drive system and a real Salmon at similar tail beat frequencies and amplitudes. Unfortunately, the data available on salmon swimming with tail beat frequencies in this sub-2Hz beat frequency range is limited. However, it is possible to make an estimate using the assumption that when salmon swim they strive to maintain a Strouhal number within the range for efficient swimming [Triantafyllou & Triantafyllou, 1995].

Using this range of Strouhal numbers (0.25 to 0.35) quoted for efficient swimming and comparing relative similar beat amplitudes for the *RoboSalmon* and real salmon an estimate of the relative performance of the *RoboSalmon* to a real salmon can be approximated as shown in Figure 5.7.

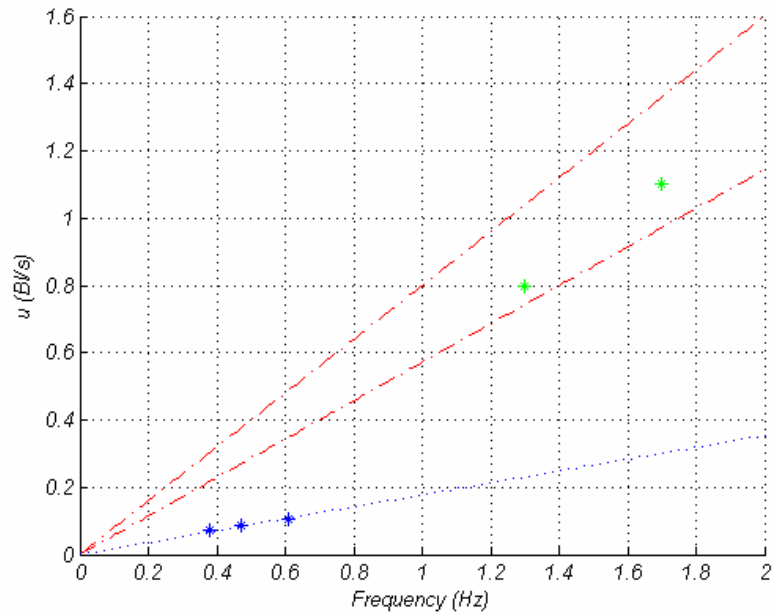


Figure 5.7: Comparison of estimated speed of real atlantic salmon of identical size to *RoboSalmon*. Estimated range of real fish swimming speed (between red dashed lines), real Salmon swimming data points (green points), experimental *RoboSalmon* speed data points (blue points), extrapolated *RoboSalmon* swimming speed (dotted line),

The swimming speed presented in Figure 5.7 is given in terms of body lengths per second in order to account for the different sizes of the salmon and the *RoboSalmon* vehicle. It is possible to do this because the information available on the Strouhal number for fish swimming is independent of the body length of the fish [Triantafyllou & Triantafyllou, 1995]. The tail beat amplitudes of the *RoboSalmon* used for the comparison in Figure 5.7 is 0.105m which is comparable to the beat amplitudes used by real fish. Real fish tend to have a tail beat amplitude of around 10% of their body length when swimming at a steady speed [Videler, 1993].

The comparison shown in Figure 5.7 indicates that the forward swimming speed obtainable with the *RoboSalmon* vehicle is less than the minimum estimated swimming speed of a real salmon by around a factor of 3.2. This discrepancy in the swimming speeds is expected as there will be areas of the *RoboSalmon* where there will be power losses due to the mechanical nature of the prototype. Examples of where such losses will occur are in the DC servo motor which at best is around 53% efficient [Mabuchi Motor, 2009], there will be losses in the force transmission of the tendons to the caudal fin and also in the way the thrust is generated by the tail as the kinematics of the tail and caudal fin are not identical to that of a real salmon. There are also hydrodynamic losses due to the

RoboSalmon not being perfectly streamlined in shape and the skin not having the same properties as real fish skin.

5.3.2 Tendon Drive Start Up Characteristics

Another interesting aspect of the motion of the tendon drive system is the start up characteristics or start up transients. These start-up transients have been measured during the same experiments used to characterize the forward swimming motion. A set of start up transients for a typical run of Program 18 (amplitude 0.15m and frequency 0.61Hz) is shown in Figure 5.8 below.

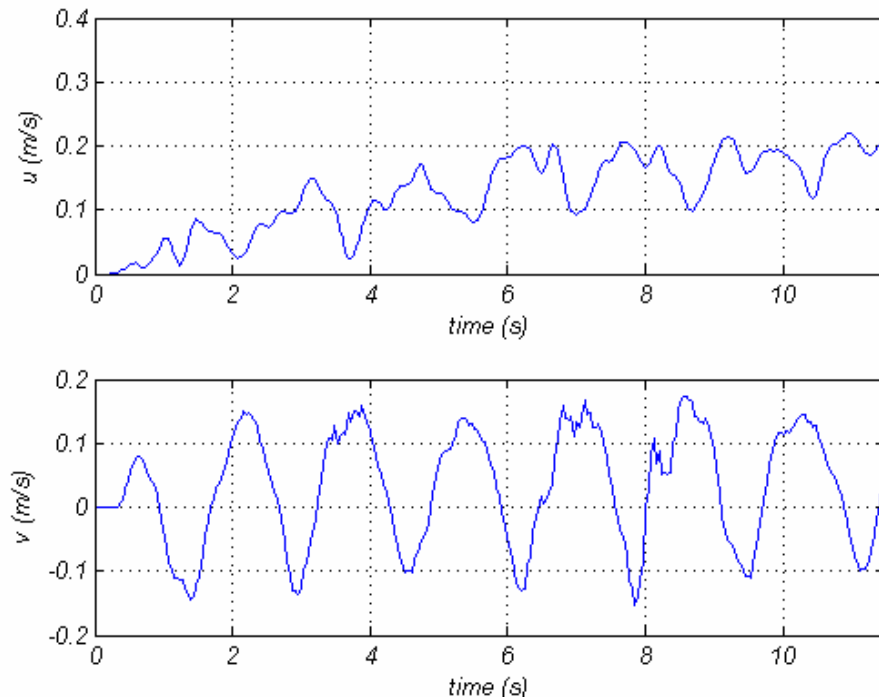


Figure 5.8: Start up characteristics in surge, u , and sway, v , for typical run of Program 18

The results in Figure 5.8 show the time taken for the *RoboSalmon* to reach its steady-state surge speed with the tail parameters of Program 18. Perhaps the most obvious aspect of these transient results is the presence of recoil motion produced as the tail moves, as discussed earlier in Chapters 3 and 4. This recoil motion presents itself as a ripple superimposed on the surge velocity. This is due to the fact that the tail motion does not produce a constant thrust, unlike other conventional forms of underwater propulsion, the thrust produced by a fish tail varies over one tail beat cycle and is usually expressed in terms of the time averaged thrust averaged over several tail beat cycles [Videler, 1993]. The velocity in sway also shows the presence of this recoil motion with the velocity oscillating about the zero velocity value.

Shown in Figure 5.9 are the surge start up transients for a number of different programs to illustrate the effect of different tail beat frequencies.

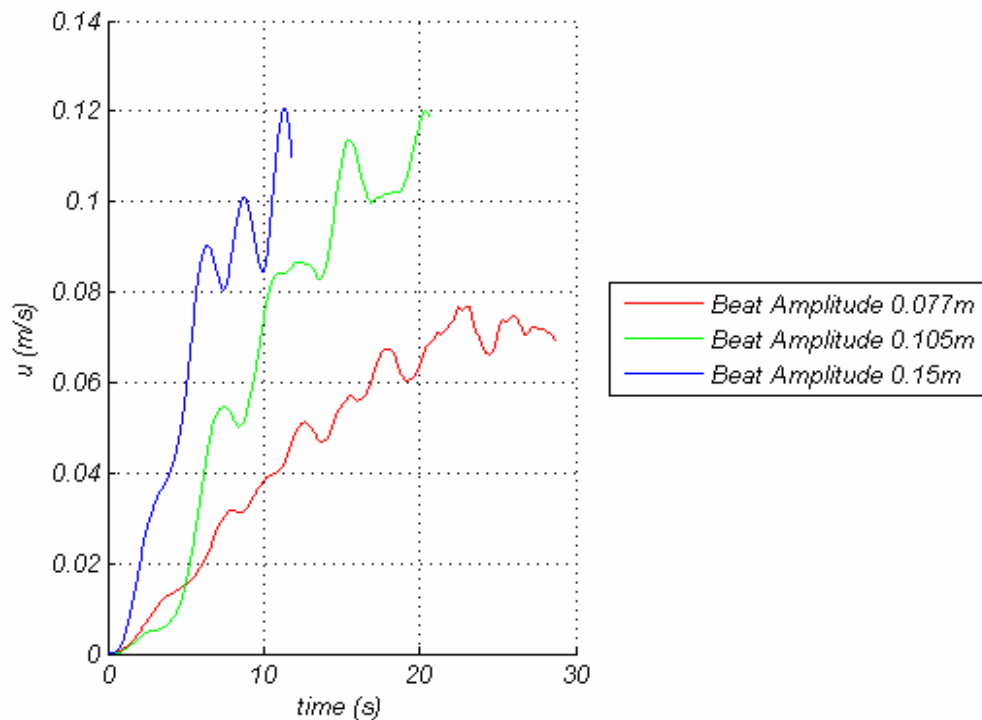


Figure 5.9: Start up transients for 3 different programs with differing tail beat amplitudes with a beat frequency of 0.38Hz

The start up responses shown in Figure 5.9 show that the higher tail beat amplitudes produce greater start up accelerations. It also highlights that in the beat amplitude of 0.105m and 0.15m that the steady state velocity was not reached within the time that the *RoboSalmon* was in the field of view of the camera. For the 0.15m tail amplitude only 12 seconds of data was collected before the vehicle left the camera field of view.

Another observation is that although the *RoboSalmon* vehicle tends to swim in an approximate straight line it tends to deviate initially from its heading in the stationary position. This deviation is illustrated graphically in Figure 5.10. The reason for this deviation has been due to the initial movement of the tail however when numerous runs are compared it seems that the deviation direction is independent of the initial tail motion as shown in Figure 5.10.

It is thought that this deviation is most likely caused by the method used to calibrate the centre of the tail prior to a set of experiments. One disadvantage of the tendon drive system is the difficulty in the exact centering of the tail in the same position in a repeatable fashion. This is due to the design and construction of the tendon drive system which produced a number of factors which affects the centre position of the tail. The two main factors are the tightness of the tendon wires and the positioning of the tail skin. In modelling the tendon drive system the tendon wires are assumed to be inelastic, i.e. they remain the same length. This is a reasonable assumption as they are made from stranded steel wire. However, during operation the tendon wires are thought to increase in length slightly as they age, which eventually causes them to break. When this happens they need to be replaced and the tail

system centre position recalibrated. The other factor is the positioning of the tail skin; at the end of every day of experimenting the *RoboSalmon* has been dismantled to determine if any leaks had occurred during operation. This dismantling involved removal of the tail skin. When the tail skin is replaced prior to commencing the next set of runs, every effort is made for the tail skin to be positioned in the same position. Naturally, this level of accuracy is difficult to achieve in practice. Also, the forward motion results presented were obtained over a period of approximately two months. Therefore, the slight changes in conditions from day to day could contribute to the variations in the observed results.

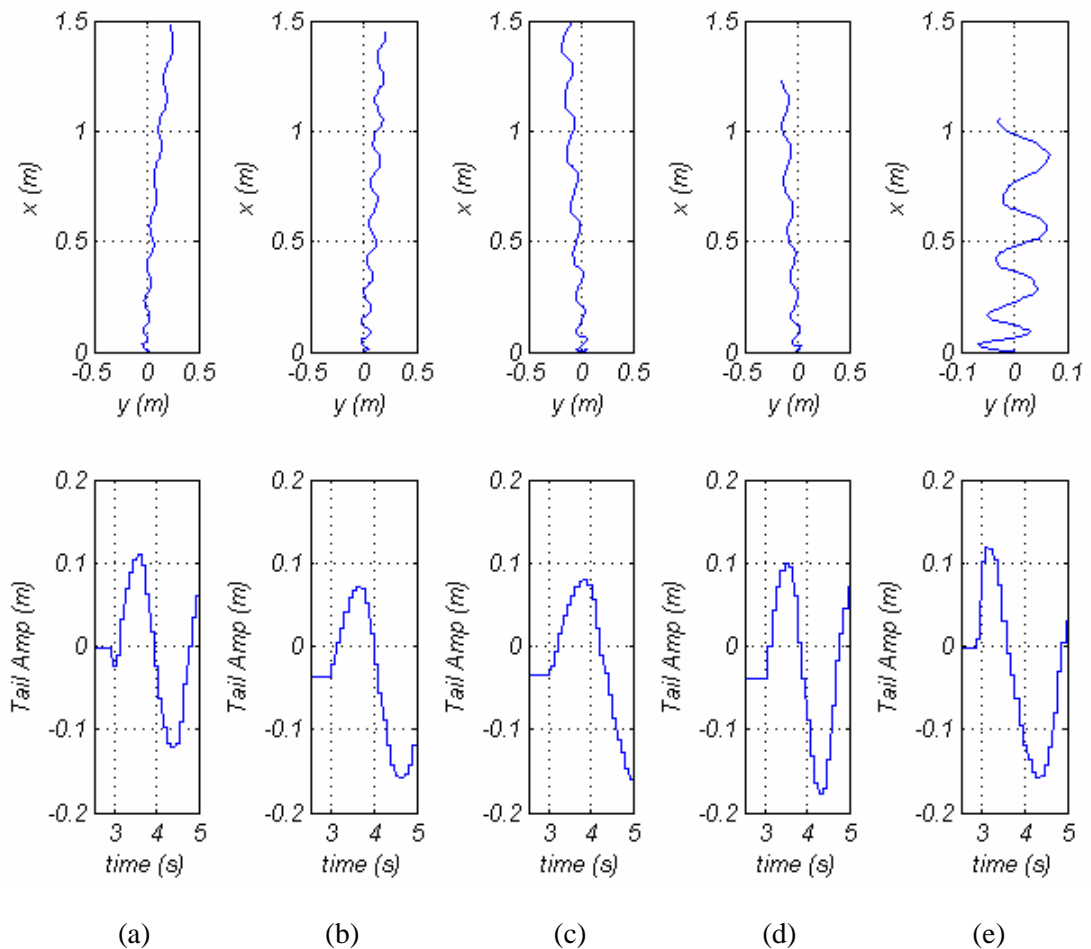


Figure 5.10: Trajectories of 5 runs of various programs indicating the x-y position data (top row) and corresponding initial tail movement (bottom row)

5.3.3 Strouhal Number

As discussed in Chapter 4, one important characteristic for efficient swimming is the Strouhal number [Triantafyllou, *et al*, 1993] which should lie in the range of 0.25 to 0.35. The data collected during each experimental run for forward swimming allows the Strouhal number to be calculated for each combination of tail beat frequency and tail beat amplitude for the tendon drive system. Table 5.2

shows the numerical values of the parameters used to calculate the Strouhal number for the tendon drive system.

From these Strouhal numbers, shown in Table 5.2, it is apparent that none of the experimental programs result in a Strouhal number which lies in the quoted range for efficient swimming. One reason for this is that fish very rarely appear to swim at low velocities in the range obtainable from the *RoboSalmon*. If they do want to swim at low speed, from observations and from the available

Table 5.2: Calculation of Strouhal number of forward swimming with tendon drive system

Program	Frequency (Hz)	Amplitude (m)	Surge Velocity (m/s)	Strouhal Number
1	1.56	0.075	0.1496	1.55
2	0.87	0.088	0.1511	1.01
3	0.61	0.105	0.1220	1.05
4	0.47	0.105	0.1097	0.899
5	0.38	0.105	0.0951	0.879
6	1.56	0.058	0.0703	2.574
7	0.88	0.068	0.1155	1.067
8	0.61	0.077	0.0884	1.021
9	0.47	0.077	0.0723	1.001
10	0.38	0.077	0.0607	0.964
16	1.56	0.107	0.1461	2.228
17	0.86	0.117	0.1913	1.040
18	0.61	0.150	0.1851	0.989
19	0.47	0.150	0.1460	0.945
20	0.38	0.150	0.1291	0.912

literature, they appear to use a burst-coast method which has an initial burst of tail oscillation followed by a period of gliding [Videler, 1993]. This swimming style is a method in which fish can reduce the energy required for swimming at slow and high swimming speeds [Videler, 1993].

5.3.4 Power

As previously discussed one of the objectives of this project is to determine the swimming characteristics of the *RoboSalmon*. The most important characteristics not yet discussed is the power requirements and the swimming efficiencies of the *RoboSalmon* vehicle.

In relation to the propulsion of the *RoboSalmon* the power can be calculated at two stages. The first is the input power supplied to the propulsion system in the form of electrical power supplied from the battery, the second is the actual useful swimming power of the vehicle as it moves.

The input power supplied to the propulsion system is measured as described in Chapter 3 by logging the onboard battery voltage and supply current to the tail propulsion system. A plot of the logged voltage and current measurements, including quiescent current, for a typical run of Program 18 is shown in Figure 5.11 below.

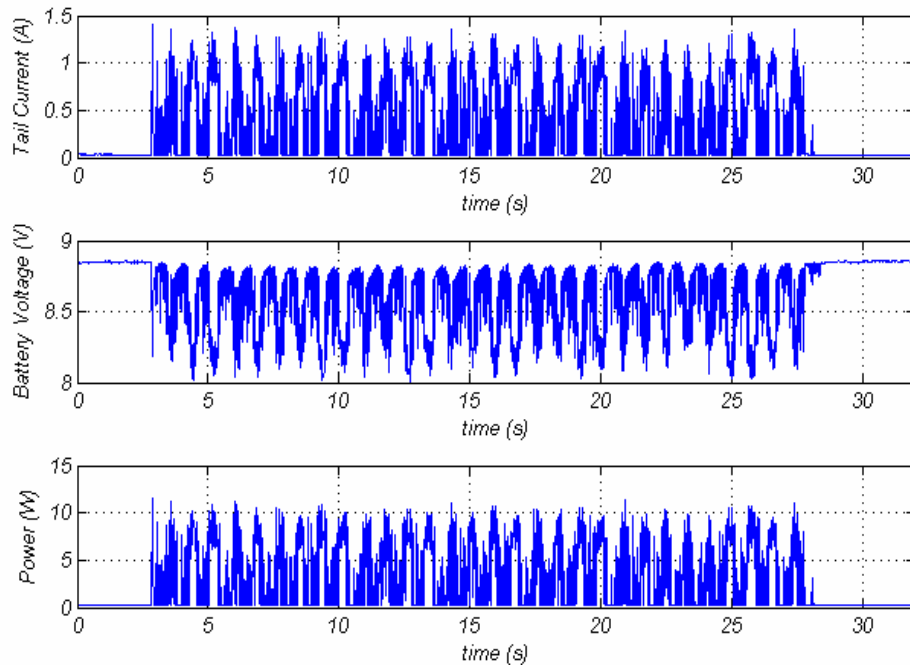


Figure 5.11: Typical plots of *RoboSalmon* tail current (top), battery voltage (middle) and power consumption (bottom) for Program 18

Figure 5.11 indicates that the power consumed by the tendon dive system is not constant but varies dramatically with the motions of the tail. The overall input power used for each of the experimental programs used for each of the surge experiments is shown in Figure 5.12.

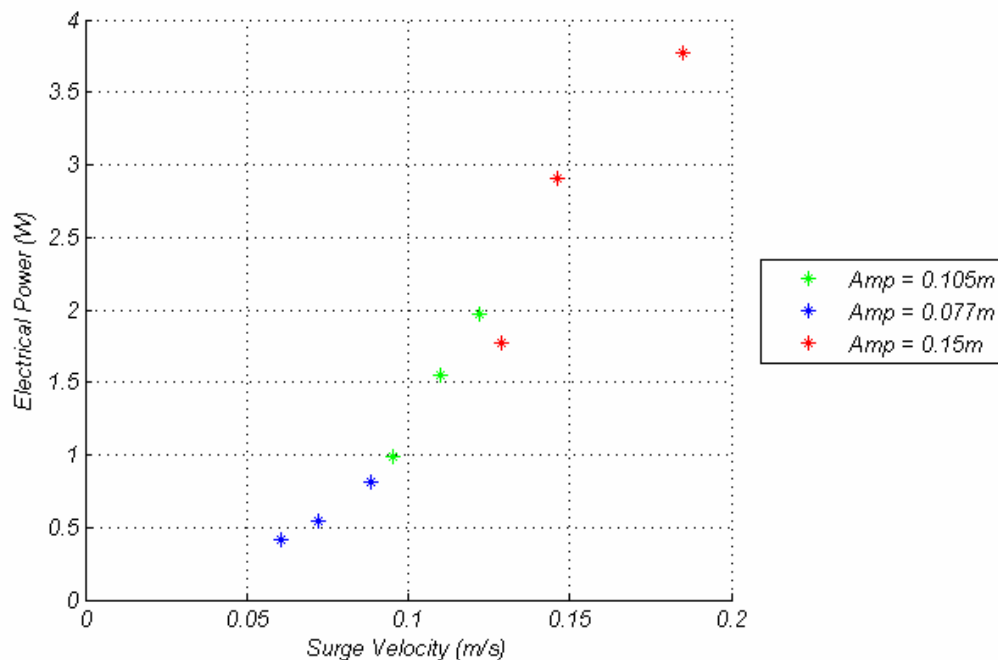


Figure 5.12: Electrical power input to the tendon drive system for each of the nine experimental programs used to investigate surge performance

Before moving onto the second stage it is interesting to look at the power consumption at this stage in more detail. When the power consumption is plotted against the tail position, shown in Figure 5.13, it is interesting to see that the maximum power consumption occurs just after the tail has passed through its centre position. This coincides with the maximum rotational speed of the DC motor within the servo.

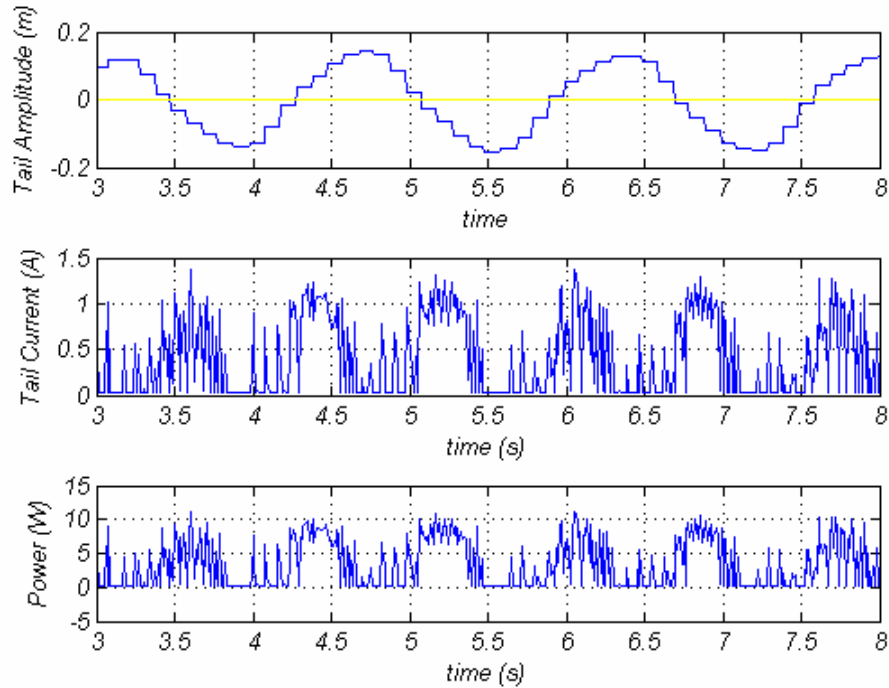


Figure 5.13: Plots of tail servo motor position (top) with tail centre position in yellow, propulsion system current (middle) and corresponding instantaneous power consumption (bottom) for a typical run of Program 18 for three tail beat cycles

Peak currents appear to occur when the servo tail is passing through its centre value. This is most likely because as the servo motor passes through the centre value the DC motor within the servo system is rotating at its fastest.

The output swimming power can be estimated using the relationship between the propulsive force and surge velocity shown in Equation (5.1) [Young & Freedman, 2000]. The swimming power is the actual useful power output of the system.

$$P_{Swim} = F \cdot u \quad (5.1)$$

Here F is the force (N), u is the surge velocity (ms^{-1}) and P_{Swim} is the power (W). In order to be able to estimate the swimming power an estimate of the thrust produced by the tail is required. This thrust estimate is calculated using Lighthill's Large Amplitude Elongated Body Theory [Lighthill, 1970] discussed in Chapter 2. A study into the power output of Atlantic Salmon used this method to estimate the power output using the kinematic parameters of the Salmon fin motions captured from video analysis along with the forward velocity [Tang & Wardle, 1992].

Figure 5.14 illustrates the estimate of swimming power using the method outlined above for the nine experimental programs used in the investigation where actuator saturation did not occur.

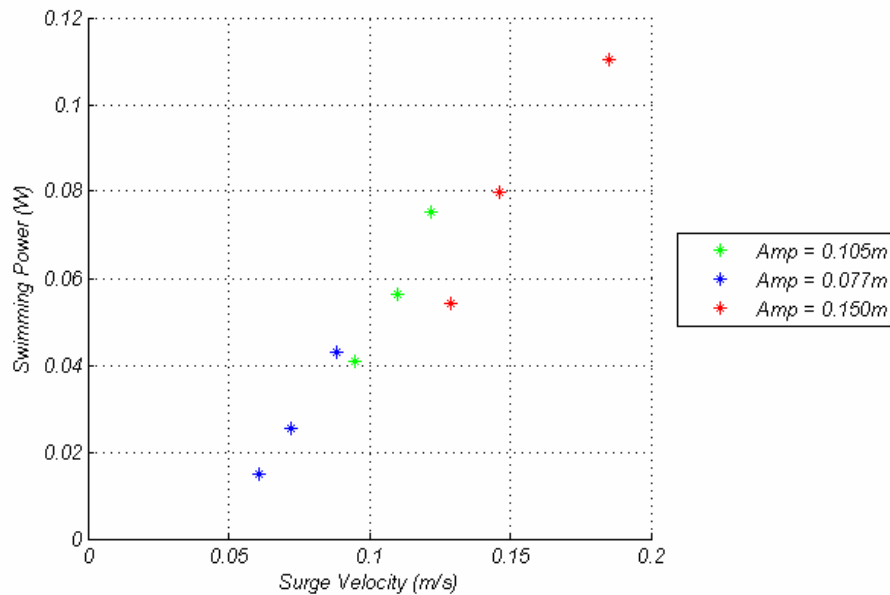


Figure 5.14: Surge swimming power calculated using an estimate of thrust produced using Lighthill's large amplitude elongated body theory and the measured surge velocity for each of the experimental programs.

The swimming power estimates shown in Figure 5.14 indicate that the relationship between the surge velocity and swimming power appear linear as expected for each tail beat amplitude tested.

5.3.4.1 Real Salmon Power Output

One of the potential benefits of biomimetic underwater propulsion is that it is more efficient than conventional propeller systems. In this study the power requirements of a propeller/rudder based system is compared to the biomimetic approach. However, one other interesting aspect is how the biomimetic system compares to a real fish.

The power output of swimming fish is of interest to biologists and there have been a number of studies on the subject [Webb, 1971; Altringham & Johnston, 1990]. There are two different biological ways in which the muscle power has been estimated, firstly using the amount of oxygen consumed by the fish under experimental conditions [Wardle, 1975; Videler, 1995] and secondly from the mass of red muscle tissue present in the fish [Altringham & Johnston, 1990]. The second method is simpler and allows for a rough comparison between real fish and the biomimetic vehicle therefore this method is used as a basis for the comparison in this study.

Most fish have several types of muscle fibre, however two types are predominantly associated with propulsion namely slow red fibres and fast white fibres [Videler, 1995]. Each of the fibre types have a different property that is used in different modes of swimming. The fast white fibres are the most

powerful fibres but become exhausted after a short duration, therefore these fibres are used in swimming with a high tail beat frequency (5-7Hz) for short burst durations [Tang, & Wardle, 1992]. The red fibres produce their maximum power output at lower tail beat frequencies (approximately 2Hz) and therefore are more suited for low speed sustained swimming [Tang & Wardle, 1992]. The contribution from the slow red fibres to high speed burst swimming is considered negligible [Tang & Wardle, 1992].

Due to the mechanics of the *RoboSalmon* its tail beat frequency is limited to less than 1Hz. To obtain a fair comparison would be to that of a real salmon of identical size, swimming at low speed using only its red muscle fibres. A maximum value of $5-8\text{Wkg}^{-1}$ is quoted for the mass-specific capacity of red muscle tissue in fish [Altringham & Johnston, 1990] and it is assumed that for *salmo salar* 3-4% of body mass is red muscle tissue [Tang & Wardle, 1992]. This value is estimated for the fish swimming at its maximum sustained swimming speed where it is assumed that all the red muscle tissue is used and that no other muscle type is involved [Tang & Wardle, 1992]. For a salmon of identical dimensions to the *RoboSalmon* the estimate for maximum swimming power output would be in the range 0.788-1.26W for its maximum sustained swimming speed. The useful swimming output power of the *RoboSalmon* vehicle is substantially lower than this.

In order to estimate power output at slower speeds than the maximum sustained swimming speed, the relationship that swimming power varies as the cube of the velocity is assumed [Tang & Wardle, 1992]. Figure 5.15 shows a plot of estimated swimming speed for a salmon of identical dimensions to the *RoboSalmon* vehicle.

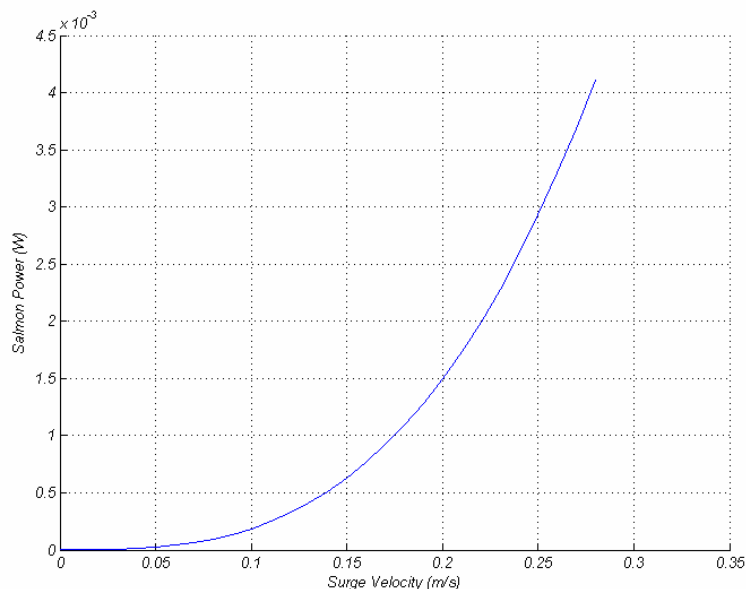


Figure 5.15: Estimates of salmon swimming power vs swimming speed. Estimate based on real salmon of identical dimensions to the *RoboSalmon* vehicle swimming at low speed using only red muscle tissue.

The estimate of swimming power output for a real salmon of similar size to the *RoboSalmon* vehicle shown in Figure 5.15 indicates just how much lower the power to velocity ratio is for the biological fish over the mechanical replicant. When the actual power outputs for similar speeds are compared, as can be seen in Table 5.3, the power used by the biological system for similar swimming speeds appears to be around a factor of 100 less than the mechanical system.

Table 5.3: Comparison of estimate of output swimming powers for *RoboSalmon* vehicle and atlantic salmon

Velocity (m/s)	<i>RoboSalmon</i> Swimming Power (W)	Salmon Power Estimate (W)
0.130	0.054	0.00041
0.146	0.079	0.00063
0.185	0.110	0.0013

This large discrepancy is not unexpected as it would be very unlikely that a mechanical system would be able to replicate the performance of a biological system. Reasons for this discrepancy are the same as the reasons presented for the discrepancy if the surge velocities, namely the inefficiency of the servo motor, power losses in the mechanics of the system and hydrodynamic losses due to the vehicle not being perfectly streamlined.

5.4 Recoil Motion

The recoil motion of the tendon drive system has already been highlighted in a number of the results presented already. For example in the surge and sway start up velocities shown in Figure 5.8 the recoil motion present is in the form of a ripple in the surge velocity and an oscillation in the sway velocity. The x-y positional data in Figure 5.2 shows the effect the recoil motion has on the trajectory, i.e. rather than travelling in a straight line the centre of mass appears to oscillate about a centre point which produces the wave like trajectories.

As well as being visible on the swimming trajectory, for surge and sway velocities the recoil motion is also present in the yaw, roll and pitch angular velocities. This recoil in yaw, roll and pitch is illustrated in Figures 5.16, 5.17 and 5.18 respectively which show typical run data for all 15 experimental programs used.

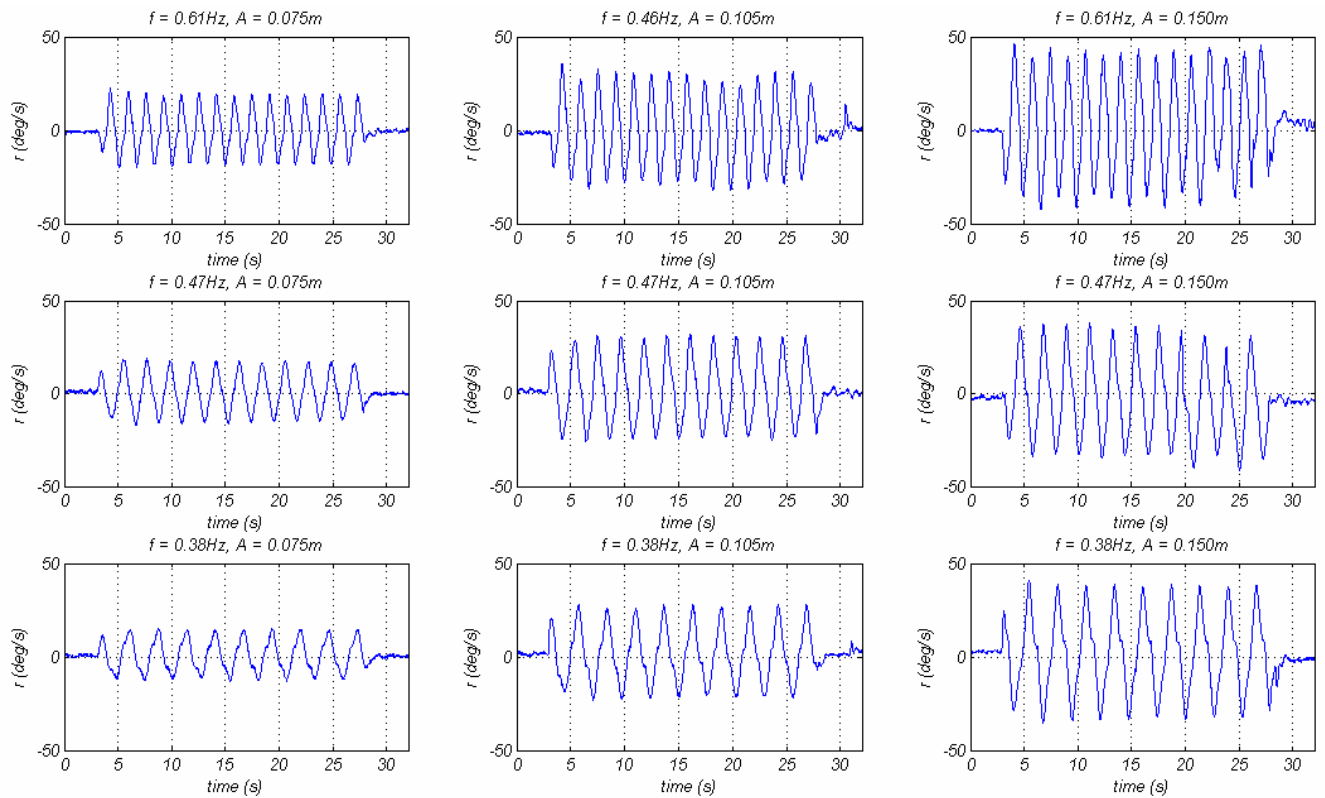


Figure 5.16: Typical yaw rate r (deg/s) experimental data from runs of all 9 experimental programs without actuator saturation. Each row contains programs with the same tail beat frequency and each column has the same tail beat amplitude. i.e. top left is the smallest beat amplitude with the highest frequency and bottom right is the largest beat amplitude and slowest frequency.

From all the graphs of the yaw rates shown in Figure 5.16 the recoil motion is apparent as the oscillation about the zero value. These graphs show that as the beat amplitude increases the peak yaw rate obtained also increases. However, increasing the beat frequency with a constant beat amplitude does not appear to have as much of an effect as altering the beat amplitude.

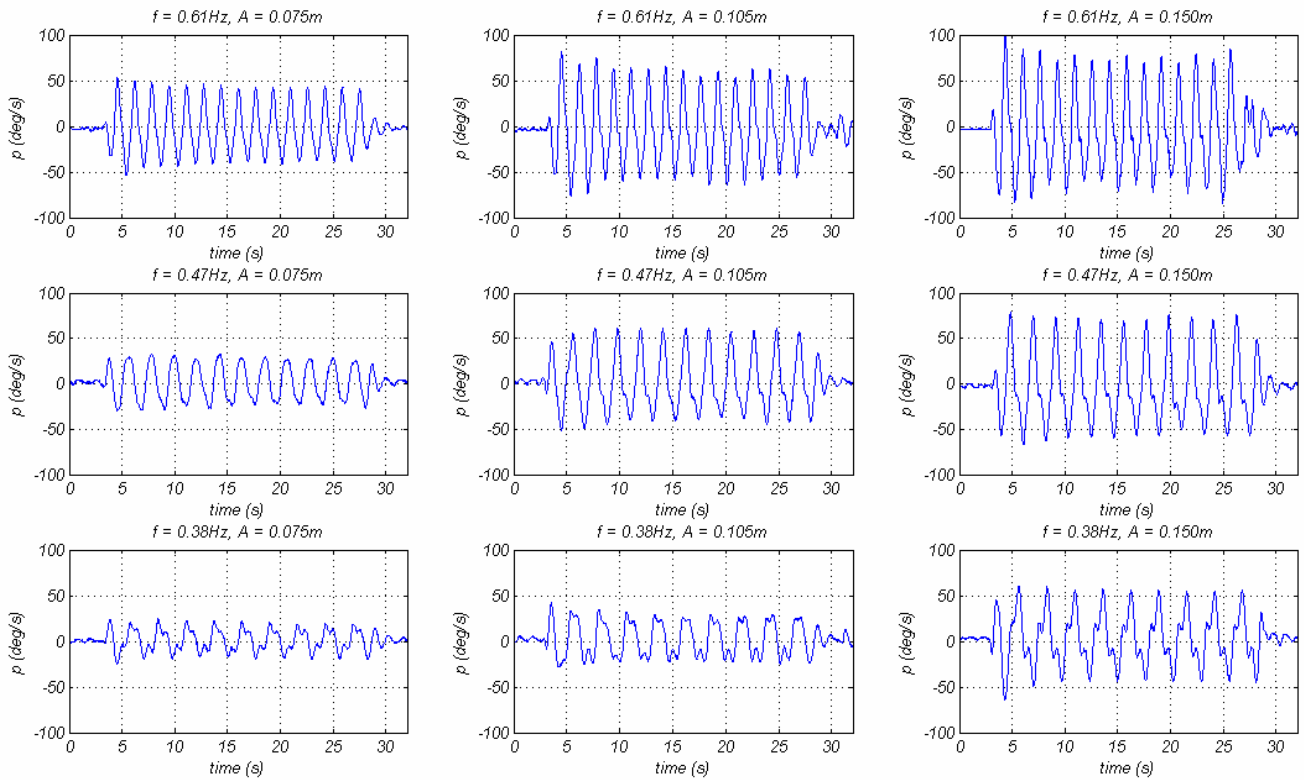


Figure 5.17: Typical Roll rate p (deg/s) experimental data from runs of all 9 experimental programs without actuator saturation. Each row contains programs with the same tail beat frequency and each column has the same tail beat amplitude. i.e. top left is the smallest beat amplitude with the highest frequency and bottom right is the largest beat amplitude and slowest frequency

The peak roll rates shown in Figure 5.17, like the yaw rates of Figure 5.16, appear to increase with increasing tail beat amplitude. However, this increase is not as pronounced as the increases present in Figure 5.16. Also, as the beat frequency is increased there is an apparent increase in the peak roll rate. Another interesting aspect about the roll rates is that at the lower beat frequency the shape of the graph is altered.

The pitch rates, shown in Figure 5.18, show that the effects of recoil are not as prominent in this axis. However, the pitch rates obtained do appear to increase with both beat frequency and amplitude.

From all the angular rate results presented in Figures 5.16, 5.17 and 5.18 a number of relationships can be observed. The axis affected least by the recoil motion is pitch as can be seen by comparing the three figures. To look at these relationships in more detail the typical peak amplitude of the oscillations in each angular degree of freedom are shown in Figure 5.19.

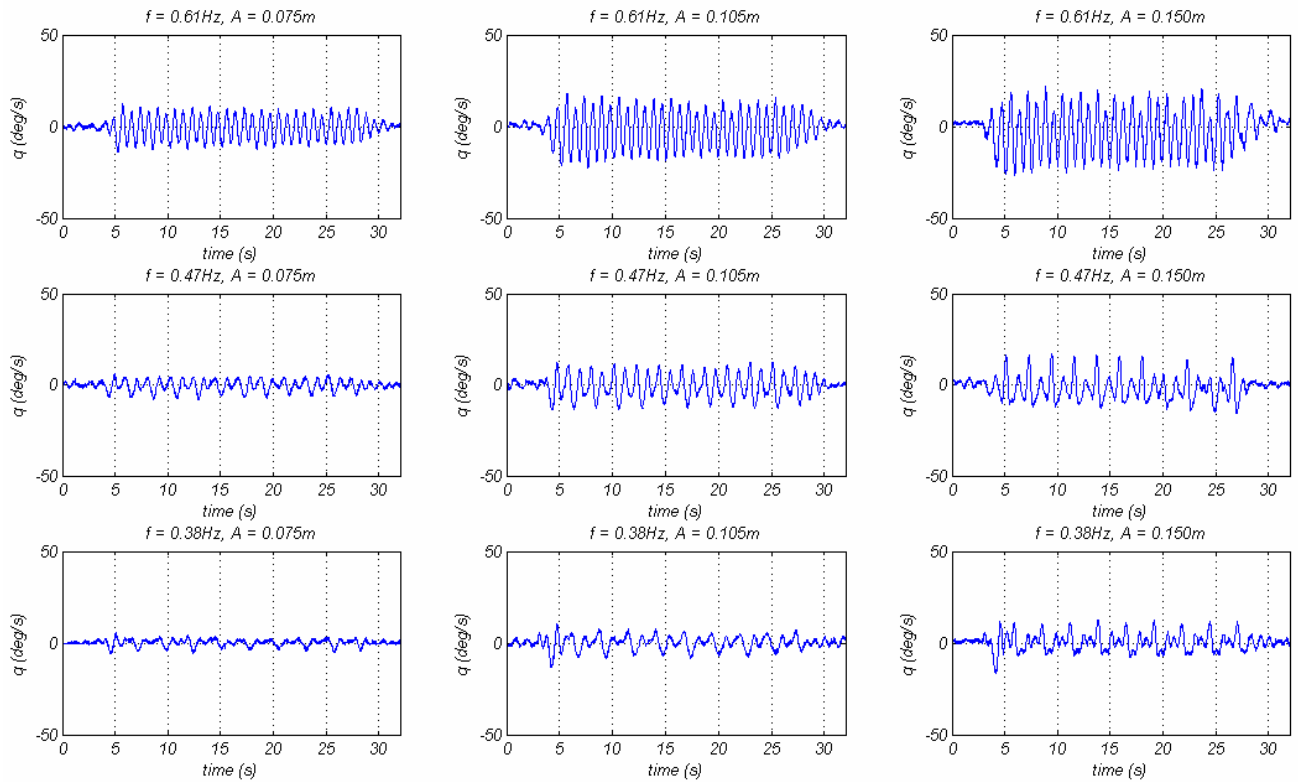


Figure 5.18 – Pitch rate q (deg/s) experimental data from runs of all 15 experimental programs. Each row contains Programs with the same tail beat frequency and each column has the same tail beat amplitude. i.e. top left is the smallest beat amplitude with the highest frequency and bottom right is the largest beat amplitude and slowest frequency

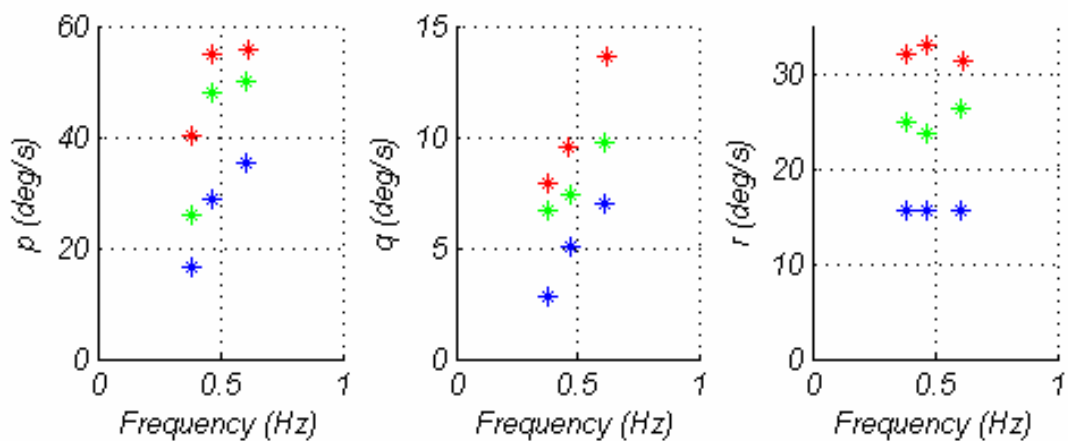


Figure 5.19: Quantitative comparison of magnitudes of recoil effects in roll, pitch and yaw angular velocities for straight swimming. The blue points indicate a nominal tail beat amplitude of 0.075m, green points a nominal amplitude of 0.105m and red points a nominal beat amplitude of 0.150m.

The plots in Figure 5.19 show quantitatively the relationships between the amplitude of recoil oscillation in each of the angular degrees of freedom for the programs with no actuator saturation. For

the roll angular velocity (p), as the frequency increases, the maximum angular velocity increases. The roll rate also appears to increase with increasing beat amplitude. However, with the limited number of data points obtained it is only possible to determine relationships over the frequencies tested. For pitch angular velocity, similar to roll, as the frequency increases with the tail beat amplitude remaining constant the maximum amplitude increases in a linear fashion. The relationship between yaw rate and frequency is different in that it appears from the tail beat frequency and amplitude combinations tested that the maximum amplitude of the yaw rate is not affected significantly by changes in frequency. The yaw angular velocity is more dependent on the beat amplitude i.e. as the beat amplitude increases the yaw angular velocity increases.

Using the angular velocities measured using the MEMs rate gyroscopes the angular displacements can be calculated by integrating the angular rate data over time. This provides a more intuitive measure of the recoil motion in terms of the angular displacement/deflection of the body in relation to the tail movements. The angular displacements in roll, pitch and yaw for the experimental programs with no actuator saturation occurring are shown in Figure 5.20.

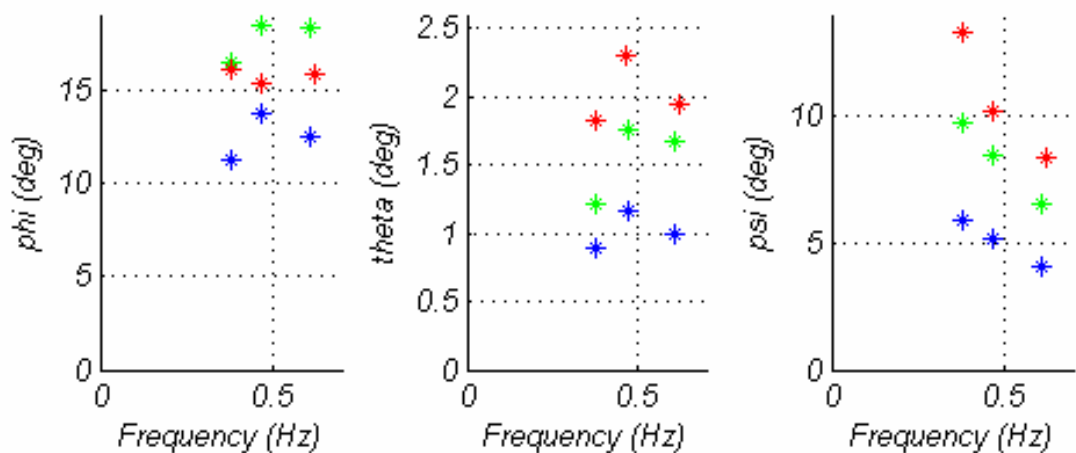


Figure 5.20: Quantitative comparison of magnitudes of recoil oscillation effects in roll (ϕ), pitch (θ) and yaw (ψ) angular displacements for straight swimming. The blue points indicate a nominal tail beat amplitude of 0.075m, green points a nominal amplitude of 0.105m and red points a nominal beat amplitude of 0.150m.

The pitch angular displacement is the smallest of the three angular displacements which is expected as the pitch angular velocity is the smallest of the three velocities. The relationship between roll angle and frequency is difficult to determine from the data collected. However the relationship between the roll angle and amplitude appears to show that the roll angle increases for increased tail beat amplitude. Finally, the relationship between the recoil yaw angle and the beat frequency appears to be clearer than the pitch and roll relationships. As the frequency increases the amplitude of the oscillations in yaw angle decreases in a linear fashion for each tail beat amplitude tested.

5.4.1 Phase of Recoil

In order to determine the tail motions that produce the recoil and to better understand the motion the phase of the recoil has to be investigated. Figure 5.21 indicates the relative phases of the tail motion, sway velocity, the yaw rate and the roll rate.

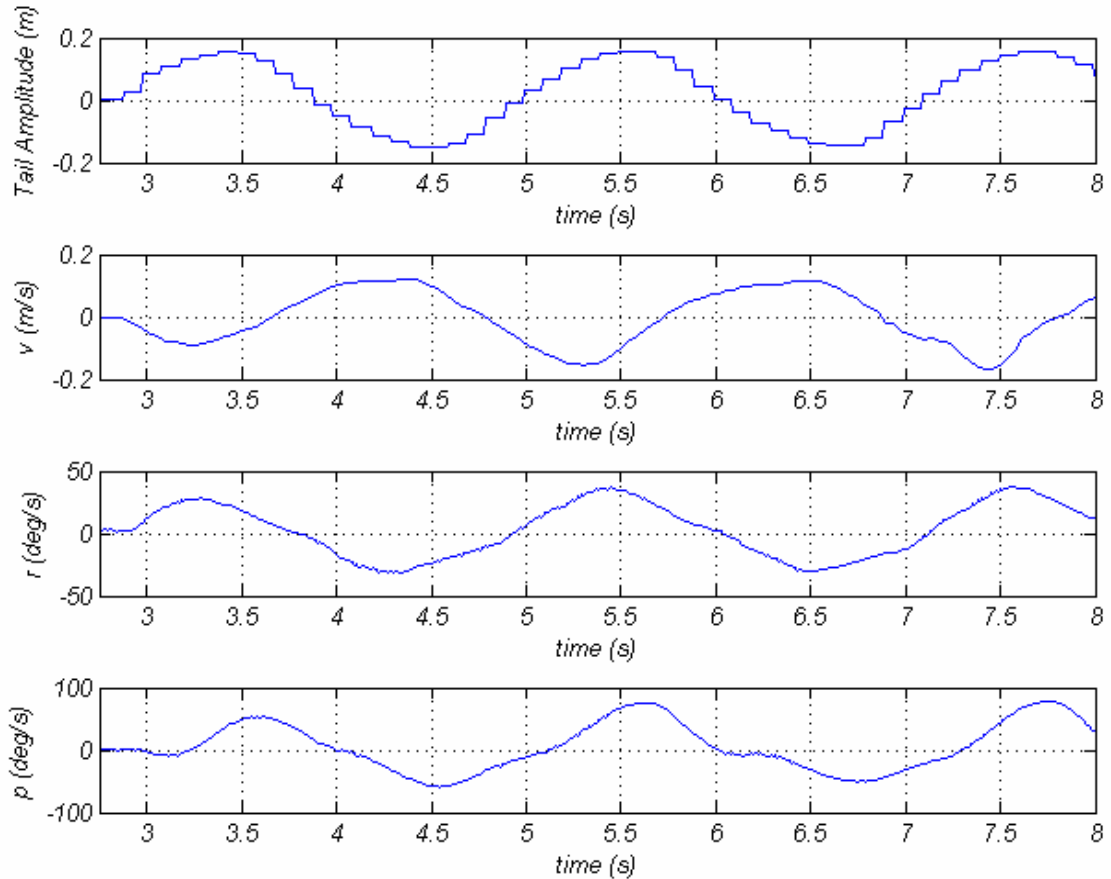


Figure 5.21: Comparison of phase between tail motion; lateral velocity, yaw angular velocity and roll angular velocity.

From the phase comparisons in Figure 5.21 it can be seen that the four variables shown are not in phase. The sway velocity is 90° out of phase with the tail motion i.e. the maximum sway velocity occurs when the tail is passing through its centre position. This point of maximum sway velocity also corresponds to the point where the tail moves fastest (i.e. in the middle of the sweep of the tail).

5.4.2 Power Expended due to recoil

As the tendon drive propulsion system on the *RoboSalmon* vehicle is actuated it provides a surge force but also produces recoil motion as discussed in the previous section. One of the objectives of this study is to investigate the power consumption and efficiencies of swimming. As the recoil is an undesired effect of propulsion using the tendon drive system it would be of interest to estimate the energy lost due to this recoil motion.

The method used to estimate the energy lost in the recoil motion is to use the rate gyro data to determine the angular kinetic energy using Equation (5.2) where E_k is the kinetic energy of the vehicle in that degree of freedom in Joules, I is the moment of inertia in kgm^2 and ω is the angular velocity in rads^{-1} .

$$E_k = \frac{1}{2} I \omega^2 \quad (5.2)$$

The moment of inertia used in Equation (5.2) depends on which angular degree of freedom is being investigated. For the calculation of the moment of inertia in roll the body is assumed to be a solid cylinder with radius equal to the maximum horizontal radius of the *RoboSalmon* vehicle and the axis of rotation parallel to the centre axis of the cylinder. A similar assumption is made for the estimation of the moment of inertia in yaw but the axis of rotation of the cylinder is perpendicular to the centre axis of the cylinder and the cylinder is assumed to be the same as the *RoboSalmon* vehicle. The equation used to estimate the moment of inertia in roll is shown in Equation (5.3) [Young & Freedman, 2000] and for yaw in Equation (5.4) [Humphrey & Topping, 1961]; where m is the mass of the *RoboSalmon* vehicle in kg, r is the maximum horizontal radius of the vehicle and h is the length of the vehicle.

$$I_{ROLL} = \frac{mr^2}{2} \quad (5.3)$$

$$I_{YAW} = \frac{1}{12} m(3r^2 + h^2) \quad (5.4)$$

Once the kinetic energy has been calculated for the recoil motion the power is obtained by differentiating the energy as power [Young & Freedman, 2000].

The average power expended in the recoil motion in roll and yaw is shown graphically in Figure 5.22. This indicates that the recoil motion in yaw expends more power than the roll recoil motion. It also shows that the recoil power consumption in roll is proportional to both the tail beat frequency and the beat amplitude whereas the power used in yaw appears to be less dependent on the beat frequency.

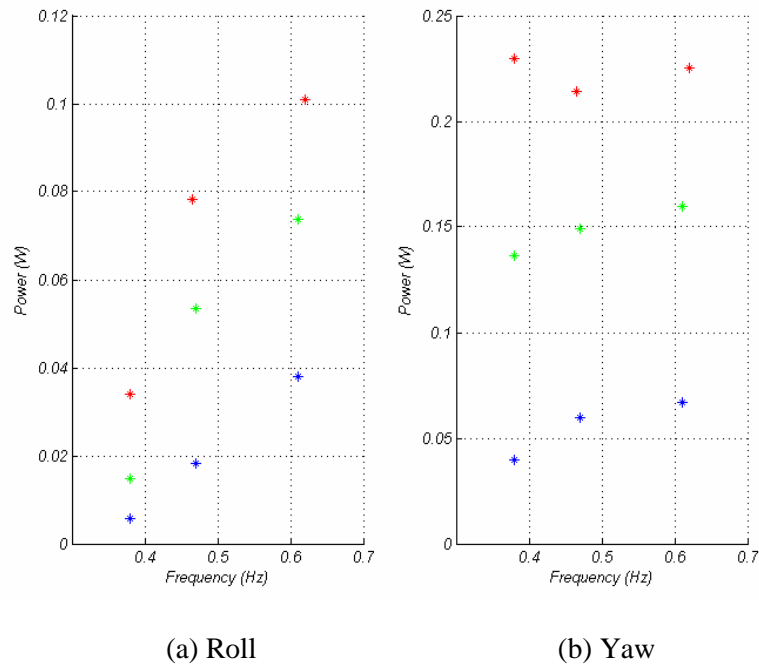


Figure 5.22: Average power expended for recoil motion in (a) Roll and (b) Yaw. The blue points indicate a nominal tail beat amplitude of 0.075m, green points a nominal amplitude of 0.105m and red points a nominal beat amplitude of 0.150m.

When these estimated results for power are compared with the power input power consumption for forward swimming shown in Figure 5.14 it can be seen that the power expended in the recoil is greater than the useful swimming power used the surge direction.

The results presented and the associated discussions about the recoil motion in the previous sections thus far have attempted to ascertain the relationships between the tail motions and the recoil motions in roll, pitch and yaw. Due to the limited number of data points obtained only qualitative relationships can be observed. However, it is apparent that the recoil motion present in the tendon drive system is highly coupled between many degrees of freedom and complex.

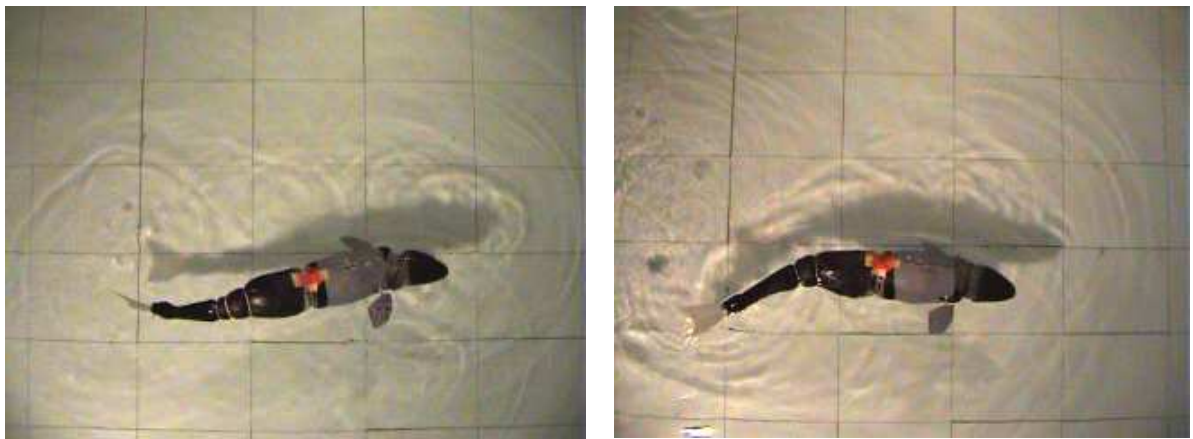
5.5 Actuated Head

With the presence of the recoil motion in yaw and roll during forward swimming and the associated energy loss it has been hoped that it may be possible to reduce the magnitude or even cancel out this unwanted motion completely using the actuated head. To test this idea a series of experiments have been carried out with the actuated head moving at various amplitudes and phases with respect to the tail. These variations in head motion have been employed in order to determine the effects this would have on forward swimming.

The experiments to investigate the effect of the actuated head on forward swimming consist of carrying out similar experiments to those carried out for the forward motion surge experiments but with the head oscillating in a sinusoidal fashion in phase with the tail with two maximum angular

deflections of 13.5° and 27° . The same set of experiments are then carried out with the head oscillating 180° out of phase with the tail motions.

Figure 5.23(a) shows the *RoboSalmon* prototype swimming with the actuated head moving out of phase with the tail and Figure 5.23(b) shows the *RoboSalmon* swimming with the actuated head moving in phase with the tail.



(a) Actuated head out of phase with tail (i.e. moving in opposite direction)

(b) Actuated head in phase with tail motion (moves in same direction)

Figure 5.23: *RoboSalmon* vehicle using actuated head whilst swimming.

A selection of results is presented below which show the effects of the actuated head with a tail beat frequency and amplitude identical to that of Program 5 in the surge experiments.

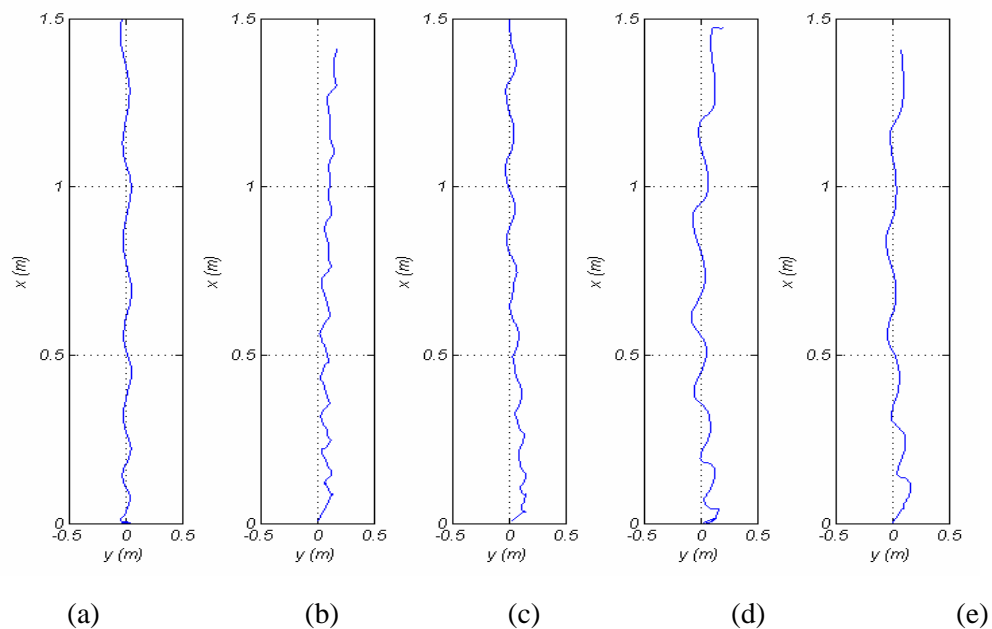


Figure 5.24: X-Y positional data for the *RoboSalmon* using program 5 (a) with no head oscillation, (b) head oscillating with 27° deflection 180° out of phase with tail, (c) head oscillating with 13.5° deflection 180° out of phase with tail, (d) head oscillating with 27° deflection in phase with tail, (e) head oscillating with 13.5° deflection in phase with tail

The X-Y positional data presented in Figure 5.24 shows how the oscillation of the actuated head affects the motion of the *RoboSalmon*. This shows that for the head movements out of phase, Figure 5.24(b) and Figure 5.24(c), produce a trajectory which is not as smooth as the trajectory with no head movements. With the head motions in phase with the tail, Figure 5.24(d) and Figure 5.24(e), the trajectory appears to have larger oscillations in the y axis.

Figures 5.25 and 5.26 show the effect that the actuated head has on the roll and yaw rates respectively. Perhaps the most obvious effect the actuated head has on the roll and yaw angular velocities is that it appears to alter the shape of the response from the response with the head stationary.

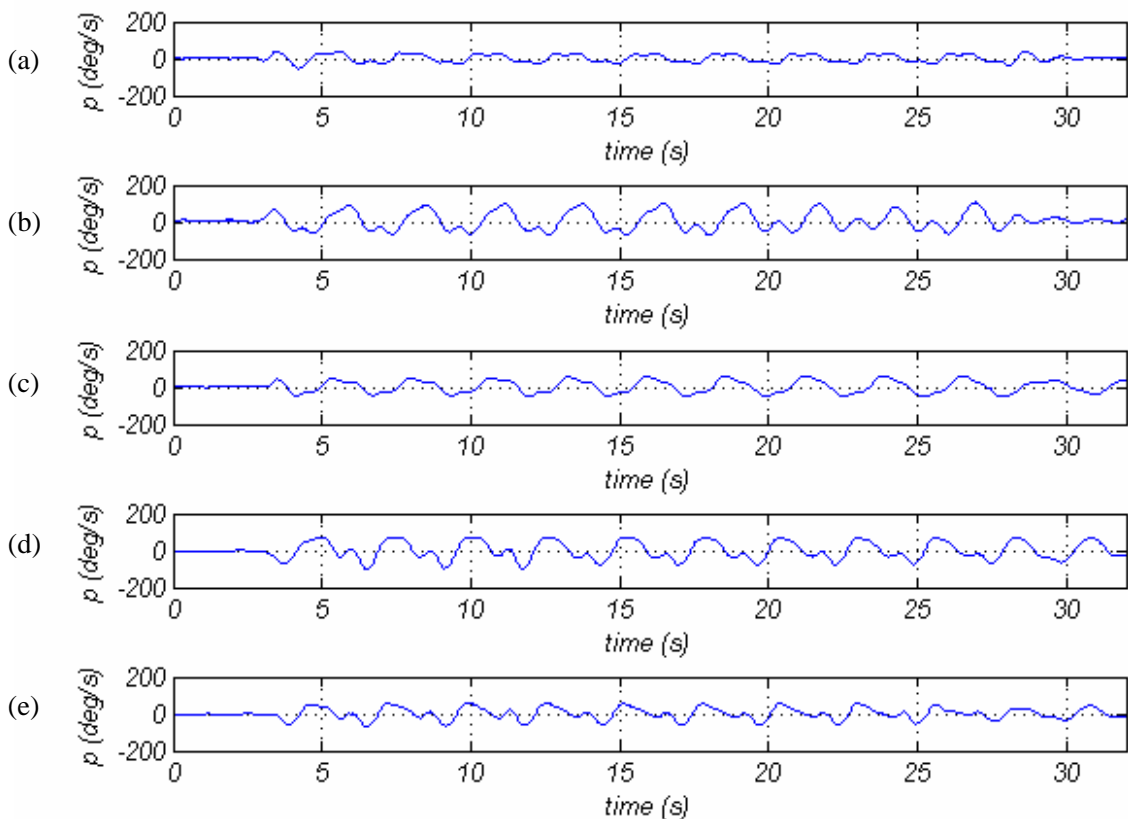


Figure 5.25: Roll rate for program 5 (a) with no head oscillation (b) head oscillating with 27° deflection 180° out of phase with tail (c) head oscillating with 13.5° deflection 180° out of phase with tail (d) head oscillating with 27° deflection in phase with tail (e) head oscillating with 13.5° deflection in phase with tail

For the roll rates shown in Figure 5.25, as well as altering the shape of the response, it also appears to increase the peak value of the angular velocity for each actuated head parameter set tested. This can be seen when comparing Figure 5.25(a) for no head movement when swimming and Figure 5.25(b) for the head oscillating with 27° deflection 180° out of phase with tail the magnitude of the peak roll is increased by approximately a factor of two. This increase in roll can be attributed to materials used for the construction of the vehicle. During the development phase the *RoboSalmon* was trimmed so that it statically its pitch and roll angles were approximately zero and so sat horizontal in the water.

However, this process was carried out with the tail and head centred. As the head and tail move they affect the centre of gravity and centre of buoyancy of the vehicle. With the tail offset the vehicle tends to roll in the direction of the tail offset due to the moment caused by the weight of the tail assembly. However, the head is constructed mostly from Styrofoam which is very buoyant and so produces a force in the opposite direction to the weight. When the tail and head are out of phase the moments cause by these forces are in the same rotational direction which will tend to increase the roll.

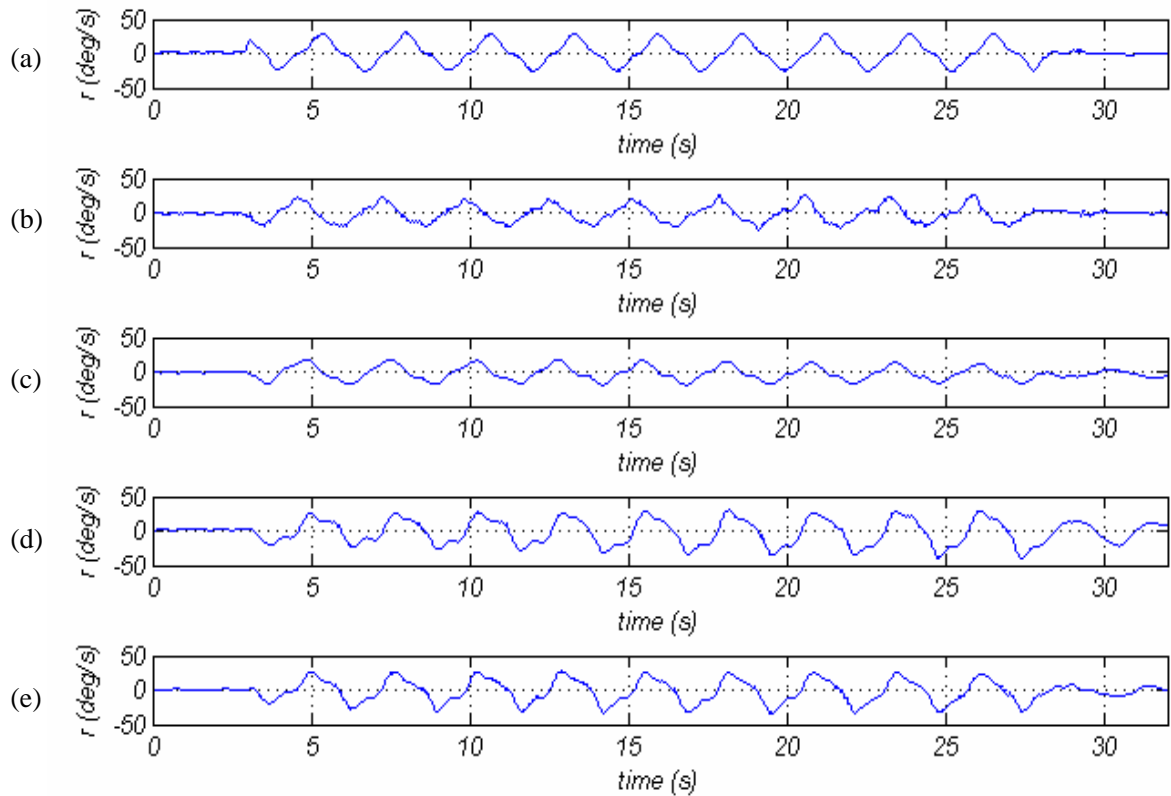


Figure 5.26: Yaw rate for program 5 (a) with no head oscillation (b) head oscillating with 27° deflection 180° out of phase with tail (c) head oscillating with 13.5° deflection 180° out of phase with tail (d) head oscillating with 27° deflection in phase with tail (e) head oscillating with 13.5° deflection in phase with tail

For the yaw angular rate the effect of the actuated head, like the effect in roll, is twofold. Firstly, the shape of the response is modified from that with no head motion. Secondly, the peak yaw rate is also modified and in the experiment with the head out of phase with the tail and the head oscillating with 13° maximum deflection the peak yaw rate is less than that with no head motion. This shows that it may be possible, with proper selection of the head angle and head phasing with respect to the tail, to reduce the effect of the recoil motion in yaw.

Another aspect to using the actuated head is the surge velocity obtained when the head is used in conjunction with the tendon drive tail system. It is apparent during experimentation that as well as

affecting the trajectory of the vehicle, the surge velocity is also affected. The surge velocities obtained from the actuated head experiments are shown in Table 5.4.

Table 5.4: Surge velocities obtained when using Actuated Head

Program	Surge Velocity (m/s)
Head Stationary	0.095
Head oscillating 180° out of phase, 27° max deflection	0.066
Head oscillating 180° out of phase, 13.5° max deflection	0.065
Head oscillating in phase, 27° max deflection	0.087
Head oscillating in phase, 13.5° max deflection	0.099

The surge velocities shown in Table 5.4 for the actuated head experiments show that the head oscillating out 180° of phase has a detrimental effect on the surge velocity. This reduction in surge velocity could be due to the increased drag caused by the increased frontal area presented to the water when the head and tail are out of phase. Also, the increased roll moment may cause a reduction in the effectiveness of the caudal fin as it will not only be moving laterally but will also have a roll component to overcome. With the head oscillating in phase with the tail there does not appear to be a significant effect on the surge velocity.

5.6 Mechanical Tail vs Propeller System

As discussed earlier one of the main aims of this project is to determine if utilising a biomimetic propulsion system has any benefits over a conventional propulsion system. In order to provide this comparison results have been obtained using a prototype which uses a propeller based propulsion system (as outlined in Chapter 3). The prototype consists of the same body and head section used for the tendon drive system but with the tail actuation system replaced with a propeller and rudder actuation scheme.

To ascertain the forward motion characteristics of the propeller system ten experimental programs have been developed as shown in Table 5.5.

Table 5.5: Forward Motion Programs for Propeller System

Propeller System Program	Prop motor PWM Duty Cycle (%)	Prop Speed (rev/s)	Rudder Angle (deg)
1	55	0.90	0
2	60	1.57	0
3	65	2.29	0
4	70	2.99	0
5	75	3.58	0
6	80	4.92	0
7	85	5.50	0
8	90	6.12	0
9	95	6.79	0
10	100	8.57	0

The first program uses a duty cycle of 55% as it has been determined experimentally that any duty cycle below this value does not provide enough torque to cause the propeller to rotate in water. This is due to the frictional losses within the DC motor gear train, shaft coupling and the stern tube. The same experimental procedure outlined in Subsection 5.2 has been used for the experiments involving the propeller system.

As discussed in Chapter 3, a common body section is used the only modification to which is in the firmware to allow the rotational speed of the propeller to be stored in the data logger. An example of data obtained for the propeller speed and corresponding current consumption is shown in Figure 5.27.

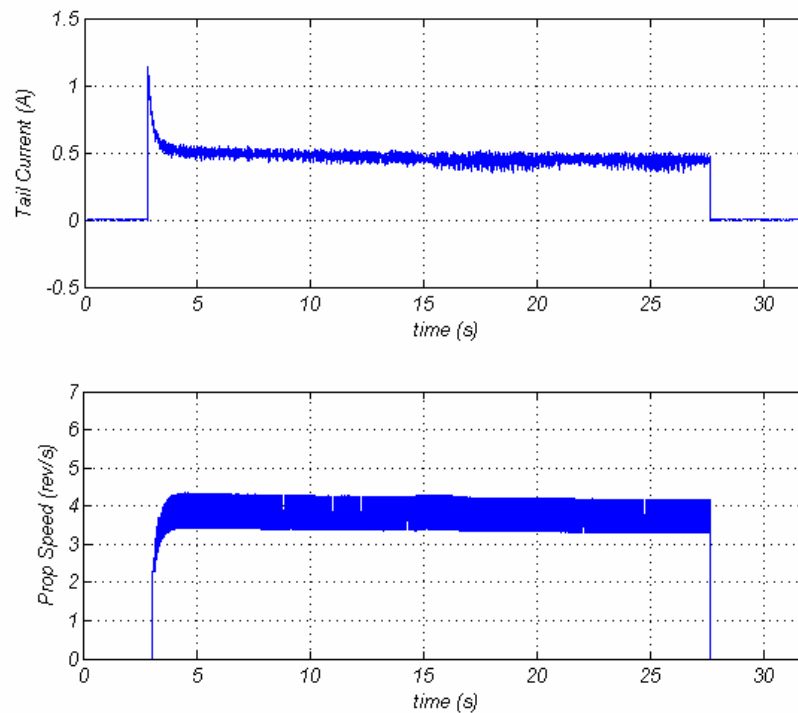


Figure 5.27: Propeller current consumption (top plot) and propeller rotational speed (bottom graph) for typical run of propeller program 5

This figure illustrates that there is an initial current spike as the motor starts moving but then settles to a reasonably steady state value. The propeller rotational speed increases from the stationary value to a maximum value then slowly decreases over the remaining time it is rotating. A ripple in the rotational velocity is visible which is due to inaccuracies of the black and white segmented disc used in the reflective optical sensor system i.e. each segment will be slightly different in size.

The following sections cover the comparison of certain important aspects of the results obtained from the two systems such as the speed achieved by the two systems, the start up transients and the input power requirements. Also, as stated in some of the available literature, speed and power consumption are the best measures of swimming performance [Schultz & Webb, 2002]

5.6.1 Speed Comparisons

Naturally the most significant comparison to be made between the two systems is the speed characteristics in terms of the range of speeds obtainable and the minimum and maximum speeds achievable. The surge velocity results obtained from the ten programs used to characterize the forward motion outlined in Table 5.5 are shown in Figure 5.28.

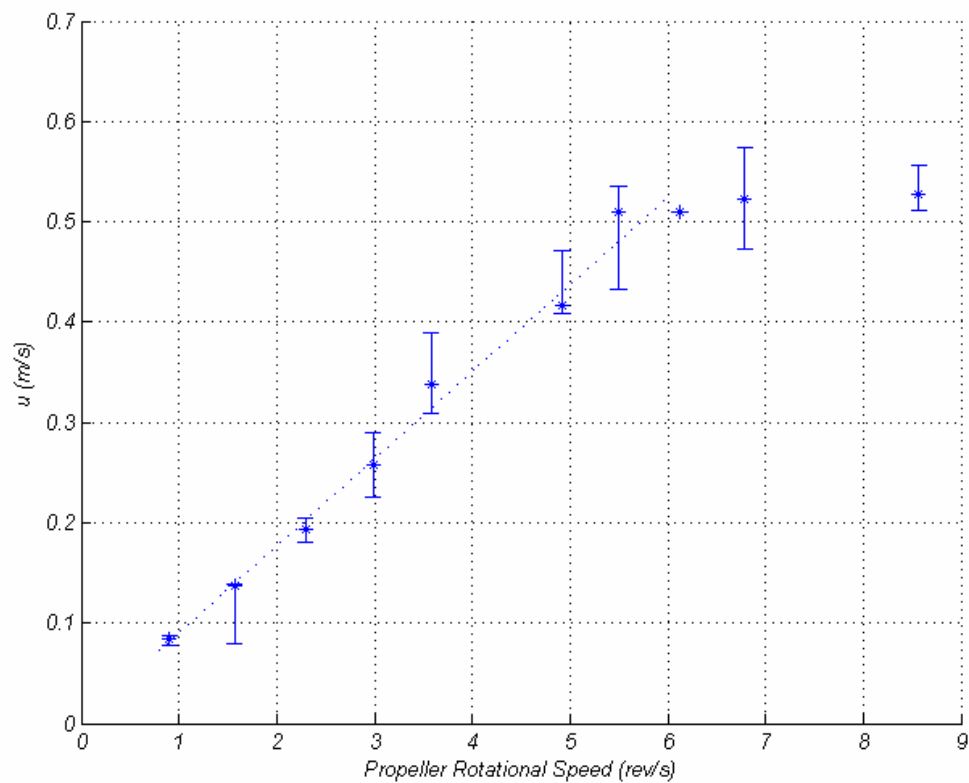


Figure 5.28: Surge velocity versus propeller speed for the propeller based system for forward motion

Figure 5.28 shows that the speed ranges from a maximum value of 0.528ms^{-1} to a minimum of 0.084ms^{-1} . The relationship between the rotational speed of the propeller and the surge velocity appears to be linear over the range up to 5.5 rev/s. After this value any increase in propeller rotational

speed does not have a significant effect on the surge velocity, which plateaus at a steady state value of 0.525 ms^{-1} .

Comparing the velocities of the propeller system to those obtainable with the tendon drive system, shown in Figure 5.4, the propeller system has a maximum velocity of approximately 2.8 times the maximum velocity obtainable with the tendon drive system. However, the tendon drive system is able to produce a minimum velocity of around 0.061 ms^{-1} which is slightly lower than the 0.084 ms^{-1} minimum surge velocity of the propeller system.

5.6.2 Start up transients

As with the tendon drive system one of the dynamic characteristics is the start up transient. The start up transients for programs 2, 3, 4 and 5 are shown in Figure 5.29. When this is compared to the start up transients of the tendon drive system, shown in Figure 5.9, it appears that the propeller based system has a greater start up acceleration.

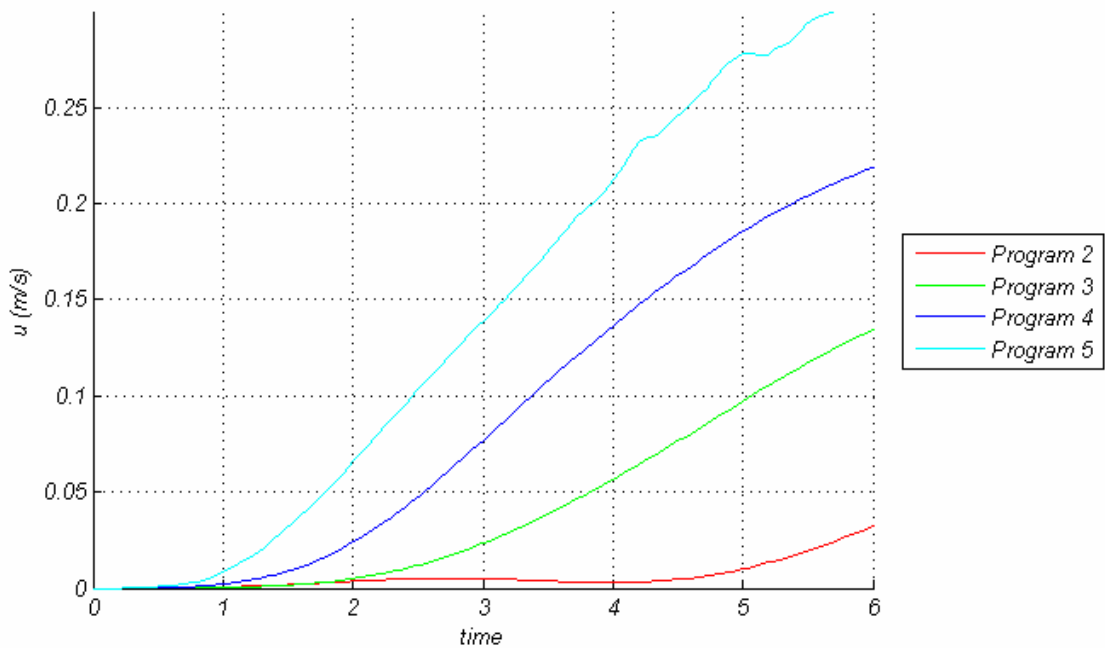


Figure 5.29: Start up transients using program 2, 3, 4 and 5 for propeller based system

One of the most notable aspects of propeller based propulsion system is the roll induced by the propeller [Greer, 2001]. This characteristic is observed when the orientation data for the vehicle is examined. Shown in Figures 5.30, 5.31 and 5.32 is the roll rate, pitch rate and yaw rate respectively for the propeller system for each of the ten programs used when investigating forward motion.

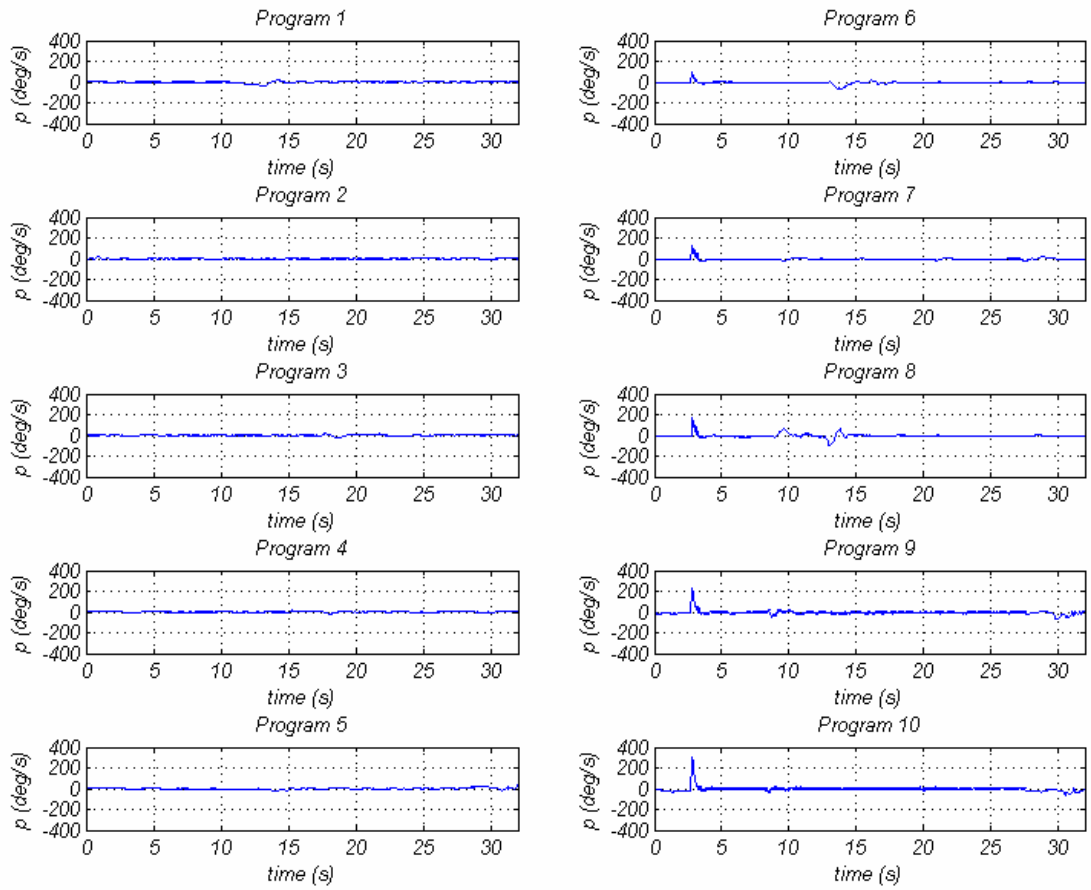


Figure 5.30: Roll rate start up transients for propeller system

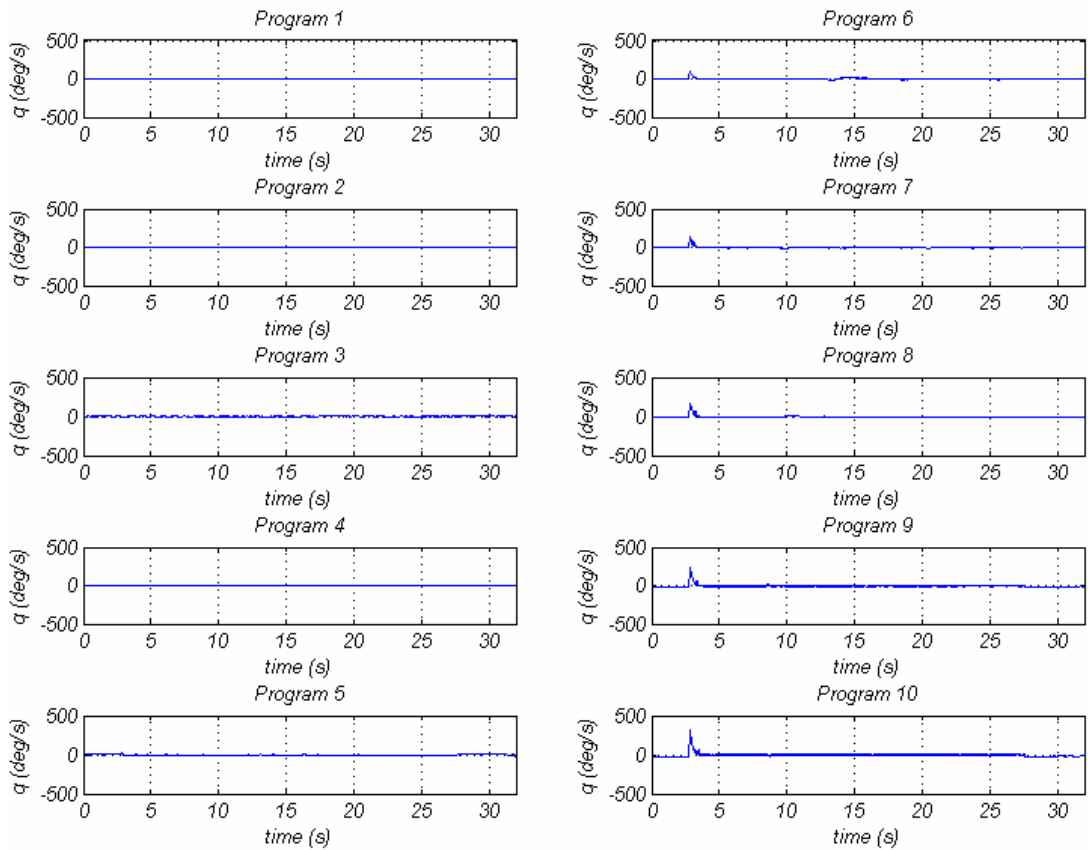


Figure 5.31: Pitch rate start up transients for propeller system

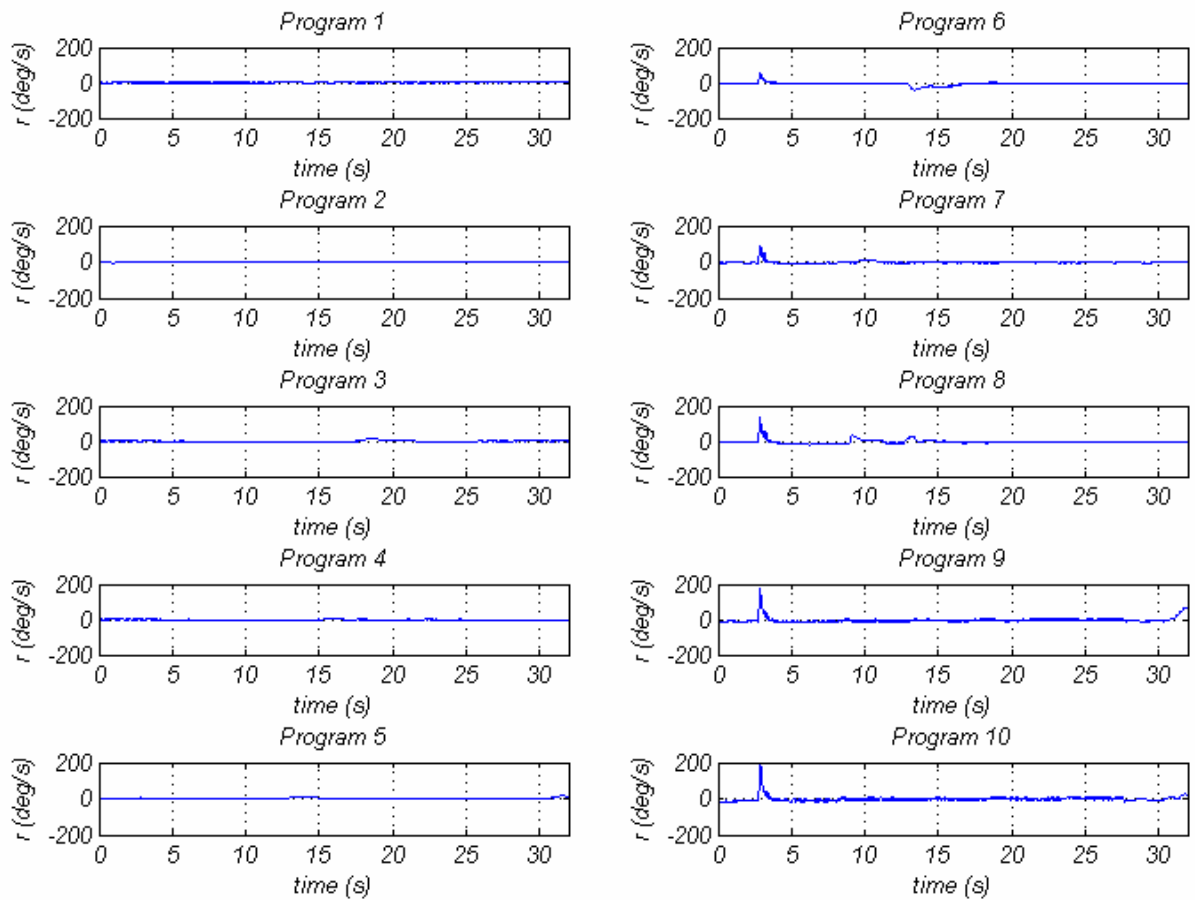


Figure 5.32: Yaw rate start up transients for propeller system

As can be seen in each of the plots in Figures 5.30, 5.31 and 5.32 there is a start up transient at 3 seconds which corresponds to when the propeller starts rotating, the magnitude of which increases with increasing propeller rotational speed (i.e. the program number increases). For program numbers 1-5 for roll, pitch and yaw rates the start up transient is not visible on these plots. However, small amounts of roll are present in all the programs.

When comparing the characteristics of the start up transients of the propeller based system and the tendon drive system one aspect in which they differ is that the transients for the tendon drive system (i.e. the recoil motion) are oscillatory in nature and tend to cancel out over a number of tail beat cycles whereas the transients of the propeller system are in one direction. Propeller based systems compensate for this propeller induced roll effect usually by setting the rudder to a certain deflection during forward motion [Fossen 1994]. One disadvantage of this is that it reduces the operational effectiveness of the vehicle due to the increased drag produced by the rudder deflection [Perez, 2005]. Another method propeller based systems use to negate this effect is to use two propellers each rotating in opposite directions [Tupper, 2004].

5.6.3 Power Comparisons

As mentioned at the start of this section one of the best measures of swimming performance is the power consumption [Schultz & Webb, 2002]. The power consumption for all the experimental programs for the propeller system is shown in Figure 5.33.

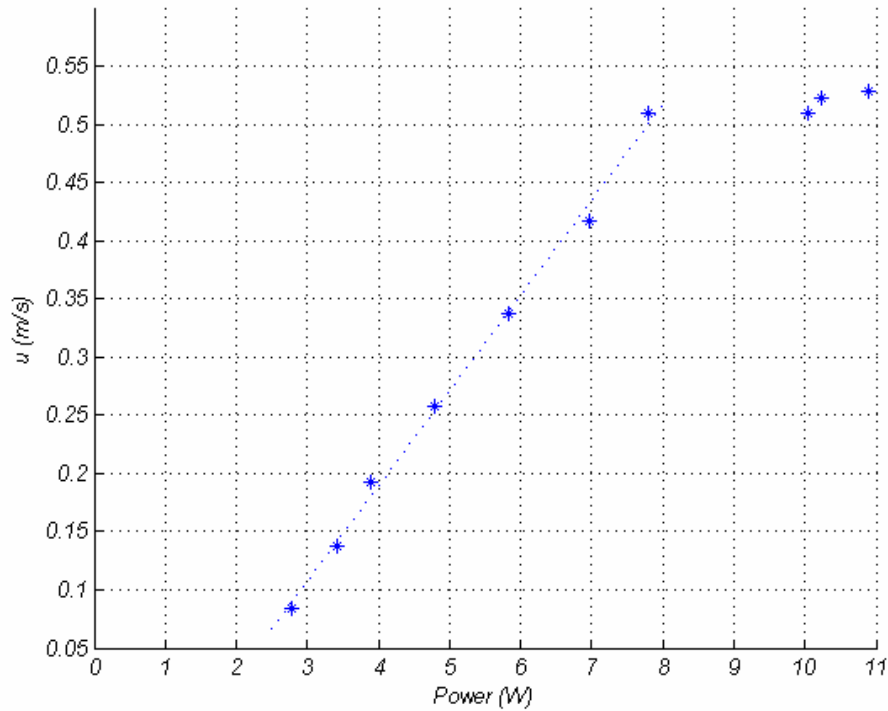


Figure 5.33: Power consumption vs surge velocity for propeller based system

For this comparison only the subset of the experimental programs for the tendon drive system and propeller system which have comparable low speeds are used. Shown in Figure 5.33 is the comparison of the power consumptions for the programs of the propeller and tendon drive system with comparable surge velocities. The graph appears to saturate around 0.52ms^{-1} , which means that for any further increase in power above around 8W no increase in surge velocity will be obtained. This saturation is most likely due to propeller cavitation [Gerr, 2001].

This comparison indicates that for the ranges of surge velocity where the two systems overlap for the lower velocities in this range the power used by the tendon drive system is less than that used by the propeller based system.

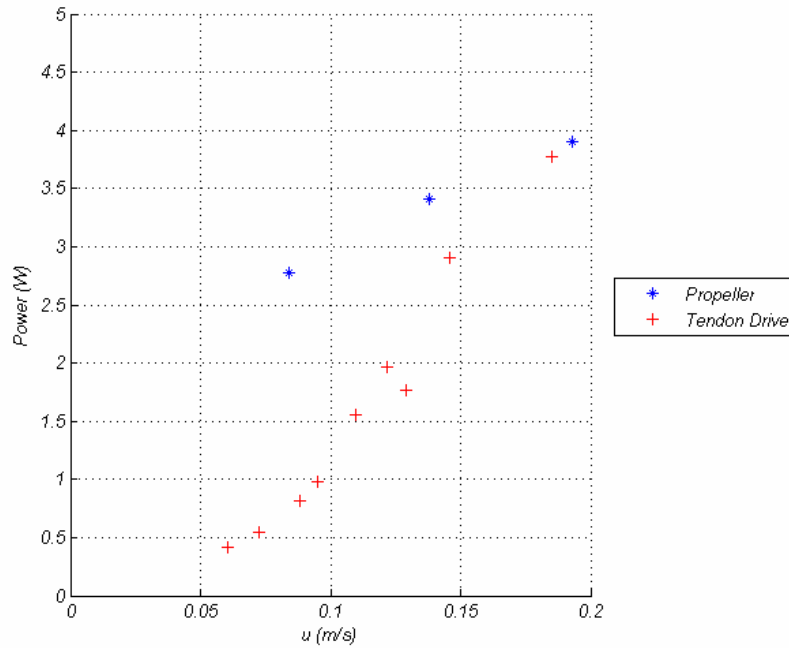


Figure 5.34: Comparison of power consumption of tendon drive system and propeller bases system

The results shown in Figure 5.34 for the power consumption for the tendon drive system and the propeller based system indicate that for the lower surge speeds the tendon drive system uses less power. However, when the surge velocity reaches around 0.18ms^{-1} the power consumptions appear to converge. This is most likely due to the servo motor in the tendon drive system being operated close to its maximum performance at this range.

The above comparison shown in Figure 5.34 has been comparing the input powers to each system versus the surge velocity obtained. Due to the electrical design of the systems they operate from different battery supply voltages, 5V for the tendon drive system and 12V for the propeller system. Therefore, perhaps a better method of comparison is to estimate and then compare the propulsive efficiencies of each system i.e. taking the ratio of useful swimming power to input electrical power. The equation used to calculate this is shown in Equation (5.5) [Sfakiotakis, *et al*, 1999].

$$\eta = \frac{\langle T \rangle u}{\langle P \rangle} \quad (5.5)$$

Where η is the efficiency (%), T is the time averaged thrust (N), u is the surge velocity and P is the time averaged power. The thrust for the tendon drive system is estimated using Lighthill's method [Videler, 1993] described in Chapter 4 and the propeller thrust is estimated from the experimental data gathered from the bollard pull tests. The estimated efficiencies produced by the tendon drive system and the propeller system is shown in Figure 5.35.

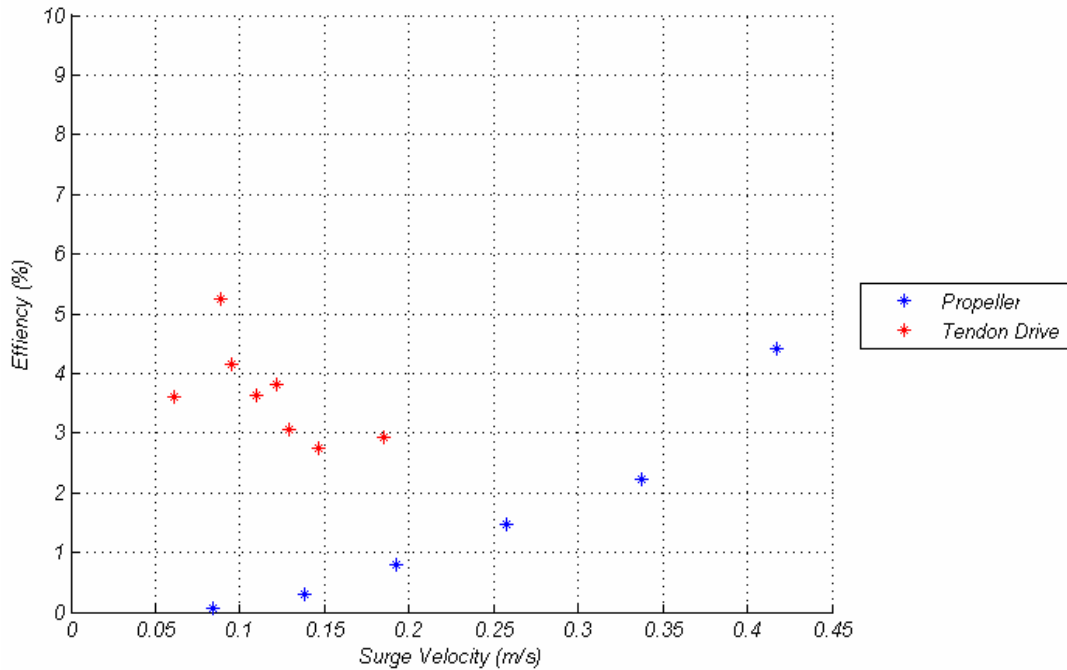


Figure 5.35: Comparison of propulsive efficiencies for the tendon drive system and propeller system for surge motion

This comparison of the efficiencies shows that for the tendon drive system at the maximum only 5% of the input power is converted to useful swimming power. However, for the range of velocities up to 0.2ms^{-1} it can be seen that there is a significant difference in the propulsive efficiencies of the systems. For example at around 0.18ms^{-1} the estimated efficiency for the propeller system is approximately 0.8% whereas for the tendon drive system the value is just under 3%.

This shows that there is an efficiency benefit to be obtained for the biomimetic system over the propeller based system for low surge velocities of less than 0.2ms^{-1} .

5.7 Summary

This Chapter has described the results obtained from the experimentation using the *RoboSalmon* prototype vehicle for studying forward motion. Firstly, the experimental procedure used to obtain the forward motion results has been discussed followed by a description of the range of the various tail beat frequency and amplitude combinations programmed into the *RoboSalmon* to obtain the forward motion results. Next, the results obtained for the surge velocity obtained for the tail beat amplitude and frequency combinations have been presented. This indicates that the greatest surge velocities are achieved for the highest beat frequency and amplitude combination. A comparison has then been made between the surge performance of the *RoboSalmon* vehicle and a real salmon which shows that the performance obtained with the prototype is less than the surge performance of a real salmon by around a factor of three.

Next the Strouhal number has been calculated for each of the surge experiments and this indicated that the ranges of Strouhal number that the *RoboSalmon* obtained during the surge experiments is out with the range quoted for efficient swimming of real fish. This was not unexpected as real fish very rarely swim at the low velocities that the *RoboSalmon* is capable of swimming at and if fish intend to swim at low velocities they would likely use a burst coast swimming method.

The power consumption and swimming power of the tendon drive system have then been compared. There then follows a discussion of the experimental recoil motion which presents results for the recoil in terms of roll, pitch and roll angular rates. Also included in this section is a description of the estimate of the power expended in the recoil motion which suggested that the power expended in the recoil motion is greater than the useful swimming power obtained. The next section covers the experimentation carried out with the actuated head system on the *RoboSalmon* during surge motion. This experimentation involved moving the head both in phase and out of phase with the tail motions and at two different angular amplitudes. Certain combinations of head motion caused the recoil to be increased and in others caused a slight reduction in the yaw recoil.

Finally, there has been a comparison between the tendon drive system and the propeller drive system. The section starts with the characterization of the propeller system in terms of surge performance and start up transients. Then the surge performance of both vehicles have been compared. This shows that the propeller system is capable of a greater surge speed than the tendon drive system, however the lowest speed obtainable is higher than the tendon drive system. The power consumption calculated from the experimental data for each system was then compared. This showed that at speeds less than 0.2ms^{-1} the tendon drive system uses less power for similar surge velocities. The propulsive efficiencies for each system are then estimated using a combination of experimental data and thrust estimates from theory. When these efficiencies are compared it shows that the tendon drive system is more efficient over the range of surge values $<0.2\text{ms}^{-1}$. However, for higher speeds the efficiencies of both systems would appear to converge if the data for the tendon drive system was extrapolated.

Chapter 6 – Results: *Manoeuvring*

6.1 Introduction

The previous Chapter has described and discussed the characteristics of the *RoboSalmon* vehicle for forward propulsion. Another important aspect of the propulsion characteristics for any vehicle is its manoeuvrability, which in naval architecture is defined as the ability of a ship to respond to its rudder and steer to a course [Tupper, 2004]. This aspect of the propulsion for a vehicle is important as it affects the handling performance of the vehicle and can limit the applications that the vehicle can be utilized for. Manoeuvrability in marine vehicles is usually measured by using a number of specific manoeuvres defined by the International Towing Tank Conference (ITTC) and International Maritime Organisation (IMO) [Fossen, 2002].

The *RoboSalmon* vehicle does not have a rudder but instead uses its tail for manoeuvring. This Chapter covers the experimental results obtained from the *RoboSalmon* vehicle utilising the tendon drive propulsion system during manoeuvring trials. The manoeuvring trials consist of a number of experiments to determine the manoeuvring performance of the vehicle when turning from stationary, the effects of turning at speed and coasted turns with the tail offset but not oscillating.

Manoeuvring with the actuated head is also investigated to ascertain if any benefits can be obtained using this system. Trials have been conducted with the actuated head angled and no tail offset to determine if the head alone can be used for turning. In addition, the effect of the head angled at specific deflections with the tail at various offsets is described in this Chapter.

The final part of this Chapter is concerned with a manoeuvring comparison between the tail and propeller based systems. A similar set of experimental trials have been carried out with the propeller and rudder based system to allow for a comparison between the two systems.

6.2 Experimental Approach

The manoeuvring capability of a marine vessel can be evaluated through the implementation of a series of standard manoeuvres, which have been set out by the ITTC and the IMO. These manoeuvres are described below -

6.2.1 Standard Turns

Standard turns are not covered specifically by the tests set out by the ITTC and IMO but have been included here as a test of the turning rates obtained for specific turning commands.

6.2.2 Turning Circle

This test is used to evaluate a vehicle steady turning radius and to determine how well the steering machine performs when course changing [Fossen, 2002]. The manoeuvre is carried out by changing the rudder angle when at a steady test speed with zero yaw rate and allowing a full turn of 360° in yaw to be achieved. The information that can be obtained from this manoeuvre is the *tactical diameter*, *advance* and *transfer* [IMO, 2002]. The *tactical diameter* is the lateral distance it takes for the vehicle to complete a 180° change of heading, the *advance* is the forward distance it takes for a 90° change of heading and the *transfer* is lateral distance it takes for a 90° change of heading [Fossen, 1995]. These parameters are indicated in Figure 6.1.

Figure image has been removed due to Copyright restrictions

Figure 6.1: Illustration of parameters calculated during *Turning Circle* manoeuvre [Fossen, 2002]

6.2.3 Zig-Zag

The *Zig-Zag* manoeuvre is conducted by first bringing the vehicle to a steady course and speed then commanding the rudder to a specific angle, such as $+20^\circ$. When the heading has changed by 20° the rudder is then commanded to -20° , and the vehicle allowed to turn until it reaches a heading of -20° . The process is then repeated a minimum of two times. This process described is called a 20-20 Zig-Zag where the first number denotes the rudder change and the second denotes the heading change [Fossen, 2002].

6.2.4 Pull Out Manoeuvre

The purpose of the Pull Out manoeuvre is to determine if the vehicle is straight line stable and involves the vehicle applying a 20° rudder angle, from a steady course, until a constant rate of turn has been achieved then returning the rudder to its zero position.

6.2.5 Stopping Test

The stopping test is used to determine how far the vehicle travels when a command for full astern is given [IMO, 2002].

6.2.6 Spiral Manoeuvre

The spiral manoeuvre is used to determine the degree of straight line stability of the vehicle. It is conducted by the vehicle first obtaining a steady course and then a 25° rudder angle to port is implemented until a steady yawing rate is obtained. Once this steady rate has been obtained the rudder angle is then decreased in steps of 5° with a constant yaw rate being obtained between steps. This is performed for rudder angle steps between 25° port and 25° to starboard.

A subset of these manoeuvres has been selected to test the *RoboSalmon* vehicle hardware. This selection has been determined by considering which manoeuvres are suitable and achievable with the experimental constraints imposed on this study. Therefore, the only manoeuvres which have been considered are standard turns, the turning circle and the pull-out manoeuvre [Fossen, 2002]. The experimental implementation of these manoeuvring performance tests is outlined below.

The experimental procedure used for the manoeuvring trials is similar to the procedure used for the forward motion experiments described in Section 5.2. For the manoeuvring trials, 58 experimental programs have been developed to investigate the manoeuvring performance of the tendon drive system. A further 22 have been developed to investigate the effect of the tendon drive tail and actuated head system operating together.

From all the experimental data obtained from the manoeuvring trails the main parameters that are used in this Chapter to evaluate the manoeuvring performance are; the yaw rate data obtained from the onboard sensor, the yaw angle obtained from the post processing of the sensor data and the x-y trajectory data obtained from the processing of the video footage.

6.3 Standard Turning

The purpose of the standard turning series of experiments is to characterise the turning performance of the vehicle in terms of yaw rate varied with different tail parameters such as beat frequency, beat amplitude and the offset of the tail centreline. This standard turning has been evaluated using two types of test; turning from stationary and turning at speed.

For the standard turning series of experiments the initial starting location of the vehicle has been positioned with the red spot on the back of *RoboSalmon* just in the field of view of the camera and close to one side of the pool. This allows the maximum turning motion to be observed for the experimental set up used in this study.

6.3.1 Turning from Stationary

The first set of experimental programs carried out as part of the manoeuvring trials covered the turning performance of the *RoboSalmon* when turning from a stationary position. This is a simple manoeuvre to study as it involves the vehicle starting from a stationary position in the field of view of the camera.

A typical run of program 32 and 46 is presented in this section. These programs have the same tail beat frequency and amplitude but program 32 has $+25^\circ$ tail offset and program 46 has -25° offset. Shown below in Figures 6.2 to 6.6 is the relevant data obtained for the two manoeuvres. Firstly Figure 6.2 shows the x-y positional data obtained for both manoeuvres from the image processing of the camera footage.

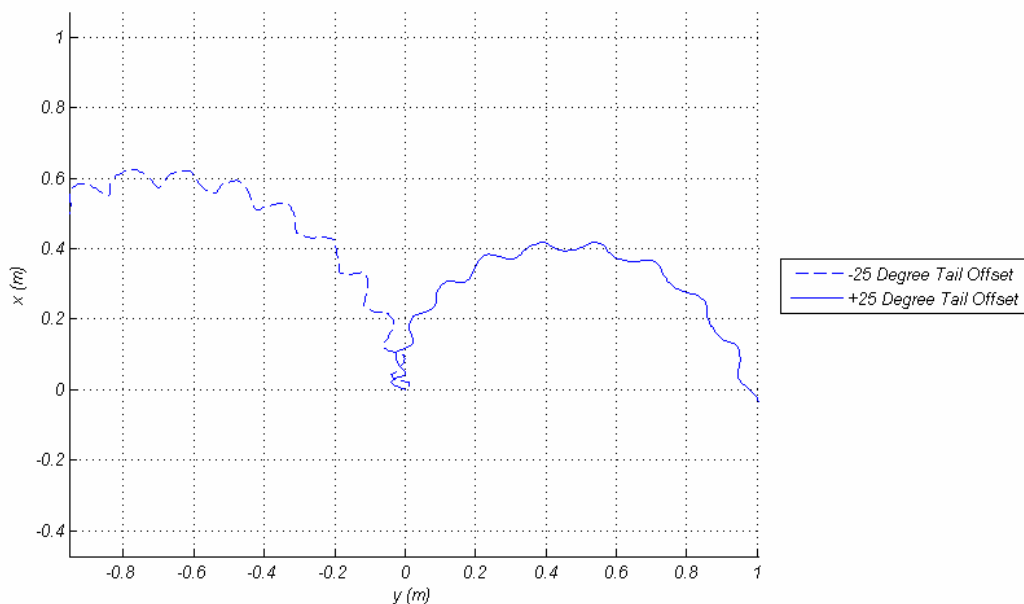


Figure 6.2: x-y positional data for typical runs with beat amplitude 0.105m and beat frequency of 0.61Hz and -25° tail centreline offset (dashed plot) and 25° offset (solid line) obtained from image processing captured video footage.

From this it is clear to see that the manoeuvres for positive and negative tail are not symmetrical as the trajectory of the $+25$ degree tail offset has more of the turn visible. The reason for this asymmetry is due to reasons stemming from the construction of the vehicle. Firstly, there may be imperfections in the hull of the vehicle which contribute to this asymmetry when turning. Secondly, as discussed in Chapter 3 there can be slight differences in the tensions of the tendon wires within the tendon drive tail system which, even when the tail is calibrated out of water, will also add to the asymmetry. In order to

see this asymmetry in more detail the corresponding yaw rate for the manoeuvres is shown in Figure 6.3.

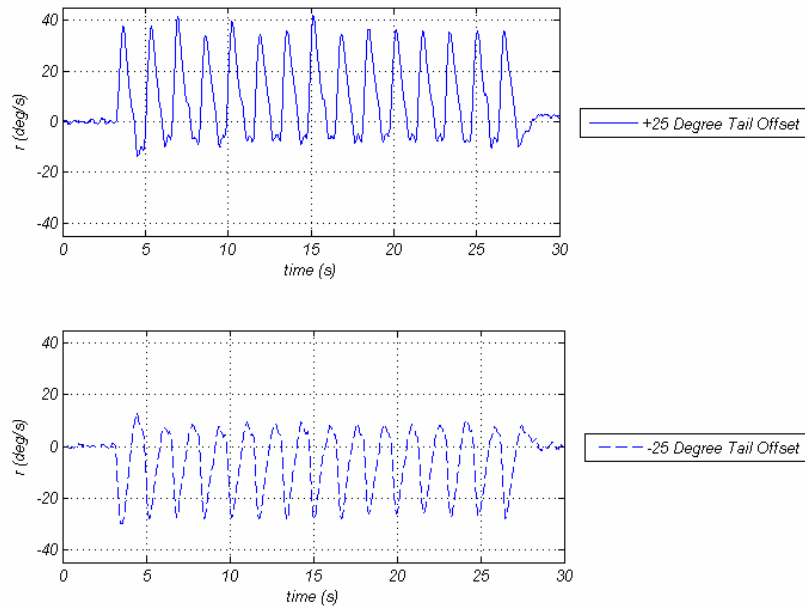


Figure 6.3: Yaw rate data for typical runs with beat amplitude 0.105m and beat frequency of 0.61Hz and -25° tail centreline offset (dashed plot) and 25° offset (solid line) obtained from onboard sensors.

The reason for the asymmetry in the trajectories in Figure 6.2 can be seen when comparing the yaw rates as they indicate that a positive tail offset produces a greater peak value for yaw rate of around 40 deg/s whereas the negative offset has a peak yaw rate of just under 35 deg/s. To see how this difference in yaw rates translates to actual yaw angle, the yaw angles obtained are presented in Figure 6.4.

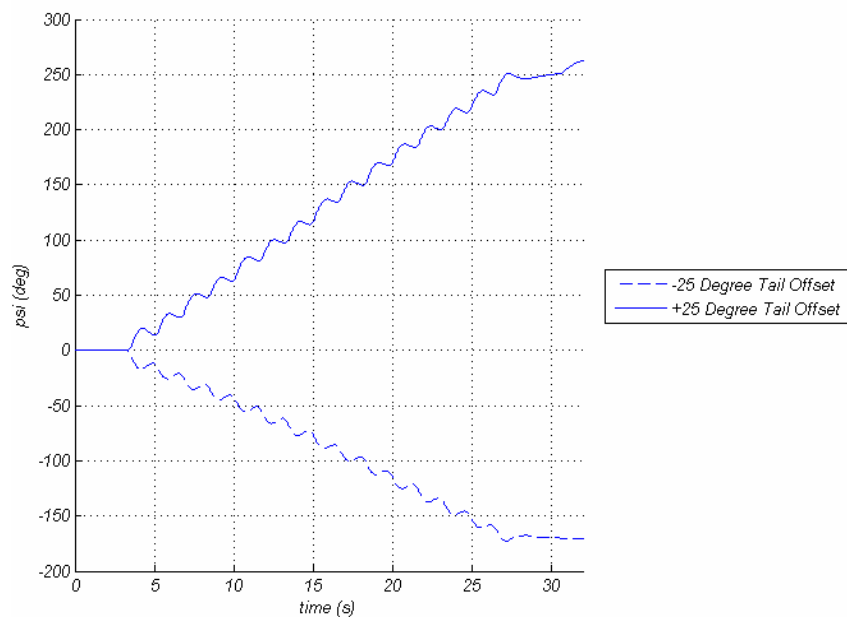


Figure 6.4: Yaw angle data for typical runs with beat amplitude 0.105m and beat frequency of 0.61Hz and -25° tail centreline offset (dashed plot) and 25° offset (solid line).

From the yaw angles of Figure 6.4 the maximum yaw angle obtained for the positive tail offset before tail oscillations ceased at 28 seconds is around 250° but for the negative offset the maximum yaw angle obtained is 175° . These maximum turning angles are not visible on the trajectory data shown in Figure 6.2 as the field of view of the camera limits the amount of the turn that can be captured. However, the yaw rate data is obtained from gyros onboard the vehicle and so the yaw rate over the full run can be captured.

Also of interest are the roll rates and roll angles obtained from the trials. Shown in Figure 6.5 below is the roll rate data for the two manoeuvres which indicate that peak roll rate for the negative offset is greater than for the positive offset. This is the opposite for the yaw rates as the positive tail offset obtained the highest peak yaw value.

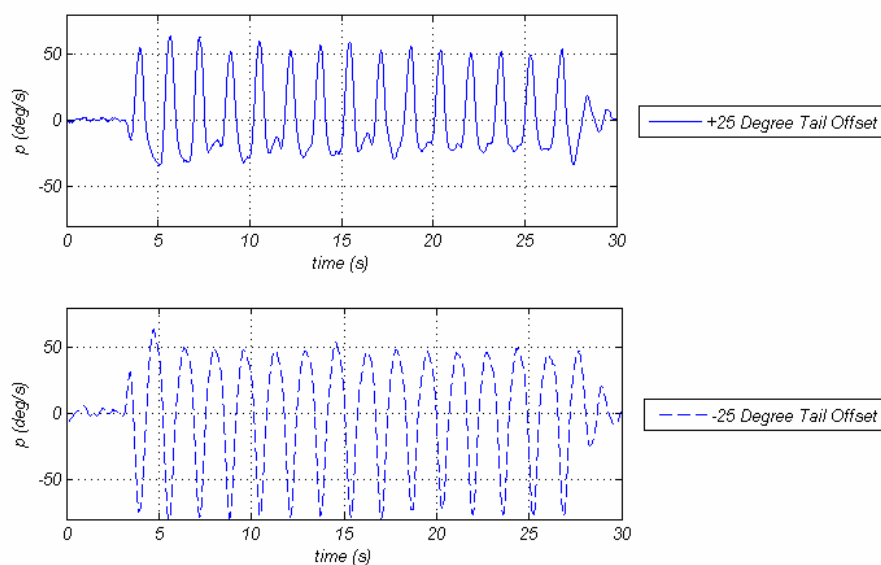


Figure 6.5: Roll rate data for typical runs with beat amplitude 0.105m and beat frequency of 0.61Hz and -25° tail centreline offset (dashed plot) and 25° offset (solid line) obtained from onboard sensors.

The roll angles obtained from post processing of the roll rate data is shown in Figure 6.6. This shows that when turning the *RoboSalmon* still oscillates in roll but the roll is increased in the direction of the turn.

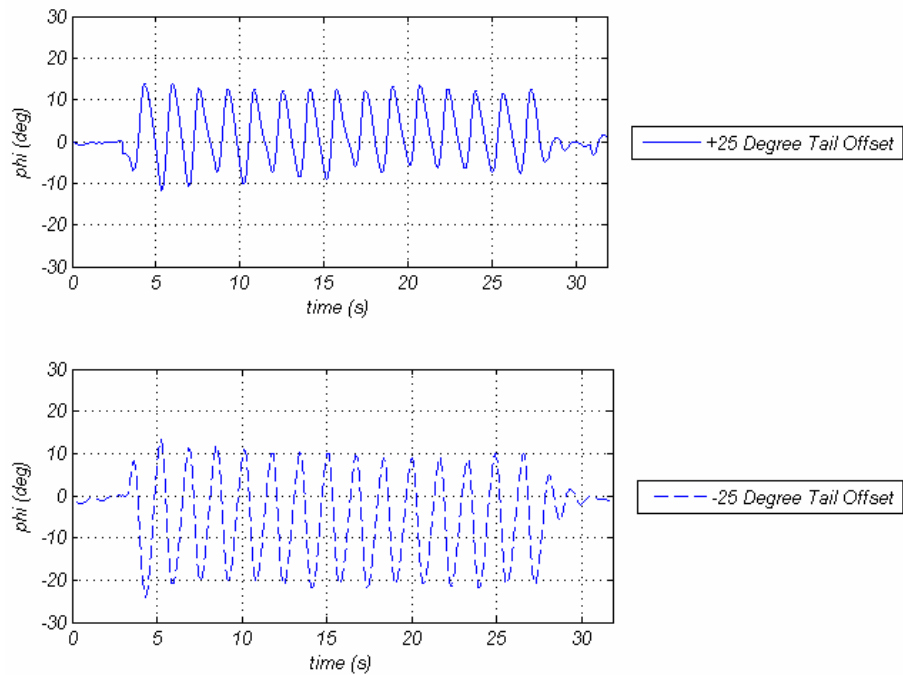


Figure 6.6: Roll angle data for typical runs with beat amplitude 0.105m and beat frequency of 0.61Hz and -25° tail centreline offset (dashed plot) and 25° offset (solid line).

The graphs presented so far in this section have shown the response characteristics of the turning from stationary manoeuvres. As with the results for the forward motion experiments, the recoil motion is prominent in all aspects of the turning manoeuvres shown in Figures 6.2 to 6.6 and presents itself as an oscillation about a mean value on all the logged sensor data. When the positive and negative offsets are compared it is apparent that there is asymmetry present in the responses with greater turning achieved for the positive offset.

The example turning from stationary manoeuvre described above and shown in Figures 6.2 to 6.4 gives an indication to the characteristic of this type of manoeuvre. However, numerous trials for turning from stationary manoeuvres have been conducted that consisted of a series of experimental programs with varying tail beat amplitude, tail beat frequency and tail centreline offset. The results for these turning from stationary manoeuvres for the average roll and yaw rates for different tail beat frequencies, tail beat amplitudes and tail offsets are shown in Table 6.1. The yaw and roll rates are averaged over three tail beat cycles in post processing, to compensate for the effects of the recoil motion. The yaw rate time constant is the time taken for the yaw response to reach 63% of its steady-state value.

Table 6.1: Yaw and roll rates for turning from stationary manoeuvre

Tail Beat Amplitude (m)	Tail Beat Freq (Hz)	Offset Angle (Deg)	Average Yaw Rate (Deg/s)	Average Roll Rate (Deg/s)	Yaw Rate Time Constant
0.075	0.61	-5	-0.09	0.004	9.03
0.075	0.61	-12	-0.77	0.3405	6.96
0.075	0.61	-16	-1.93	0.28	4.97
0.075	0.61	-25	-4.41	-0.17	3.37
0.075	0.47	-5	-0.79	0.14	7.72
0.075	0.47	-12	-1.59	0.59	6.50
0.075	0.47	-16	-2.84	-0.27	5.57
0.075	0.47	-25	-4.86	-0.21	4.41
0.105	0.61	-5	-3.05	-0.14	5.55
0.105	0.61	-12	-4.39	0.09	4.71
0.105	0.61	-16	-5.34	-0.72	2.45
0.105	0.61	-25	-6.23	0.328	2.84
0.105	0.47	-5	-1.49	-0.76	5.34
0.105	0.47	-12	-3.97	0.2653	3.22
0.105	0.47	-16	-6.82	-0.08	3.95
0.105	0.47	-25	-7.38	0.29	4.8
0.15	0.61	-5	-1.8	-0.92	4.88
0.15	0.61	-12	-4.23	-1.5	4.35
0.15	0.61	-16	-5.24	-0.16	2.13
0.15	0.61	-25	-8.62	-0.45	1.73
0.075	0.61	12	2.63	0.43	2.72
0.075	0.61	25	3.44	0.41	1.43
0.075	0.47	12	3.26	-0.31	4.53
0.075	0.47	25	4.02	0.36	3.21
0.105	0.61	12	6.41	0.38	2.88
0.105	0.61	25	9.82	0.73	2.51
0.105	0.47	12	5.76	0.79	4.57
0.105	0.47	25	8.56	0.31	3.46
0.15	0.61	12	11.09	-0.31	2.41
0.15	0.61	25	12.27	0.17	1.98

From the results shown in Table 6.1 it can be seen that as the tail offset angle increases, the average yaw rate increases for any particular beat amplitude and frequency combination. Another interesting aspect is the relatively low average roll rates which are due to the averaging of the recoil induced oscillations in roll rate data. From observations of the *RoboSalmon* completing this trial it is apparent that, although the vehicle rolls, it does tend to return to the same angular roll position when the tail is at its centre position which correlates with the low average roll rate obtained.

In order to compare the yaw rates obtainable from the various tail beat parameters described in Table 6.1 the yaw rates and corresponding tail offsets are shown in Figure 6.7. This information is presented in the standard way that yaw rates and rudder angles are presented for ships.

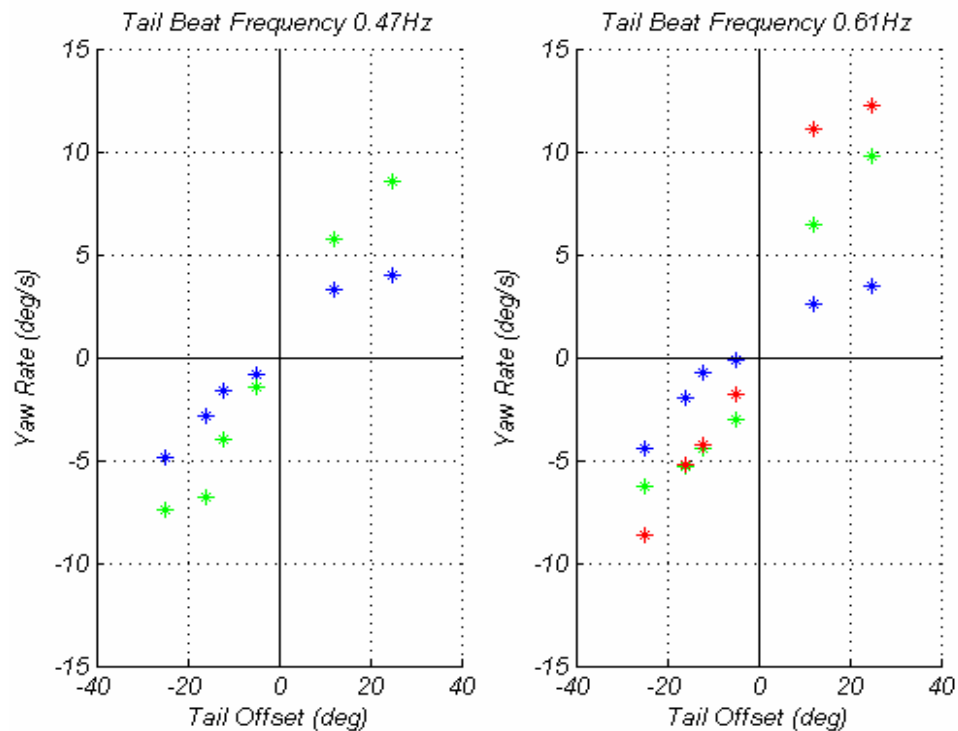


Figure 6.7: Relationship between yaw rates and tail beat frequency and amplitude. Blue points denote tail beat amplitude of 0.075m, green points 0.105m and red points 0.15m.

The results from Figure 6.7 highlight that the turning performance of the tendon drive system is not symmetrical. This can be seen for similar tail beat parameters but the opposite offset direction. There are a number of factors which contribute to this asymmetry such as the mechanics of the tendon drive tail system which leads to small differences during each tail beat due to the under-actuated nature of the tail system. These small differences could effectively present themselves as a built in tail offset. Another factor is the manufacture of the body section which may lead to slight imbalances in weight and buoyancy distribution. These slight imbalances could lead to the slight differences in the positive and negative roll moments produced by the recoil motion which in turn could contribute to the asymmetry in the turning performance.

6.3.2 Turning at Speed

The next set of experiments carried out evaluates the turning performance of the *RoboSalmon* when turning from a steady speed. In order to carry out this set of experimental trials the *RoboSalmon* has to start the manoeuvre out with the field of view of the camera. This is required so that the vehicle can obtain a steady speed before entering the field of view and so that the point at which turning starts is captured on the video footage. The *RoboSalmon* has been programmed to swim in a straight line for 8 seconds before adding an offset to the tail centreline.

Trajectories from two experimental trials for the turning at speed manoeuvre are shown in Figure 6.8.

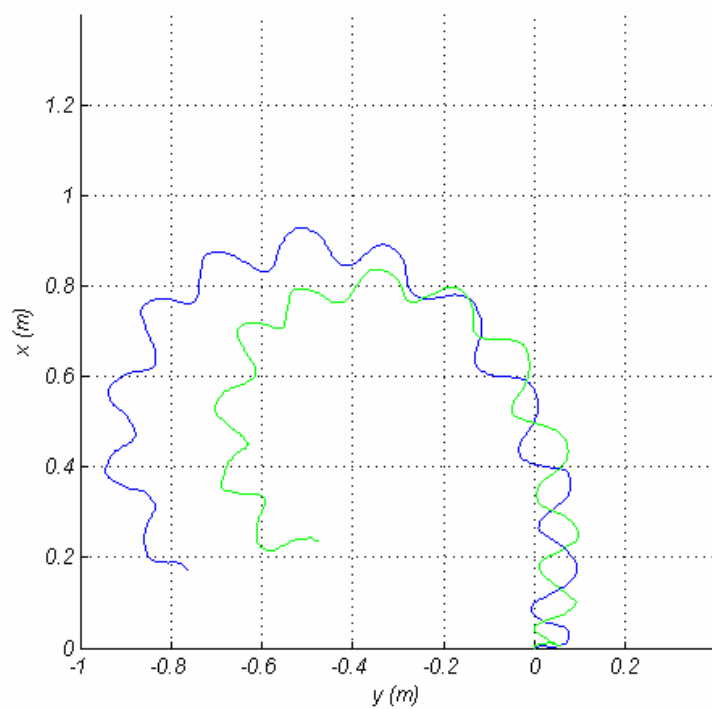


Figure 6.8: X-Y trajectory turning at speed manoeuvre for tail beat amplitude of 0.15m at beat frequency of 0.48Hz for tail offset of -12° (blue line) and -16° (green line)

From the x-y trajectory shown in both manoeuvres the *RoboSalmon* travels forward approximately 0.4 m before the turning starts. Then from the partial turning circles visible for each of the two tail offsets, as expected the larger offset (green line) has the smaller turning circle. The corresponding yaw rates for the manoeuvre are shown in Figure 6.9.

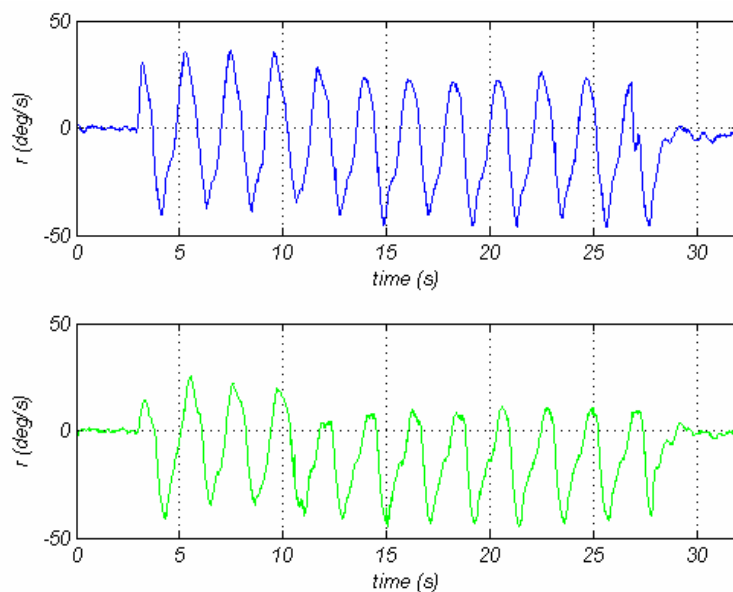


Figure 6.9: Turning at speed manoeuvre yaw rates for tail beat amplitude of 0.15m at beat frequency of 0.48Hz for tail offset of 12° (blue line) and 16° (green line)

These plots of the yaw rates clearly indicate the effect that implementing a tail offset after a period of forward swimming. The vehicle starts moving after 3 seconds then continues forward for 8 seconds with a beat amplitude of 0.15m and a beat frequency of 0.48Hz. Then at time 11 seconds the tail offset is implemented which results in the mean value of the yaw oscillations moving to a steady yaw rate. The values from the time averaged yaw rates obtained from these experiments are shown in Table 6.2.

Table 6.2: Tail parameters and yaw rates for turning at speed manoeuvre

Amplitude (m)	Frequency (Hz)	Tail Offset Angle (deg)	Average Yaw Rate (deg/s)	Yaw Rate Time Constant
0.15	0.48	-12	-8.20	2.11
0.15	0.48	-16	-12.15	1.95
0.15	0.48	-25	-14.11	-

The time averaged yaw rates obtained show that when compared to the turning from stationary manoeuvre that there is an increase in the yaw rate when turning at speed. In order to visualise the actual turning angle obtained the yaw angles for each experiment are shown in Figure 6.10.

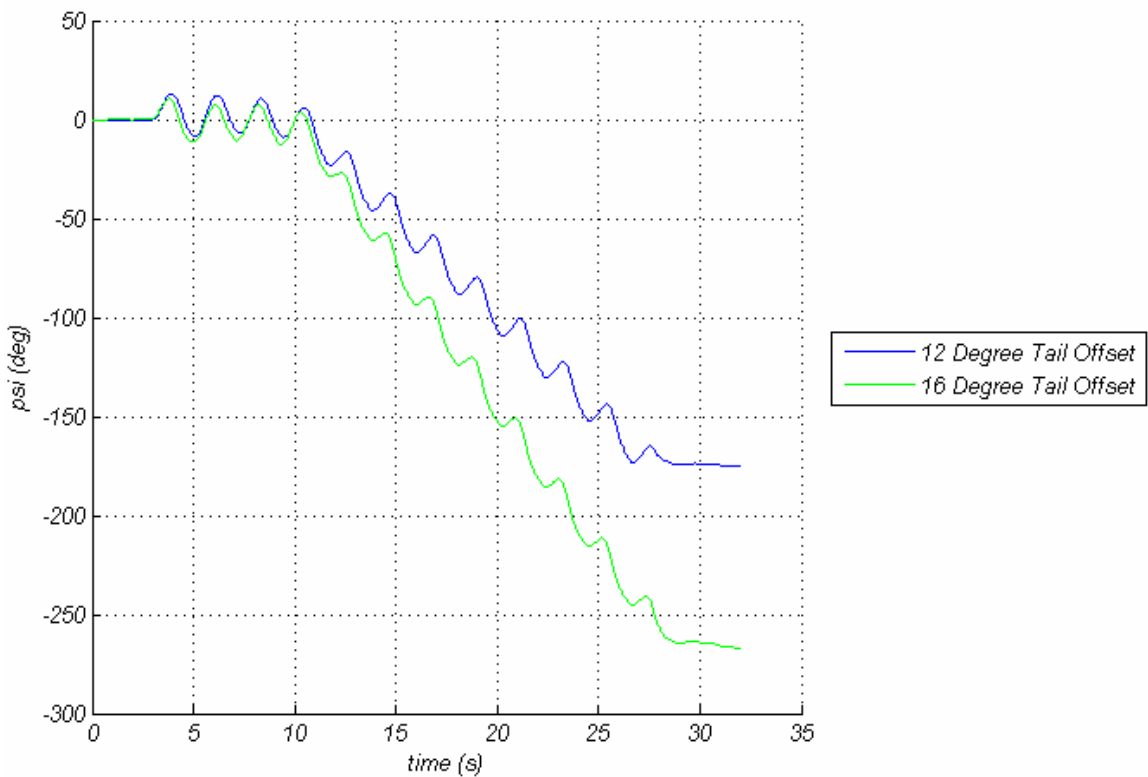


Figure 6.10: Yaw angle for turning at speed manoeuvre

The yaw angles shown in Figure 6.10 reinforce the concept that the greater the tail offset the larger the yaw angle obtained.

6.3.3 Coasted Turns

As discussed briefly in Chapter 3 and Chapter 5 fish use their tail in different ways to obtain a forward propulsive force or to manoeuvre. One tactic fish can employ is coasting to reduce the energy cost of swimming [Videler, 1993]. This section covers the experimental trials of the *RoboSalmon* vehicle carrying out coasted turns.

In a coasted turn the vehicle swims forward for a period of 8 seconds to obtain a sufficient surge velocity, then the tail oscillation is stopped with a constant tail offset is maintained for 17 seconds. At the end of this period the tail returns to its centre position. A selection of results showing the x-y positional data for coasted turns using three tail offsets is shown in Figure 6.11.

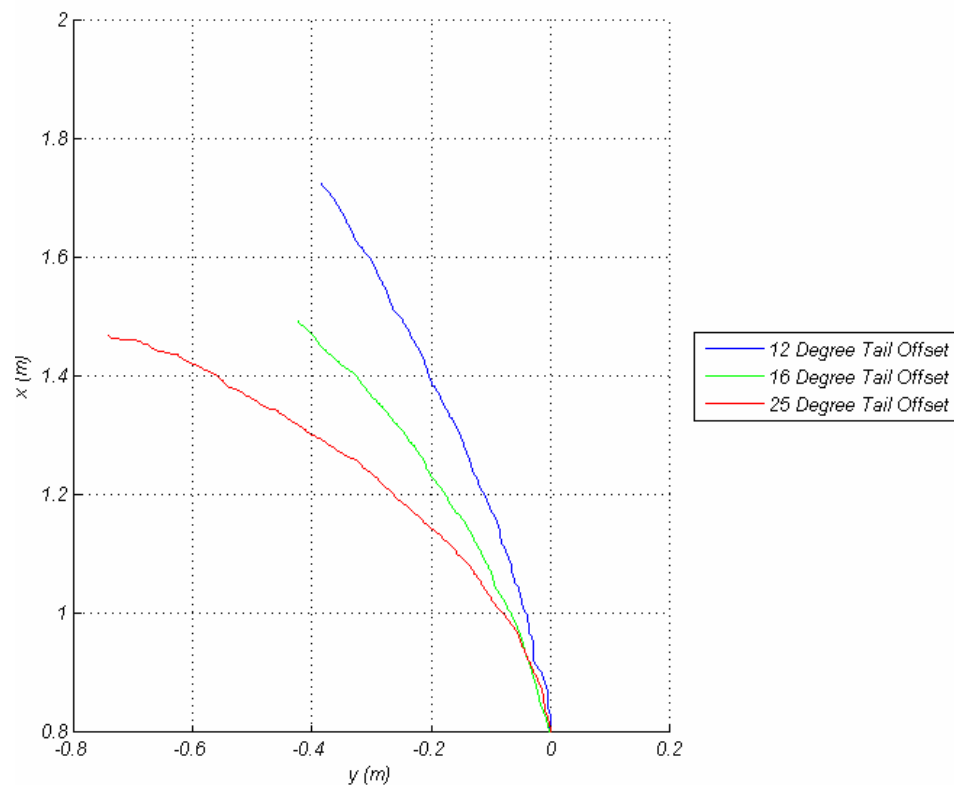


Figure 6.11: X-Y positional data for coasted turns with three offsets with initial tail beat frequency of 0.48Hz and nominal beat amplitude of 0.15m

This plot shows that implementing a steady tail offset with no tail oscillations after a period of straight swimming allows turning to be achieved. It also shows that the greater the tail offset the sharper the turn is completed.

The yaw rate data obtained for the same three coasted turns is shown in Figure 6.12.

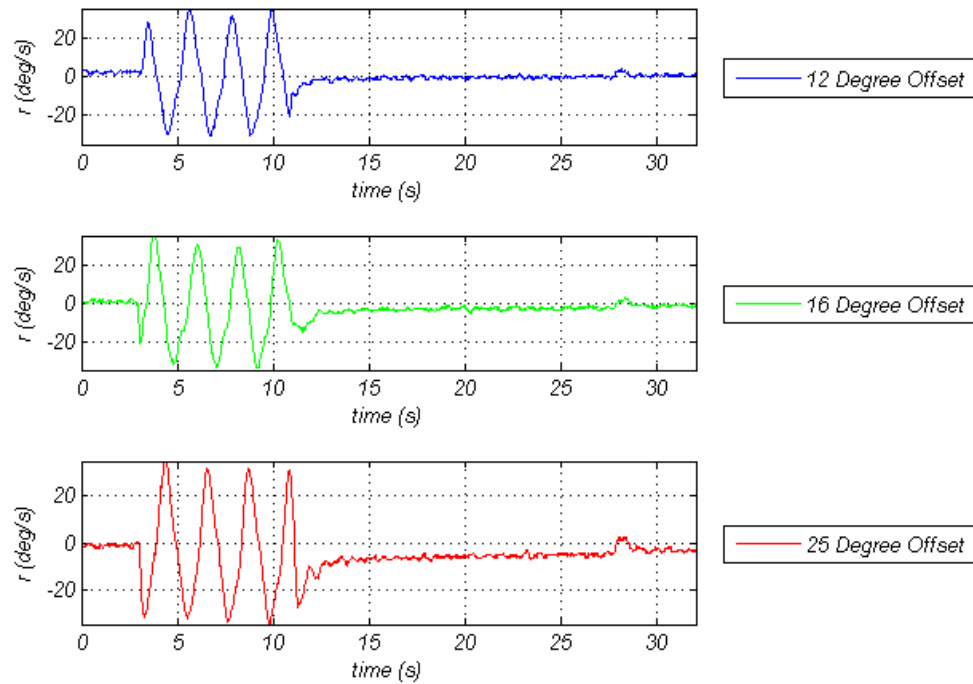


Figure 6.12: Yaw rate data for coasted turns for three tail offsets

The yaw rate data shown in Figure 6.12 illustrates that the vehicle swims forward from a stationary position for 3 seconds. Tail oscillations stop at 12 seconds with a constant tail offset implemented. The *RoboSalmon* then carries out a coasted turn until 28 seconds when the tail is set back to its centre position. From the yaw rate data presented it is apparent that during the coasting part of the manoeuvre (12-28 seconds) the yaw rate is greatest for the largest tail offset.

These results obtained for the coasted turn experimental trials shown in Figures 6.11 and 6.12 show that this method of manoeuvring is a feasible way to carry out a low speed turn. One advantage of this type of turn is that during the coasted part of the manoeuvre there is no recoil motion present. Another benefit of this method of turning is that the power consumption is reduced when compared to that of a powered turn. This aspect is highlighted in the current consumptions shown in Figure 6.13 (quiescent current has been removed for comparison).

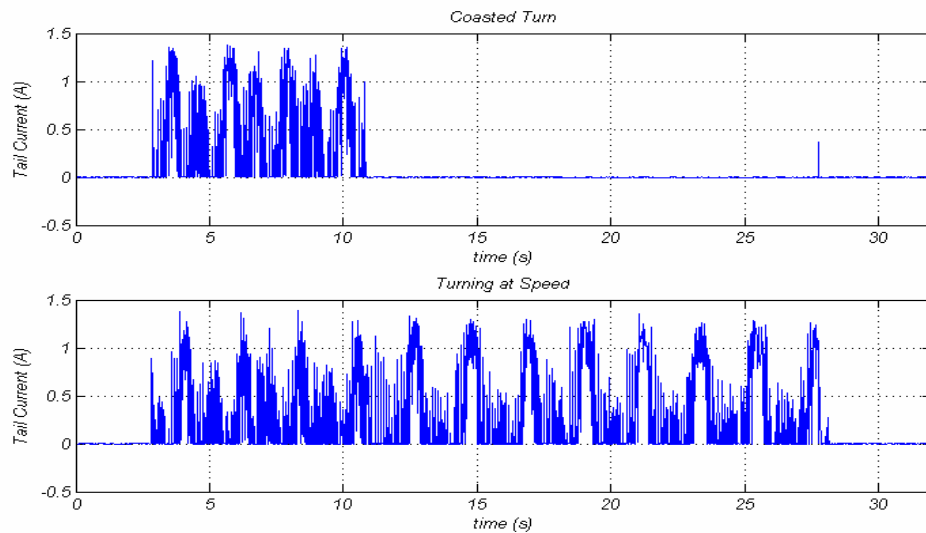


Figure 6.13: Current consumption for coasted turn (top) and for turning at speed manoeuvre (bottom)

For the coasted turn the current consumption is reduced to almost zero when the tail oscillations stop and coasting commences at 12 seconds. On the plot for the coasted turn there is a spike in the current at 28 seconds which corresponds to the servo motor bring the tail back to its centre position. The current drawn during coasting in theory should only be the holding current drawn by the servo motor to hold its commanded offset position. However, for the powered turn the current consumption is greater as tail oscillations are used for turning. Also, with the powered turns manoeuvres will be able to be conducted in less time when compared to using coasted turns due to the higher yaw rates obtainable.

6.4 Actuated Head

As discussed in Chapter 3 and Chapter 5, *RoboSalmon* is equipped with a fully actuated head section. For forward propulsion the actuated head has been used to compensate for the recoil motion produced by the tendon drive propulsion system with limited success. However, this mechanism can provide apparent benefits for turning manoeuvres.

Two types of experiments have been carried out with the actuated head system. The first involves manoeuvring with an offset in the actuated head system and no offset on the tendon drive tail and the other involved an offset in the actuated head system and a complementary offset in the tendon drive propulsion system. Both these manoeuvres are investigated in this section.

6.4.1 Actuated Head Only Turning

A number of experiments have been carried out to determine if the actuated head can be used for manoeuvring. These trials involved utilising the tendon drive tail system with no offset at beat amplitudes of 0.105m and 0.15m with a beat frequency of 0.48Hz. The results are shown in Figure

6.14, which presents the trajectories of the *RoboSalmon* during 4 experimental trials with head only turning.

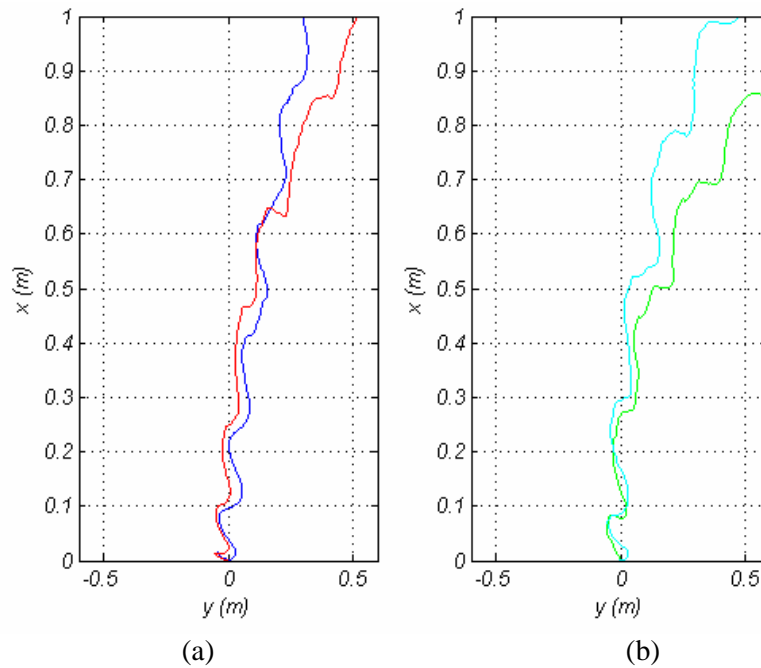


Figure 6.14: X-Y positional data for (a) Turning with head angled at 13.5° (blue) and 27° (red) at tail beat frequency of 0.48Hz and beat amplitude of 0.105m (b) Turning with head angled at 13.5° (cyan) and 27° (green) at tail beat frequency of 0.48Hz and beat amplitude of 0.15m

These results show that it is possible to use an offset on the head for manoeuvring. The yaw rates for the head only turning are shown in Figures 6.15 and a table with the time averaged yaw rates for each trial is shown in Table 6.3.

Table 6.3: Average yaw rates from head only turning

Actuated Head Angle (degrees)	Nominal Tail Beat Amplitude (m)	Average Yaw Rate (deg/s)
13.5	0.105	0.689
27	0.105	2.23
13.5	0.150	1.22
27	0.150	6.32

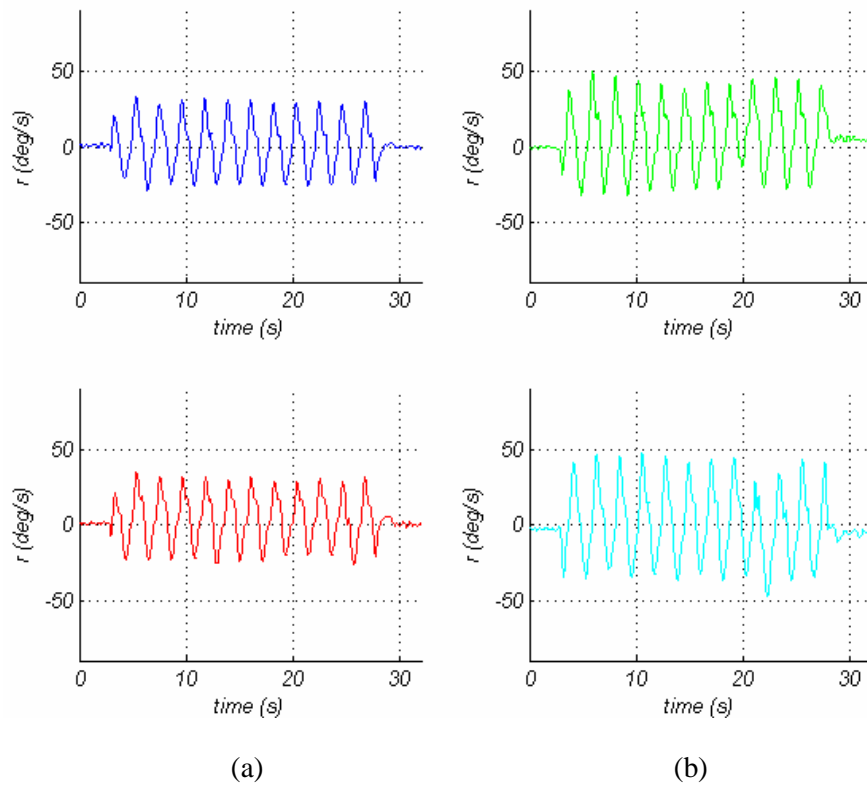


Figure 6.15: Yaw rate data for (a) Turning with head angled at 13.5° (blue) and 27° (red) at tail beat frequency of 0.48Hz and beat amplitude of 0.105m (b) Turning with head angled at 13.5° (cyan) and 27° (green) at tail beat frequency of 0.48Hz and beat amplitude of 0.15m

The yaw rate responses shown in Figure 6.15 highlight the turning aspects of the head only turning. As expected the peak amplitudes for the yaw recoil oscillations in the plots for the 0.15m tail beat amplitudes are greater than the 0.105m nominal beat amplitudes. It is also possible to observe that the average value of the recoil oscillations is above zero for all the plots. These average values for the yaw rates are shown in Table 6.3.

The yaw rate data shown in Figure 6.15 and Table 6.3 indicate that using only the head for turning is not as effective as using the tendon drive tail system. It is clear to see that the maximum possible time averaged yaw rate obtainable for the head only turning at a beat amplitude of 0.105m is 2.23 degrees per second whereas using the tail a maximum of 7.38 degrees per second can be achieved. Another aspect to consider when using the head system is that due to the use of an additional actuator to control the head movements the overall power consumption of the vehicle will be increased.

Although the yaw rates obtained from using the actuated head are small one possible use for the head system could be for small course corrections or to correct for the asymmetry in the tendon drive tail system.

6.4.2 Actuated Head and Tail

Another subset of experiments carried out involves the use of the actuated head in conjunction with the tendon drive tail system. This is achieved by angling the head with respect to the body at an angle of 13.5° and 27° at various combinations of tail offset for trails turning from stationary and turning at speed.

6.4.2.1 Turning from Stationary

Results are shown in Figure 6.16 for the x-y positional data for turning with the actuated head at two head offsets with the same tail beat frequency and amplitude. Figure 6.16 also includes the result for the experiment with the same tail beat frequency and offset with the head centred to allow for a comparison to be made. The corresponding yaw and roll rates for the same manoeuvres are shown in Figures 6.17 and 6.18 respectively.

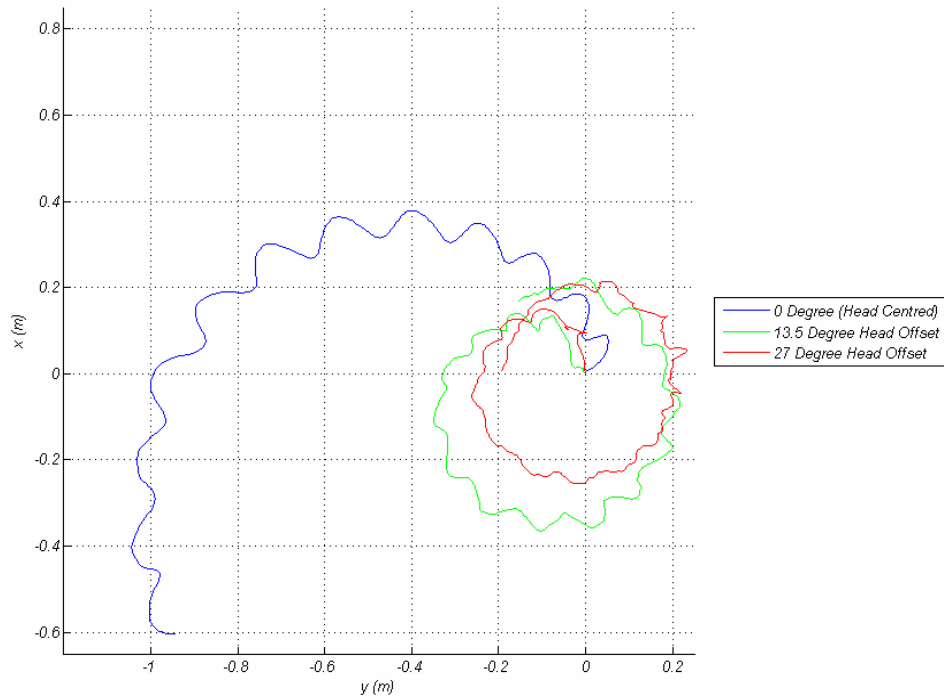


Figure 6.16: X-Y positional data for turning from stationary manoeuvre with actuated head at offset of 0° , 13.5° and 27° with the same tail beat amplitude, frequency and offset.

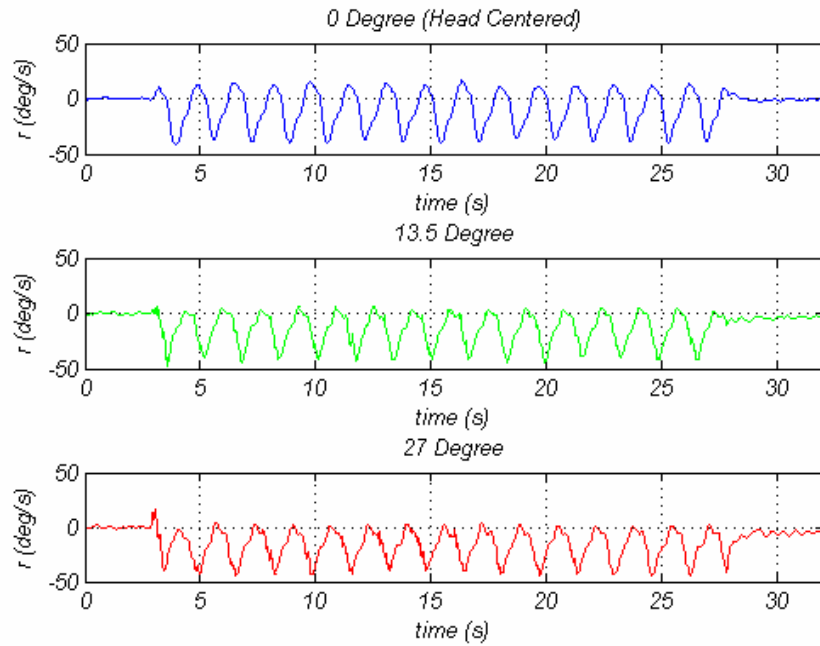


Figure 6.17: Yaw rate data for turning from stationary manoeuvre with actuated head at offset of 0° , 13.5° and 27° with the same tail beat amplitude, frequency and offset.

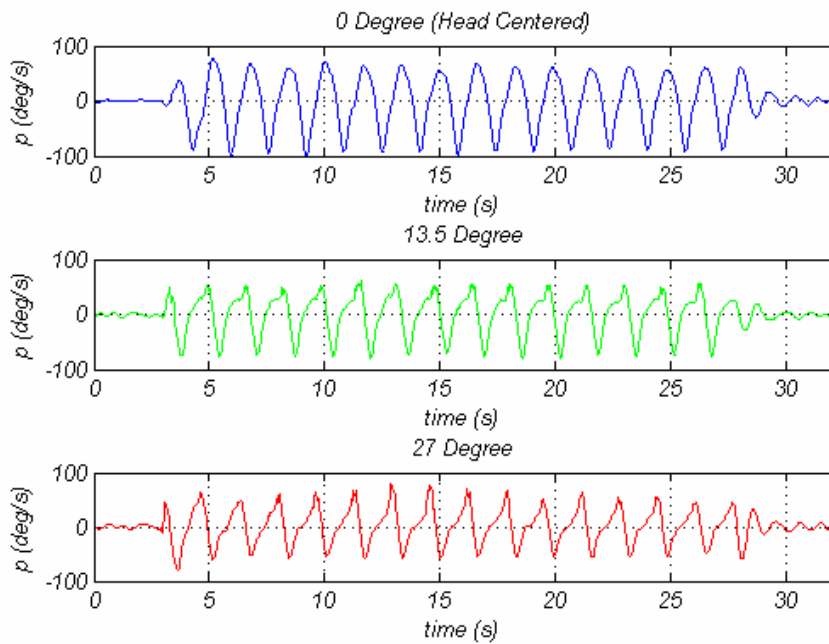


Figure 6.18: Roll rate data for turning from stationary manoeuvre with actuated head at offset of 0° (blue plot), 13.5° (green plot) and 27° (red plot) with the same tail beat amplitude, frequency and offset.

The results for the x-y positional data shown in Figure 6.16 indicate that the use of the actuated head in conjunction with an offset of the tendon drive tail system has a significant effect on the turning radius obtained experimentally. It is apparent from the results that the turning radius is reduced by a

factor of two when the actuated head is employed. This is significant as it shows that use of an actuated head system in conjunction with the tendon drive tail system can greatly improve turning performance.

From the yaw rates shown in Figure 6.17 it can be seen that for the head angled the yaw rate only crosses the zero value for short intervals value unlike the yaw rate with the head centred which has both positive and negative yaw rates. This has the effect of increasing the magnitude of the time averaged yaw rate and could explain the decreased turning circle. For the roll rates shown in Figure 6.18 angling the head has the effect of altering the shape of the recoil oscillations. The yaw angles obtained from these trails is shown in Figure 6.19.

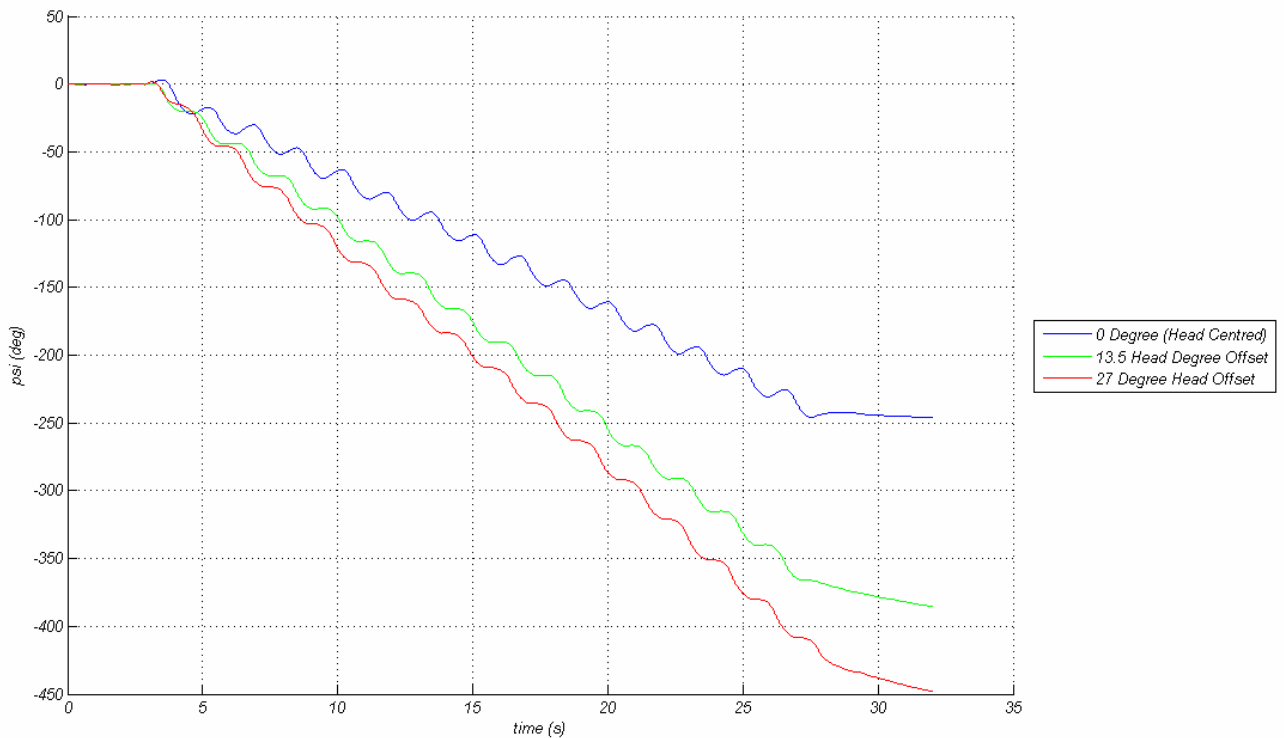


Figure 6.19: Yaw angles for turning with actuated head and tail.

These plots of the yaw angles show that the vehicle starts moving after 3 seconds, then moves with the tail and head offset for 25 seconds, then the tail stops oscillating at 28 seconds. The yaw angles obtained reinforce the concept that the increase in performance of using the actuated head as for the 27° head offsets the maximum yaw angle obtained before the tail stopped oscillating is 430° whereas for no head offset the yaw angle obtained is around 240°.

6.4.2.2 Turning at Speed

The next set of trials involves using the actuated head system for turning manoeuvres while the vehicle is travelling at a non-zero surge speed. This manoeuvre involves the *RoboSalmon* starting just in the field of view of the camera to allow a steady forward speed to be reached. Then after 12 seconds the

tail is offset at 25° and the head is offset at an angle of either 13.5° or 27° . This type of manoeuvre enables the effect of established forward speed has on the turning capability of the vehicle using the actuated head system.

Figure 6.20 shows the X-Y positional data obtained for the two powered turns with the actuated head. Also shown is the positional data for the run with the same tail parameters but with the head centred (0° head offset). The three runs shown in Figure 6.20 have the same tail beat amplitude of 0.15m and beat frequency of 0.48 Hz.

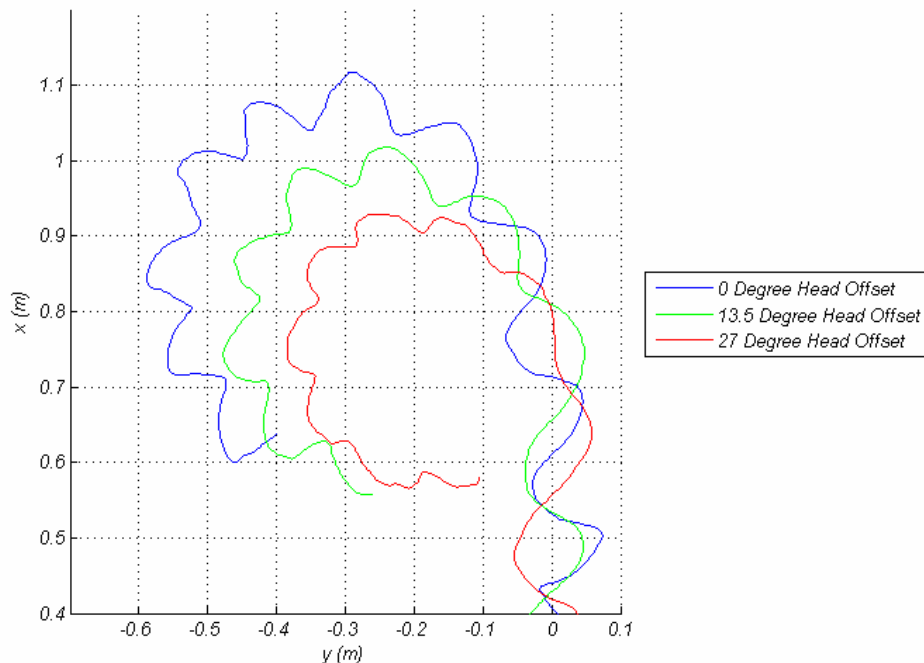


Figure 6.20: X-Y positional data for powered turns with head offsets and head centred for comparison. Tail beat frequency of 0.48Hz and beat amplitude of 0.15m.

The trajectories shown in Figure 6.20 show that when using the head and tail systems together a turn of around 275° is achievable for the 27° tail offset. The turning radius for the runs with the actuated head is reduced by around 0.1m for the 13.5° offset and around 0.2m for the 27° head offset when compared to the run with no had offset. Also of interest is that the time taken for each of the turns shown above, after the tail and head offsets are implemented, is 16 seconds. Another aspect to note is that the recoil motions appear to be slightly different for each run, this is due to the different start up motions of the tail. However, turning is started at the same position in each run. It also shows that an improved turning radius is possible with the combination of head and tail systems acting together. The corresponding yaw rates for this manoeuvre are shown in Figures 6.21.

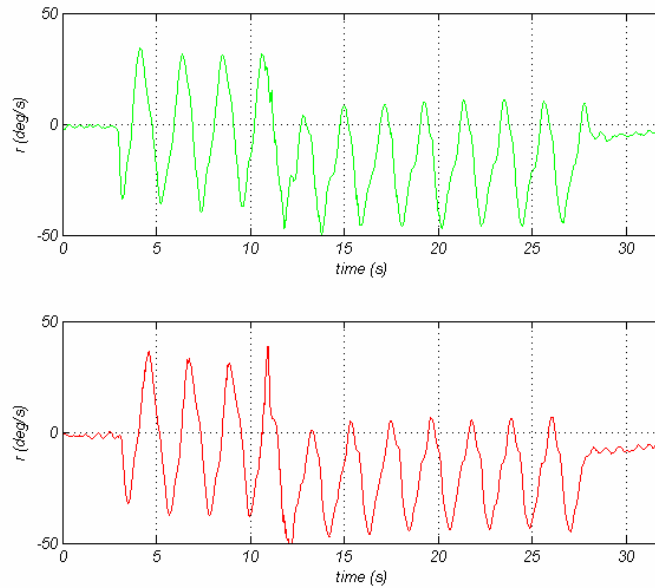


Figure 6.21: Yaw rate data for powered turn with tail beat frequency of 0.48Hz and beat amplitude of 0.15m with head angle of 13.5° (green plot) and head angle of 27° (red plot) when turning

From the yaw rates in Figure 6.21 the plots are similar in shape to that for the powered turn with no head offset shown in Figure 6.9. When turning starts at 11 seconds the steady state value of the yaw oscillations changes from zero during the straight swimming to the new steady state turning value. To see in detail the effects of the actuated head and tail systems when acting together the numerical values for the yaw rates obtained are shown in Table 6.4 along with the same values for the turning with the head centred for comparison.

Table 6.4: Tail parameters and yaw rates for turning at speed manoeuvre

Amplitude (m)	Frequency (Hz)	Tail Offset Angle (deg)	Head Offset Angle (deg)	Average Yaw Rate (deg/s)
0.15	0.48	-25	0	-14.11
0.15	0.48	-25	13.5	-17.73
0.15	0.48	-25	27	-18.72

The values shown in Table 6.4 indicate that with the actuated head system an increase in yaw rate of around 30% is obtainable by using the head system in conjunction with the tail system. Corresponding roll rates for the manoeuvres are shown in Figure 6.22.

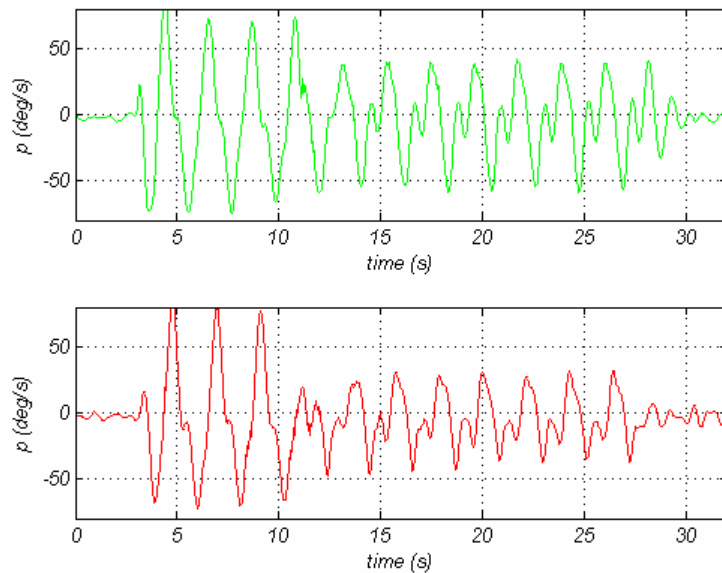


Figure 6.22: Roll rate data for powered turn with tail beat frequency of 0.48Hz and beat amplitude of 0.15m with head angle of 13.5° (green plot) and head angle of 27° (red plot) when turning

From the plot of the roll rate data (Figure 6.22) it can be seen that when the turning starts and the head is angled (at 12 seconds) the oscillations in roll appear to reduce significantly. This is due to the effect the actuated head has on the trim of the vehicle which adds more resistance to the roll motion.

The results shown in Figures 6.20, 6.21 and 6.22 indicate that, like the turning from stationary manoeuvre, increasing the actuated head angle while turning can improve the turning radius when compared to the same with the head centred. This is most likely be due to the way that the yaw and roll rate are affected by the positioning of the head. The positioning of the head will affect the roll and yaw moments generated in two ways. Firstly, with the head angled it acts like a rudder and creates a turning moment. Secondly, as the head moves it affects the trim of the vehicle which can assist with the turning process.

6.5 Turning Circle

As discussed earlier in this Chapter one of the standard manoeuvres that most vessels undergo is the turning circle. The turning circle requires that the maximum rudder angle is used for the test [IMO, 2002]. As the *RoboSalmon* does not have a rudder therefore the maximum tail offset of 25° will be used. Another difference between the method used in this study to investigate the turning circle and the specified method is the heading change. Due to the experimental equipment only a partial turn could be completed rather than the full 360° heading change specified [Fossen 2002].

Shown in Figure 6.23 is the x-y trajectory for the *RoboSalmon* when executing a turning at speed manoeuvre with a tail beat frequency of 0.48Hz and beat amplitude of 0.15m with the actuated head centred.

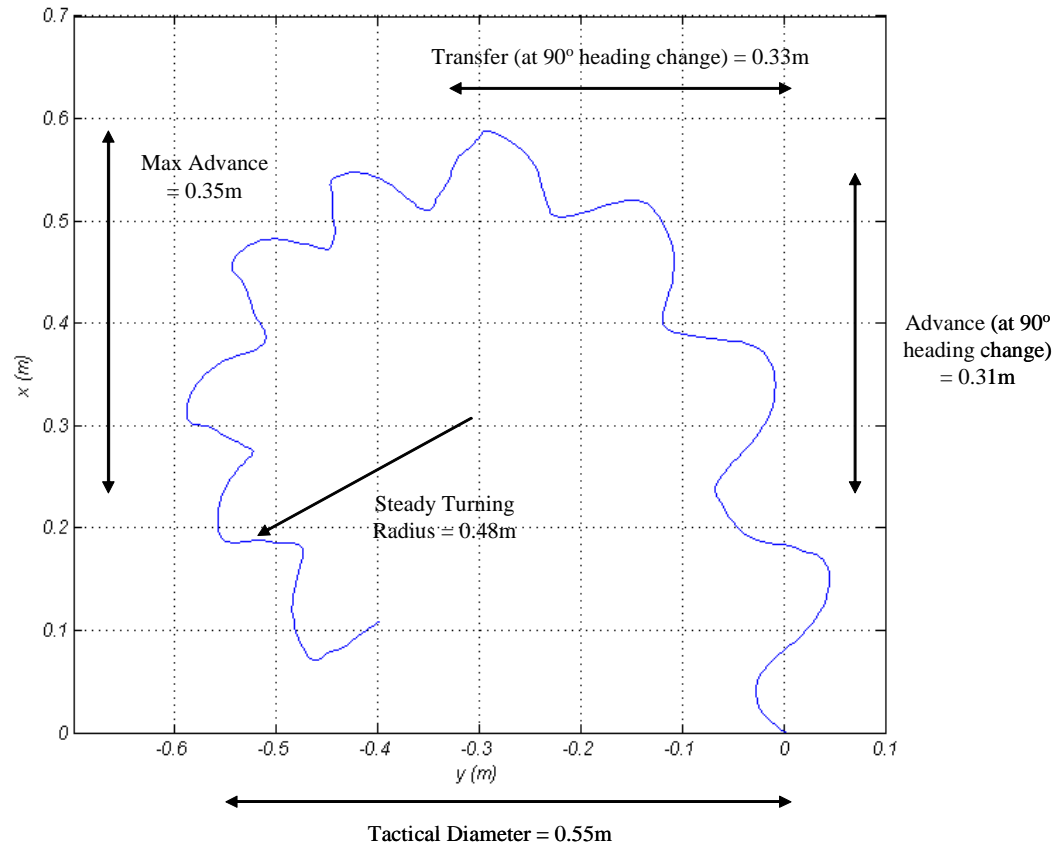


Figure 6.23: Turning circle parameters for RoboSalmon tendon drive system

The turning circle illustrated in Figure 6.23 shows that the approximate steady turning radius is 0.48m. This is just over half the body length of the *RoboSalmon* vehicle. One method that is used to compare the turning of different ships is the ratio of the Tactical Diameter to the length of the vehicle. Typical values for this ratio are around 3 for a frigate and a ratio of 4.5 would be usual for merchant ships [Tupper, 2004]. The value for the *RoboSalmon* with the tendon drive propulsion system is 0.65. This shows that the *RoboSalmon* can be considered to be relatively manoeuvrable vehicle.

6.6 Pull Out Manoeuvre

This section describes the pull out manoeuvre that has been investigated during experimental trials. The particular pull out manoeuvre that has been implemented in this study does not follow exactly the defined method described in Fossen [2002]. This is due to the experimental set up used which only allowed for a limited range of data to be obtained due to the size of the test pool and the field of view of the video camera. Therefore, rather than a steady rate of turn being achieved the *RoboSalmon* turned for a fixed time. Another reason for this modification to the pull out manoeuvre is that achieving a steady rate of turn with the prototype vehicle is difficult to measure onboard. This is due to the recoil motion present which tends to cause the yaw and roll rates to oscillate about an average value.

The pull out manoeuvre variant used in these experimental trials consists of the vehicle accelerating from stationary for a fixed time of 10 seconds with no tail offset, then implementing a constant tail offset for 5 seconds, then removing the tail offset and continuing swimming for a further 10 seconds. Results for the pull out manoeuvre are shown in Figure 6.24 for the x-y positional data for both positive and negative offsets ($\pm 16^\circ$) and the corresponding yaw and roll rates in Figure 6.25. The reason for selecting $\pm 16^\circ$ was that it lies in the middle of the range of the most effective offsets tested for turning. Also $\pm 16^\circ$ corresponds to a proportionally similar value to the value of 20° rudder usually specified for the pull out when the ranges of the actuators are factored in.

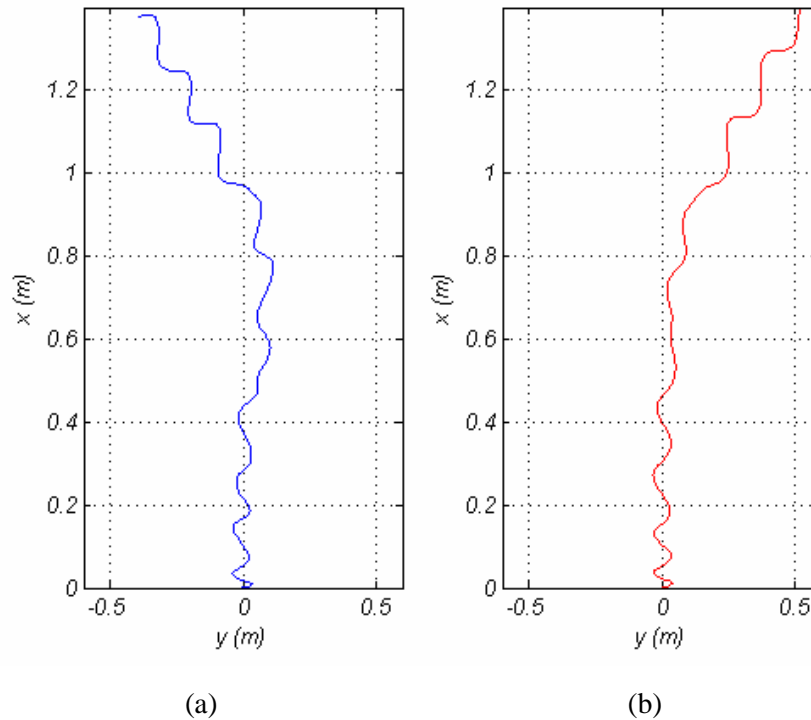


Figure 6.24: X-Y positional data for pull out manoeuvre for tail offset of (a) -16° (blue plot) and (b) $+16^\circ$ (red plot)

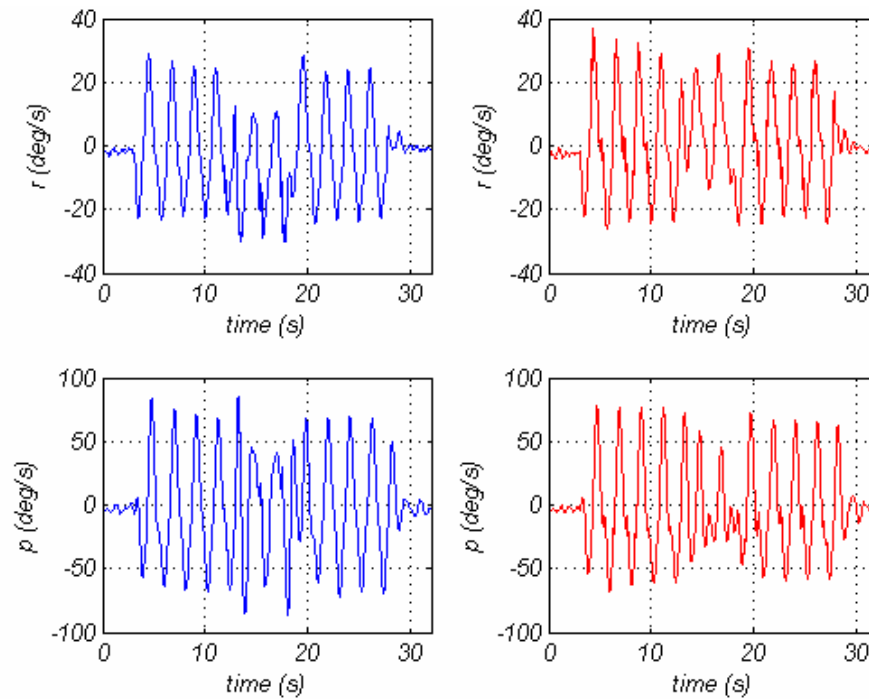


Figure 6.25: Yaw rate (top) and roll rate (bottom) data for Pull Out manoeuvre for tail offset of (a) - 16° (blue plots) and (b) $+16^\circ$ (red plots)

The results of the pull out manoeuvre presented in Figure 6.24 and Figure 6.25 highlight a number of aspects of the characteristics of the tendon drive system. Both positive and negative manoeuvres use a tail beat frequency of 0.48Hz and a beat amplitude of 0.105m. As with all the other manoeuvres the recoil motion is present and as discussed in Section 6.3 the asymmetry in the turning performance of the system is apparent in Figure 6.24. The maximum lateral displacement for the negative tail offset is greater than the positive offset. This indicates that the turning performance can be influenced by where in the tail beat cycle the offset command is received. With the positive offset (red plot in Figure 6.24) the turning appears to cause a discontinuity in the swimming motion which causes the vehicle to move slightly in the y direction. This discontinuity is visible in the red plot but does not have such an impact on the manoeuvre. The cause of this discontinuity is the way in which the tail responds to an offset command. As soon as the change in offset command is received the tail attempts to go to this desired value no matter where the tail is in its current tail beat cycle. In the red plot the offset command appears to be received when the tail is at its centre value, however, in the blue plot it is received when the tail is at its maximum lateral displacement.

The aim of the pull out manoeuvre is to determine if a marine vehicle is straight line stable or not [Fossen, 2002]. A ship is said to be unstable if the rate of turn of the vessel does not return to an equilibrium point after a disturbance [Fossen, 2002]. Although the pull out manoeuvre has not been conducted exactly as specified, from the results obtained it does indicate that after the tail offset is removed the vehicle tends to continue in a straight line as shown in Figure 6.24. Also, when the yaw

rates are compared, when the offset is removed the yaw rates do appear to return to similar oscillatory values. These two aspects indicate that the *RoboSalmon* as a vehicle is stable.

6.7 Power Consumption

Another important aspect to the manoeuvring performance of the *RoboSalmon* vehicle is the power consumption when executing a turn. The current draw for two programs with the same beat frequency and beat amplitude, one with and one without a tail offset are shown in Figure 6.26.

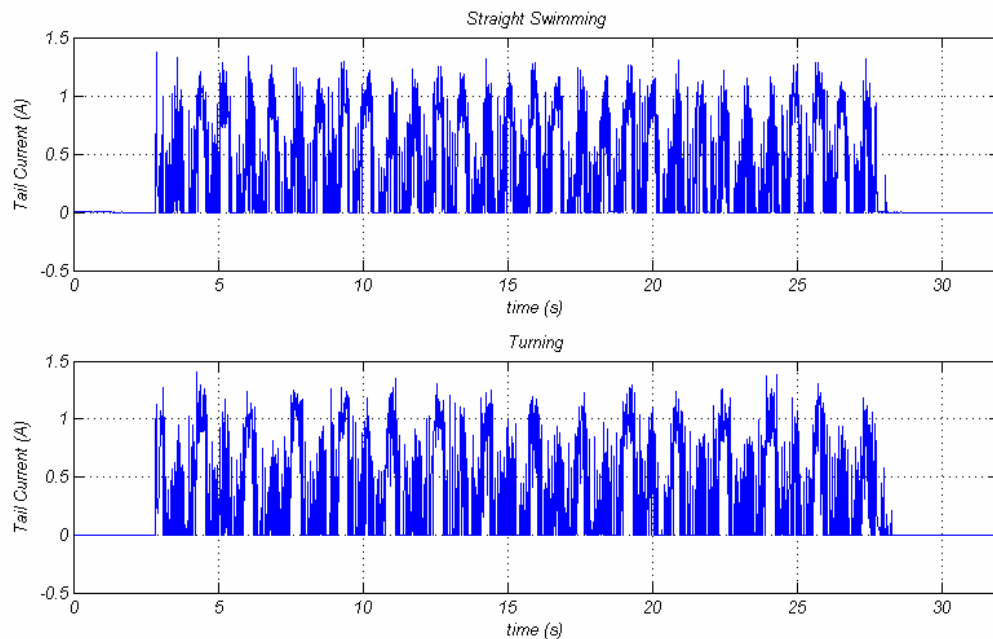


Figure 6.26 – Current consumption for straight swimming (top plot) and turning (bottom plot)

These current results highlight two interesting aspects to the turning manoeuvre. For straight swimming the peaks in the current appear to be approximately similar in amplitude. However, in the turning manoeuvre every second peak has its amplitude is reduced. The reason for this is that when the servo motor is moving the tail the current draw is greatest when the tail is moving through its centre value heading towards the maximum lateral displacement as described in Section 5.3.4. However, the current draw when the tail is returning from the maximum displacement the current draw is minimised as the tail construction acts like a spring to return it to its centre position. Therefore, over one tail beat cycle there is two large current peaks; one when the tail is going to its maximum positive lateral displacement and one when its going to its maximum negative lateral displacement. When the offset is implemented the tail flaps more to one side than the other and so over one beat cycle there will only be one large current peak as can be seen in the bottom plot of Figure 6.26. However, when the average current draw is compared for straight swimming and turning they are in a similar range because when the offset is implemented a greater lateral displacement will be required and therefore more current will be drawn to achieve this. This is illustrated in Table 6.5.

Table 6.5: Power Consumption for turning with tendon drive system

Freq (Hz)	Tail Beat Amplitude (m)	Tail Offset Angle	Average Yaw Rate (deg/s)	Power Consumption (W)
0.61	0.105	0	0	1.97
0.61	0.105	-5	-3.05	1.99
0.61	0.105	-12	-4.39	2.033
0.61	0.105	-16	-5.34	2.0144
0.47	0.105	0	0	1.55
0.47	0.105	5	-1.49	1.51
0.47	0.105	-12	-3.97	1.53
0.47	0.105	-16	-6.82	1.54

The data presented in Table 6.5 highlights that there is not a significant different between the power consumption for straight swimming and for that of turning. The two aspects of current draw for the turning manoeuvre discussed above; the increase in the lateral displacement when the beating is offset and the restoring force of the tail, appear to cancel each other out. Therefore, it appears that for manoeuvring there is not a significant difference in the current draw between straight swimming and turning

6.8 Propeller & Rudder Based System

This section presents the results from the manoeuvring trials completed with the propeller and rudder based system described in Chapter 3. A similar format of trials have been carried out for manoeuvring using the propeller and rudder system as those completed with the tendon drive system, i.e. turning from stationary and turning at speed. This allows a comparison to be made between the two systems. For the manoeuvring trials, experiments with the actuated head have not been conducted due to time constraints.

6.8.1 Turning from Stationary

For the turning from stationary trials the propeller based system has been positioned just in the field of view of the camera at the start of each run. The turning rate is evaluated using six different rudder angles ($\pm 15^\circ$, $\pm 30^\circ$ and $\pm 45^\circ$) at four different nominal propeller rotational speeds (0.8, 1.6, 3 and 6.4 rev/s). Figure 6.27 shows the x-y trajectory for the propeller and rudder based system for rudder angles of $+15^\circ$, $+30^\circ$ and $+45^\circ$ with a nominal propeller rotational speed of 3.2 revs^{-1} .

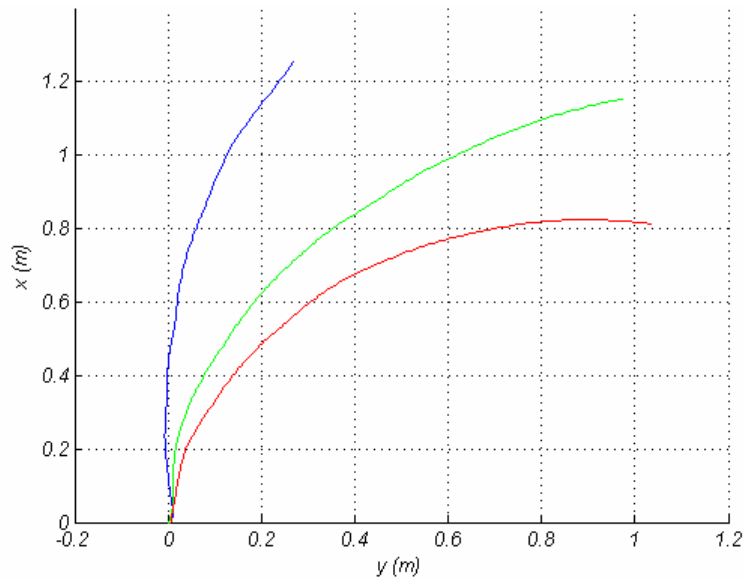


Figure 6.27: X-Y trajectory of propeller and rudder system for rudder angles of $+15^\circ$ (blue plot), $+30^\circ$ (green plot) and $+45^\circ$ (red plot) with a nominal propeller rotational speed of 3.2 rev/s

These trajectories show that the greater the rudder angle the sharper the turn carried out, however a complete 180° course change is not possible with any of the turning from stationary manoeuvres with the propeller and rudder system in the field of view of the camera. In order to compare the turning performance with the tendon drive system the yaw rates need to be compared.

The yaw rates obtained from the experimental trials for rudder angles of $\pm 15^\circ$ and $\pm 30^\circ$ and propeller speeds are shown in Figure 6.28.

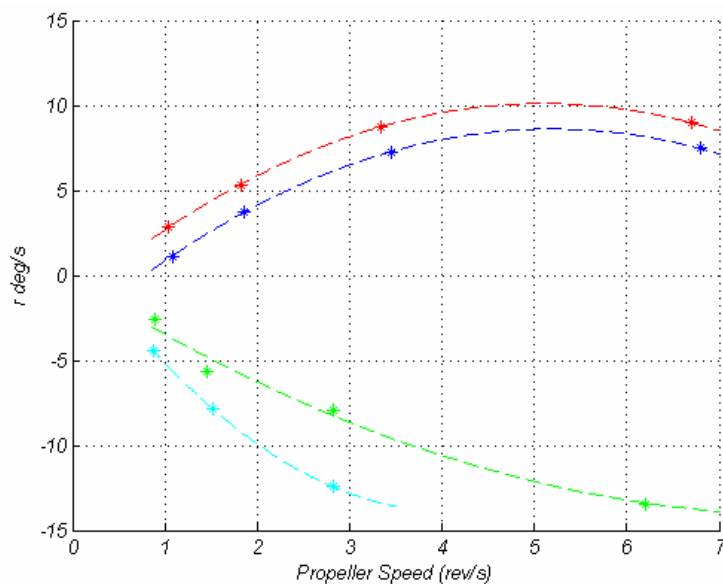


Figure 6.28: Yaw rates obtainable for different propeller speeds for the propeller and rudder based system. Red points indicate $+30^\circ$ Rudder, Blue points $+15^\circ$ Rudder, Green points -30° and Cyan points -15° Rudder

These results indicate that like the tendon drive system, the turning manoeuvre is not symmetrical about the surge axis as a negative rudder command appears to produce a larger yaw rate than the same positive command. When these results are compared with the turning characteristics of the tendon drive system it is clear that the asymmetry present in both propulsion systems is in opposite directions. This implies that one contributing factor to this asymmetry may be asymmetry present in the physical implementation of each of the propulsion systems. In the propeller based system this may be due to the construction and layout of the propeller and rudder configuration and in the tendon drive system as mentioned previously could be due to the limitations of the tendon drive tail.

Another interesting aspect to note is that when the yaw rates obtained from both systems are compared they fall in a similar range of obtainable yaw rates. However, due to the nature of the rudder based system the actual turning radius achieved is significantly larger than the turning radius achieved with the tendon drive system. From the turning results for the tendon drive system shown in Figure 6.1 it is possible for the vehicle to turn by more than 180° in less than 1.3m in the sway axis. However, in all of the propeller and rudder based experiments it has not been possible to turn by this amount in the field of view of the camera. This is due to the turning force generated by the rudder which is proportional to the flow over the rudder surface and thus proportional to the surge velocity of the vehicle. Therefore, in order to turn effectively, a surge velocity of a sufficient magnitude is required to produce the turning forces and moments as this system is a flight vehicle which does not employ thrusters. This in turn limits the turning radius of the vehicle and is the reason why certain underwater vehicles employ thrusters in the sway axis for manoeuvring [Bradbeer1, *et al*, 2004].

6.8.2 Turning at Speed

The trials for the propeller and rudder system turning at speed have been conducted using the largest rudder deflection possible of $\pm 45^\circ$ at four different propeller rotational speeds. Due to the greater acceleration of the propeller and rudder based system the time for forward propulsion before turning commenced has been reduced to 7 seconds for the propeller speeds of 0.8 revs^{-1} and 1.6 revs^{-1} and to 3 seconds for the propeller speeds of 3 revs^{-1} and 6.4 revs^{-1} . These times have been reduced to maximise the time that the vehicle is within the field of view of the video camera whilst allowing enough time for a sufficient speed to be obtained. Turning trajectories for the turning at speed trials are shown in Figure 6.29 for rudder angles of $\pm 45^\circ$.

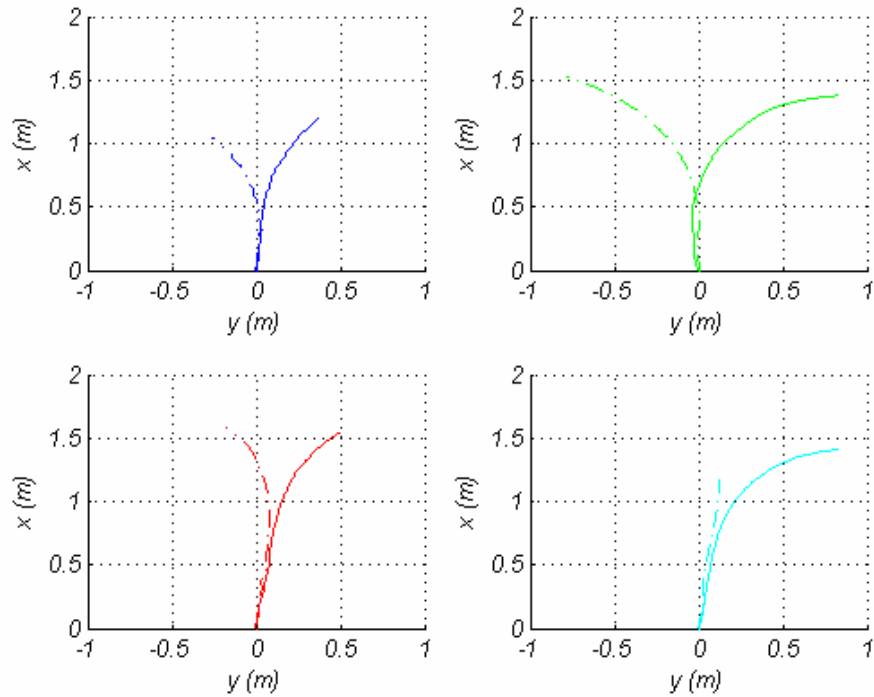


Figure 6.29: X-Y trajectory for turning at speed manoeuvre for the propeller and rudder based system for rudder deflections of $+45^\circ$ (solid line) and -45° (dashed line) at nominal propeller speeds of 0.8 revs^{-1} (blue plots), 1.6 revs^{-1} (red plot), 3 revs^{-1} (green plot) and 6.4 revs^{-1} (cyan plot)

From the turning trajectories shown in Figure 6.28 a number of interesting aspects of this manoeuvre are apparent. The effect of the propeller induced roll is visible in the majority of these results as a tendency for the vehicle's trajectory to drift in the positive y direction. The largest effect of this induced roll is shown in the last plot where for the -45° rudder angle (dashed cyan line) the turning is significantly less than the corresponding $+45^\circ$ rudder angle. This is because at this propeller speed the large roll induced is such that the component of force produced by the rudder in the Earth-fixed sway axis is reduced. The reason for this reduction is that the rudder is angled in the vertical plane due to this induced roll.

6.9 Comparison of Tendon Drive and Propeller/Rudder Systems

As one of the main objectives of this work is to investigate the potential benefits of a biomimetic propulsion system over a conventional propulsion system, the results obtained from experimentation with the two systems are compared and discussed.

From the turning from stationary trials for each system it is apparent that a similar range of yaw rates is obtainable, with the maximum measured propeller and rudder based system capable of slightly higher rates of 14.23 degs^{-1} compared to the maximum of 12.27 degs^{-1} for the tendon drive system. However, when the effective turning radii are compared the tendon drive system is capable of a course change of 180° in under 0.6m , whereas a course change of 180° is not possible with the propeller

based system in the field of view of the camera. This is most likely due to the propeller and rudder system requiring a sufficient surge velocity to produce the required flow over the rudder control surfaces and generate the required turning moment for the manoeuvre. The yaw rate of the tendon drive system is not as dependant on the surge velocity as the propeller system therefore is capable of turning with significantly smaller radii. A selection of the power consumptions for the propeller/rudder system and the tendon drive system are shown in Figure 6.30.

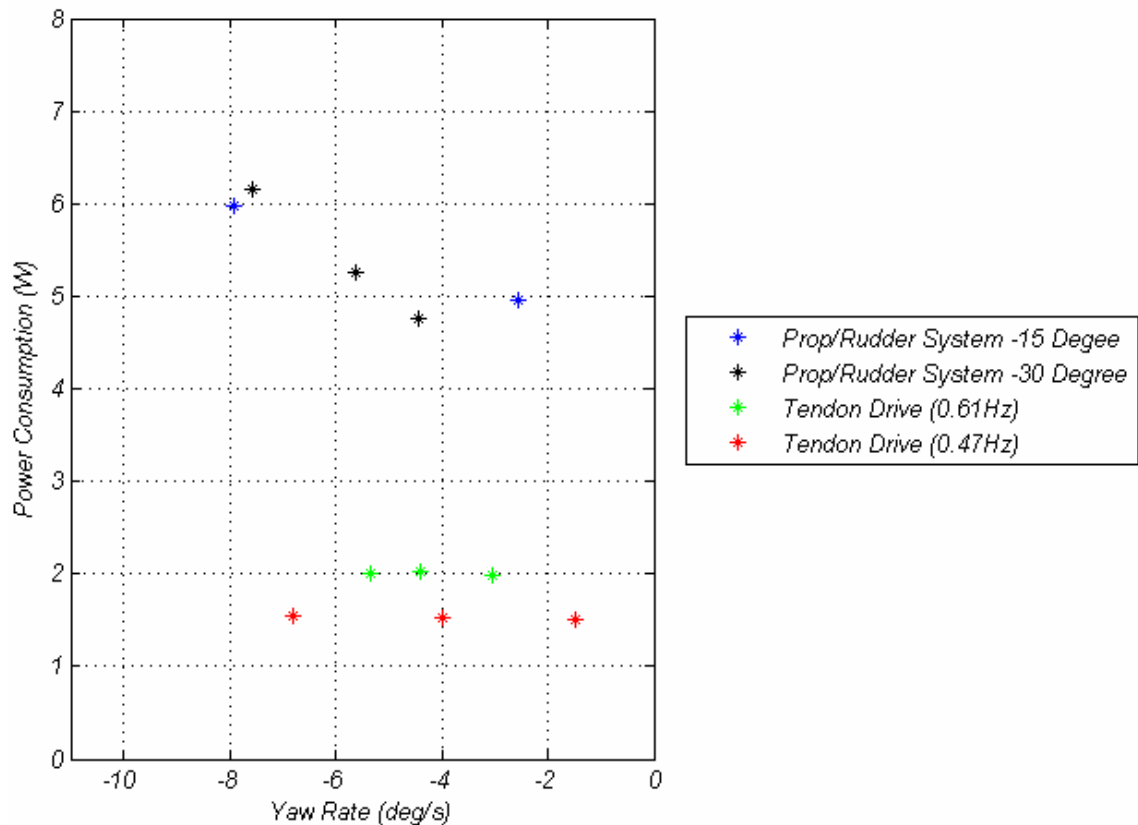


Figure 6.30 – Comparison of power consumptions for turning from stationary manoeuvre for tendon drive system and propeller system. Propeller system has rudder set to -15° and -30° with increasing propeller speeds. The tendon drive system has the beat frequencies of 0.47Hz and 0.61Hz, both with a nominal beat amplitude of 0.105m

These power consumptions presented cover a comparable range of yaw rates for both systems. The relatively constant power consumption for the tendon drive system is apparent in Figure 6.30 as the power consumption does not appear to change significantly for increasing tail offsets at the same beat amplitude and frequency parameters. It also highlights that the power used by the tendon drive system, for the parameters tested, is less than the power used for the propeller and rudder system for similar yaw rates.

When the turning at speed manoeuvres are compared a similar trend is observed for the turning from stationary manoeuvre. For the tendon drive system, carrying out a turning at speed trial the turning radii obtained are reduced further over the turning from stationary trials. The propeller and rudder

based system is still not able to achieve a course change of 180° in the field of view of the camera. This highlights the large turning radius required by this system especially when compared to the tendon drive system that are able, under a number different of tail parameters, to obtain a full 180° in the same area.

Another manoeuvring characteristic to compare is the asymmetry in each system. Asymmetry is present in each system which is due to the imperfections in the construction of each propulsion system. As previously discussed one of the limitations of the tendon drive system is that it is an under-actuated system i.e. one servo is controlling tendon wires that cause ten revolute joints to rotate. Due to this design and the small variations in the tendon wires during experimentation it is possible that there are slight variations in the tail tip position during each trail. This would explain some of the drift experienced during the forward motion experiments in Chapter 5 and would also explain the asymmetry in the yaw rates obtained from the turning manoeuvres as the slight variations in tail motions would be added or subtracted from the intentional offsets added to the tail for turning.

When comparing the power consumptions for both systems the tendon drive system has the advantage. The results presented in Chapter 5 have already shown that for straight swimming the tendon drive system uses less power and is more efficient than the propeller and rudder system. Section 6.7 has shown that there is not a significant difference in the power consumptions for straight swimming and for manoeuvring. Due to the propeller and rudder system using two separate actuators, one for the propeller and one for the rudder, there will be an increase in current for the propeller and rudder system when turning. This is because the servo motor controlling the rudder requires current to hold the rudder in position while turning. Therefore, as well as the tendon drive system showing better turning performance capabilities it also uses less current and thus less power than the propeller and rudder based system.

6.10 Summary

This Chapter has presented the experimental results obtained from the manoeuvring trials carried out for the *RoboSalmon* vehicle. The Chapter starts with an overview of the experimental procedure and programs used throughout the manoeuvring trails. Results for the *RoboSalmon* turning from a stationary position are then presented along with a discussion of the characteristics observed. Responses show the relationships between the tail offsets and the yaw rate obtained and a discussion of the asymmetry of the manoeuvring characteristics is presented. The next set of trials conducted was turning from speed which involved the vehicle travelling in a straight trajectory for 8 seconds then adding an offset to the tail for manoeuvring.

The use of the actuated head for turning is then discussed with a series of experimental trials which involve only offsetting actuated head for turning, using the actuated head and tendon drive tail systems together for turning from stationary and turning at speed. These trials indicate that it is possible to use the actuated head alone for turning although it is not as effective as using the tail for turning. They also

indicate that the use of the head and tail systems together can improve the turning performance by further reducing the turning radius by approximately a factor of two for the turning from stationary manoeuvre.

A pull out manoeuvre is then used with the tendon drive system which proves the tendon drive system is capable of carrying out manoeuvres in a similar manner to a conventional vehicle. The Pull Out manoeuvre also indicates that the *RoboSalmon* using the tendon drive propulsion system is straight line stable.

The next section presents the results obtained from the propeller and rudder based system which characterise the turning performance of the system when turning from stationary and turning at speed to allow for a comparison between the biomimetic and conventional systems.

Finally, the comparison between the biomimetic and conventional systems is presented which indicates that manoeuvring advantages can be obtained by using a tendon drive system in terms of reducing the turning radius. The main conclusions that can be drawn from the manoeuvring trials is that the tendon drive system can achieve superior low speed turning performance when compared to the propeller and rudder based system in terms of turning rates and turning radii. The other conclusion is that the use of the actuated head can significantly improve the turning performance when used in conjunction with the tendon drive tail system.

Chapter 7 – Results: *Simulation*

7.1 Introduction

This Chapter presents simulation results for trials conducted using the mathematical model of the *RoboSalmon* discussed in detail in Chapter 4. These simulation studies involve experiments that have been difficult to realise with the available hardware and time constraints. Such experiments include swimming with a high tail beat frequency, burst-coast swimming, full turning circles, and a standard zig-zag manoeuvre.

Throughout this thesis the focus has been on the biomimetic tendon drive propulsion system. The work has demonstrated the manoeuvrability of this system and the benefits in efficiencies at low speeds when compared to the propeller based system. However, a number of limitations are also present in the tendon drive system. These include the actuator saturation in the servo which restricts the maximum tail beat frequency and the presence of substantial recoil motion. There are numerous ways in which a biomimetic propulsion system can be realised, thus this Chapter also presents a simulation study of an underwater biomimetic propulsion system with a different actuation scheme. This system is called the individually actuated system and is constructed from a tail with five segments, each of which is actuated individually by a DC servo motor. Although this system has not been realised in hardware due to time constraints and the resources available for the project, the simulation study attempts to estimate the performance of this system and determine how the performance of this system compares to the tendon drive system.

7.2 Tendon Drive System Simulation

A number of simulation studies have been carried out using the model developed in Chapter 4. The resulting simulation results have been used to investigate aspects of the propulsion system that are not investigated experimentally. In total three simulation studies have been carried out, the first simulating the tendon drive system at tail beat frequencies higher than the maximum of 0.61Hz before actuator saturation occurs. The second study involves simulations of burst-coast swimming. This is a swimming technique that fish use to conserve energy when swimming by using cyclic bursts of swimming movements followed by a period where the body is kept motionless and the fish glides or coasts through the water [Videler, 1993]. The third study involves simulations of a standard zig-zag manoeuvre [IMO, 2002].

7.2.1 Swimming with High Tail Beat Frequencies

The current tendon drive system is only able to produce tail beat frequencies of around 0.6 Hz before the onset of actuator saturation as discussed in Chapter 5. This is due to the speed-torque

characteristics of the DC servo motor used within the tendon drive system [Mabuchi Motor, 2009]. This simulation study attempts to investigate the performance of the tendon drive system if a higher performance motor is used and also to assist with the specifying of a motor for the system.

From the model validation results shown in Appendix C it is apparent that the model of the tendon drive system is a reasonable representation of the real system. The one difference in the validation results which does not correlate well is the time constant for the surge velocity, however the steady state surge velocity obtained does correlate. Simulated surge velocity results are presented in Figure 7.1 for tail beat frequencies of 1Hz, 2Hz, 4Hz, 6Hz and 8Hz. The corresponding tail beat amplitude used in the simulations is 0.085m which corresponds to 10% of the body length of the *RoboSalmon*. This value has been selected as real fish tend to use this approximate percentage amplitude value for swimming [Videler, 1993]. These specific tail beat frequencies are not achievable with the hardware of the tendon drive system due to the performance limitations of the servo motor in terms of loaded speeds obtainable.

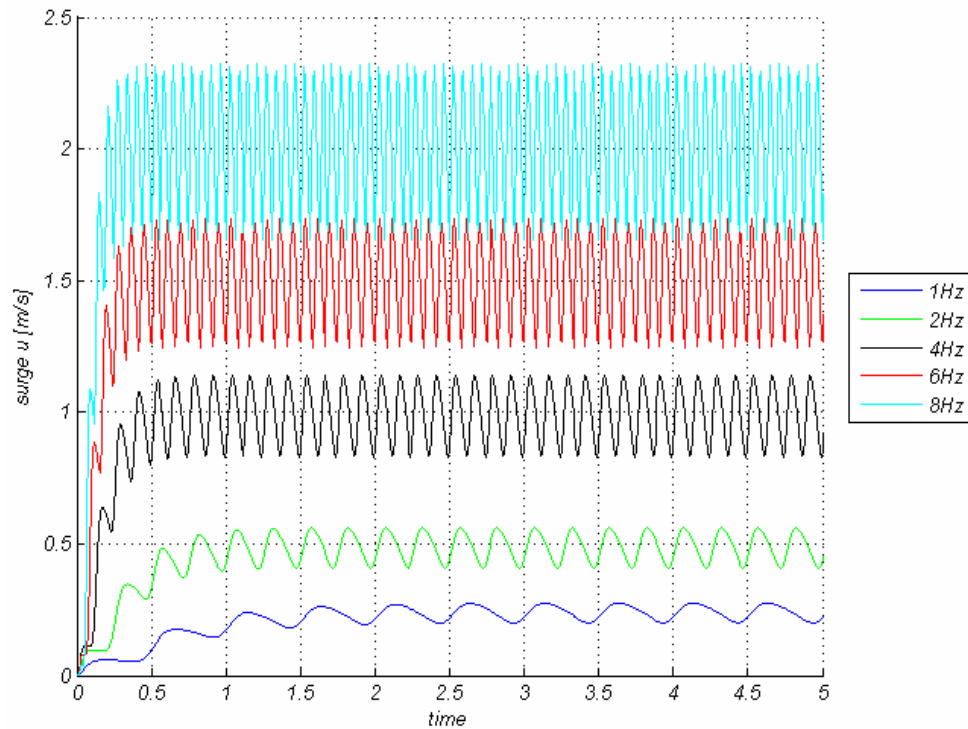


Figure 7.1: Simulated surge velocities at high tail beat frequencies with beat amplitude of 0,085m

As expected, the simulated surge results show that as the beat frequency is increased the surge velocity increases in a proportional manner. It can be seen that the surge ripple amplitude also increases with increasing tail beat frequency. However, from the simulation study it appears that this ripple amplitude is more sensitive to changes in tail beat amplitude. . This is indicated in Figure 7.2 below which shows the surge velocities obtained for three tail beat frequencies at three separate beat amplitudes.

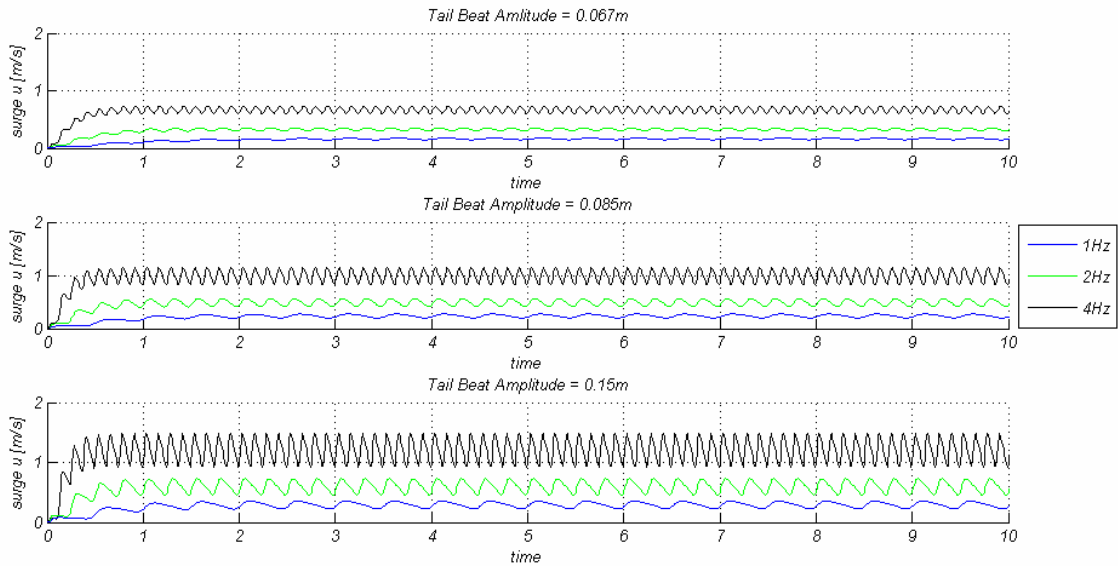


Figure 7.2: Simulated surge velocities obtained for three tail beat frequencies of 1Hz, 2Hz and 4Hz, simulated at three beat amplitudes of 0.067m, 0.085m and 0.135m

The surge velocity ripple shown in Figure 7.2 for each combination of beat frequency and amplitude show that the ripple amplitude is more sensitive to beat amplitude than to beat frequency. This could be the reason for fish usually swimming at a relatively constant beat amplitude and only varying the beat frequency to alter speed as the ripple velocity will not be increased as much as if they varied the amplitude..

The same linear relationship between beat frequency and surge velocity, as shown in Chapters 5 and 6, can be seen more clearly in the surge simulation results presented in Figure 7.2. Also shown in Figure 7.3 is data relating to actual salmon swimming in the form of real data points (green points that have been scaled to length of *RoboSalmon*). The region between the red dashed lines indicate the predicted range of efficient swimming using the range of the Strouhal number from 0.25 to 0.35 [Triantafyllou & Triantafyllou, 1995]. This indicates that data points for real salmon swimming speed lie within this predicted range of increased efficiency.

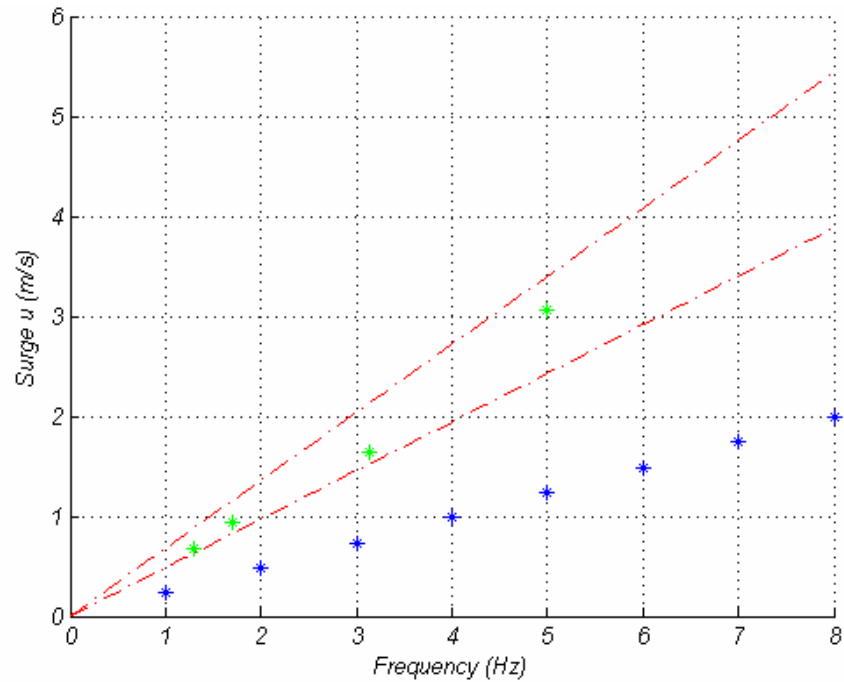


Figure 7.3: Comparison of estimated surge velocities with real Salmon. Region between red dashed lines indicate the range of efficient swimming for Strouhal numbers between 0.25 and 0.35. Blue points indicate simulated *RoboSalmon* surge velocities. Green points indicate real Salmon data.

However, when the simulated surge velocity is compared with the actual salmon surge speeds it can be seen that the simulated surge velocities are less than the real salmon surge velocities by a factor of approximately two. As expected this discrepancy is due to fact that the *RoboSalmon* model is mostly based on the dynamics of a marine vessel with a rigid hull. The only biological aspect of the model is the way in which the thrust is estimated (see Chapter 4). What accounts for the increased surge speeds of the real salmon is the drag reduction mechanisms employed by fish such as the mucus on the skin and the undulatory nature of the tail [Fish, 1998].

When the simulated start up transients are observed there is an initial small offset in the yaw angle due to the initial movement of the tail. This is expected when conducting the experimental trials however it is not obvious as other factors come into play such as the asymmetries of the tail system.

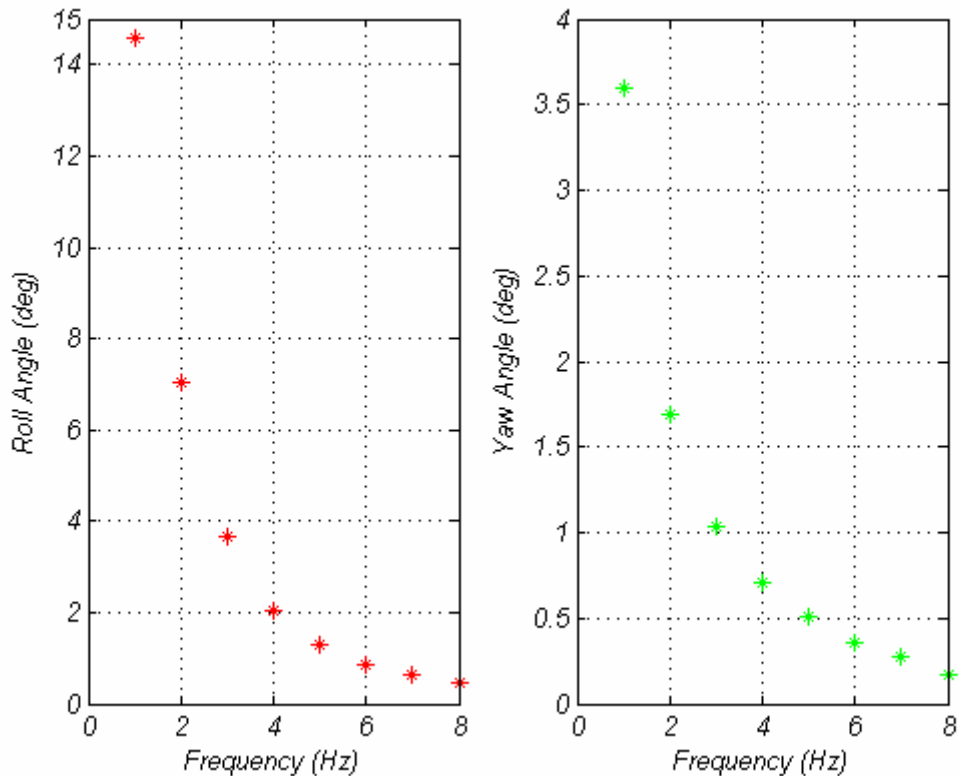


Figure 7.4: Simulated recoil motion in yaw and roll angles for high tail beat frequencies

Another interesting aspect of these simulations is that the simulated recoil motion is significantly reduced as shown in Figure 7.4. These plots indicate that there is what appears to be an exponentially decaying relationship between tail beat frequency and the corresponding angular displacements in yaw and roll. Therefore, there may be significant benefits in terms of surge velocity and recoil reduction for the *RoboSalmon* for swimming at high tail beat frequencies.

However, in order to obtain the benefits with higher beat frequencies a higher performance servo would be required. A higher performance servo would be larger and have greater power consumption than the current servo motor used. Use of such a servo would cause problems in terms of space available within the vehicle to house the new motor and could also negate the efficiency benefits of the tendon drive system. This indicates that a different approach to the actuation of the tail system such as the fully actuated approach, discussed in the next section, would be a better option.

7.2.2 Turning Circle

The turning circle manoeuvre, discussed previously in Chapter 6, is a means of comparing the turning performance of different ships. This section investigates the turning circles at higher tail beat frequencies than the current hardware is capable of. The frequency selected for this turning circle investigation is 1Hz. This is thought to be a reasonable beat frequency for normal steady-state swimming as data is available for real fish swimming within this frequency range [Videler, 1993].

Figure 7.5 shows the turning circle obtained for this beat frequency at a beat amplitude of 0.15m. This beat amplitude was selected as it would allow for a comparison to be made between the experimental turning circle discussed in Chapter 6 and the simulated turning circle.

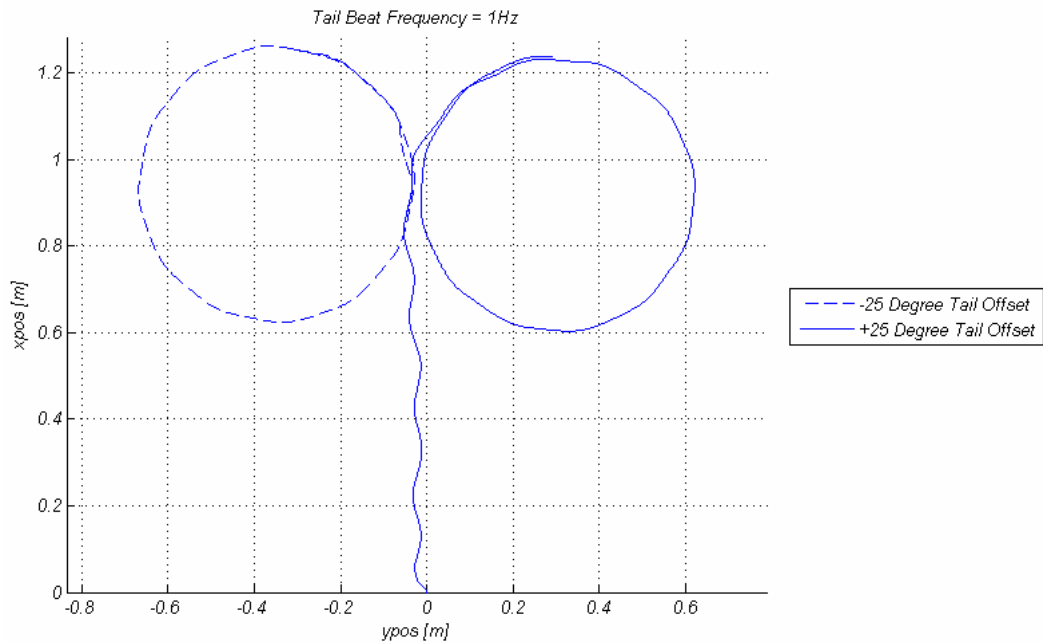


Figure 7.5: Turning circle for tendon drive system with tail beat frequency of 1Hz and beat amplitude of 0.15m.

Firstly, from the turning circle manoeuvre of Figure 7.5 the negative yaw offset caused during start up is visible as the straight course is angled. The tactical diameter obtained for the experimental turning circle in Chapter 5 is 0.55m at a beat frequency of 0.48Hz and amplitude of 0.15m. The simulated turning circle has the same beat amplitude but around double the frequency. Doubling of the beat frequency has the effect of increasing the tactical diameter to 0.67m as shown in the simulated result. This is expected due to the increase in the surge velocity obtained with the doubled beat frequency.

Another aspect of increasing the beat frequency is that the lateral recoil displacements are reduced. The experimental turning circle had a lateral peak to peak recoil oscillation of just under 0.1m however, with the increased beat frequency this has been reduced by a factor of two.

7.2.3 Burst-Coast Swimming

One type of swimming technique that is employed by many species of fish is burst-coast swimming. This technique consists of cyclic bursts of swimming followed by a period where the fish remains motionless and glides or coasts [Videler, 1993]. Fish employ this technique to conserve energy, and a saving of around 50% can be achieved when compared to burst and coast swimming for high swimming speeds [Videler, 1993]. Figure 7.6 shows a simulated burst coast manoeuvre for the *RoboSalmon* tendon drive system.

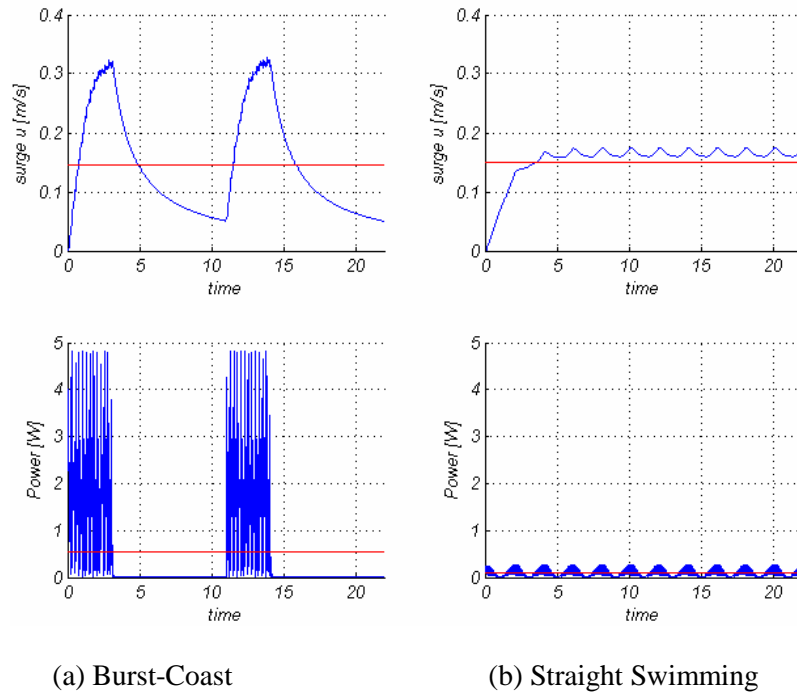


Figure 7.6: Simulated Burst-Coast swimming for *RoboSalmon*. (a) Burst-Coast (b) Straight swimming for comparison. Top Graphs show surge velocity and bottom graphs show estimated power. Average values are shown by the red lines.

The burst coast simulation shown above uses a 3 second tail frequency burst of 3Hz followed by 6 seconds of coasting. In order to obtain a similar average speed when swimming a tail beat frequency of 0.3Hz was required as shown in Figure 7.6(b). However, when the power consumptions are compared it is apparent that from the simulations no energy saving is obtained using the tendon drive system as more average power is required over the same time period for the burst swimming than for the straight swimming with the constant tail beat frequency. The reason for this is that fish have different muscle tissues, each of which is suited to a particular type of swimming, i.e. red muscles for steady swimming and high energy white muscles for brief periods of fast swimming [Videler, 1993]. The *RoboSalmon* on the other hand has only the one servo motor for actuation and this has to attempt to provide actuation for fast and slow swimming.

7.2.4 Zig-Zag Manoeuvre

As discussed in Chapter 6 the manoeuvring performance of marine vehicles is usually evaluated through a number of standard trials [IMO, 2002]. Two of these standard manoeuvres, the turning circle and the pull out manoeuvre, were conducted using the *RoboSalmon* hardware in experimental trials.

The zig-zag manoeuvre is carried out by setting a 20° rudder angle from an initially straight course [IMO, 2002]. This rudder angle is kept constant until the heading has changed by 20° , at which time the rudder is then set to -20° and is maintained until a -20° change in heading is obtained [Fossen, 2002].

Due to the limitations of the prototype the standard zig-zag manoeuvre could not be carried out experimentally. In order to conduct a zig-zag real-time feedback for the yaw angle would be required and this was not possible with the current firmware on the vehicle. Due to the yaw recoil present in the system obtaining an actual real-time yaw angle is problematic. This is because of the oscillations about a steady state yaw value and so the yaw angle of the vehicle is not always representative of the actual heading. In order to compensate for these oscillations the yaw angle is only considered valid when the tail system is at its centre position. This corresponds to the vehicle being on the steady state yaw value. The simulated 20-20 zig zag is shown in Figure 7.7.

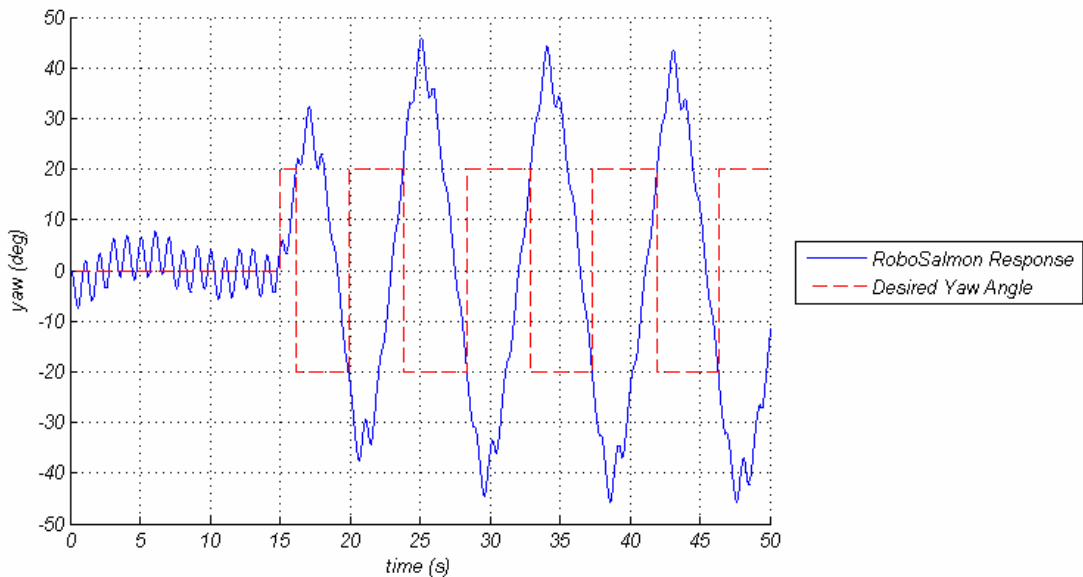


Figure 7.7: Simulated 20-20 zig-zag manoeuvre with tail beat frequency of 1Hz and tail beat amplitude of 0.085m

As discussed in Section 7.2.1 during the initial start up transient of the tendon drive system there is an initial offset in the yaw angle. Therefore, the first part of the zig-zag manoeuvre is to correct for this yaw angle offset. This is achieved using a simple Proportional controller for the yaw angle [Bolton, 2002]. Once the yaw angle of 0 degrees is reached then the zig-zag commences, this is at 15 seconds in Figure 7.7.

The results of the zig-zag simulation indicate that the *RoboSalmon* is capable of conducting the manoeuvre in a similar fashion to a conventional marine vehicle. However, the presence of the recoil motion coupled with the good turning performance leads to the large overshoot present. This is because the yaw angle is only sampled twice per tail beat cycle and in the period between samples the vehicle is still turning. Therefore, in order to improve the zig-zag performance either the recoil motion in yaw has to be reduced significantly or a specialist control system should be developed that accounts for the yaw recoil.

7.3 Individually Actuated System Simulation

The modelling and experimentation presented in this work has evaluated the performance of the *RoboSalmon* vehicle utilizing a tendon drive propulsion system. This type of propulsion has certain benefits such as that it uses only one actuator (a DC servo motor) to control forward motion and manoeuvring. However, the system has several limitations such as the actuator saturation at tail beat frequencies greater than 0.61Hz and the large recoil motion present.

This work has shown that using a biomimetic approach to underwater propulsion has a number of benefits but the method of actuation suffers from some limitations. One solution that may overcome some of these limitations is the use of a different method of actuation of the biomimetic tail system. A tail actuation system that could be used is the individually actuated tail system. This tail system has a number of revolute jointed-segments within the tail structure with a servo motor mounted on each segment. This design allows each segment of the tail to be actuated individually and could allow higher beat frequencies to be achieved as the load is spread across several motors instead of the one servo in the tendon drive system. The following section describes the modelling of this individually actuated system with five segments to allow for simulations to be conducted to compare the performance of this system with the tendon drive system.

7.3.1 Modelling

For the most part the modelling approach for the individually actuated tail system is similar to that used for modelling the tendon drive system with a small number of differences. The thrust and drag forces are modelled in exactly the same way but due to the nature of the tail kinematics of the individually actuated system the heave and pitch of the caudal fin can be out of phase whereas in the tendon drive system the maximum heave and pitch occur at the same instant. This has the effect of altering the estimate of thrust produced using the method outlined in Section 4.5.1.4 and also altering when the maximum drag occurs due to the angle of the caudal fin. The following sections describe the main differences between the tendon drive model and the individually actuated tail.

7.3.1.1 Kinematic Curve Fitting

One of the main advantages of the five segment individually actuated tail is that it should be a closer representation of the undulatory motion of a real fish compared to the tendon drive system. However, in order to achieve this undulatory motion with five revolute segments within the tail a method of determining the angular position of each motor output shaft is required. This is achieved by using the mathematical equation of the ideal propulsive wave that a fish passes along its body and fitting each of the five segments to it to represent the ideal propulsive wave as closely as possible [Kim & Youm, 2004; Liu et al, 2005].

The fitting process starts at the position of the first tail segment and systematically calculates the distance from that point to every point on the ideal curve. The coordinates of the other end of the

segment are equal to when the linear distance calculated equals the length of the segment. This process then repeats until all the segments are fitted. Knowing the coordinates of each end of each segment allows the position and orientation of each segment to be obtained. The relative orientation or angular displacements of each of the five tail segments over one complete beat cycle is shown in Figure 7.8.

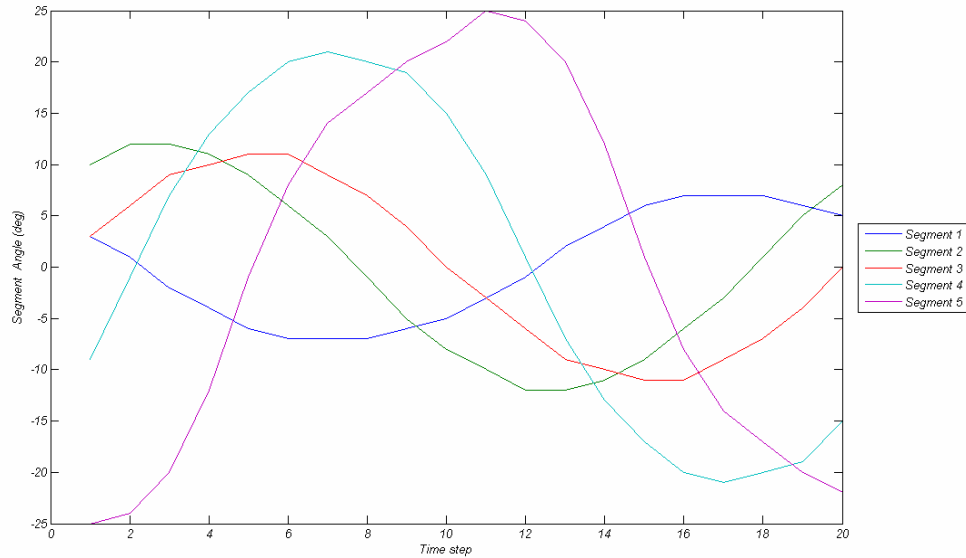


Figure 7.8: Angular displacements of each individually actuated tail segment shown at 20 points over one complete tail cycle. Segment 1 is attached to the body and each subsequent segment is connected to the next in numerical sequence..

In order to view the kinematic benefits of the individually actuated tail, plots of the tendon drive system and the individually actuated system are compared with the predicted kinematics of a real salmon in Figure 7.9

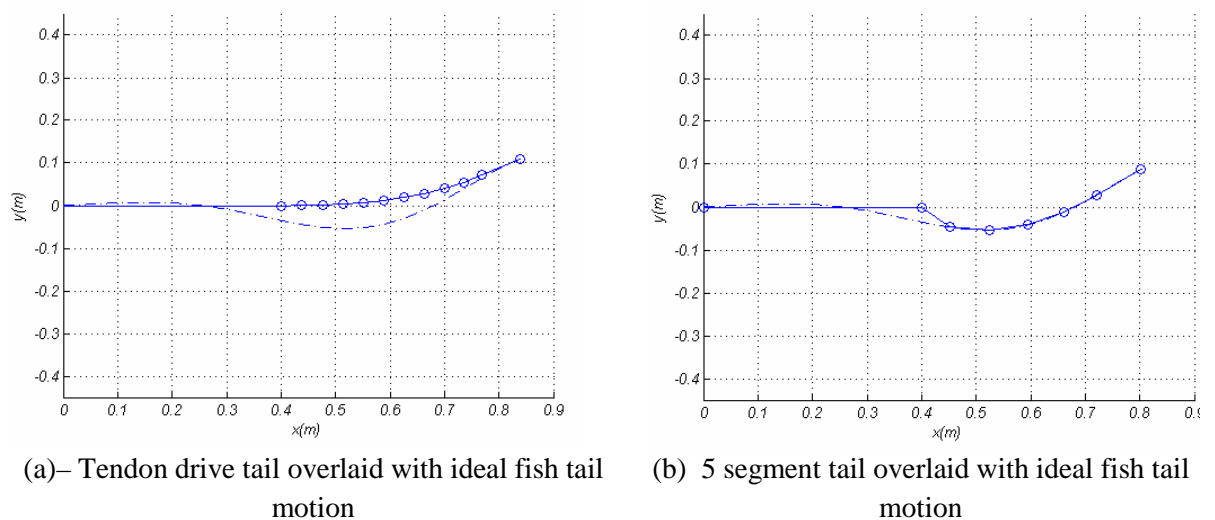


Figure 7.9 – Kinematics of *RoboSalmon* tail actuation systems (solid blue lines) compared with estimated kinematics of real salmon (dot-dash line)

The comparison of the two systems with predicted real salmon data indicate that the individually actuated system can provide significantly better matching to the undulatory motion of real salmon.

Using the calculated angular displacement for each segment the angular displacement of the Caudal fin can be calculated by summing all the previous segment angles. The lateral displacement of the fin tip can also be calculated using these kinematics, thus allowing the thrust to be estimated using the same method as employed for the tendon drive system as discussed in Chapter 4.

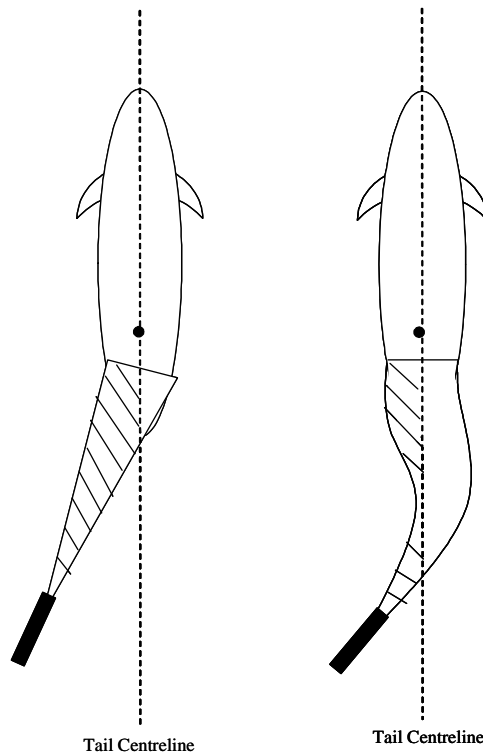
7.3.2 Servo Motors

One of the main differences in the individually actuated tail system is the number of servo motors used to move the tail. As discussed the tendon drive system uses only one servo motor but this tail actuation system uses five similar servo motors. Using five servo motors allows approximate realization of the undulatory motion illustrated in Figure 7.9, which is extremely close to real fish swimming gate. These five motors acting together provide a tail with greater torque and speed capabilities.

Each of the five servo motors is modelled in the same way as the servo motor for the tendon drive system. The only difference between each servo is the representation of the load. Each servo motor along the tail has a decreasing load i.e. size of tail section to be moved decreases for the servo motors that are further from the vehicle hull. The angular position of each servo at each part of a tail cycle is determined using the curve fitting method described above. With the lateral position and angular deflection of the Caudal fin known, the thrust can be estimated using the formulation of Lighthill's large amplitude elongated body theory discussed in Chapter 4.

7.3.3 Recoil Motion

Naturally there is recoil motion generated by the undulation of the individually actuated tail. However, this recoil motion is reduced due to a number of physical factors. Firstly, the recoil motion in roll is less than in the tendon drive system because of the mass distribution about the centre axis of the vehicle. This is similar to one of the proposed methods that real fish use to limit recoil motion and is illustrated in Figure 7.10.



(a) tendon drive system (b) individually actuated tail system

Figure 7.10: Illustration of tail mass distribution

As can be seen in Figure 7.10, in the tail section, the mass of the tail is distributed across both sides of the tail centreline. However, when compared to the tendon drive system the tail mass is all over to one side of the centreline of the vehicle. This should reduce the recoil roll moments produced by the vehicle as it moves and so reduce the effects of the recoil in this axis.

Also, the recoil motion in yaw is reduced due to there being five motors within the tail compared with one motor in the tendon drive system. With only one servo motor in the tendon drive system as the servo moves the tail to one side the body moves in reaction to this motion as the whole tail is across the centreline. However, in the individually actuated tail the undulatory wave like motion of the servos means that sections of the tail are present on each side of the centreline. This balance of sections on either side of the centreline reduces the pendulum-like influence of the tail during undulation. Hence the effect of the recoil in yaw is reduced.

7.3.4 Individually Actuated System: Overall Input Forces & Moments

The overall control forces and moments for the individually actuated tail system are shown in Equation (7.1).

$$\begin{aligned}
X_T &= F_{Thrust} \cdot \cos(\theta_{centre}) \\
Y_T &= F_{Thrust} \cdot \sin(\theta_{centre}) \\
K_T &= 0.5 \cdot m_{tail} \cdot g \cdot l_{TC} \\
N_T &= Y_T \frac{l}{2} + \tau_{RECOIL}
\end{aligned} \tag{7.1}$$

The surge propulsion force X_T is derived from the thrust F_{Thrust} produced from the actuated tail estimated using Lighthill's large amplitude elongated body theory as described in Chapter 4. This thrust term is multiplied by the cosine of the tail centre line θ_{centre} to represent the reduction in surge thrust when the tail is offset for manoeuvring. For the sway force Y_T the component of thrust acting along the y body axis is calculated by using the sin of the tail angle relative to the centreline. The roll moment K_T is modelled in the same way as the roll for the tendon drive system but the effective lateral displacement of the centre of mass of the tail is less. The yaw moment N_T is modelled as a fraction of the sway thrust plus an additional term for the recoil torque τ_{RECOIL} .

7.3.5 Individually Actuated System: Surge Simulations

Using the mathematical model described in the previous sections a number of simulation studies have been carried out to investigate the forward motion of this system. The surge velocities obtained for a three applied tail beat frequencies are shown in Figure 7.11.

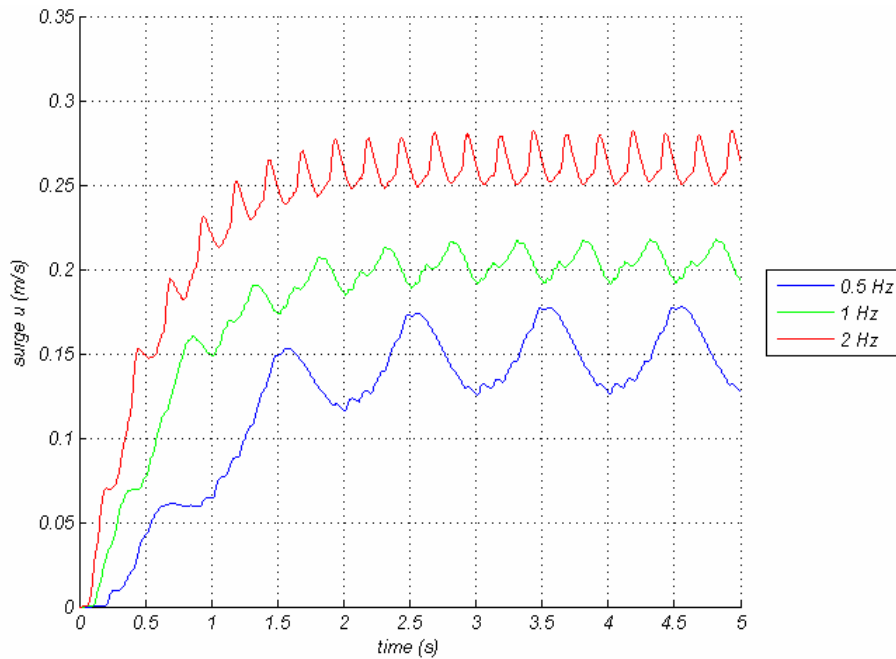


Figure 7.11: Simulated surge velocities for the individually actuated tail system for beat velocities of 0.5Hz, 1Hz and 2Hz at a beat amplitude of 0.15m

These simulated surge velocities indicate that using the individually actuated tail system higher surge velocities can be obtained for the same beat frequencies and amplitudes than with the tendon drive system. The reason for this is due to the undulatory motion that this tail system is capable of and so

will more closely represent the swimming motion of a real fish. Also, from the model a higher beat frequency of approximately 2Hz should be obtainable from the system before actuator saturation occurs. The reason for this is that the load on the tail will be split between the five servo motors rather than concentrated on one servo in the tendon drive system.

When the recoil motion for this system is investigated it is found that it is significantly reduced over that of the tendon drive system. This is illustrated for the peak yaw and roll angles obtained during forward swimming in Figure 7.12.

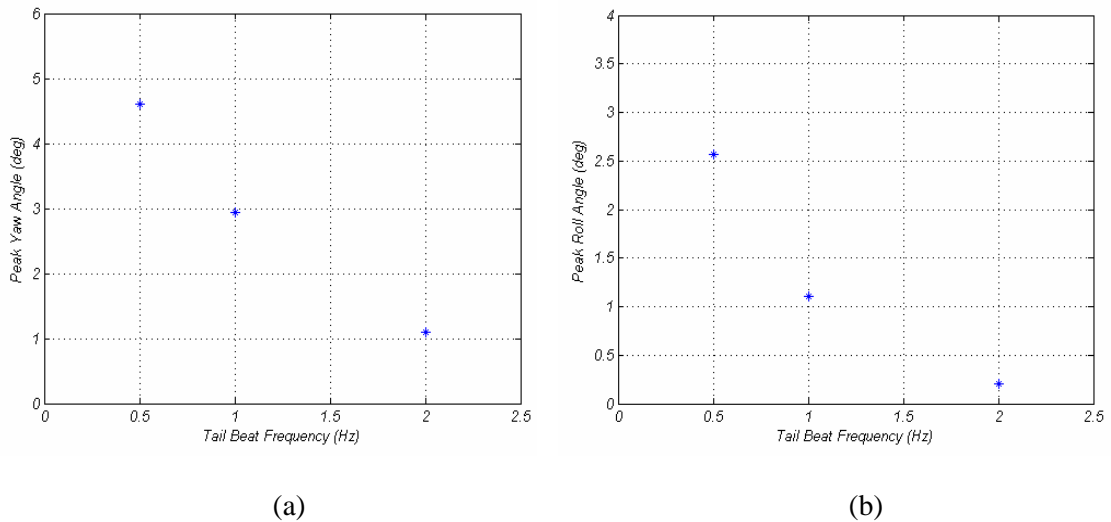


Figure 7.12 – Peak yaw angle (a) and roll angle (b) recoil for individually actuated system during straight swimming

When the peak yaw and roll recoil angles are compared with the experimental results from the tendon drive system shown in Figure 5.20 the simulated values for the individually actuated system are substantially lower. For the same tail parameters as simulated in the individually actuated system the roll angle is reduced by a factor of approximately 3 and yaw by a factor of approximately 2. This shows that there may be benefits of using an individually actuated system in terms of greater surge speed and recoil reduction for similar tail parameters.

For a practical implementation of such a system there may be additional benefits. One such benefit is that since each revolute joint segment in the tail is actuated individually more accurate and repeatable control over the caudal fin positioning may be achievable. The tendon drive system on the other hand is an under-actuated system with one servo controlling ten revolute joints. With the addition of the tendon wires which wear out over time the exact positioning of the caudal fin can vary slightly between tail beats. This variation is thought to be one of the factors which contribute to the system manoeuvring being asymmetrical.

7.3.6 Individually Actuated System : *Manoeuvring Simulations*

Extensive manoeuvring simulation trials were not conducted with the individually actuated system as the tail kinematics used for turning would be similar to that used by the tendon drive system. As such the manoeuvring performance obtainable will be comparable to this system in terms of yaw rates and turning circles.

The parameters chosen for this test were the same as for the simulated turning circles used for the tendon drive system presented in 7.2.2 i.e. 1Hz tail beat frequency and 0.15m beat amplitude. The simulated turning circle for the individually actuated system is shown in Figure 7.13.

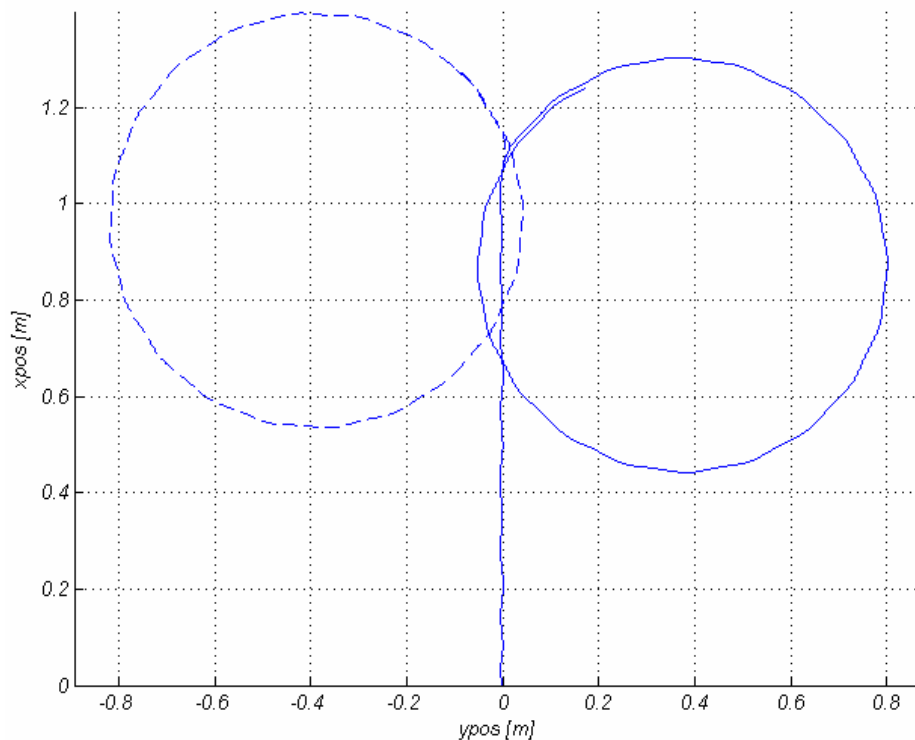


Figure 7.13: Turning circle for individually actuated system with tail offset of 20°

The turning circle results indicate that the system is capable of turns with a radius increased by approximately 25% to that of the tendon drive system with similar tail parameters. One reason for this increase in turning diameter is due to the higher surge velocity that the individually actuated system is capable of.

7.4 Summary

This Chapter has presented a discussion of two simulation studies carried out using the *RoboSalmon* mathematical models. The first simulation study involves simulation of the surge performance of the *RoboSalmon* with the tendon drive system using tail beat frequencies higher than that obtainable with the hardware. These simulations indicated that surge velocities of up to 0.26 ms^{-1} may be obtainable if

a servo capable of this performance could be obtained. At these higher simulated tail beat frequencies the recoil motion was significantly reduced.

The next simulation study described is the investigation into a tail actuation system that utilises five revolute tail segments with the tail all of which are actuated individually by separate servo motors. In order to use this system the relative rotational positions of each servo motor are required over a tail beat cycle. This is achieved using a curve fitting method which fits the five segments to the ideal fish kinematics. This is discussed along with the results which show the phasing of each of the five motors for one beat cycle. The kinematics obtainable with this tail system are then compared with the tendon drive system and the ideal fish kinematics.

The modelling methodology used to describe the individually actuated system is similar to that used to model the tendon drive system with a few differences which are discussed. Surge simulations are then carried out with this model which show that using this tail actuation scheme a greater surge velocity is obtainable. The simulations also show that the recoil motion is reduced significantly over the tendon drive system.

Chapter 8 – Conclusions and Further Work

8.1 Conclusions

Over the past two decades the development and use of unmanned underwater vehicles, particularly AUVs, has increased significantly in many application areas. In parallel to this, interest in the field of biomimetics has led to numerous research projects focusing on biologically inspired underwater propulsion systems for underwater vehicles. The aim of this work was to investigate fish-like biological inspired propulsion systems to determine if any benefits could be obtained from utilising such a system over a conventional propeller and rudder based system. This involved developing and constructing a prototype vehicle, named the *RoboSalmon*, with a biomimetic fish-like propulsion system. The biomimetic propulsion system operated by means of two tendon wires running the length of a tail made from ten revolute joints. At one end the tendon wires were attached to the rigid caudal fin assembly and to an servo motor at the other end. The reciprocal motion of the servo motor creates the side to side flapping motion of the tail and caudal fin. Experimentation with the *RoboSalmon* prototype allowed the performance of the tendon drive system to be evaluated for straight swimming and manoeuvring. In order to compare a biologically inspired system with a conventional propeller and rudder system the *RoboSalmon* hardware was reconfigured with propeller and rudder and a similar series of experiments conducted. This experimentation was the main method by which the benefits of the use of a biomimetic propulsion system were determined. An additional objective of this work was the development of a mathematical model that describes the performance of the *RoboSalmon* with both propulsion systems. The development and validation of this model will allow future investigations to be conducted in to the design of appropriate control systems for the *RoboSalmon* vehicles.

The first part of the work carried out was the design, development and construction of the *RoboSalmon* prototype hardware. Chapter 3 describes the *RoboSalmon* hardware in detail, covering the reasons for the design decisions and an overview of all of the onboard electronic and mechanical systems. Firstly, the work on the initial prototype which showed that the tendon drive system could produce a surge force was discussed. Only qualitative data was obtained from the initial prototype due to a number of hardware limitations. The reasons for a number of the design improvements made for the next prototype, such as onboard instrumentation, improved reliability and actuated head system are discussed. Each onboard electronic system is discussed, detailing the components used and giving an overview of the embedded software developed.

The development of the mathematical model is described in Chapter 4. This modelling process covers the kinematics and dynamics of the *RoboSalmon* vehicle to assist with the understanding of the

dynamics of the swimming process. Details of the method used to model the tendon drive propulsion system and the propeller and rudder system are presented. Details of the modelling of the recoil motion are also given. The use of two model validation techniques, analogue matching and integral least squares, show that the model is a reasonable approximation of the performance of the *RoboSalmon* vehicle. This Chapter also covers the experimental laboratory set-up used to conduct the experimentation which covers the test equipment, test pool and camera system. The image processing algorithms used to determine the position of the *RoboSalmon* from the captured video footage are described.

Chapter 5 presents the results for the experimental trials relating to forward motion. The chapter starts with an overview of the experimental procedure used for the trials and details of the tail parameters used for each of the twenty programs are given. Surge results are then presented which showed a number of trends in the data gathered including increasing surge velocity with increasing tail beat frequency. Tail beat frequencies of greater than 0.61Hz led to actuator saturation occurring which in turn led to the full beat amplitude for that particular program not being met. The highest obtainable surge velocity before actuator saturation occurred was 0.18ms^{-1} which was achieved at a tail beat frequency 0.61Hz and a nominal tail beat amplitude 0.15m. From the surge data for the programs without actuator saturation there appeared to be a linear relationship between the tail beat frequency and surge velocity. The surge velocities obtained for the *RoboSalmon* were then compared to the swimming performance of a real Salmon. This showed that the swimming speed of the *RoboSalmon* obtained for a particular beat frequency was lower than that achievable by a real Salmon by around a factor of 3.2 which was due to the mechanical nature of the system.

Recoil motion present in the surge experiments is then discussed and results presented which highlighted that the recoil was a highly complex and coupled motion. The power consumption of the tendon drive system for the various surge velocities is then presented and discussed. For the maximum surge velocity obtainable the average power consumption was 3.8W. The maximum instantaneous power consumption was found to be when the tail was crossing the centre position which corresponds to the maximum instantaneous tail velocity. Investigation of the use of the actuated head system to compensate for the recoil motion indicated that no significant reduction in the recoil motion was found with the actuated head parameters investigated. However, a reduction in recoil might be possible with further investigation.

Finally, the experimental trials with the propeller based system are presented. These results showed that the propeller based system was capable of a significantly higher maximum surge velocity of 0.52ms^{-1} , almost three times the maximum surge velocity of the tendon drive system. However, the tendon drive system was able to maintain a slower minimum speed than the propeller based system and for surge velocities less than 0.18ms^{-1} the tendon drive system used less power for the same velocities. When the efficiencies of the systems are compared in terms of estimated output swimming

power as a percentage of input electrical power the tendon drive system was found to be more efficient by a factor of three for the surge velocity of 0.18ms^{-1} .

The experimental results of the manoeuvring trials for both the tendon drive and propeller and rudder systems are presented in Chapter 6. For each propulsion system a number of manoeuvring trials were conducted. These included turning from stationary, turning at speed and a pull out manoeuvre. The results indicated that the tendon drive system was capable of a significantly improved turning radius over the propeller and rudder based system. Use of the actuated head for manoeuvring of the tendon drive system was also investigated and showed that with using the actuated head in conjunction with the tendon tail system a significant improvement in turning could be achieved over turning with the tail alone. The results for the tendon drive system also showed that when manoeuvring, the tendon drive system used similar amounts of power when compared to travelling in a straight motion.

Chapter 7 presents a discussion of a number of simulation studies carried out as part of this work. The first simulation study involved estimating the surge performance of the tendon drive system at beat frequencies higher than those achievable with the current servo motor. These simulations indicate that at these higher beat frequencies the yaw and roll recoil motions are reduced. The next simulation study conducted is an investigation into a tail actuation system that uses individual motors to actuate each joint in the *RoboSalmon* tail. This study covers the modelling of this tail system and an estimation of its swimming performance which shows that slightly improved surge performance can be obtained over the tendon drive system. It also shows that the recoil motion could be reduced due to the undulatory nature of this tail which is closer to the motion used by real fish. The benefits of using this system are also presented which show that more accurate control of the tail can be achieved as each joint is actuated individually whereas the tendon drive system is an under actuated system. Therefore, some of the limitations of the tendon drive system such as tendon wear and variable tendon tension could be overcome by using this system. The manoeuvring of this system is not covered in detail as the dynamic performance of the system will be very similar to that of the tendon drive system due to the nature of the tail joint positions when turning.

This work set out to analyse the performance of a fish-like biomimetic underwater propulsion system to determine whether it is a viable option for the propulsion of AUVs and if there are any benefits of utilising such a system. Through the use of the *RoboSalmon* prototype, which uses a biomimetic tendon drive propulsion system, the swimming performance of the system has been measured experimentally and shows that the system is capable of forward swimming and completing basic manoeuvres. When compared to real Salmon the performance of the *RoboSalmon* has reduced surge velocities obtainable and higher power consumption. The work has also produced a mathematical model of the *RoboSalmon* vehicle with the tendon drive propulsion system to describe the dynamics of the swimming process and to assist with the understanding of the recoil motion. This model has been validated using the data gathered from the physical *RoboSalmon* system and shows good correlation with this experimental data. The benefits of using such a biomimetic propulsion have also been

determined experimentally. This was achieved through the comparison of the performance of the *RoboSalmon* with a biomimetic tendon drive tail and a similar system that utilised a conventional propeller and rudder based system for propulsion. Although the propeller based system was capable of a higher maximum surge velocity, in terms of the efficiencies the tendon drive system was found to be more efficient than the propeller system for low surge speeds of less than 0.2ms^{-1} . For manoeuvring the tendon drive system was found to have a superior performance. Although similar yaw rates were obtained from both systems as the propeller and rudder system is a flight vehicle the yaw rate will be dependant on the surge speed. The tendon drive system is not as dependent on surge velocity and so this system is capable of turns with a significantly smaller radius, with some tail parameters allowing a 180° change of heading in under one body length of the vehicle. It was also found that with the tendon drive system there is not a noticeable increase in the power consumption between forward swimming and turning when the same tail beat frequency and amplitude parameters are used. The actuated head system used on the *RoboSalmon* showed that the use of the head when turning could further improve the turning performance of the vehicle.

Overall the work completed within this project has shown that a biomimetic fish like propulsion system is a potentially viable form of propulsion system for AUVs. Within the limitations of the data these results show that the biomimetic system investigated may have advantages over a conventional propeller and rudder based system in terms of greater propulsive efficiencies and increased vehicle manoeuvrability. Further investigation and development of this technology could lead to the development of AUVs with significantly increased efficiencies and manoeuvrability thus allowing longer and more challenging missions to be undertaken.

8.2 Further Work

The work described in this thesis investigated the benefits of utilising a biomimetic propulsion system over the use of a conventional propeller based system for a small underwater vehicle. The results presented indicate that a power reduction at low speed can be achieved and that manoeuvrability is increased compared to a propeller and rudder based system. However, with the validated mathematical model developed and hardware platform in the form of the *RoboSalmon* vehicle constructed it is possible to carry out further work. The next sections discuss some areas where the work discussed in this thesis could be taken further.

8.2.1 Modelling and Simulation

During the experimental trials of the *RoboSalmon* one characteristic that has been observed is the presence of recoil motion which exceeded anticipated levels.. Modelling of the recoil motion has been undertaken to make the simulated recoil motion as accurate as possible but from the model validation results it can be seen that improvements could be made. This could lead to a simulation study on methods that could be implemented to reduce the recoil motion.

Another aspect which would improve the modelling would be to validate the model in the full six degrees of freedom. Due to the restrictions of the experimental hardware and size of the test pool available the results obtained only allow for validation of the model in four degrees of freedom – surge, sway, roll and yaw. If a larger test pool was available then it would be possible to conduct further experiments into the depth control of the *RoboSalmon* vehicle and thus facilitate validating the model in the remaining two degrees of freedom – heave and pitch.

The main focus of the modelling and simulation carried out in the project has been to create a simplified model that predicts the performance of the *RoboSalmon* vehicle using the tendon drive propulsion system and the propeller/rudder system. One area of the model which could be improved would be the use of Computational Fluid Dynamics (CFD) to gain a better understanding of the thrust and drag forces produced by the tendon drive system during swimming.

8.2.2 Further Experimentation with *RoboSalmon*

With the current *RoboSalmon* hardware platform it would be possible to conduct numerous additional trials and experiments with only minor firmware changes required. This was one of the main aims when designing the *RoboSalmon*; to develop a flexible modular platform that could be adapted as required for different experiments.

Using the existing tail systems (the tendon drive and propeller/rudder systems) further experimentation could be conducted in a number of areas including investigation into more open loop manoeuvres.

Development of the hardware for the individually actuated segmented tail discussed in Chapter 7 could also be undertaken. This new tail, in conjunction with the existing body and experimental set up, would then allow for experimentation with the system to be conducted to allow for validation of the mathematical model and evaluation of the performance of this design of tail actuation system.

8.3 Improvements to *RoboSalmon* Platform and System

One of the main areas where improvements could be made to the *RoboSalmon* vehicle is in the IMU. The current IMU uses MEMs rate gyroscopes and accelerometers to measure the angular rates and accelerations in the six degrees of freedom. The processing used on the sensor reading consists of hardware low pass filtering of the data on the board and some simple post-processing of the data after each trial. For the short experimental run times used (<32 seconds) the errors present in the reading due to drift present in the MEMs devices and the integration errors are within acceptable limits. However, if increased run time is required then improvements would be required to the IMU to reduce the errors. This could take the form of additional processing of the data perhaps using a Kalman filter or the use of a more accurate low drift sensors or the use of a Commercially-available Off- The Shelf (COTS) IMU.

During the design of the current *RoboSalmon* vehicle rigid servo driven pectoral fins were included with the aim of using them as dive planes to allow for an investigation into depth control of the

vehicle. Testing of these fins showed that they did not provide sufficient downward force to cause the vehicle to dive. This was due to a number of factors including the maximum surge speed obtainable from the tendon drive not being sufficient and also because of the oscillatory nature of the recoil motion of the vehicle which prevented a steady flow of water over the surfaces of the dive planes. Therefore, an alternative depth control system could be investigated such as the use of a miniature compressed variable ballast system or a swim bladder type to allow for the depth of the vehicle to be controlled. Another approach that could be investigated for depth control, which is used by some fish species, is to pitch the tail system with respect to the body to produce the forces necessary for diving.

One additional modification that would be beneficial to the *RoboSalmon* platform would be to redesign the layout of the circuit boards within the vehicle using surface mount components and a multi-layered printed circuit. This would lead to more compact printed circuit boards and could perhaps allow for the option of a small payload, such as additional sensors, to allow for further experimentation.

References

- Alexander, R.M., 2002. *Principals of Animal Locomotion*. Princeton New Jersey, Princeton University Press.
- Altringham, J.D., & Johnston, I.A., 1990. Scaling Effects on Muscle Function: Power Output of Isolated Fish Muscle Fibres Performing Oscillatory Work. *Journal of Experimental Biology*, Vol.151, pp. 453-467.
- Alvarado, P.V., & Youcef-Toumi, K., 2006. Design of Machines with Compliant Bodies for Biomimetic Locomotion in Liquid Environments. *Journal of Dynamic Systems, Measurement and Control*, Vol. 128 (1), pp. 3-11.
- Analog Devices, *Data sheet ADXRS300EB*, $\pm 300^\circ/\text{s}$ Single Chip Rate Gyro Evaluation Board.
- Anderson, J., 1978. *An Introduction to Flight: its Engineering and History*. 2nd Ed. London, McGraw/Hill.
- Anderson, M.J. & Kerrebrock, P.A., 1999. The Vorticity Control Unmanned Undersea Vehicle [VCUUV]: An Autonomous Robot Tuna. *11th International Symposium on Unmanned Untethered Submersible Technology*, Durham NH.
- Anderson, J.M. & Chhabra, N.K., 2002. Manoeuvring and Stability Performance of a Robotic Tuna. *Integrative and Comparative Biology*, Vol. 24, pp.118-126.
- Bainbridge, R., 1958. The Speed of Swimming of Fish as Related to Size and to the Frequency and Amplitude of the Tail Beat. *Journal of Experimental Biology*, Vol. 35, pp. 109-133.
- Bakaric, V., Vukic, Z., Antonic, R., 2003, Scope and Application of Reconfigurable Control, *Proceedings of the 11th Mediterranean Conference on Control and Automation*, Greece, pp. 6
- Ballard, R.D., Yoerger, D.R., Stewart, W.K., & Bowen, A., 1991. Argo/Jason: A Remotely Operated Survey And Sampling System For Full-ocean Depth. *Proceedings of the Ocean's '91. Conference: Oceans Technologies and Opportunities in the Pacific for the 90's*, 1st-3rd Oct 1991, Vol. 1, pp. 71-75.
- Bar-Cohen, Y., 2003. Biologically Inspired Intelligent Robotics. *Proceedings of the SPIE Smart Structures Conference*, San Diego, Paper 5051-02.
- Bar-Cohen, Y., 2005. Biomimetics: mimicking and inspired-by biology. *Proceedings of the SPIE Smart Structures Conference*, Jet Propulsion Lab, California Institute of Technology, San Diego, CA., SPIE Vol. 5759-02.

- Bar-Cohen, Y., 2006. Biomimetics: Using nature as an inspiring model for human innovation. *Journal of Bioinspiration & Biomimetics*, Vol 1, Issue 1, pp 1-12
- Barrett, D.S., Triantafyllou, M.S., Yue, D. K. P., Grosenbaugh, M.A., & Wolfgang, M.J., 1999. Drag reduction in fish-like locomotion. *Journal of Fluid Mechanics*, Vol. 392, pp. 183-212.
- Bechtel, W., Abrahamsen, A., 1991, *Connectionism and the Mind An Introduction to Parallel Processing in Networks*, Basil Blackwell Inc.
- Benson, H., 1996. *University Physics*. Revised ed. USA, John Wiley & Sons, Inc.
- Behnke, S., Schreiber, M., Stuckler, J., Renner, R., & Strasdat, H., 2006. See, walk, and kick: Humanoid robots start to play soccer. *6th IEEE-RA S International Conference on Humanoid Robots*, Geneva, 4-6th Dec. 2006, pp. 497-503.
- Blidberg, D. R., 2001. The Development of Autonomous Underwater Vehicles (AUV): A Brief Summary. *Proceedings of IEEE/ ICRA 2001 Conference*, 21-26th May 2001, Seoul Korea.
- Bingham, D., Drake, T., Hill, A., & Lott, R., 2002. The application of autonomous underwater vehicle (AUV) technology in the oil industry -vision and experiences. In *FIG XXII International Congress*, Washington, USA.
- Bone, Q., & Moore, R.H., 2008. *Biology of Fishes*. 3rd Ed., New York, Taylor & Francis.
- Boston Dynamics Website: <http://www.bostondynamics.com> (Accessed 2008).
- Boston Engineering Corporate Website: <http://www.boston-engineering.com> (Accessed 2009).
- Bulgin Website: <http://www.bulgin.co.uk> (Accessed 2007).
- Burcher, R. & Rydill, L., 1994. *Concepts in Submarine Design: Cambridge Ocean Technology Series 2*. Cambridge UK, Cambridge University Press.
- Brierley, A. S., Fernandes, P.G., Brandon, M, A., Armstrong, F., Millard, N. W., McPhail, S.D., Stevenson, P., Pebody, M., Perrett, J., Squires, M., Bone, D.G., Griffiths, G., 2003. An investigation of avoidance by Antarctic krill of RRS James Clark Ross using the Autosub-2 autonomous underwater vehicle. *Fisheries Research*, Vol. 60, pp. 569–576.
- BSI, Website <http://www.bsigroup.com> (accessed 2007).
- Carlton, J, 2007, *Marine Propellers and Propulsion*, 2nd Ed, Oxford UK, Elsevier Ltd,
- Cavallo, E., Micheli, R.C., & Filaretov, V.F., 2003. Conceptual Design of an AUV Equipped with a Three Degrees of Freedom Vectored Thruster. *Journal of Intelligent and Robotic Systems*, vol. 39, pp. 365–391.
- Chopra, M.G., 1974. Hydromechanics of lunate-tail swimming propulsion. *Journal of Fluid Mechanics*, Vol. 64 (2), pp. 375-391.

- Colgate, J.E., & Lynch, K.M., 2004. Mechanics and Control of Swimming: A review. *IEEE Journal of Oceanic Engineering*, Vol. 29 (3), pp. 660-673.
- Collar P.G., & McPhail, S.D., 1995. Autosub: an autonomous unmanned submersible for ocean data collection. *Electronics & Communication Engineering Journal*, Vol. 7 (3), pp. 105-114.
- Corfield, S., & Hillenbrand, C., 2003. Defence Applications for Unmanned Underwater Vehicles. In: G. Griffiths, ed. *Technology and Applications of Autonomous Underwater Vehicles*. London, Taylor & Francis, Ch.10, pp.161.
- Cousteau Society Website: <http://www.cousteau.org> (Accessed 2009).
- Crespi, A., Badertscher, A., Guingard, A., & Ijspeert, A.J., 2005. Swimming and Crawling with an Amphibious Snake Robot. *Proceedings of the 2005 IEEE International Conference on Robotics and Automation*, 18-22 April 2005, pp. 3024-3028.
- Dickinson, M.H., 1999. Bionics: Biological insight into mechanical design. *Proceedings of the National Academy of Sciences of the United States of America*, Vol. 96 (25), pp.14208-14209.
- Drucker, E. G., & Lauder, G. V., 1999. Wake structure and force in slow and fast fishes swimming fish: three-dimensional vortex wake dynamics quantified using digital particle image velocimetry. *Journal of Experimental Biology*, vol. 202 (18), pp.2393-2412.
- Dutton, K., Thompson, S., & Barraclough, B., 1998. *The Art of Control Engineering*, Reading MA, Addison-Wesley.
- El Daou, H., Guinot, J. C., Libourel, P.A., Renous, S., & Bels, V., 2008. Biomimetic Approach for Tortoise Like Robot Modelling and Control. In: L. Marques, et al., Ed. 2008. *Advances in Mobile Robotics*. USA, World Scientific Publishing Co., Sec. 4, pp. 182-189.
- Eriksen, C.C, Osse, T.J., Light, R.D., Wen, T., Leham, T.W., Sabin, P.L., Ballard, J. W., & Chiodi, A.M., 2001. Seaglider: a long-range autonomous underwater vehicle for oceanographic research. *IEEE Journal of Oceanic Engineering*, Vol. 26 (4), pp. 424-436.
- Fish, F.F., 1998. Imaginative solutions by marine organisms for drag reduction. *Proceedings of the Eleventh International Symposium on Unmanned Untethered Submersible Technology (UUST)*. Autonomous Undersea Systems Institute, Lee, NH.
- Fish, F. E., 2002. Balancing requirements for stability and manoeuvrability in cetaceans. *Journal of Integrated Comparative Biology*, Vol. 42, pp. 85-93.
- Fish, F.E., Lauder, G.V., Mittal, R., Techet, A.H., Triantafyllou, M.S., Walker, J.A., & Webb, P.w., 2003. Conceptual Design for the Construction of a Biorobotic AUV Based on Biological Hydrodynamics. *Proceedings of the 13th International Symposium on Unmanned Untethered Submersible Technology*. Autonomous Undersea Systems Institute, Durham New Hampshire.

- Fossen, T.I., 1995. *Guidance and Control of Ocean Vehicles*. West Sussex UK, John Wiley & sons Ltd.
- Fossen, T.I., 2002. *Marine Control Systems*. Norway, Marine Cybernetics.
- Franklin, G., Powell J., Emama-Naeini, A, 1991. *Feedback Control of Dynamic Systems*. 2nd Edition, USA, Addison-Wesley Publishing Company
- Freescale Semiconductor Website: <http://www.freescale.com> (Accessed 2008).
- Gerr, D., 2001. *Propeller handbook: The complete Reference for Choosing, Installing and Understanding Boat Propellers*. 2nd ed. Maine USA, International Marine.
- Goett, H.J., & Bullivant, W.K., 1938. *Tests of N.A.C.A. 0009, 0012, and 0018 Airfoils in the Full-scale Tunnel*. Report no:675, pp. 639-649.
- Gonzalez, R.C., Woods, R., & Eddins, S., 2004. *Digital Image Processing Using Matlab*. New Jersey USA, Pearson Prentice Hall.
- Gibson, R.J., 1993. The Atlantic salmon in fresh water: spawning, rearing and production. *Reviews in Fish Biology and Fisheries*, Vol. 3, pp. 39-73.
- Gravagne, I.A., Rahn, C.D., & Walker, I.D., 2001. Good Vibrations: Vibration Damping Setpoint Controller for Continuum Robots. *Proceedings of the IEEE International Conference on Robotics and Automation 2001*, Vol. 4, pp. 3877-3884.
- Graver, J.G., 2003. Underwater Glider Model Parameter Identification. *Proceedings of the 13th International Symposium on Unmanned Untethered Submersible Technology*, August 2003, Durham, NH.
- Gray, J., 1936. Studies in Animal Locomotion : VI. The Propulsive Powers of the Dolphin. *Journal of Experimental Biology*, Vol. 13, pp. 192-199.
- Gray, G., 1992. *Development and Validation of Nonlinear Models for Helicopter Dynamics*, PhD Thesis, Department of Electronic and Electrical Engineering, University of Glasgow.
- Gray, G.J., Murray-Smith, D.J., Yun, L., & Sharman, K.C., 1998. Nonlinear model structure identification using genetic programming. *Control Engineering Practice*, 1998 (6), pp 1341 – 1352.
- Griffiths, G. ed., 2003. *Technology and Applications of Autonomous Underwater Vehicles*. London, Taylor & Francis.
- Griffiths, G., Jones, C.P., Ferguson, J. & Bose, N., 2007. Undersea Gliders. *Journal of Ocean Technology 2007*.
- Griffiths, G., Millard, N.W., Stevenson, P., McPhail, S.D., Pebody, M., Perrett, J.R., Webb, A.T., Squires, M., & Harris, A.J.K., 1999. AUTOSUB – Results from the First 200 Missions. Paper

presented at: *AUV Technological: Commercial Viability and Technological Achievements, IBC Global Conferences Ltd*, London, 7 -8th December 1999.

Hitec RCD Website: <http://www.hitecrd.com> (Accessed 2007).

Humphrey, D., & Topping, J., 1961. *A Shorter Intermediate Mechanics*. London, Longmans.

Hoar W.S., & Randall, D.J., 1978. *Fish Physiology: Volume VII*. New York, Academic Press, Inc.

Hoerner, S.F., 1965. *Fluid-dynamic drag: practical information on aerodynamic drag and hydrodynamic resistance*, New Jersey, Brick Town.

HydroComp Inc, 2003, *When Does Shallow Water Become A Problem?*, Technical Report 124, <http://www.hydrocompinc.com/knowledge/whitepapers/HC124-ShallowWater.pdf>

Ibrahim, D. 2008. *Advanced PIC Microcontroller Projects in C: From USB to RTOS with the PIC18F Series*. Oxford, Elsevier Ltd.

IEEE Spectrum Magazine: <http://www.spectrum.ieee.org/robotics/military-robots/defense-contractors-snap-up-submersible-robot-gliders>, September 2008.

Imlay, F.H., 1961. *The Complete Expressions for "Added Mass" of a Rigid Body Moving in an Ideal Fluid*. Virginia, USA, Hydromechanics Laboratory Research and Development Report.

International Oceans Systems, Underwater Magazine 2003: <http://www.intoceansys.co.uk/profile.php> (Website Accessed 2008).

InvenSense, 2008: http://www.invensense.com/shared/pdf/DS_IDG300.pdf Datasheet IDG-300 Dual Axis Gyroscope .

Jalving, B., 1999. Depth accuracy in seabed mapping with underwater vehicles. *Proceedings of the Oceans '99 MTS/IEEE Conference –Riding the Crest into the 21st Century*, 13-16th September 1999, Seattle, Vol. 2, pp. 973-978.

Kermode, A.C., 1987. *Mechanics of Flight*. 9th Ed. Essex, UK, Longman Scientific & Technical.

Kim, E., Youm, Y., 2004. Design and Dynamic Analysis of Fish Robot: PoTuna. *Proceedings of the 2004 IEEE International Conference on Robotics & Automation*, New Orleans.

Kim, E., Youm, Y., 2005. Simulation Study of Fish Swimming Modes for Aquatic Robot System. *Proceedings of the IEEE 12th International Conference on Advanced Robotics, ICAR '05*, pp.39-44.

Kirkwood, W., 2007. AUV Technology and Application Basics. *Slides from Tutorial session- Oceans 2007 Conference*, Vancouver, 29th Sep- 4th Oct 2007.

Kemp, M., Hobson, B., & Long, J.H., 2005. Madeline: An Agile AUV Propelled by Flexible Fins. *Proceedings of the 14th International Symposium on Unmanned Untethered Submersible Technology (UUST)*. Autonomous Undersea Systems Institute, Lee, New Hampshire, USA.

- Lai, P.S.K., 1990. *Oscillating Foil Propulsion*. PhD Thesis, University of Glasgow.
- Lauder, G.V., Drucker, E.G., 2002. Forces, Fishes, and Fluids: Hydrodynamic Mechanisms of Aquatic Locomotion. *News Physiol Sci*, Vol. 17: pp. 235-240.
- Lauder, G.V., Drucker, E.G., 2004. Morphology and Experimental Hydrodynamics of Fish Fin Control Surfaces. *IEEE Journal of Oceanic Engineering*, Vol. 29 (3), pp.556-571.
- Lauder G.V. & Drucker, 2004. Morphology and experimental hydrodynamics of fish fin control surfaces. *IEEE Journal of Oceanic Engineering*, Vol. 29, Issue 3, pp. 556-571.
- Lauder, G.V. & Madden, G.A., 2006. Learning from Fish: Kinematics and Experimental Hydrodynamics for Roboticians. *International Journal of Automation and Computing 4 (2006)*, pp. 325-326.
- Leonard, N.E., & Graver, J.G., 2001. Model-based feedback control of autonomous underwater gliders, *IEEE Journal of Oceanic Engineering*, Vol.26 (4), pp.633-645.
- Lewis, F., Jagannathan, S., Yeşildirek, A., 1999, *Neural Network Control of Robot Manipulators and Nonlinear Systems*, Taylor & Francis, UK
- Lighthill, M.J., 1960. Note on the swimming of Slender Fish. *Journal of Fluid Mechanics*, Vol. 9, pp. 305–317
- Lighthill, M.J., 1971. Large-amplitude elongated-body theory of fish locomotion. *Proceedings of the Royal Society of London*, Vol. 179, pp.125-138.
- Liu, J., Dukes, I., Knight, R., & Hu, H., 2004a. Development of Fish-like Swimming Behaviours for an Autonomous Robotic Fish. *IEE, Proceedings of the Control 2004*, ID217.
- Liu, J., & Hu, H., 2004b. Building a 3D Simulator for Autonomous Navigation of Robotic Fishes. *IEEE/RSJ International Conference on Intelligent Robots and Systems (IROS)*, pp. 613-618.
- Liu, J., Dukes, I., & Hu, H., 2005a. Novel Mechatronics Design for a Robotic Fish. *IEEE/RSJ International Conference on Intelligent Robots and Systems (IROS)*, Edmonton, Canada, pp. 2077-2082.
- Liu, J., & Hu, H., 2005b. Mimicry of Sharp Turning Behaviours in a Robot Fish. *IEEE/RSJ International Conference on Robotics and Automation*, Barcelona, Spain, pp. 3318-3323
- Listak, M. Martin, G. Pugal, D. Aabloo, A. Kruusmaa, M. Marthinussen, R., Vestgard, K., 2005, Design of a Semiautonomous Biomimetic Underwater Vehicle for Environmental Monitoring, *Proceedings of the International Symposium of Computational Intelligence in Robotics and Automation*, pp. 9-14
- Klepaker, K.A., & Storkersen, N., 2004. HUGIN-AUV Concept and Operational experiences to date. *Proceedings of Oceans '04 MITS/IEEE Techno-Ocean '04*, Japan, 9-12 Nov 04, Vol. 2, pp. 846-850.

Martins, A., Matos, A., Cruz, N., & Pereira, F.L., 1999. IES an open system for underwater inspection. *Proceedings from OCEANS '99 MTS/IEEE: Riding the Crest into the 21st Century*, Seattle, 13-16 Sep 1999, Vol. 2, pp. 549-554.

Mathworks Website: <http://www.mathworks.co.uk/> (Accessed 2007).

Mazumdar, A., Alvarado, P.V. Y., & Youcef- Toumi, K., 2008. Manoeuvrability of a Robotic Tuna with Compliant Body. *Proceedings from IEEE International Conference on Robotics and Automation*, USA, 19-23 May 2008, pp. 683- 688.

- (a) Matko, D., Karba, R., Zupancic, B., 1992. *Modelling and Simulation of Continuous Systems*. New York, Prentice Hall.

MBARI Website: <http://www.mbari.org> (Accessed 2007).

McIssac, K.A., & Ostrowski, J.P., 2003. Motion Planning for Angulliform Locomotion. *IEEE Transactions on Robotics and Automation*, Vol. 19 (4), pp. 637-652.

MFA ComoDrills Website: http://www.mfacomodrills.com/gearboxes/919d_series.html (Accessed 2008).

Morgansen, K.A. Duidam, V. Mason, R.J. Burdick, J.W. Murray, R.M, 2001, linear control methods for planar carangiform robot fish locomotion, *Proceedings of the International Conference on Robotics and Automation*, Vol. 1, pp. 437-434

Morgansen, K.A., Triplett, B.I., & Klien, D.J., 2007. Geometric Methods for Modeling and Control of Free-Swimming Fin-Actuated Underwater vehicles, *IEEE Transactions on Robotics*, Vol.6, pp.1184-1199.

Michel, J.L., & Ballard, R.D., 1994. The RMS Titanic 1985 Discovery Expedition. *Proceedings of the IEEE Oceans Conference*, 13-16th September 1994, Vol. 3, pp. 132-137.

Microchip Technology Inc. *Datasheet DSPIC30F4013*:

<http://ww1.microchip.com/downloads/en/DeviceDoc/70138F.pdf> (Accessed 2007).

Microchip Technology Inc. *Datasheet PIC18F2480*:

<http://ww1.microchip.com/downloads/en/DeviceDoc/39637c.pdf> (Accessed 2008).

MIT RoboTuna II Webpage: <http://web.mit.edu/towtank/www/Tuna/Tuna2/tuna2.html> (Accessed 2007).

Moyle, P.B., & Cech, Jr., J.J., 2004. *Fishes: An Introduction to Ichthyology*. 5th Edition, USA, Prentice Hall, Inc.

Murray-Smith, D.J., 1995. *Continuous System Simulation*. London, Chapman & Hall.

Niku, S.B., 2001. *Introduction to Robotics: Analysis, Systems, Applications*. New Jersey, Prentice Hall.

- Norcross, B.L., & Mueter, F.J., 1999. The use of an ROV in the study of juvenile flatfish. *Fisheries Research*, Vol. 39 (3), pp. 241-251.
- Paap, K.L., Christaller, T., & Kirchnre, F., 2000. A robot snake to inspect broken buildings. *Proceedings of the 2000 IEEE/RSJ International Conference on Intelligent Robots and Systems*, Japan, 31 Oct – 5 Nov 2000, Vol. 3, pp. 2079 – 2082.
- Pazuk, K., 1999. AN713: Controller Area Network (CAN) Basics. *Microchip Technology Inc.*, <http://ww1.microchip.com/downloads/en/AppNotes/00713a.pdf>
- Pedley, T.J., Hill, S.J., 1999. Large-Amplitude Undulatory Fish Swimming: Fluid mechanics Coupled to Internal Mechanics. *The Journal of Experimental Biology*, Vol. 202 (23), pp. 3431-3438.
- Perez, T., 2005. *Ship motion control: course keeping and roll stabilisation using rudder and fins*. Germany, Springer-Verlag London Limited.
- Pettersen, K.Y., & Egeland, O., 1996. Exponential stabilization of an underactuated surface vessel. *Proceedings of the 35th IEEE conference on Decision and Control*, Japan, 11-13 Dec 1996, Vol. 1, pp. 967-972.
- Piotrowski, J., 2008. *A Fin Tuned design*. The Economist, Nov 19th 2008.
- Podder, T.K., Sibenac, M., Thomas, H., Kirkwood, W.J., & Bellingham, J.G., 2004. Reliability Growth of Autonomous Underwater Vehicle – Dorado. *Proceedings of Oceans 2004 MTS/ IEEE Conference, 9th – 12th November 2004*, vol. 2, pp.856 – 862.
- Pololu Website: http://www.pololu.com/file/0J37/ssc03a_guide.pdf (Accessed 2008).
- Purcell, M., Von Alt, C., Allen, B., Austin, T., Forrester, N., Goldsborough, R., & Stokey, R., 2000. New Capabilities of the REMUS Autonomous Underwater Vehicle. *Proceedings from the Oceans 2000 MTS/IEEE Conference and Exhibition*, USA, 11-14 Sep 2000, Vol. 1, pp. 147-151.
- Rapid Electronics Website: <http://www.rapidonline.com> (Accessed 2008).
- Reap Systems, Company Website: <http://www.reapsystems.co.uk/> (Accessed 2009)
- Rives, P., & Borrelly, J. J., 1997. Underwater pipe inspection task using visual servoing techniques. In *Proceedings of the 1997 IEEE/RSJ International Conference on Intelligent Robots and Systems, IROS '97*. September, 1997, Vol. 1, pp. 63–68.
- RF Solutions Ltd: (Accessed 2007),
http://www.rfsolutions.co.uk/acatalog/FM_T7G_R7G_Modules.html
- Roberts, G.N., & Sutton, R., 2006. *Advances in Unmanned Marine Vehicles*. Hertfordshire, The Institution of Electrical Engineers.
- Rudnick, D.L., Davis, R.E., Eriksen, C.C., Fratantoni, D.M., & Perry, M.J., 2004. Underwater Gliders for Ocean Research. *Marine Technology Society Journal*, Vol. 38 (1), pp.48 -59.

- Sargent, R.G., 2005. *Verification and Validation of Simulation Models*. Proceedings of the 37th Winter Simulation Conference, Orlando, Florida, pp. 130-143.
- Saunders, A. Nahon, M., 2002, The effect of forward vehicle velocity on through-body AUV tunnel thruster performance, MTS/IEEE Oceans 2002, 29th-31st Oct 2002, Vol. 1, pp. 250-259
- Schwarzenbach, J., & Gill, K.F., 1992. *System Modelling and Control*. 3rd Ed., London, Butterworth-Heinemann.
- Schultz, W.W., & Webb, P.W., 2002. Power Requirements of Swimming: Do New Methods Resolve Old Questions? *Journal of Integrative and Comparative Biology*, Vol. 42 (5), pp. 1018-1025.
- Seabotix Website: <http://www.seabotix.com> (Accessed 2009).
- Sfakiotakis, M., Lane, D.M., & Davies, J.B.C., 1999. Review of Fish Swimming Modes for Aquatic Locomotion. *IEEE Journal of Oceanic Engineering*, Vol. 24 (2), pp. 237-252.
- Shan, Y., & Koren, Y., 1993. Design and Motion of a Mechanical Snake. *Proceedings of IEEE Transactions on Systems, Man and Cybernetics*, Vol.23 (4), pp. 1091-1100.
- Sherman, J., Davis, R.E., & Owens, W.B., & Valdes, J., 2001. The autonomous underwater glider "Spray." *IEEE Journal of Oceanic Engineering*, Vol. 26 (4), pp.437-446.
- Sibenac, M., Kirkwood, W.J., McEwen, R., Shane, F., Henthorn, R., Gashler, D., & Thomas, H., 2002. Modular AUV for routine deep water science operations. *Proceedings of the Oceans '02 MTS/IEEE Conference*, Vol.1, pp. 167-172.
- SMD Hydrovision Website: <http://www.smd.co.uk> (Accessed 2009).
- Solan, M., Cardinale, B.J., Downing, A.L., Engelhardt, K.A.M., Ruesink, J.L., & Srivastava, D.S., 2004. Extinction and Ecosystem Function in the Marine Benthos. *Science*, Vol. 306 (5699), pp. 1177-1180.
- Sony 2005, Instruction manual for DCR19E Mini DV Camcorder: <http://www.sony.co.uk/section/home>
- Spancion Website (Accessed 2008): <http://www.spancion.com/Products/Pages/ProductDetails.aspx?ProdID=S25FL128P>
- Sparkfun Electronics Website: <http://www.sparkfun.com/commerce/categories.php> (Accessed 2008).
- Sparenberg, J.A., 2002. Survey of the mathematical theory of fish locomotion. *Journal of Engineering Mathematics*, Vol. 44 (4), pp. 395-448.
- Stich, T.J., Sporre, J.K., Velasco, T., 2000, The Application of Artificial Neural Networks to Monitoring and Control of an Induction Hardening Process, *Journal of Industrial Technology*, Vol 16, No 1, pp. 1-16.

- Streitlien, K., & Triantafyllou, G.S., 1998. On Thrust Estimates for Flapping Foils. *Journal of Fluids and Structures*, Vol. 12, pp.47-55.
- Stremmer, F.G., 1992, *Introduction to Communication Systems*, 3rd Ed, Addison Wesley
- Sze, S.M., 2002. *Semiconductor Devices: Physics and Technology*. 2nd Ed., New York, John Wiley & Sons Inc.
- Tang, J., & Wardle, C.S., 1992. Power Output of Two Sizes of Atlantic Salmon (*Salmo Salar*) at Their Maximum Sustained Swimming Speeds. *Journal of Experimental Biology*, Vol. 166, pp. 33-46.
- Techet, A.H., Hover, F.S., & Triantafyllou, M.S., 2003. Separation and Turbulence Control in Biomimetic Flows. *Journal of Flow, Turbulence and Combustion*, Vol. 71, pp. 105-118.
- Terada Y., & Yamamoto, I., 2006. Robotic Fish and its Application. *2006 IEEE International Symposium on Industrial Electronics*, 9-13 July 2006, Vol. 4, pp. 3062-3065.
- Titterton, D. & Weston, J., 1997. Strapdown Inertial Navigation Technology, *IEE Radar, Sonar, Navigation and Avionics*, No 5, IEE.
- Triantafyllou, G., Triantafyllou, M.S., & Grosenbaugh, M.A. , 1993. Optimal thrust development in oscillating foils with application to fish propulsion. *Journal of Fluids Structure*, Vol. 7, pp. 205–224.
- Triantafyllou, M.S., & Triantafyllou, G.S., 1995. An Efficient Swimming Machine. *Scientific American*, Vol. 272 (3), pp. 64-71.
- Triantafyllou, M.S., Triantafyllou, G.S., & Yue, D.K.P., 2000. Hydrodynamics of Fishlike Swimming. *Annual Review of Fluid Mechanics*, Vol. 32, pp. 33-53.
- Triantafyllou, M.S., Techet, A.H., & Hover, F.S., 2004. Review of Experimental Work in Biomimetic Foils. *IEEE Journal of Oceanic Engineering*, Vol. 29 (3), pp. 585-594.
- Tuck, K., 2007. Implementing Auto-Zero Calibration Technique for Accelerometers. *Application note for Freescale Semiconductor, Inc.*
- Tupper, E.C., 2004. *Introduction to Naval Architecture: formerly Muckle's Naval Architecture for Marine Engineers*. 4th Ed. Oxford, Elsevier Butterworth – Heinemann
- Underwater Magazine, 2003: <http://www.underwater.com> (Accessed 2008).
- University of Washington Website: <http://vger.aa.washington.edu/links.html> (Accessed 2008).
- US Navy SBIR Website: <http://www.navysbir.com> (Accessed 2009).
- Vasilescu, I, Kotay, K., Rus, D., Dunbabin, M., & Corke, P., 2005. Data Collection, Storage, and Retrieval with an Underwater Sensor Network. *Proceedings of the 3rd international conference on Embedded networked sensor systems*, California, USA, pp.154-165.
- Vaccaro, R.J., 1995. *Digital Control: A State-Space Control*. London, McGraw-Hill.

- Videler, J. J., 1993. *Fish Swimming: Fish and Fisheries Series 10*. London, Chapman & Hall
- Videler, J.J. & Wardle, C.S., 1991. Fish swimming stride by stride: speed limits and endurance. *Reviews in Fish Biology and Fisheries*, 1, pp.23-40.
- Vincent, J.F.V., 2003. Biomimetic modelling. *Proceedings of the Royal Society of London*, Vol. 358 (1437), pp. 1597 – 1603.
- Vestgard, K., 2003. The HUGIN Autonomous Underwater Vehicle Concept – The Innovation Pathway to Success. *Business Briefing: Exploration & Production*, pp. 1-3.
- Von Alt, C. J., Allen, B., Austin, T., & Stokey, R., 1994. Remote Environmental Measuring Units. *Proceedings of the Autonomous Underwater Vehicle Conference*, Cambridge, MA, 19-20 July 1994, pp.13-19.
- Von Alt, C.J., 2003. REMUS 100 Transportable Mine Countermeasure Package. *Proceedings of Oceans 2003 Conference*, 22-26 Sep 2003, Vol. 4, pp.1925-1930.
- Wardle, C. S., 1975. Limit of Fish Swimming Speed. *Nature*, Vol. 225, pp. 725-727.
- Watts, C, McGookin, E. & Macauley, M., 2007. Modelling and Control of a Biomimetic Underwater Vehicle with a Tendon Drive Propulsion System. *Proceedings of IEEE/OES Oceans 2007*, Aberdeen, 18-21 June 2007.
- Watts, C.M., McGookin, E & Macauley, M.. Biomimetic Propulsions Systems for Mini-Autonomous Underwater Vehicles. *Student Paper/Poster MTS/IEEE Oceans 2007*, Vancouver, Canada, 29th Sept – 4th Oct, 2007.
- Watts, C.M. & McGookin, E. Modelling and Simulation of a Biomimetic Underwater Vehicle. *Grand Challenges in Modelling and Simulation*, SummerSim'08, Edinburgh, 16th -19th June, 2008.
- Webb, P.W., 1971. The Swimming Energetics of Trout. *Journal of Experimental Biology*, Vol. 55, pp. 489-520.
- Webb, P.W., 1977. Effects of Median-Fin Amputation on Fast-Start Performance of Rainbow Trout (*Salmo Gairdneri*). *Journal of Experimental Biology*, Vol.68, pp. 123-135.
- Webb, D.C., Simonetti, P.J., & Jones, C.P., 2001. SLOCUM: An Underwater Glider Propelled by Environmental Energy. *IEEE Journal of Oceanic Engineering*, Vol. 26 (4), pp. 447- 452.
- Wernli, R.L., 2002. AUVs – A Technology Whose Time Has Come. *Proceedings of the 2002 International Symposium on Underwater Technology*, pp.309 -314.
- Whitcomb, L.L., 2000. Underwater Robotics: Out of the Research and into the Field. Proceedings of the IEEE 2000 International Conference on Robotics and Automation.
- WHOI Website: <http://www.whoi.edu> (Accessed 2009).

- Wolfgang, M.J., Anderson, J.M., Grosenbaugh, M.A., Yue, D.K., & Triantafyllou, M.S., 1999. Near-body Flow Dynamics in Swimming Fish. *The Journal of Experimental Biology*, Vol. 202, pp. 2303-2327.
- Wood, S., Rees, M., & Pfeiffer, Z., 2007. The Development of an Autonomous Underwater Powered Glider for Deep-Sea Biological: Chemical and Physical Oceanography. *Proceedings of OCEANS 2007 Conference – Europe*, Vol. 18 (2), pp.1-6.
- Worrall, K.J., & McGookin, E.W., 2006. A Mathematical Model of a Lego Differential Drive Robot. *Proceedings of 6th UKACC Conference*, Glasgow, 30th August – 1st September 2006.
- Wolf, M.I., Licht, S.C., Hover, F., & Triantafyllou, M.S., 2006. Open Loop Swimming Performance of ‘Finnegan’ the Biomimetic Flapping Foil AUV. *Proceedings of the Sixteenth International Offshore and Polar Engineering Conference*, San Francisco, May 28-June 2, 2006.
- Yamakita, M., Hashimoto, M., & Yamada, T., 2003. Control of locomotion and head configuration of 3D snake robot (SMA). *Proceedings of the ICRA '03 IEEE International Conference on Robotics and Automation*, Vol. 2, pp. 2055-2060.
- Yamamoto, I., Terada, Y., Nagamatu, T., Imaizum, Y., 1995. Propulsion System with Flexible/Rigid Oscillating Fin. *IEEE Journal of Oceanic Engineering*, Vol. 20 (1), pp. 23-30.
- Young, J.Z., 1962, *The Life of Vertebrates*. Second Ed. Oxford, Oxford University Press, pp 204-206.
- Young, H.D., & Freedman, R.A., 2000. *University Physics with Modern Physics*. 10th ed., USA, Addison –Wesley Longman, Inc.
- Yu, J., Wang, S., & Tan, M., 2003. Basic Motion Control of a Free-swimming Biomimetic Robotic Fish. *Proceedings of the 42nd IEEE Conference on Decision and Control*, Maui, Hawaii, December 2003, pp. 1268-1273.
- Yu, J., Tan, M., Wang, S., & Chen, E., 2004, Development of a Biomimetic Robotic Fish and Its Control Algorithm. *IEEE Transactions on Systems and Cybernetics – part B: Cybernetics*, Vol. 34 (4), pp.1798-1810.
- Yu, J., Wang, S., & Tan, M., 2005. A Simplified Propulsive model of a bio-mimetic robot fish and its realization. *Robotica*, Vol. 23, pp. 101-107.
- Yuh, J., 1995. Development in Underwater Robotics, *Proceedings of the 1995 IEEE International Conference on Robotics and Automation*, Japan, 21-27th May 1995, Vol. 2, pp. 1862-1867.
- Yuh, J., 2000, Design and Control of Autonomous Underwater Robots: A Survey, *Journal of Autonomous Robots*, Vol. 8, pp. 7-24.

Appendix A.1 RoboSalmon Circuit Schematics

This appendix contains the circuit schematics and brief operational description for all the electronic systems within the *RoboSalmon* vehicle.

Main Control Board

The main control board is located in the upper body enclosure and has the central PIC processor, data logger, IMU components and Buzzer. Due to the size of the circuit the layout is spread over two, two layer boards where are stacked in the upper body enclosure. The circuit reads the sensor values either directly through the ADC on the PIC or receives the data via the CAN bus. The sensor data is then stored in the FLASH memory of the data logger. The circuit schematic is shown in Figure A.1.1 for the lower circuit board and in Figure A.1.2 for the top circuit board.

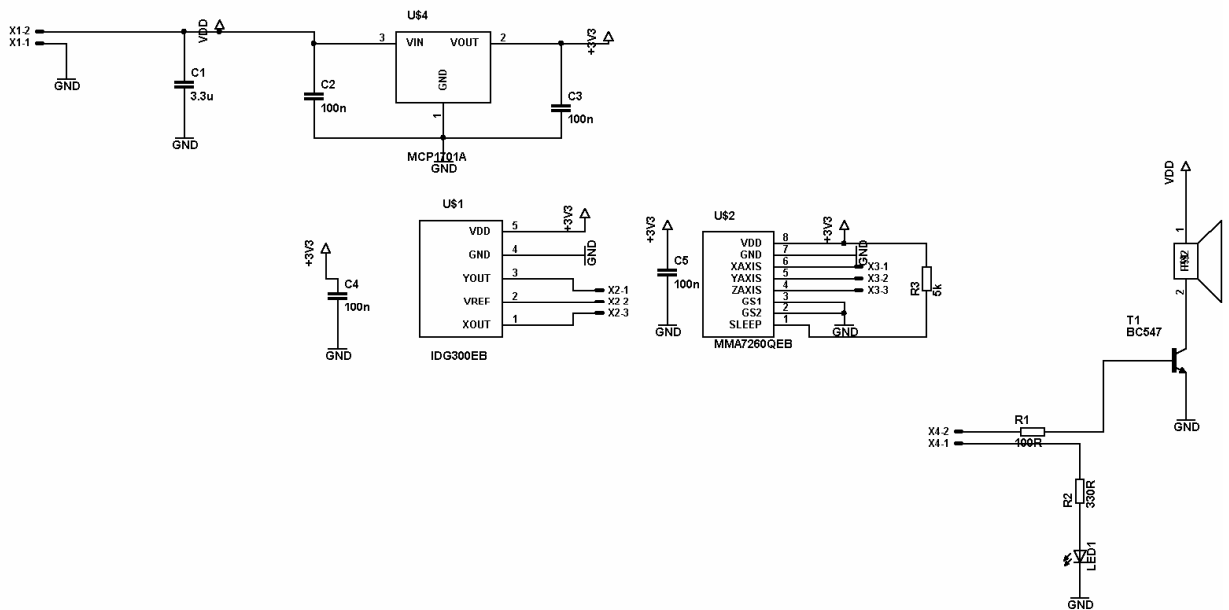


Figure A.1.1: Main control – lower circuit

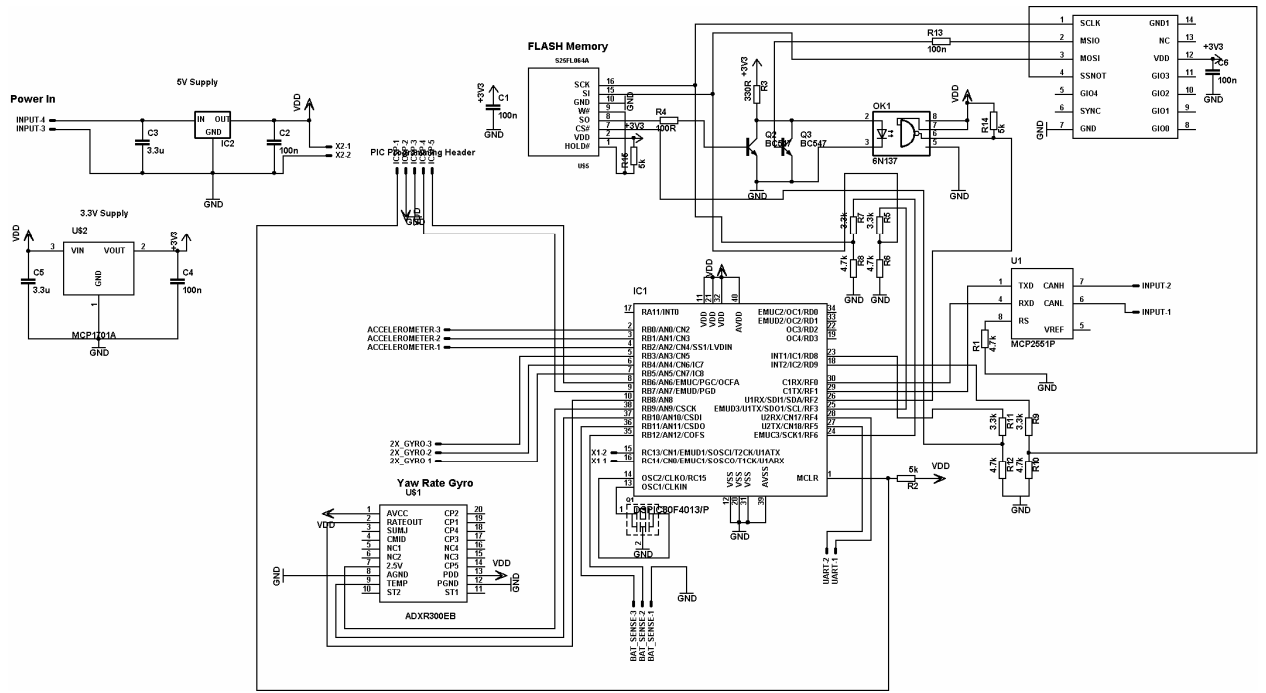


Figure A.1.2: Main control – top circuit schematic

Power Distribution/Current Logging

The power distribution/current logging circuit is located in the upper body enclosure. The function of this circuit is to provide power distribution in two channels; one to the body systems and one for the tail system. Each channel has current sense circuitry to allow for the current to be determined. There is also a potential divider circuit that divides down the battery voltage and allows for it to be measured. The circuit schematic is shown in Figure A.1.3.

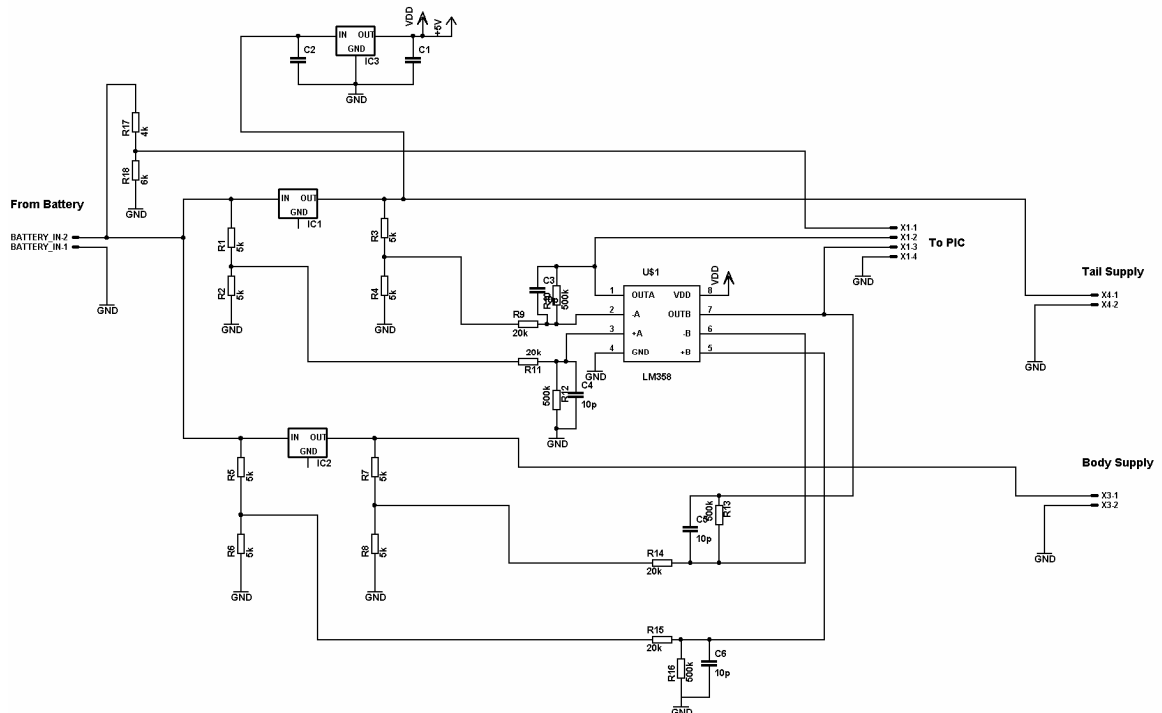


Figure A.1.3: Power distribution/ current logging circuit schematic

Fin and Head Control Board

The fin and head control board is located in the lower body enclosure and is responsible for receiving fin/head positional commands via the CAN bus, decoding the command and then outputting the required command to the servo control board. The circuit schematic is shown in Figure A.1.4.

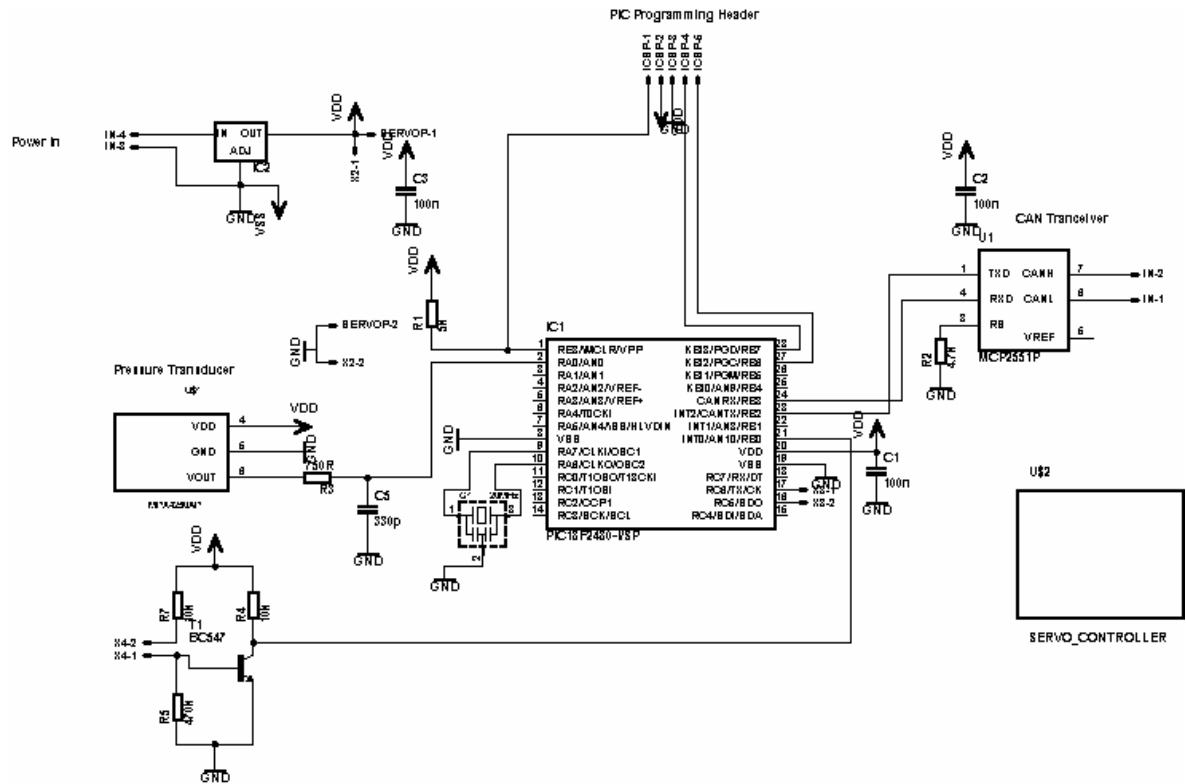


Figure A.1.4: Fin and head control circuit schematic

RF Receiver Head Circuit

The RF Receiver Head circuit is located in the head enclosure at the front of the *RoboSalmon* vehicle. The function of this circuit is to receive RF commands sent from the Remote Control unit. When a RF command is received it is decoded by the RF decoder IC which then passes the received decoded data in serial format to the PIC. The PIC then processes this data and then sends the appropriate commands out via the CAN Bus. Due to the space restrictions within the head enclosure the circuit is spread over two stacked PCBs. The circuit schematic is shown in Figure A.1.5 for the lower circuit board and in Figure A.1.6 for the top circuit board.

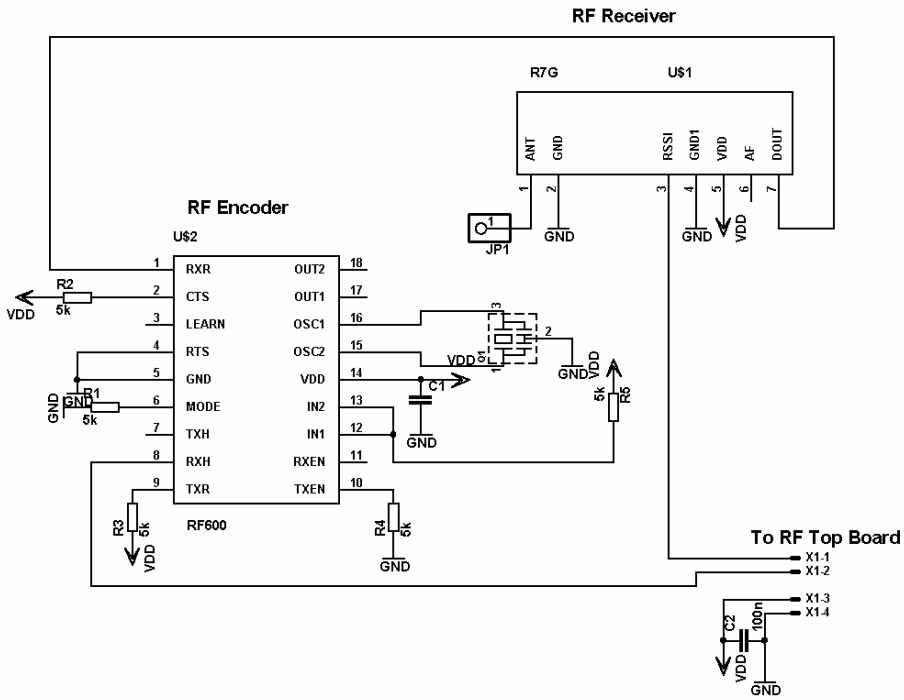


Figure A.1.5: RF receiver head circuit schematic (lower board)

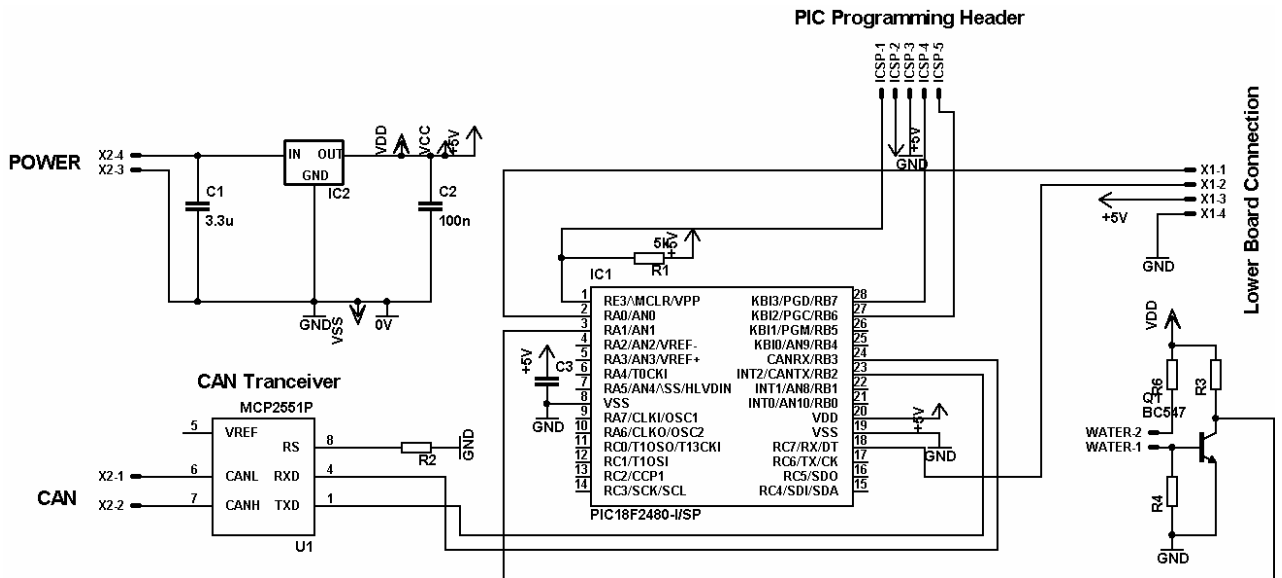


Figure A.1.6: RF receiver head circuit schematic (top board)

Tendon Drive Control Board

The Tendon drive Control circuit is located in the tendon drive tail assembly. The function of this circuit is to receive commands relating to the control of the tail via the CAN bus. These commands allow the tail beat frequency, amplitude and offset to be set.

When the circuit receives a command it calculates how this command should be implemented in terms of direct control of the servo motor. The circuit is also responsible for determining the current tail position using the potentiometer connected to the tail and transmitting this value across the CAN Bus. The circuit schematic is shown in Figure A.1.7.

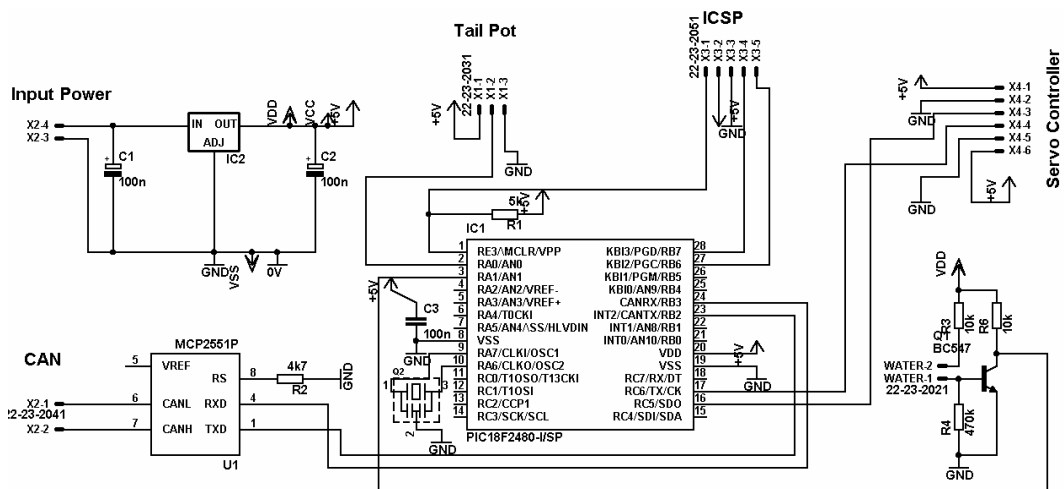


Figure A.1.7: Tendon drive control board schematic

Appendix A.2 – Propeller System Bollard Pull Test Results

As discussed in Chapter 3 the purpose of the bollard pull test is to obtain an estimate of the thrust produced by the propeller. Determination of the thrust produced allows for more accurate modelling of the propeller system and allow for the swimming power of the vehicle to be established. This in turn will facilitate the comparison of the biomimetic tendon drive system and the propeller and rudder based system.

The Bollard pull test conducted involved the experimental equipment and set up shown in Figure A.2.1. Only the propeller tail system in isolation was used for this test to allow for direct measurement of the voltage and current from the PSU.

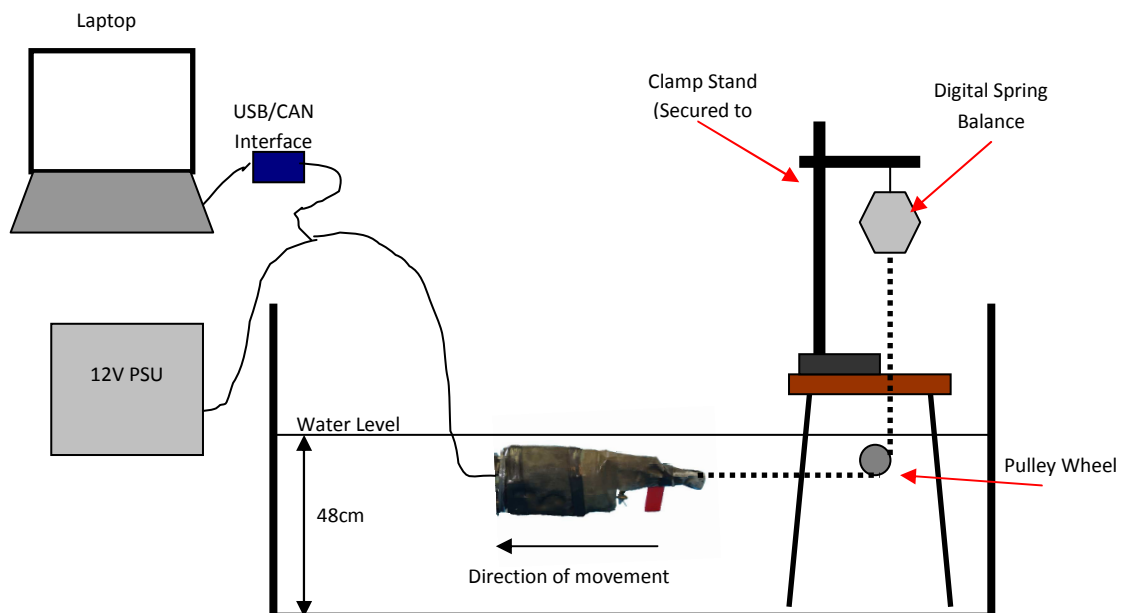


Figure A.2.1: Diagram of experimental set up used for bollard pull tests

Eight different duty cycle commands were sent to the DC motor controlling the propeller and the corresponding propeller rotational speed was continually updated and sent via the CAN bus to the laptop display. These parameters were noted along with the voltage and current displayed on the PSU. The weight reading from the digital spring balance was also recorded. This weight reading was then multiplied by the acceleration due to gravity (9.81 ms^{-2}) to provide an estimate of the force produced by the propeller. This experimental process was repeated for all six of the propellers investigated.

Results obtained for the thrust versus current for each propeller investigated is shown in Figure A.2.2.

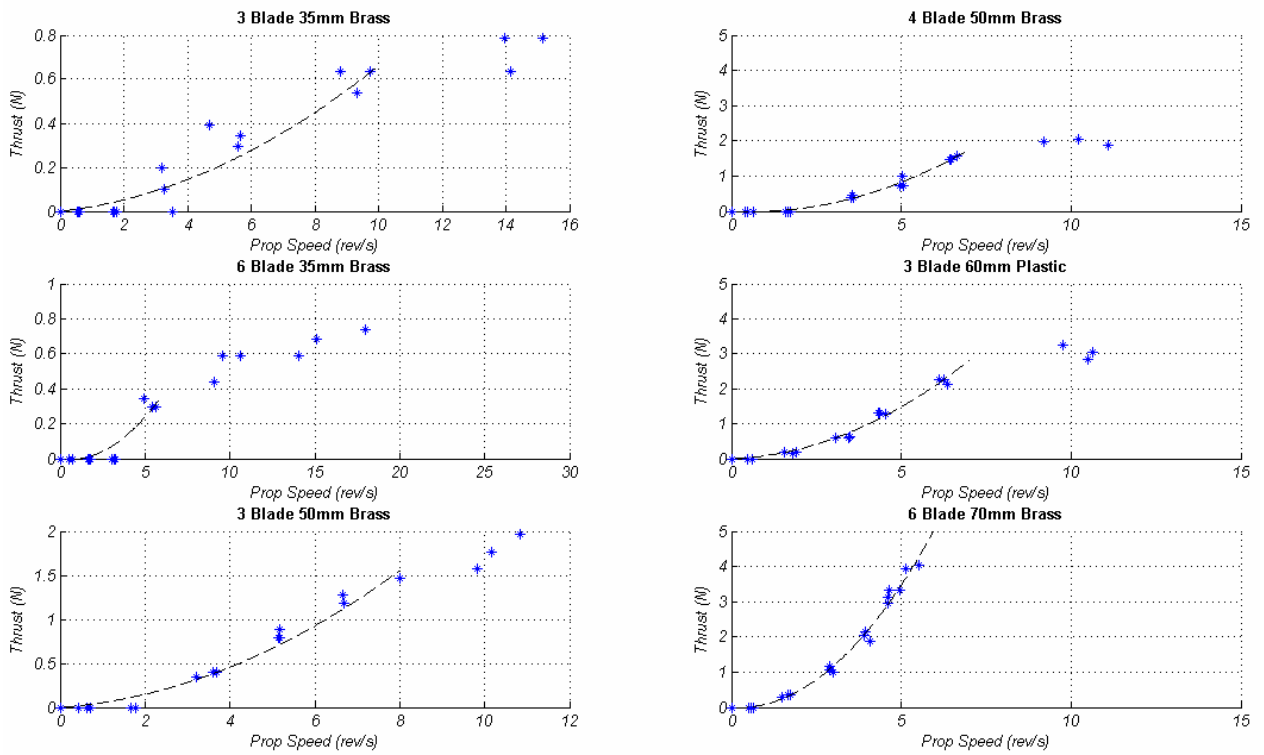
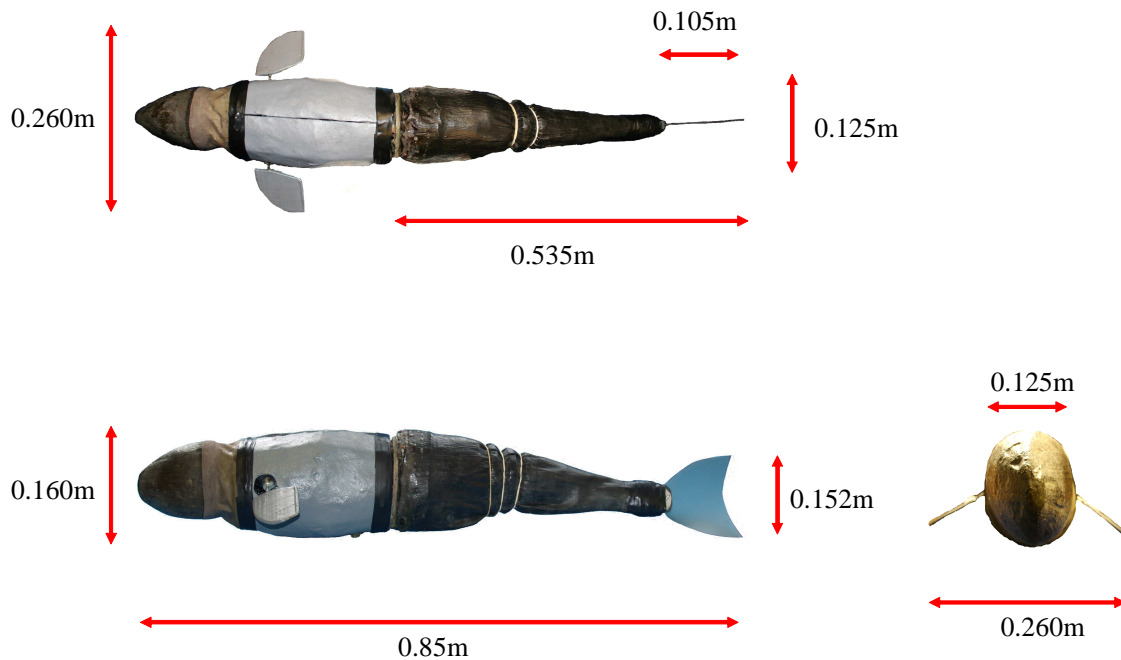


Figure A.2.2: Bollard pull experimental results for propeller speed vs thrust produced for the 6 propeller types tested.

From the thrust versus current results it is apparent that the 6 blade 70mm brass propeller provides significantly more thrust than any of the other propellers. Initial tests with this propeller when attached to the tail and body assembly showed that the surge velocities obtained were far greater than those obtainable with the tendon drive system. Therefore, the propeller selected was the 3 blade 50mm brass prop as this had a greater dynamic range and would allow for a similar range of surge velocities and so facilitate a direct comparison between the biomimetic system and the conventional system.

Appendix A.3 – RoboSalmon Vehicle Specifications

A.3.1 RoboSalmon Tendon Drive System Specifications



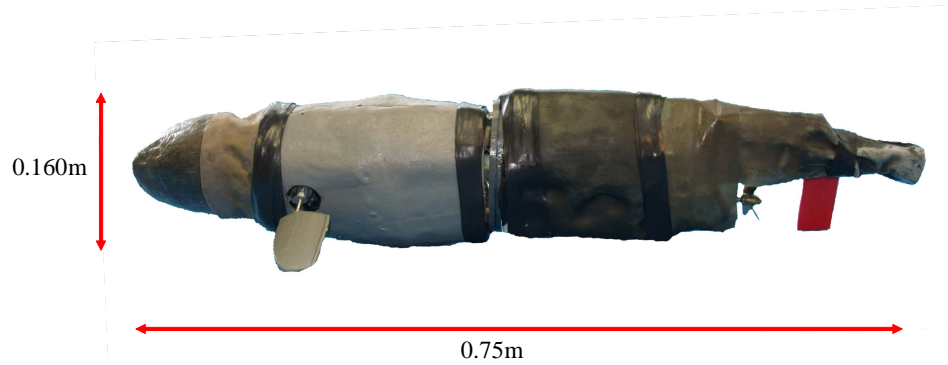
Vehicle specification

Total Mass	=	4.88 kg
Tendon Drive Mass	=	1.85 kg
Body Mass	=	3.03 kg
Displacement	=	4.9 Litres (approximately)
Power Source	=	6x NIMH AA

Servo Motor Specification

Model	=	HS-5645 Digital Servo
Gear Ratio	=	246:1
DC Motor	=	Mabuchi Motor RF-130CH
Inductance	=	0.1 H
Resistance	=	8.6 Ω
Torque Constant	=	0.0062 NmA ⁻¹
EMF Constant	=	0.0062 Vrad ⁻¹ s ⁻¹

A.3.2 RoboSalmon Propeller/Rudder System Specifications



Vehicle specification

Total Mass	=	4.88 kg
Propeller System Mass	=	1.88 kg
Body Mass	=	3.00 kg
Displacement	=	4.9 Litres (approximately)
Power Source	=	12x NIMH AA

Motor specification

Model	=	MFA Como Drills RE540/1
Gear Ratio	=	11:1
Inductance	=	0.1 H
Resistance	=	0.852 Ω
Torque Constant	=	0.00692 NmA^{-1}
EMF Constant	=	0.00692 $\text{Vrad}^{-1}\text{s}^{-1}$

Appendix B – Mathematical Model Equations

This appendix includes the equations used within the mathematical model of the *RoboSalmon*. The state equations for each of the 6 degrees of freedom is shown in equations (B.1) to (B.6).

$$\text{Surge:} \quad \dot{u} = \frac{mvr - mwq + X_t + X_D - Y_v vr + Z_w wq}{m - X_{\dot{u}}} \quad (\text{B.1})$$

$$\text{Sway:} \quad \dot{v} = \frac{-mur + mwp + Y_t + Y_D + X_{\dot{u}} ur - Z_w pw}{m - Y_{\dot{v}}} \quad (\text{B.2})$$

$$\text{Heave:} \quad \dot{w} = \frac{-muq + mvp + Z_D - X_{\dot{u}} uq + Y_v vp}{m - Z_{\dot{w}}} \quad (\text{B.3})$$

$$\text{Roll:} \quad \dot{p} = \frac{K_t + K_D - J_z qr + J_y qr - Y_v vw + Z_w vw - M_{\dot{q}} qr + N_r qr}{J_x - K_{\dot{p}}} \quad (\text{B.4})$$

$$\text{Pitch:} \quad \dot{q} = \frac{M_t + M_D - J_x qr + J_z rp - Z_w wu + X_{\dot{u}} wu + K_{\dot{p}} rp - N_r rp}{J_y - M_{\dot{q}}} \quad (\text{B.5})$$

$$\text{Yaw:} \quad \dot{r} = \frac{N_t + N_D - J_y pq + J_x pq - X_{\dot{u}} uv + Y_v uv - K_{\dot{p}} pq + M_{\dot{q}} pq}{J_z - N_{\dot{r}}} \quad (\text{B.6})$$

The kinematic relationships used to translate these body-fixed linear and angular velocities to linear and angular velocities in the Earth-fixed frame were shown in matrix form in Equations 4.5 and 4.6 in Chapter 4. Expanding this relationship for each degree of freedom produces Equations (B.7) to (B.12) [Fossen, 2002].

$$\begin{aligned} \dot{X}_E &= u \cos \psi \cos \theta + v(\cos \psi \sin \theta \sin \phi - \sin \psi \cos \phi) \\ &\quad + w(\sin \psi \sin \phi + \cos \psi \cos \phi \sin \theta) \end{aligned} \quad (\text{B.7})$$

$$\begin{aligned} \dot{Y}_E &= u \sin \psi \sin \phi + v(\cos \psi \cos \phi + \sin \phi \sin \theta \sin \psi) \\ &\quad + w(\sin \theta \sin \psi \cos \phi - \cos \psi \sin \phi) \end{aligned} \quad (\text{B.8})$$

$$\dot{Z}_E = -u \sin \theta + v \cos \theta \sin \phi + w \cos \theta \cos \phi \quad (\text{B.9})$$

$$\dot{\theta} = p + q \sin \phi \tan \theta + r \cos \phi \tan \theta \quad (\text{B.10})$$

$$\dot{\phi} = q \cos \phi - r \sin \phi \quad (\text{B.11})$$

$$\dot{\psi} = q \frac{\sin \phi}{\cos \theta} + r \frac{\cos \phi}{\cos \theta}, \quad \theta \neq \pm 90^\circ \quad (\text{B.12})$$

The constants used within the model are defined below:

Mass	m	=	4.88	kg
Length	l	=	0.85	m
Displacement	V	=	~4.9	L
Semi-axis	a	=	0.425	m
(Prolate Ellipsoid)	b	=	0.08	m
	c	=	0.08	m
Caudal Fin Height	h	=	0.15	m
Caudal Fin Length	l_{FIN}	=	0.105	m
Caudal Fin Area	A_{FIN}	=	0.0079	m ²
Moments of Inertia	J_x	=	0.0125	kgm ³
	J_y	=	0.1825	kgm ³
	J_z	=	0.1825	kgm ³
Added Mass Derivatives				
	$X_{\dot{u}}$	=	-0.4296	
	$Y_{\dot{v}}$	=	-4.1957	
	$Z_{\dot{w}}$	=	-4.1957	
	$K_{\dot{p}}$	=	0	
	$M_{\dot{q}}$	=	-0.1098	
	$N_{\dot{r}}$	=	-0.1098	

Appendix C – Model Validation

C.1 Tendon Drive System

This section provides the model validation data for the mathematical model of the tendon drive system. As discussed in Chapter 4 two methods of model validation are used; Analogue Matching and Integral Least Squares. The aim of this model validation section is to show how well the mathematical model of the *RoboSalmon* and associated propulsion systems represents the real system. This is achieved by comparing the simulation results with the experimental results for a number of different experiments. A multi-rate simulation technique was used, with the step size of the vehicle dynamics five times that of the motor dynamics.

The following sections contain the validation results for the both validation techniques used for five different experiments; 3 for straight swimming, 1 for turning from stationary and one for a pull out manoeuvre. On the validation results shown in the subsequent pages the experimental data is shown in red and the model data is shown in blue.

Due to the experimental equipment available the data gathered only allows for the model to be validated for surge and sway velocities, roll and yaw rates, caudal fin amplitude, and tail system current and x and y displacements. The diagram in Figure C.1 indicates how each of the sensor values relates to the motion of the body fixed frame of the *RoboSalmon* vehicle

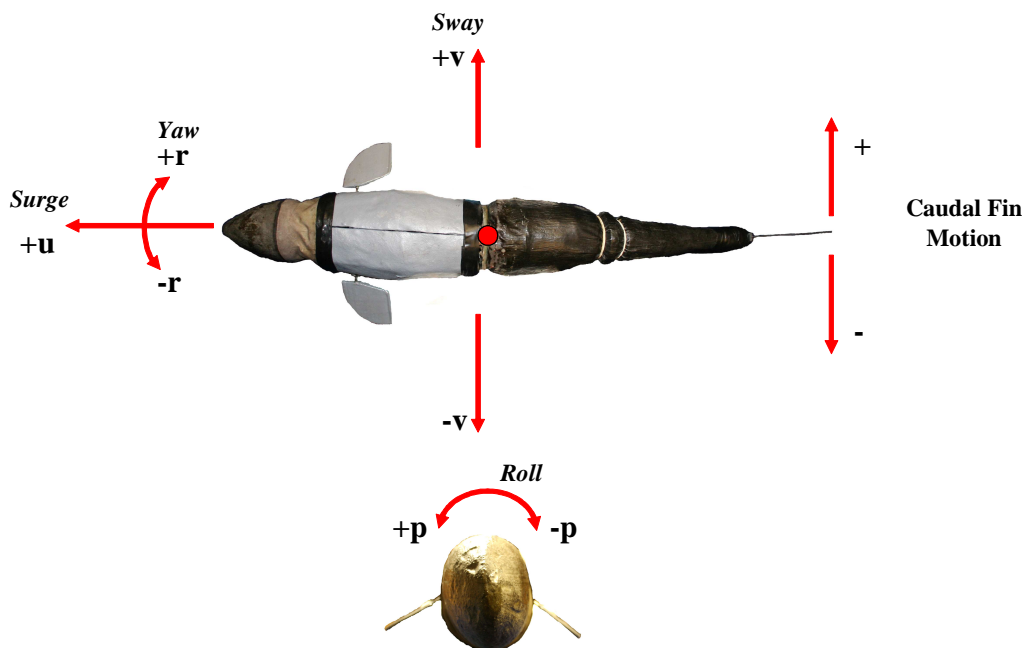


Figure C.1: IMU Sensor Orientations

Program 5 – Forward Swimming Validation (1)

This experimental program is for straight swimming and has a nominal tail beat frequency of 0.38Hz and a nominal beat amplitude of 0.105m. The analogue matching results are shown in Figure C.2.

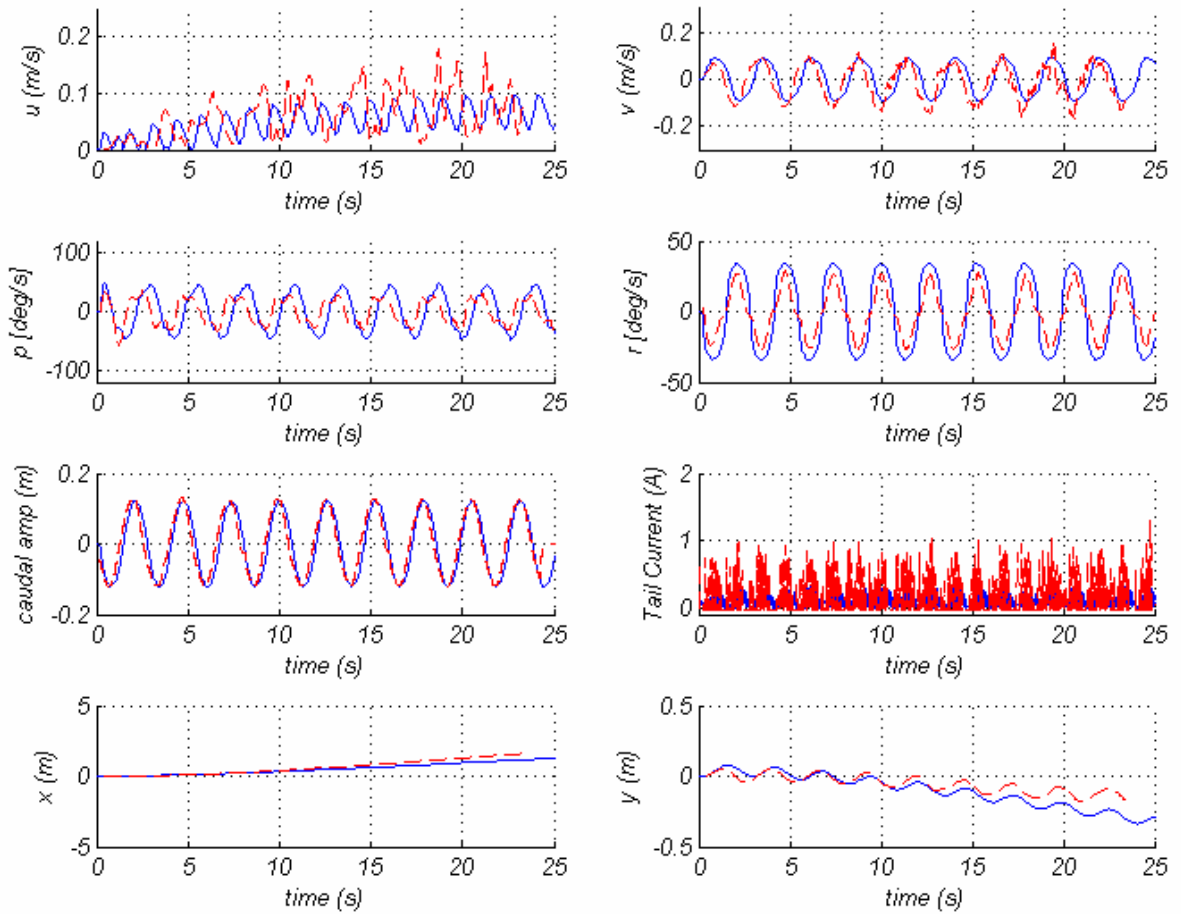


Figure C.2: Analogue matching validation for program 5 (Forward Motion), red trace experimental data, blue trace simulation

Table C.1: Model Validation ILS Values for Program 5 (Forward Motion)

Variable	ILS Values
u (ms^{-1})	1.25
v (ms^{-1})	10.29
p (degs^{-1})	2023400
r (degs^{-1})	940880
Caudal Fin Amplitude (m)	23.89
Tail Current	112.27
x (m)	24.88
y (m)	7.32

Program 8 – Forward Swimming Validation (2)

This experimental program is for straight swimming and has a nominal tail beat frequency of 0.61Hz and a nominal beat amplitude of 0.075m. The analogue matching results are shown in Figure C.3.

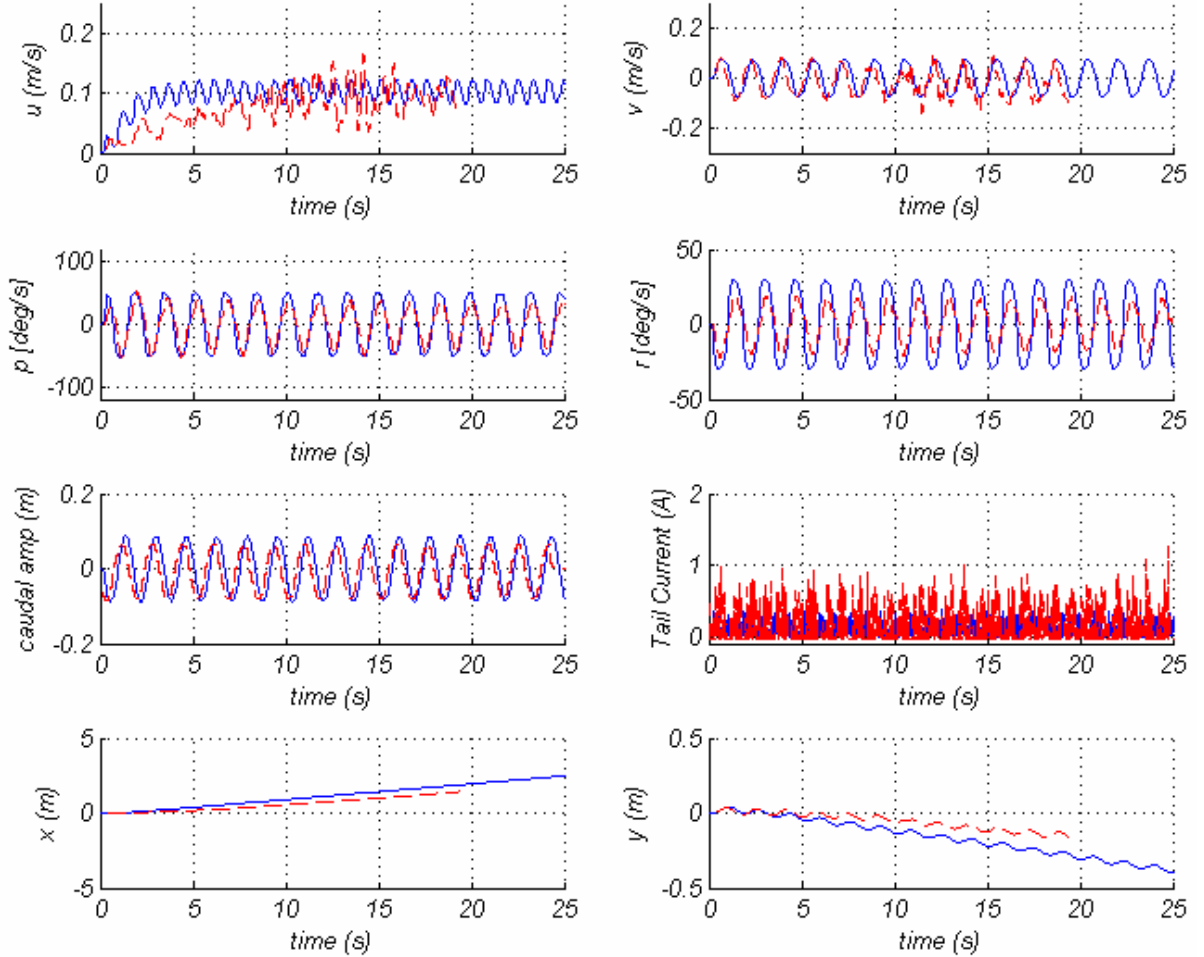


Figure C.3: Analogue Matching Validation for Program 8 (Forward Motion), red trace experimental data, blue trace simulation

Table C.2: Model Validation ILS Values for Program 8 (Forward Motion)

Variable	ILS Values
u (ms^{-1})	0.93
v (ms^{-1})	2.95
p (degs^{-1})	8731700
r (degs^{-1})	1729630
Caudal Fin Amplitude (m)	14.86
Tail Current	112.78
x (m)	67.7
y (m)	16.2

Program 18 – Forward Swimming Validation (3)

This experimental program is for straight swimming and has a nominal tail beat frequency of 0.61Hz and a nominal beat amplitude of 0.15m. The analogue matching results are shown in Figure C.4.

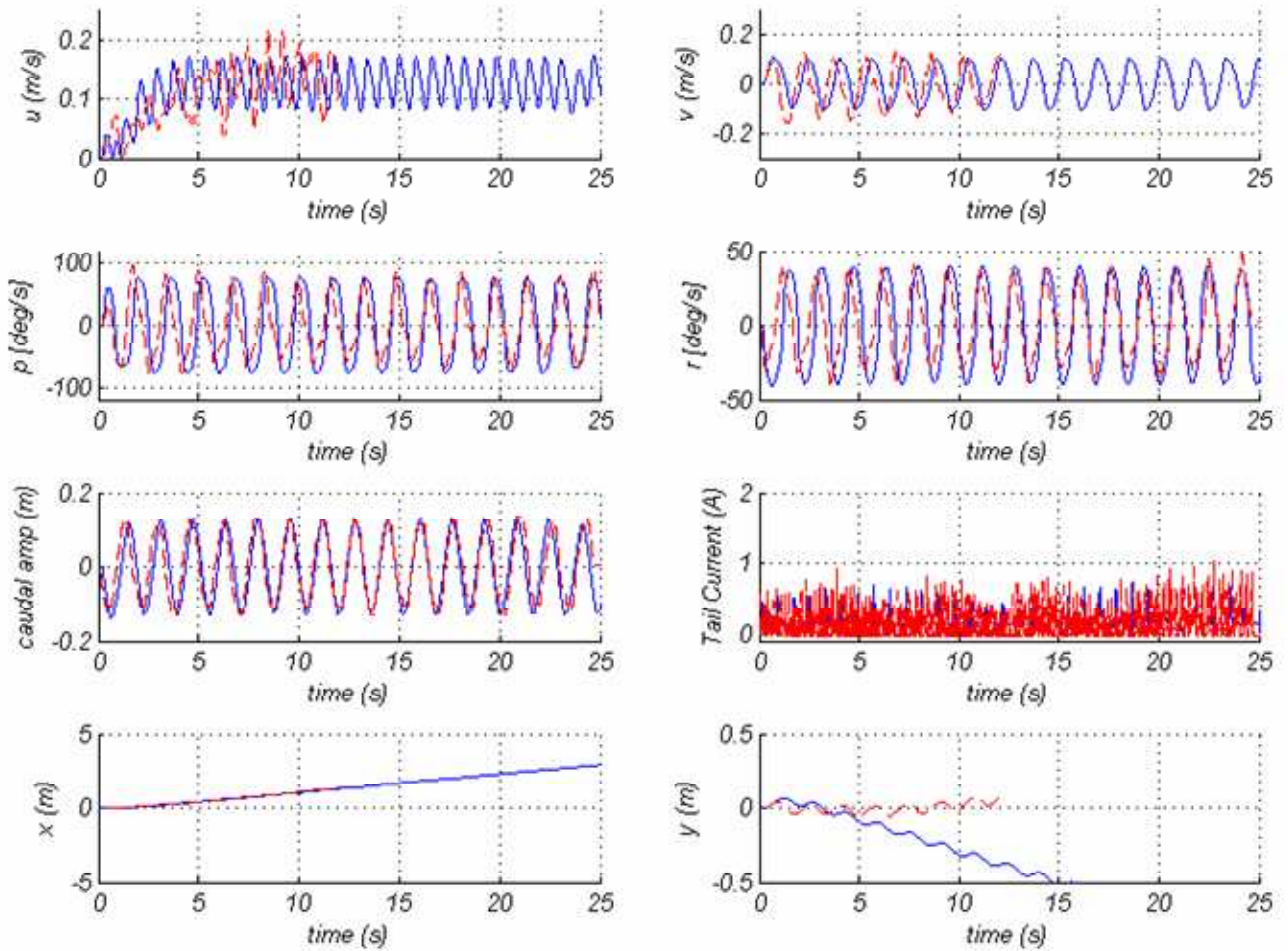


Figure C.4: Analogue Matching Validation for Program 18 (Forward Motion), red trace experimental data, blue trace simulation

Table C.3: Model Validation ILS Values for Program 18 (Forward Motion)

Variable	ILS Values
$u \text{ (ms}^{-1}\text{)}$	0.85
$v \text{ (ms}^{-1}\text{)}$	5.4358
$p \text{ (degs}^{-1}\text{)}$	297580
$r \text{ (degs}^{-1}\text{)}$	226650
Caudal Fin Amplitude (m)	2.37
Tail Current	59.16
$x \text{ (m)}$	0.49
$y \text{ (m)}$	10.05

Program 42 – Turning from Stationary Validation (1)

This experimental program is for turning from stationary manoeuvre and has a nominal tail beat frequency of 0.61Hz and a nominal beat amplitude of 0.105m and a tail offset of -25 degrees. The analogue matching results are shown in Figure C.5.

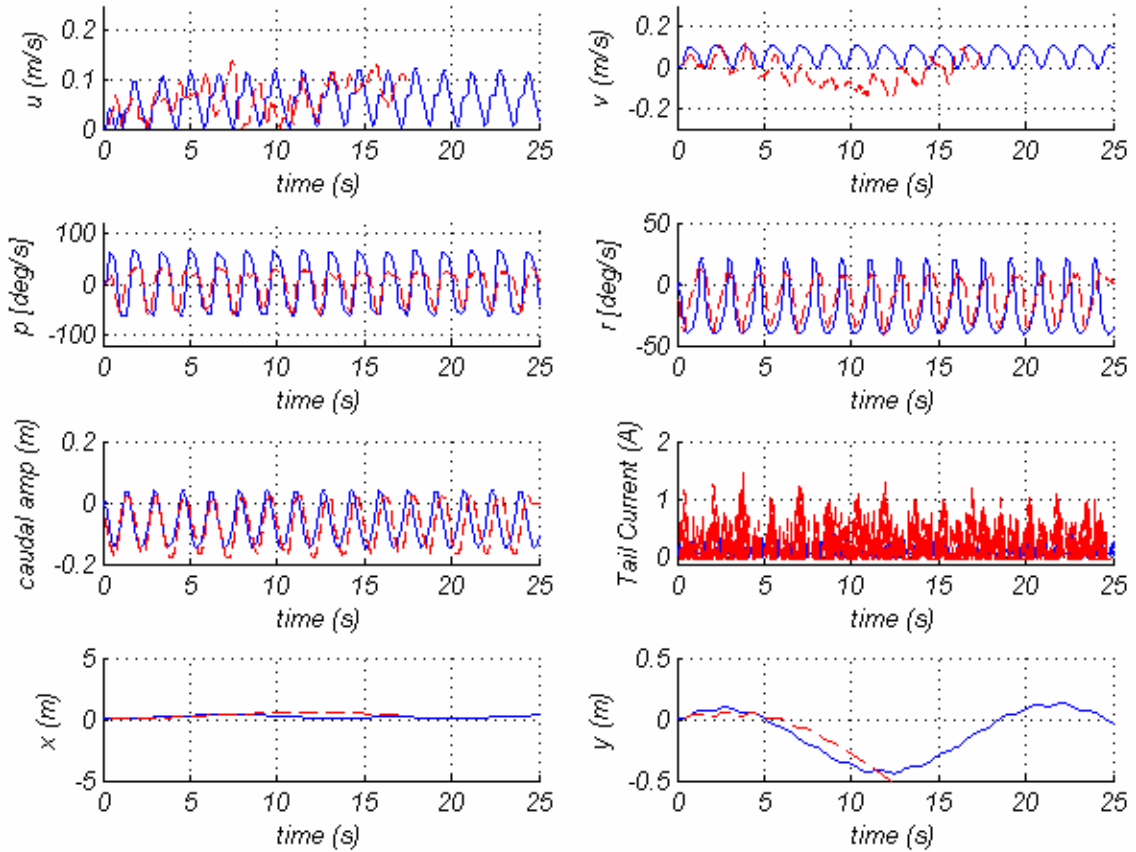


Figure C.5: Analogue Matching Validation for Program 42 (Manoeuvring), red trace experimental data, blue trace simulation

Table C.4: Model Validation ILS Values for Program 42 (Manoeuvring)

Variable	ILS Values
$u \text{ (ms}^{-1}\text{)}$	1.07
$v \text{ (ms}^{-1}\text{)}$	3.22
$p \text{ (degs}^{-1}\text{)}$	9422100
$r \text{ (degs}^{-1}\text{)}$	3112200
Caudal Fin Amplitude (m)	70.93
Tail Current	160
x (m)	30.34
y(m)	193.54

Program 128 – Pull Out Manoeuvre Validation

This experimental program is for a Pull Out manoeuvre and has a nominal tail beat frequency of 0.48Hz and a nominal beat amplitude of 0.075m. The *RoboSalmon* swims straight for 10 seconds then implements a -16 degree tail offset for two seconds then removes the offset and swims straight. The analogue matching results are shown in Figure C.6.

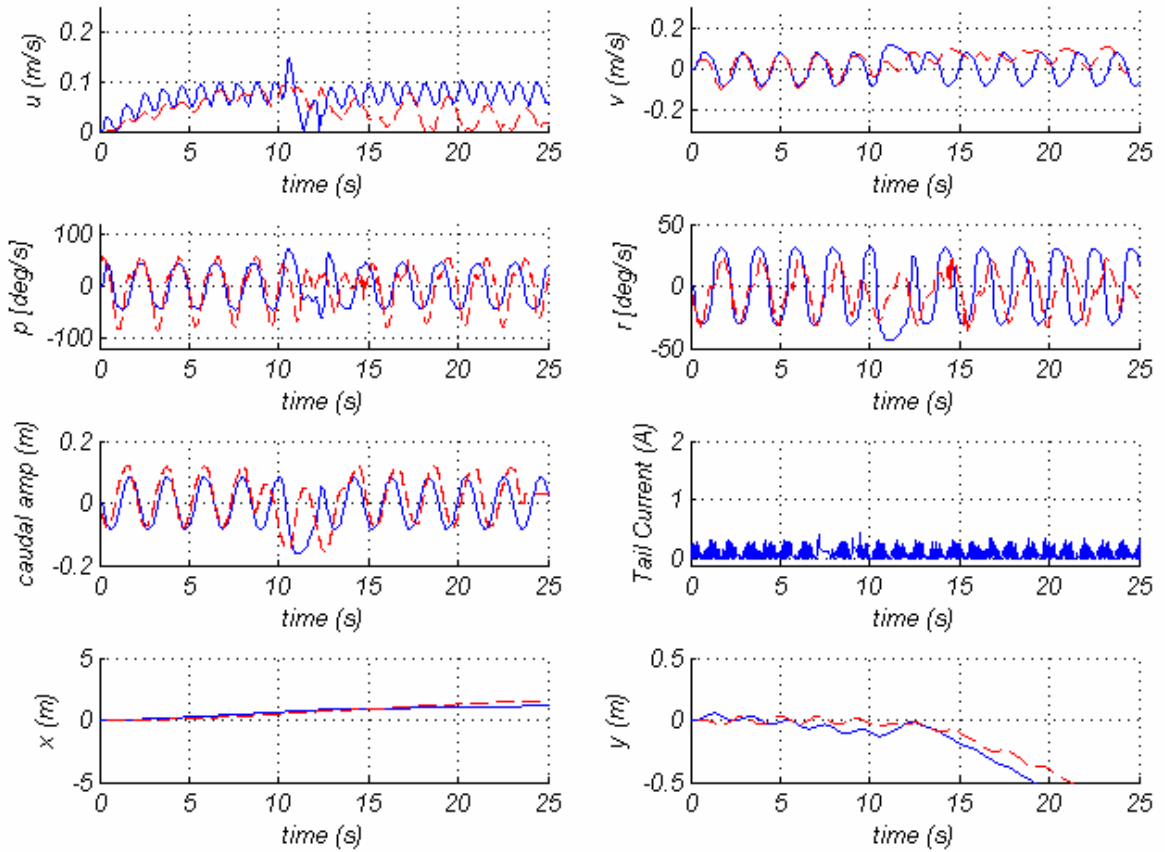


Figure C.6: Analogue Matching Validation for Program 128 (Pull Out Manoeuvre), red trace experimental data, blue trace simulation

Table C.5: Model Validation ILS Values for Program 128 (Pull Out Manoeuvre)

Variable	ILS Values
u (ms^{-1})	1.00
v (ms^{-1})	5.14
p	4458100
r	1405200
Caudal Fin Amplitude (m)	37.48
Tail Current	*
x (m)	19.75
y (m)	6.0856

* No current data is available for pull out Manoeuvres due to fault in current sense circuit